Factor Graph-based Receivers for Multi-Carrier Transmission in Two-Way Relaying and Massive Machine Type Communications

Dissertation
zur Erlangung des akademischen Grades
Doktor der Ingenieurwissenschaften (Dr.-Ing.)
vorgelegt dem Fachbereich 1 (Physik/Elektrotechnik)
der Universität Bremen

von

Dipl.-Ing. Matthias Woltering

Tag des öffentlichen Kolloquiums:	22. Okt. 2019
Gutachter der Dissertation:	Prof. Dr.-Ing. A. Dekorsy
	Prof. Dr.-Ing. T. Kaiser
Weitere Prüfer:	Prof. Dr.-Ing. K.-D. Kammeyer
	Prof. Dr.-Ing. M. Schneider

Universität Bremen

Bremen, Okt. 28, 2019

Danke für dein Lächeln!

07.07.2019

Preface

Die vorliegende Arbeit entstand während meiner Tätigkeit als wissenschaftlicher Mitarbeiter am Arbeitsbereich Nachrichtentechnik des Instituts für Telekommunikation und Hochfrequenztechnik der Universität Bremen.

Mein ausdrücklicher Dank gilt Herrn Prof. Dr.-Ing. Armin Dekorsy dafür, dass er mir die Promotion ermöglichte und mich stets dabei unterstützte. Hierbei sind die vorbildliche Betreuung während meiner Zeit im Arbeitsbereich und die zahlreichen Hinweise und Vorschläge während meiner Arbeit hervorzuheben.

Ebenfalls herzlich bedanken möchte ich mich bei Herrn Prof. Dr.-Ing. Thomas Kaiser von der Universität Duisburg für die Erstellung des Zweitgutachtens und seine wertvollen Anmerkungen zu dieser Arbeit sowie bei den Herren Prof. Dr.-Ing. Karl-Dirk Kammeyer und Prof. Dr.-Ing. Martin Schneider für ihre Tätigkeit als Prüfer.

Für das angenehme, freundschaftliche und familiäre Arbeitsklima über Jahre danke ich sämtlichen Kollegen. Den Herren Dr.-Ing. Dirk Wübben, Dr.-Ing. Carsten Bockelmann, Dr.-Ing. Florian Lenkeit und Dr.-Ing. Fabian Monsees gilt mein ganz besonderer Dank für zahlreiche fachliche Diskussionen und Anregungen, die diese Arbeit in nicht unerheblichem Maße beeinflusst haben. Ganz besonders gilt mein Dank den beiden letztgenannten, denen ich fachlich sowie privat sehr viel zu verdanken habe.

Ihnen sowie Dipl.-Ing. Ban-Sok Shin und M.Sc. Johannel Demel bin ich weiterhin verbunden für die sorgsame Durchsicht des dieser Arbeit zugrunde liegenden Manuskripts.

Darüber hinaus danke ich der Deutschen Forschungsgemeinschaft (DFG) für die teilweise Finanzierung meiner Forschungstätigkeit.

Zuletzt möchte ich mich herzlichst bei meiner Familie und insbesondere meinem Vater und meiner Mutter bedanken, die immer hinter mir stehen und standen. Ihre bedingungslose Unterstützung in meiner bisherigen Karriere und gerade in der letzten Phase der Fertigstellung dieser Arbeit hatte einen großen Anteil am Gelingen meiner Promotion. Ohne ihren Rückhalt wäre diese Arbeit nicht zustande gekommen.

Bremen im Oktober 2019

Matthias Woltering

Contents

Chapter 1

Introduction

1.1 Motivation and Focus

The nature of communication has evolved in recent years from purely human driven communication—with the demand for voice calls and simple data packages such as short message service (SMS)—to a mixture of high-speed human communication and machine-driven communication [Sch15, KD18]. This leads to networks that support an increasing number of services with different Quality of Service (QoS) requirements and an increasing number of devices. This development comes at the expense of a wide range of different needs of services that have serious implications for the architecture of mobile communication systems. Some forecasts predict an explosion of connected devices already in the near future [Cis19].

In the history of mobile communication systems, the first generation (1G) was developed primarily for the human voice. Also, the first development for digital mobile communication in Global System for Mobile Communications (GSM) (2G) was mainly designed for the transmission on *human speech*. Here, the communication between a base station (BS) and the user is realized as a single-carrier (SC) transmission with Gaussian minimum shift keying (GMSK) with a possible maximum data rate of 9.6 kbit/s for small data transmissions. The application of General Packet Radio Service (GPRS) (practically up to 54 kbit/s) by the use of channel bundling and Enhanced Data Rates for GSM Evolution (EDGE) (with up to 220 kbit/s) by using a more efficient symbol mapping 8-phase shift keying (PSK) exhausted the opportunity for further growth, but enabled the first meaningful use in terms of usability of data services for the Internet via Wireless Application Protocol (WAP). The third generation (3G) Universal Mobile Telecommunication

System (UMTS) was designed to handle upcoming demand on *data services* over the air and the Physical (PHY) layer multiple access (MA) scheme is based on the code domain, where users are multiplexed using code division multiple access (CDMA), *i.e.* by different code sequences. Data rates of up to 384 kbit/s can be achieved here. With the extension to High Speed Packet Access (HSPA) with higher-order symbol mapping and the application of multiple input multiple output (MIMO) techniques, data rates of up to 42 Mbit/s are achievable.

The current standard in the mobile communications world is Long Term Evolution (LTE) (4G), where a more *flexible design* was the main criterion to cover a wide range of applications. The PHY layer multiple access scheme is orthogonal frequency division multiple access (OFDMA)-based on cyclic prefix-based orthogonal frequency division multiplexing (CP-OFDM), which is an orthogonal multi-carrier (MC) scheme that applies a rectangular waveform to each sub-carrier. It offers simple 1-tap frequency domain equalization techniques for synchronous transmissions. The separation into time-slots and sub-carriers allows a flexible assignment of the data symbols to this so called time-frequency (TF) grid (also called resource elements in LTE). LTE is designed by flexible use of bandwidth configurations, *i.e.* B=1.4 MHz, 3 MHz, 5 MHz, 10 MHz, 15 MHz and 20 MHz to achieve data rates up to 300 Mbit/s.

Further progress in the context of 4G has been achieved in LTE-advanced through the application of carrier aggregation, an improved implementation of the multi-antenna technique MIMO with 8x8 MIMO in the downlink. Additionally, relay nodes are introduced in LTE-advanced, which are small base stations with low power to increase the coverage and decrease the power needed to serve a higher number of devices. However, LTE and LTE-advanced have been tailored to meet the needs of high bandwidth of wirelessly connected users. To this end, the PHY layer was designed to be strictly synchronous and orthogonal during transmission.

In contrast, the new communication needs such as in two-way relaying channel (TWRC), in *massive* machine type communication (mMTC) or others suffer from the cumbersome synchronism implementation for a massive number of devices [Wu17, BPN$^+$16, SW19]. Accurate synchronization is difficult to implement and disproportionate, especially with a massive number of user nodes. Since the goal for the future is that even small active devices such as mobile phones or other devices should support the network, the limitation to orthogonal and synchronous systems is hardly possible.

In the past, the application of CP-OFDM in LTE has still shown the flexibility of this MA scheme. The MC transmission schemes with their flexible assignment of time and frequency resources form the basis for future systems. However, the use of new waveforms with better spectral shape is preferred to the rectangular waveform used in CP-OFDM in LTE.

For this reason, the need for a new MC scheme using waveforms with well-localized shape in time and frequency domain and flexible use of resources in both dimensions was addressed in several major projects such as 5th Generation Non-Orthogonal Waveforms for Asynchronous Signalling (5GNOW), Physical Layer For Dynamic Spectrum Access And Cognitive Radio (PHYDYAS), and Mobile and wireless communications Enablers for the Twenty-twenty Information Society (METIS) for the new 5th Generation (5G) of the mobile communication system and beyond [MA15, MHMR18, LZ16].

Accompanying the development of this dissertation, the mobile community has seen numerous waveform suggestions for the so-called 5G new radio [DPS18]. Most of the proposals that are MC waveforms are variants of CP-OFDM. The trend is to optimize CP-OFDM in some way—sub-carrier filtering or pulse shaping, filtering groups of sub-carriers that allow successive symbols to overlap over time, eliminating cyclic prefixes, replacing cyclic prefixes with zeros or another sequence [MA15]. Various waveforms have become strong competitors for 5G—numerous research publications have shown that CP-OFDM has been outperformed [ZBT$^+$16]. For a long time, it looked like any MC waveform could be part of 5G, except CP-OFDM.

In December 2018 the first definition of the 5G standard according to Third Generation Partnership Project (3GPP) Release 15 was published [3GP18] and updated in March 2019 [3GP19]. For 5G according to 3GPP Release 15, the standardization organization had decided to use CP-OFDM as the access method [DPS18]. Unlike LTE, 5G now also supports the CP-OFDM method in the uplink.

Today, from a standardization perspective, CP-OFDM seems to be the best choice of key performance indicators—multi-antenna compatibility, high spectral efficiency. Especially the low implementation complexity and the already broad development of software and hardware, which already exists, was a main argument for the decision to reuse CP-OFDM for the new radio 5G. Nevertheless, the new needs in communication will further lead to discussion that the traditional orthogonal frequency division multiplexing (OFDM) will be unable to meet many new demands required for the new mobile generations by its own and the research and development on other waveforms is still ongoing in the future.

Consequently, an overall system design must be robust in terms of timing inaccuracies. The design of the waveforms improves robustness against transceiver mismatches, and as adequate synchronization of multiple distributed nodes is a difficult task, adapting these innovative non-orthogonal waveforms to different scenarios, such as two-way relaying systems [Sch16] and mMTC communication [HWC+17], is a very promising approach.

1.2 Thesis Origin and Objectives

Future communication systems will have to be much more flexible to the needs of users and the underlying applications. It is becoming apparent that in the future many devices with different requirements will want to exchange information wirelessly. Simple single point-to-point (P2P) links alone will no longer be sufficient to meet this need for communication. In addition to P2P, we consider two further scenarios for improving the individual needs of the underlying technology.

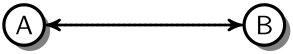

Figure 1.1: Point to point transmission.

- An important scenario beside unidirectional P2P transmission (shown in Fig. 1.1) is **two-way relaying (TWR) transmission**, where data symbols are exchanged via an auxiliary relay, as shown in Fig. 1.2. For example, relaying is considered as a key technology on the PHY layer to enhance future wireless communication systems in terms of coverage extension and system throughput and was introduced in LTE-advanced. However, since the deployment of relay nodes also entails impairments due to the half-duplex constraint, sophisticated cooperative communication approaches are indispensable. In order to support the exchange of messages between two nodes, the concept of two-way relaying has recently aroused tremendous interest starting by the application of network coding (NC) [ACLY00], as it enables the simultaneous transmission of both directions using the same resources. The relay may be a low-power cellular base station, another mobile subscriber in a communication environment, or even a satellite, for example, when we look at space communication. To improve effective bandwidth efficiency, both data streams are sent simultaneously to the relay, which is sensitive against synchronization errors. Innovative

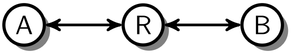

Figure 1.2: Two-way relay transmission.

waveforms and advanced coding and modulation concepts, including **physical layer network coding (PLNC)**, are urgently needed to achieve high spectral efficiency while remaining robust to imperfections in the transceiver design [HLL14].

- Another challenge for future wireless communication systems is a **massive number** of Internet of Things (IoT) devices that do not explicitly require an increased data rate. This third scenario is a **multi-point transmission** illustrated in Fig. 1.3, in which a massive number of cheap sensor nodes wants to transmit their status to a base station. They have a completely different type of communication, such as sporadic transmission of really small data packets for sending simple status messages. This property was also seen by the 3GPP group, so they defined a first step to operate IoT devices with LTE in a narrow band and it is therefore called narrow band Internet of Things (NB-IoT)[WLA+17, 3GP17]. In such a scenario with a massive number of nodes, the probability of concurrent transmission of nodes is very high and was so far avoided by collision avoidance techniques, and resources are still specified orthogonal, which reduces the efficiency and limits the number of devices served. One approach to solving this problem is to apply direct random access (DRA) to the PHY layer to reduce the amount of signaling required for such a scenario. A key technology for estimating the unknown activity information in DRA is **compressed sensing-multi-user detection (CS-MUD)**, in which the activity of the nodes and the transmitted data are estimated together. This scenario also requires a robust MA scheme that allows reliable communication from a massive number of devices to a BS. In particular, the new requirement for the mobile interface are changing because the type of communication is changing to a sporadic transmission of small packets with high reception accuracy.

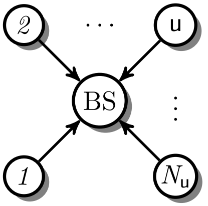

Figure 1.3: Multi-point transmission.

> This change will be a major challenge for the design of new PHY layer solutions in the future.

Nevertheless, in all these three scenarios a synchronous transmission is helpful or even required, but the realization is cumbersome and sometimes impossible. For TWR transmission, it has been already shown that these timing and frequency offsets can lead to considerable degraded performance in the transmission to the relay **[WLW^{+}14]** and [Wu17]. The multi-point channel, which serves a much higher number of users, is also sensitive to these affected offset transmissions. A key technology already mentioned, *i.e.* MC methods with well-localized waveforms, for future systems were already proposed in the early 1960s by Saltzberg and Chang [Sal67, Cha66]. These schemes are proved to be very robust MC methods for single point transmissions [BN10] and further offer a good spectral shape. Furthermore, non-orthogonal MC schemes are even more promising in an offset affect transmission [KM98]. These technologies can be seen as one key components for the two-way and multi-point channels mentioned above, as unfortunately one cannot remove or ignore the timing and frequency offsets but has to deal with them.

Thus, the scope of this work is the application of MC schemes with well-localized waveforms in the above mentioned scenarios to improve the performance under timing and frequency offsets.

However, the non-orthogonal MC schemes applying well-localized waveforms will always inherently introduce interference terms even in a perfectly synchronized transmission, and the challenge is to design an equalizer being able to deal with the introduced but known interference. Therefore, the use of MC schemes with non-orthogonal waveforms inherently includes an equalizer design, which is found in this work with the concept of the factor graph-based approach as a realizable and flexible solution. Especially the interaction of the selected waveform and the resulting influence on the receiver provides a design framework that can adapt very well to the channel conditions.

MC schemes with well-localized waveforms and factor graph-based equalizer (FGE) in TWR transmission, and multi-point channel are very interesting for the future demand, which have been investigated only individually so far. In an OFDM setup, however, some publications exist that analyze a combination of TWR and FGE. To the best of the author's knowledge, there are no publications other than his own, that analyze non-orthogonal MC with general waveforms and FGE in P2P, TWR or multi-point context. The goal of this thesis is, thus, to partially close this gap by giving an overview of the potential of non-orthogonal MC schemes and a proper adapted equalizer design. To this end, the presented schemes are investigated regarding their performance under timing and frequency offsets towards the application in future mobile communication systems.

1.3 Contribution and Thesis Structure

The main contribution of the work can be found in its own previous publications and is highlighted in relation to each of the following chapters. Additionally, the state of the art (SotA) of MC, TWRC and CS-MUD are given also in the related chapters.

- **Chapter 2** discusses the basics of P2P transmission in terms of the underlying structure, such as channel coding, symbol mapping, a brief discussion of general MC transmit signals, and the transmission over a physical doubly-dispersive channel. First extensions to multi-point channels and the general but brief discussion of factor graph (FG)-based symbol estimation are given for P2P reception, which serves as basis for the following chapters. A deeper description on FGs and estimation techniques can be found in **Appendix B**.

- Since MC transmission is the fundamental consideration of this thesis, **Chapter 3** focuses on famous MC candidates known from literature. In addition to the famous orthogonal CP-OFDM, also windowed-cyclic prefix-orthogonal frequency division multiplexing (w-CP-OFDM), universal filtered - orthogonal frequency division multiplexing (UF-OFDM), and offset quadrature amplitude modulation/orthogonal frequency division multiplexing (OQAM/OFDM) are introduced as orthogonal schemes. Furthermore, the promising non-orthogonal candidates like quadrature amplitude modulation/filter-bank multi-carrier (QAM/FBMC), general frequency division multiplexing (GFDM), and cyclic prefix-based filter-bank multi-carrier (FBMC) (CP-FBMC) are introduced [**SPS+15**]. All schemes are classified and a common representation for all MC schemes in a uniform context is derived in this thesis, which serves as a basis for the subsequent chapters. The schemes are compared in terms of spectral shape and the properties of the effective channel matrix.

- **Chapter 4** is based on the preliminary work of the project priority program “Communication in Interference Limited Networks (COIN)”, which was partially supported by the German Research Department (DFG) and summarized in [WLW+16a, WLW+16b, Uts16]. The content and achievements of this chapter are based on the third part of this project COIN III titled “Joint Optimization of Generalized MC Waveforms and Power Allocation for Two-Way Relay Systems”.

- Following the introduction of the fundamental idea of a TWRC based on Fig. 1.2, the considered system model, and PLNC detection schemes known from literature, the combination of general MC schemes, in particular quadrature amplitude modulation (QAM)-based FBMC, and TWRC is introduced. Initial analyses related to the combination were published in [**SWW$^+$14**].
- Next, the pure effects of synchronous frequency-flat channels and the influence of the general MC schemes in TWRC are analyzed. In the publication [**WLW$^+$14**], the sensitivity of carrier frequency offset (CFO) were shown by a CP-OFDM-based software-in-the-loop implementation on hardware demonstrators of the Arbeitsbereich Nachrichtentechnik (ANT) institute.
- Based on the findings that the system is very sensitive to frequency and timing offsets, the even more extreme impact of doubly-dispersive channels in TWRC with general waveforms is the topic of the subsequent discussion and are part of the work [Min15] and published in [**WWD$^+$15b**] by the application of a linear equalizer, [**WWD15a**] with additional soft interference cancellation (sIC)
- Since offset quadrature amplitude modulation (OQAM)-based FBMC is also a MC scheme applying well-localized waveforms and being known to be robust in P2P scenarios, a comparison between OQAM-based and QAM-based FBMC was shown in [**WZWD16**], which shows that QAM-based FBMC has superior performance than OQAM-based FBMC in a one antenna case with relaying and is not that sensitive against phase errors.
- Almost all previous results are summarized in the book chapter [**WSW$^+$16**]. Therein, the equalizer at the relay is based on these linear equalization concepts and on sIC.
- Different receiver structure known from literature are represented by FGs and extended to deal with the influences of the doubly-dispersive channels and general waveforms. The combination of general waveforms and the FGE at the relay provides control over the computational complexity and error rate performance at the relay. The concept of FGE, robust MC schemes with general waveform in TWRC was first presented in [**WWD16**] by the author and the journal article [**WWD18**] consolidates this concept to obtain the final structure as presented here.

In addition to the conference and journal publication, the main contribution of this chapter lies in the common consideration of all introduced schemes. Furthermore, various simulation performance evaluations were performed and are shown and discussed.

- **Chapter 5** introduces a practical system concept for the multi-point scenario in Fig. 1.3, which, in contrast to current radio transmission standards, is tailored to the requirements of mMTC. For this purpose, three key components are combined to fit the needs of a such a system: 1) CS-MUD for detection of a massive number of nodes, 2) MC transmission applying well-localized waveforms for allocating the sensor nodes within a narrow-band system, and 3) non-orthogonal pilot symbols. The combination of these key components allows the use of DRA with a significant reduced signaling overhead.
    - The combination of all components is called multi-carrier compressed sensing multi-user detection (MCSM) and allows a simple sensor node implementation with low signaling overhead as introduced in [**MWBD15b**]. This makes it possible to use very cheap sensor nodes and shifts the detection of activity and data estimation to the BS.
    - This chapter addresses the key challenges for aggregating a massive number of machine type communication (MTC) especially in an asynchronous reception, which is also addressed by [**MWBD15a**].
    - Beyond the simulative evaluation of MCSM in this chapter, practical verification through a CP-OFDM-based software-in-the-loop implementation of MCSM was demonstrated on hardware demonstrators published in [**BMWD15, WMBD16**]. Here we were able to show that simulations and practical over the air transmissions match.
    - However, the need for a further generalization to the use of robust MC schemes is required because in a realistic scenario synchronization of a massive number of nodes is difficult or somehow infeasible. The main new contribution of this thesis is given within this chapter by the extension of MCSM with general MC schemes, which provides better activity and data detection under offset-affected reception at the BS. Furthermore, the use of a FG-based data estimation in MCSM with simple channel estimation technique is proposed. These new concepts have not been published yet.

The MCSM system concept is filed as a patent under [**MWBD16a**] in Germany, [**MWBD15c**] in Luxembourg, [**MWBD16b**] at the European patent office, the Patent Cooperation Treaty (PCT) [**MWBD16c**], [**MWDB18b**] in the USA, and [**MWDB18a**] in China.

1.4 Notation and Conventions

Here, the most important nomenclature of the entire thesis is given. Unless otherwise stated, this nomenclature applies to all parts of this work. The extended list of this nomenclature can be found in the list of symbols at the end of this work.

- Small italic characters denote scalars a and bold lowercase characters denote a column vector $\mathbf{a}$. Upper case bold characters denote a matrix $\mathbf{A}$.
- One column of a matrix $\mathbf{A}$ is given by $\mathbf{A}_{:,j}$ and one row of a matrix $\mathbf{A}$ by $\mathbf{A}_{i,:}$.
- The vector operator $\mathbf{a} = \text{vec}\{\mathbf{A}\}$ stacks each column $\mathbf{A}_{:,i}$ into a vector consecutively or vice versa using $\mathbf{A} = \text{vec}\{\mathbf{a}\}$.
- An underlined letter $\underline{\mathbf{a}}$ is used for a frame of signals. Thus, $\underline{\mathbf{a}}$ is a stacked column vector and $\underline{\mathbf{A}}$ is a stacked matrix.
- Sets are indicated by calligraphic characters $\mathcal{A}$ and $|\mathcal{A}|$ is the cardinality of the set.
- The $\text{diag}\{\mathbf{A}\}$ operator returns the diagonal elements of the matrix $\mathbf{A}$. A pure diagonal matrix, where non-zero elements are only on the main diagonal of a matrix is denoted by $\mathbf{\Sigma}$.
- A letter with tilde $\tilde{a}$, $\tilde{\mathbf{a}}$, or $\tilde{\mathbf{A}}$ denotes a soft estimate of the corresponding variable a, $\mathbf{a}$, or $\mathbf{A}$, respectively.
- A letter with hat $\hat{a}$, $\hat{\mathbf{a}}$, or $\hat{\mathbf{A}}$ denotes a hard estimate of the corresponding variable a, $\mathbf{a}$, or $\mathbf{A}$, respectively.
- The transposed of a matrix $\mathbf{A}$ is denoted by $\mathbf{A}^{\mathsf{T}}$ and $\mathbf{A}^{\mathsf{H}}$ denotes the hermitian of the matrix $\mathbf{A}$. $\mathbf{A}^{-1}$ denotes the matrix inverse, and $\mathbf{A}^{\dagger}$ the Moore Penrose inverse of matrix $\mathbf{A}$.
- The $N \times N$ identity matrix is denoted as $\mathbf{I}_{N\times N}$. The $N \times L$ all zero matrix is denoted as $\mathbf{0}_{N\times L}$.

- The Kronecker product of two matrices $\mathbf{A}$ and $\mathbf{B}$ is denoted by $\mathbf{A} \otimes \mathbf{B}$. With matrix $\mathbf{A} \in \mathbb{C}^{m \times n}$ and matrix $\mathbf{B} \in \mathbb{C}^{p \times q}$, the Kronecker product is $\mathbf{A} \otimes \mathbf{B} = \begin{bmatrix} a_{11}\mathbf{B} & \cdots & a_{1n}\mathbf{B} \\ \vdots & \ddots & \vdots \\ a_{m1}\mathbf{B} & \cdots & a_{mn}\mathbf{B} \end{bmatrix} \in \mathbb{C}^{mp \times nq}$.
- $\delta(\cdot)$ describes the Dirac distribution.
- The sign $\oslash$ determines the point-wise division.
- A Galois field with base q is denoted by $\mathbb{F}_q$.
- The bit-wise eXclusive OR (XOR) operation of bits a and b is denoted by $a \oplus b$.
- A probability density function (PDF) of the random variable Y is written as $p_Y(Y = y)$ with realization y, a likelihood function of the random variable X with realization x based on the observation Y with realization y is written as $p_{Y|X}(Y = y|X = x)$. For simplicity, the base of the random variable is often omitted, like $p(y) = p_Y(Y = y)$ and $p(y|x) = p_{Y|X}(Y = y|X = x)$. A probability mass function (PMF) is written as $\Pr(x)$. We do not differ between the random variables and their realizations within this thesis.
- A PDF of the Gaussian distribution is denoted by $\mathcal{N}\left(\overline{\mu}, \sigma^2\right)$ with mean value $\overline{\mu}$ and variance σ^2. The PDF of the uniform distribution $\mathcal{U}(a, b)$ has a constant amplitude $\frac{1}{b-a}$ in the interval $[a, b]$.
- The logarithm with base 2 is given by $\log_2(\cdot)$.
- The function $x(t)$ and $X(f)$ are connected via the Fourier transformation $X(f) = \mathcal{F}\{x(t)\}$.

Chapter 2

Fundamentals and Preliminaries

2.1 Overview

This chapter deals with the basics of general wireless transmission, on which the following chapters are based. Onto this end, we will first focus on a general unidirectional P2P transmission as an equivalent baseband model shown in Fig. 2.1 before generalizing the wireless channel model to multi-point channels. One may note that the overall detection, decoding and equalization process in this thesis is based on FG-related message passing estimation techniques. Therefore, each block is subsequently introduced and represented by FGs. A general discussion on the subject of FGs is given in

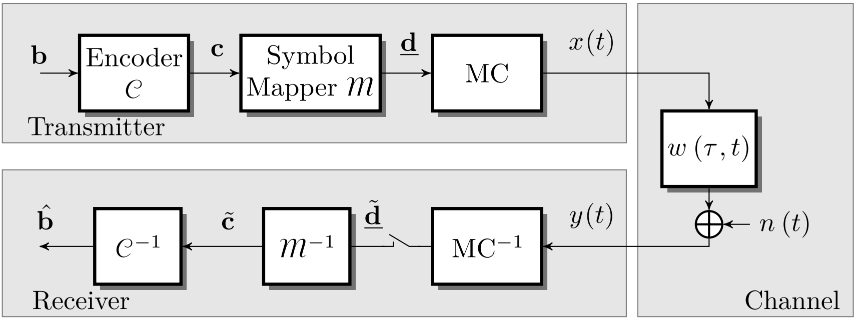

Figure 2.1: System model of an unidirectional P2P transmission.

Appendix B for the interested reader. In Fig. 2.1, the transmitter (Tx) is a general function that maps the discrete information sequence $\mathbf{b}$ to a time continuous signal $x(t)$ to produce a reliable and bandwidth efficient transmit signal. This mapping can usually be decomposed into three main blocks. The first two blocks, namely the *encoding* block $\mathcal{C}$ and the *symbol mapping* block $\mathcal{M}$, are described in Section 2.2 and Section 2.3, respectively. The third block *modulation*, (herein we only use MC transmissions) weights each complex symbol from the symbol mapper block with a general waveform to physical resources in time and frequency domain. This is the main challenge of this thesis. Therefore, it is generally presented in Section 2.4 and described in detail in Chapter 3 with concrete transmission schemes. The transmit signal $x(t)$ is transmitted via a wireless time-variant unidirectional P2P channel with impulse response $w(t, \tau)$ and received at the destination as received signal $y(t)$ as discussed in Section 2.5. The receiver (Rx) has the task to recover the information sequence $\mathbf{b}$ and is briefly introduced in Section 2.6.

2.2 Channel Coding

The principle idea of *channel encoding* is to introduce additional information (*redundancy*) to the information sequence $\mathbf{b}$, which can be used at the receiver to detect or even correct errors in case of an erroneous transmission.

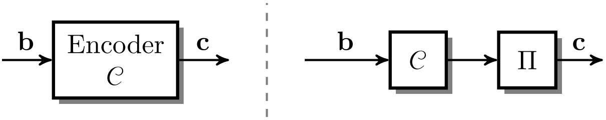

Figure 2.2: Encoder.

In general, an encoder $\mathcal{C}$ maps the binary information sequence $\mathbf{b} \in \mathbb{F}_2^{N_\mathbf{b}}$ of length $N_\mathbf{b}$ to a binary code sequence $\mathbf{c} \in \mathbb{F}_2^{N_\mathbf{c}}$ with code rate $R_\mathrm{c} = \frac{N_\mathbf{b}}{N_\mathbf{c}}$ by

$$\mathbf{c} = \Pi\left(\mathcal{C}\left(\mathbf{b}\right)\right), \tag{2.1}$$

as also depicted in Fig. 2.2. An optional interleaver $\Pi(\cdot)$ scrambles the information bits before transmission. The de-interleaver at the receiver ensures the de-correlation of error-events introduced by the transmission over a channel. A random interleaver is always assumed if not otherwise stated.

In this work, two types of encoding schemes are considered, which provide forward error correction (FEC) capabilities. One is a capacity approaching low density parity check (LDPC) encoding scheme and the other one is a convolutional code. Furthermore, a cyclic redundancy check (CRC) code is applied as an outer code to check the decoding success but it is not discussed in this thesis. More information on CRC codes can be found in [PB61, Fri95].

LDPC Encoding

In his Ph.D. thesis, Gallager invented the concept of LDPC codes and described the relationship between coded bits using a graphical model [Gal62]. LDPC codes are a special kind of linear block codes, which map an information word **b** linearly to a code word **c** by[1]

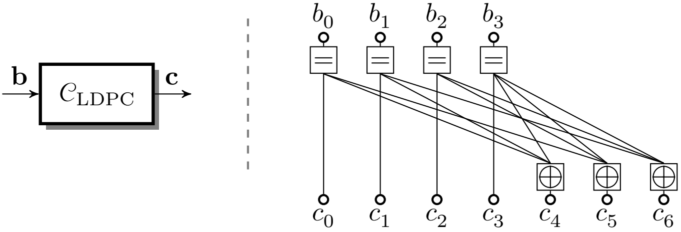

Figure 2.3: General FG of LDPC encoding with parity check matrix **H** given the example (2.4).

$$\mathbf{c} = \mathbf{G}\mathbf{b} \tag{2.2}$$

where $\mathbf{G} \in \mathbb{F}_2^{N_\mathbf{c} \times N_\mathbf{b}}$ is the generator matrix. The validity of a code word can be verified with the parity check matrix **H** like

$$\mathbf{H}^\mathsf{T}\mathbf{c} = \mathbf{0}, \tag{2.3}$$

where the parity check matrix fulfills the condition $\mathbf{H}^\mathsf{T}\mathbf{G} = \mathbf{0}$.

By utilizing the parity check matrix as a FG, the famous belief propagation algorithm, also known as sum-product algorithm (SPA), which is a message passing algorithm, can be applied for decoding. As will be introduced in Appendix B, a connection in a FG is generated by the “1s” in the corresponding adjacency matrix **A**, which for LDPC is $\mathbf{A} = \mathbf{H}$. The SPA exchanges messages on the edges of the FG and approximates or even solves the symbol-by-symbol maximum a-posteriori (MAP) estimation problem (B.6). As the complexity grows with the number of edges, Gallagers idea

---

[1] In this thesis column vectors are used in contrast to the common convention in coding literature, where row vectors are usually used.

was to use a low number of "1s" in the parity check matrix. However, the complexity of the SPA was still too high to be computed in 1963. After inventing the turbo principle in [BGT93] by Berrou *et al.*, MacKay rediscovers the idea of Gallagers LDPC codes in [MN97] and Richardson and Urbanke showed the capacity approaching property of proper designed LDPC codes under message-passing decoding [RU01]. Nowadays, LDPC codes are widely used in communication systems, like Worldwide Interoperability for Microwave Access (WiMax) [IEE06], Wireless Local Area Network (WLAN) [IEE09, IEE12], digital video broadcast, terrestrial 2nd Generation (DVB-T2) [ETS15] or digital video broadcast, satellite 2nd Generation (DVB-S2)[ETS14] and further more.

As an example, a linear Hamming code (7,4,3) with generator matrix **G** and the corresponding parity check matrix **H** are given as

$$\mathbf{G} = \begin{bmatrix} 1 & 0 & 0 & 0 \\ 0 & 1 & 0 & 0 \\ 0 & 0 & 1 & 0 \\ 0 & 0 & 0 & 1 \\ 1 & 1 & 0 & 1 \\ 1 & 0 & 1 & 1 \\ 0 & 1 & 1 & 1 \end{bmatrix} \qquad \mathbf{H} = \begin{bmatrix} 1 & 1 & 0 & 1 & 1 & 0 & 0 \\ 1 & 0 & 1 & 1 & 0 & 1 & 0 \\ 0 & 1 & 1 & 1 & 0 & 0 & 1 \end{bmatrix} \quad . \tag{2.4}$$

Although this matrix is not of low dense, it is used to principally show the corresponding FG in Fig. 2.3 on the right-hand side. For the design of LDPC codes, we refer to [BKA04, SFRU01].

Convolutional Encoding

Another type of codes used in this work is the concept of convolutional codes invented by Peter Elias in 1955 [Ber74], where the code sequence is generated by a sliding window combining (adding in $\mathbb{F}_2$) a various subset of information bits in this window. The encoding of convolutional codes can be realized by shift registers as depicted in Fig. 2.4 on the left-hand side. As an example, the non-recursive convolutional code with code rate $R_\mathrm{c} = \frac{1}{2}$ with generator polynomials $g_0\left(D\right) = 1 + D + D^2$ and $g_1\left(D\right) = 1 + D^2$ is used resulting in two memory elements D and a constraint length of three.

Applying the sequence MAP problem (as also introduced in the Appendix B), the receiver should determine the "most likely transmitted" sequence. In contrast to a brute force search considering all possible sequences, a powerful and widely used method solving this problem is the Viterbi algorithm [Vit67], which is based on a trellis representation [For73].

Due to its memory elements the convolutional code can be interpreted as a hidden Markov model and thus a FG as a state-space model [Wym07] can

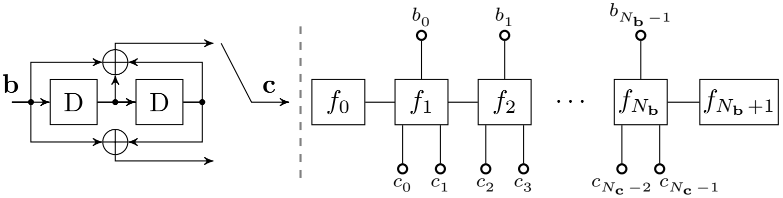

Figure 2.4: Realization of a convolutional code by shift registers with generator polynomials $g = [7_8, 5_8]$ in octal representation on the left-hand side. The corresponding FG is depicted on the right side.

be used illustrated in Fig. 2.4 on the right-hand side. Here, the function f_ϖ determines the state transition of the memory elements per information bit b_ϖ with $\varpi = 0, \ldots, N_\mathbf{b} - 1$, where f_0 and $f_{N_\mathbf{b}+1}$ correspond to the initial and final state, respectively. The algorithm applied on the state-space model is the famous forward-backward algorithm, which was invented in [BCJR74] called Bahl-Cocke-Jelinek-Raviv (BCJR) algorithm solving the symbol-by-symbol MAP problem (*cf.* (B.6)). The complexity is mainly controlled by the number of possible states available at each state transition. The application of convolutional codes is very popular, especially the implementation as concatenated codes used for turbo decoding, for example, as implemented in LTE [STB11] or UMTS [HT11].

2.3 Symbol Mapping

The task of the symbol mapper denoted by $\mathcal{M}$ in Fig. 2.1 is the mapping of the code bit sequence $\mathbf{c} \in \mathbb{F}_2^{N_\mathbf{c}}$ to a symbol sequence[2] $\underline{\mathbf{d}} \in \mathbb{C}^{N_\mathbf{d}}$ in the complex plane. The symbol mapper $\mathcal{M}$ is defined by the symbol alphabet $\mathcal{D}$ with cardinality $|\mathcal{D}| = M$. In general, one complex symbol d of the vector $\underline{\mathbf{d}}$ is generated by a code bit group $\check{\mathbf{c}} = [c_c, \ldots, c_{c+\log_2(M)-1}]$ of dimension $\log_2(M)$ resulting in a number of complex symbols $N_\mathbf{d} = N_\mathbf{c} / \log_2(M)$[3]. The amount of information bits per complex symbol is given by the ratio

$$\varrho = \frac{N_\mathbf{b}}{N_\mathbf{d}} = \frac{N_\mathbf{b}}{N_\mathbf{c}} \log_2(M) = R_\mathrm{c} \log_2(M)\,. \tag{2.5}$$

The choice of the symbol alphabet $\mathcal{D}$ and thus the mapping of code bits tuples has a significant impact on the performance of the overall system

---

[2] Throughout this work, the symbol vector $\underline{\mathbf{d}}$ is a frame-based vector denoted by an underlined vector. [3] Note that the encoder adds $N_\mathbf{c} \mod \log_2(M)$ zeros, if needed, to ensure that $N_\mathbf{d}$ is an integer number.

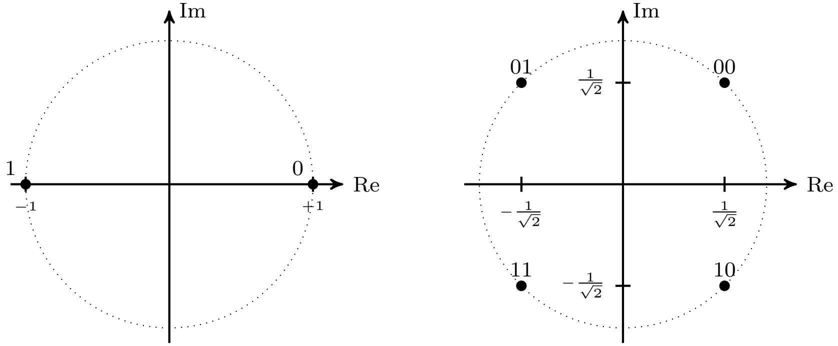

a) BPSK b) QPSK

Figure 2.5: Symbol mapping and symbol alphabet of BPSK and QPSK.

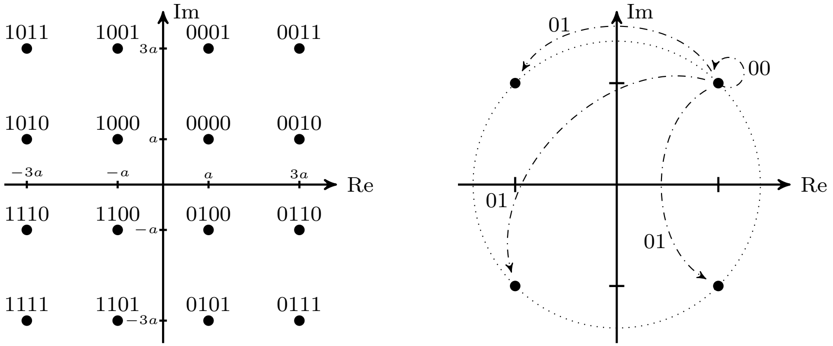

a) 16QAM b) D-QPSK

Figure 2.6: Symbol mapping and symbol alphabet of 16-QAM with normalization constant $a = 1/\sqrt{10}$ and D-QPSK.

performance as bandwidth efficiency η or frame error rate (FER) performance. The symbol mapping schemes in this thesis are described in detailed below. We assume unit power symbol mapping with $\mathrm{E}\{|d|^2\} = 1$.

- ***M*-ary phase shift keying (*M*-PSK):** In M-PSK mapping the complex symbols are arranged on a unit circle in the complex plane as illustrated in Fig. 2.5. All symbols in the set $\mathcal{D}$ have the same amplitude and the possible angles are $\frac{2\pi}{M}q + \phi_0$ with $q = 0, \ldots, M-1$ with an arbitrary starting phase ϕ_0. With $M = 2$ and $\phi_0 = 0$ the symbol

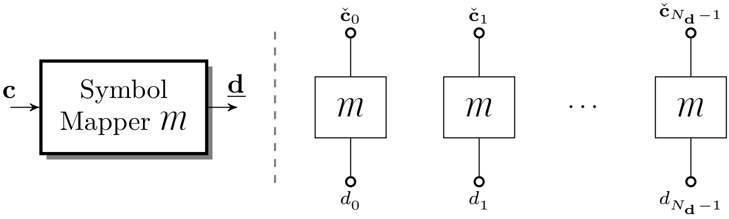

Figure 2.7: General factor graph of symbol mapper.

mapping is called binary phase shift keying (BPSK) (*cf.* Fig. 2.5a), which is purely real, whereas for $M = 4$ results in quaternary phase shift keying (QPSK) (*cf.* Fig. 2.5b with $\phi_0 = \pi/4$). By applying gray mapping, we obtain the mapping of code bit tuples to symbols as labeled in the figure.

- **M-ary quadrature amplitude modulation (M-QAM):** In M-QAM mapping the amplitudes of the real and the imaginary part have the same Euclidean distances in the complex plane. The special case $M = 4$ achieves the same mapping as QPSK with starting phase $\phi_0 = \pi/4$ illustrated in Fig. 2.5b. The QAM with $M = 16$ is depicted in Fig. 2.6a. Furthermore, by delaying either the real or the imaginary part by half of the symbol duration, the OQAM mapping is achieved.

- **Differential-M ary-phase shift keying (D-M-PSK):** Contrarily to the aforementioned mapping schemes, where the code bit tuples are directly mapped to the symbols, differential symbol mapping maps the information to the difference between two consecutive symbols. First M-PSK symbol mapping is performed. Afterwards the difference mapping is done, as $\mathring{d}_i = d_{i-1}\mathring{d}_{i-1}$ for $i = 1, \ldots, N_\mathbf{d}$ with an arbitrarily chosen initial symbol, *e.g.* $\mathring{d}_0 = (1 + j)/\sqrt{2}$. The resulting symbols for $M = 2$ are shown in Fig. 2.6b, where the arrows denote the difference between the upper right symbol to the other symbols. This approach is mostly used for incoherent reception, where the receiver has no knowledge of the carrier phase.

The block diagram and the FG representation of the symbol mapper m are illustrated for the coherent mappings in Fig. 2.7.

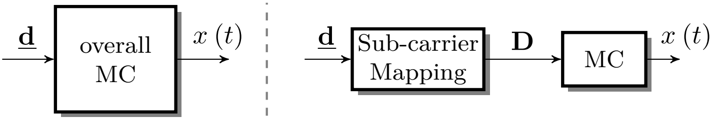

Figure 2.8: General multi-carrier block.

2.4 Multi-Carrier Transmit Signal

The complex symbols $\underline{\mathbf{d}} \in \mathbb{C}^{N_{\mathbf{d}}}$ are mapped by a MC transmission scheme to a time-continuous transmit signal $x(t)$ as depicted in Fig. 2.8. A sub-carrier mapping block rearranges the **frame-based symbol vector** $\underline{\mathbf{d}}$ to a **frame-based symbol matrix** $\mathbf{D} \in \mathbb{C}^{N_{\mathrm{SC}} \times N_{\mathrm{TS}}}$, with N_{SC} and N_{TS} denoting the number of sub-carriers and time-symbols, respectively. Herein, a so-called "localized" mapping is used, *i.e.* all used sub-carriers are adjacent, which can be realized by a simple serial to parallel (S/P) mapping by the vectorization operator $\mathbf{D} = \mathrm{vec}\{\underline{\mathbf{d}}\}$. By applying

$$x(t) = \sum_{k} \sum_{\ell} d_{k,\ell} g^{\mathrm{Tx}} (t - \ell T_0) e^{j2\pi k F_0 t} e^{j\phi_{k,\ell}}, \tag{2.6}$$

each element $d_{k,\ell}$ of matrix $\mathbf{D}$ is shifted to the corresponding TF point $(\ell T_0, kF_0)$ and weighted by transmit filter $g^{\mathrm{Tx}}(t)$. The time index ℓ and the frequency index ℓ are introduced and used for this purpose. The choice of this function $g^{\mathrm{Tx}}(t)$ and the symbol spacing T_0 in time and F_0 in frequency direction mainly determine the used MC transmission scheme.

As the MC concept is a key technology of this thesis, we will introduce the concept of MC schemes in a separate chapter. Thus, in Chapter 3 we will give an outlook on orthogonal transmission schemes offering perfect symbol reconstruction. The concept of perfect reconstruction essentially defines the conditions under which a signal passing through the multi-carrier system (without any impact like wireless channel or noise) remains undistorted in amplitude and phase without further processing [BMN11, SGA13]. Furthermore, non-orthogonal schemes with a robust design under timing offset (TO), carrier frequency offset (CFO) or a more severe impact like time-variant channels will be introduced.

2.5 Transmission over Doubly-Disturbed Channels

In this section, we start with the discussion of a transmission over a time-variant unidirectional P2P channel and its representations, before we generalize it to multi-point channels considered in Chapter 4 and Chapter 5 [MH03, MH11].

Point-to-Point Channels

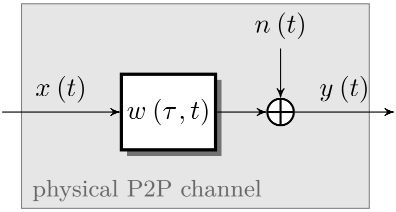

Figure 2.9: Block diagram of a point-to-point channel.

The signal $x(t)$ generated by the MC block of the transmitter is sent via a wireless, generally time-variant channel with the *time-variant impulse response* $w(\tau,t)$ to a receiver, where t is the time and τ is the time interval between excitation and reception (or also called delay or shift in time). Throughout this work we also use the term τ for time shifts with other origins than delay, since the mathematical description is the same. In general, the time-variance is due to the mobile setup, however even if the Tx and Rx remain static the transmission can be affected by moving objects that are reflecting, shadowing or scattering. Also in a completely static scenario non-ideal oscillators are another source of time-variation in a wireless channel. The received signal at the destination illustrated in Fig. 2.9 results in

$$y(t) = \int_{-\infty}^{\infty} x(t-\tau)\, w(\tau,t)\, \mathrm{d}\tau + n(t) \quad , \tag{2.7}$$

where $n(t)$ is additive white Gaussian noise (AWGN) with $\mathcal{N}\left(0,\sigma_{\mathrm{n}}^{2}\right)$.

Time-variant channels and their representations A time-variant channel can be described by the time-variant impulse response $w(\tau,t)$ or the *time-variant transfer function* $W_{\mathrm{TF}}(f,t)$, which is the representative function in the frequency domain (f denotes the frequency). Both functions are connected by the Fourier transformation *w.r.t.* the delay τ by

$$W_{\mathrm{TF}}\left(f,t\right) = \int\limits_{-\infty}^{\infty} w\left(\tau,t\right) e^{j2\pi f\tau} \mathrm{d}\tau. \tag{2.8}$$

In contrast to the time-invariant case, where the channel remains unaltered due to time changes and thus is fully determined by the aforementioned functions, the time-variant channel has two more representations: 1) the *Doppler-variant impulse response* $s\left(\tau,\nu\right)$ and 2) the *Doppler-variant transfer function* $s_{\mathrm{TF}}\left(f,\nu\right)$, where ν is called Doppler shift, which can be interpreted as shift in the frequency domain. Throughout this work we also use the term ν for frequency shifts with other origins than Doppler, since the mathematical description is the same. Similar to (2.8) also the other functions are connected by a corresponding Fourier transformation *w.r.t.* the delay τ, the time t, the Doppler shift ν or the frequency f, where Fig. 2.10 shows the relation between these functions. The Doppler-variant impulse response is given by

$$\begin{tikzcd}
 & \boxed{W_{\mathrm{TF}}\left(f,t\right)} \arrow[dr, "t \circ\!-\!\bullet\, \nu"] & \\
\boxed{w\left(\tau,t\right)} \arrow[ur, "\tau \circ\!-\!\bullet\, f"] \arrow[dr, "t \circ\!-\!\bullet\, \nu"'] & & \boxed{s_{\mathrm{TF}}\left(f,\nu\right)} \\
 & \boxed{s\left(\tau,\nu\right)} \arrow[ur, "\tau \circ\!-\!\bullet\, f"'] &
\end{tikzcd}$$

Figure 2.10: Relation between the channel functions.

$$s\left(\tau,\nu\right) = \int\limits_{-\infty}^{\infty} w\left(\tau,t\right) e^{j2\pi\nu t} \mathrm{d}t \quad . \tag{2.9}$$

This function is also called *delay-Doppler spreading function* because it characterizes the impact of the wireless channel *w.r.t.* the delay shift τ and the Doppler shift ν. The Doppler-variant transfer function $s_{\mathrm{TF}}\left(f,\nu\right)$ is generated by the Fourier transformation of the Doppler-variant impulse response *w.r.t.* the delay τ by

$$s_{\mathrm{TF}}\left(f,\nu\right)=\int\limits_{-\infty}^{\infty} s\left(\tau,\nu\right)e^{j2\pi f\tau}\mathrm{d}\tau. \tag{2.10}$$

Further parameters and physics on time-variant channels So far, we have seen which function can represent a time-variant channel. One typical model of a linear time-variant channel used within this work can be given by the impulse response as

$$w\left(\tau,t\right)=\sum_{\gamma=0}^{N_{\mathrm{path}}-1}\varsigma_{\gamma}\delta\left(\tau-\tau_{\gamma}\right)e^{j\nu_{\gamma}t} \tag{2.11}$$

and the corresponding delay-Doppler function then reads

$$s\left(\tau,\nu\right)=\sum_{\gamma=0}^{N_{\mathrm{path}}-1}\varsigma_{\gamma}\delta\left(\tau-\tau_{\gamma}\right)\delta\left(\nu-\nu_{\gamma}\right)\quad, \tag{2.12}$$

where ς_{γ} is the complex channel coefficient, τ_{γ} is a time-delay and ν_{γ} a shift in frequency direction of the γ^{th} path out of N_{path} paths in total.

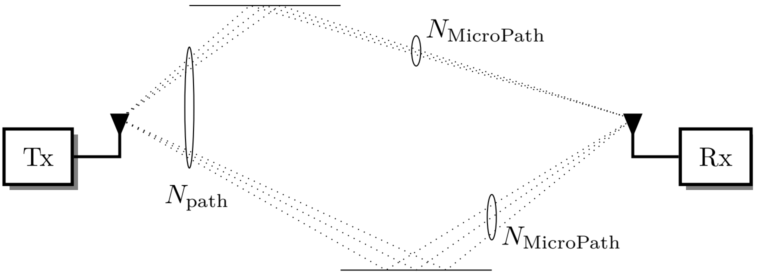

Figure 2.11: Mobile wireless radio channel.

Usually, within a radio communication as in Fig. 2.11, the electromagnetic waves interact with objects (so-called scatterer) as buildings, trees, cars or mountains. Each macro path is assumed to have $N_{\mathrm{MicroPath}}$ micro paths at each of these scatterer, where each micro path is disturbed along the surface of the object by a complex channel coefficient. With these assumptions, the general equation (2.12) related to [Sch01, Vog06, KD18] can be rewritten into

$$s\left(\tau,\nu\right)=\sum_{q=0}^{N_{\mathrm{MacroPath}}-1}\varsigma_{q}\delta\left(\tau-\tau_{q}\right)\sum_{\iota=0}^{N_{\mathrm{MicroPath}}-1}\delta\left(\nu-\nu_{q,\iota}\right)e^{j\phi_{q,\iota}} \tag{2.13}$$

with the assumption that the change in amplitude for different micro paths is irrelevant. However, the change in phase has to be considered, thus, the frequency shift $\nu_{q,\iota}$ and the phase shift $\phi_{q,\iota}$ are micro path dependent.

The parameters in (2.13) can be classified as follows

- **Scatterer:** The number of scatterer or number of overall macro paths is denoted by $N_{\text{MacroPath}}$. The channel is called multi-path channel, if $N_{\text{MacroPath}} > 1$.
- **Micro path:** The number of micro paths per object is given by $N_{\text{MicroPath}}$.
- **Delay spread:** The cluster of time delays τ_q is also known as delay spread. The time delay with the largest delay is known as $\tau^{\max}$.
- **Doppler spread:** The frequency shifts $\nu_{q,\iota}$ are known as Doppler spread with the largest spread $\nu^{\max}$.

Both spreads can be decomposed into a static and a variable part. The frequency shift can be decomposed into $\nu_{q,\iota} = \nu_{\text{D}}(q,\iota) + \Delta\nu$, where $\Delta\nu$ is a constant part, *e.g.* a CFO and ν_{D} denotes the Doppler frequency, with

$$\nu_{\text{D}}(q,\iota) = \frac{v_0 f_0 \cos(\alpha_{q,\iota})}{c_0} \quad . \tag{2.14}$$

It depends on the carrier frequency f_0, the relative velocity v_0, and on the angle of arrival $\alpha_{q,\iota}$ [KD18, Pro07]. c_0 is the speed of light.

The coherence bandwidth B_{c} is the bandwidth of a wireless channel in which the transfer function W_{TF} remains roughly constant and it can be approximated by

$$B_{\text{c}} \approx \frac{1}{\tau^{\max}} \tag{2.15}$$

Similarly, the coherence time τ_{c} can be approximated by

$$\tau_{\text{c}} \approx \frac{1}{\nu^{\max}} \quad , \tag{2.16}$$

in which the channel is not changing over time, thus, it can be approximated as a time-invariant channel.

Multi-Point Channels

Up to here, we focused on a unidirectional P2P transmission from a transmitter to a receiver equipped with one antenna each. In this thesis basically the generalization to a more dimensional problem is important. Beside the unidirectional P2P channel, Chapter 4 deals with a two-point channel, where two user nodes A and B simultaneously transmit over an assisting relay R to the other user. The received signal at the relay can be given as

$$y\left(t\right)=\int\limits_{-\infty}^{\infty}x^{\mathsf{A}}\left(t-\tau\right)w^{\mathsf{A}}\left(\tau,t\right)\mathrm{d}\tau+\int\limits_{-\infty}^{\infty}x^{\mathsf{B}}\left(t-\tau\right)w^{\mathsf{B}}\left(\tau,t\right)\mathrm{d}\tau+n\left(t\right) \tag{2.17}$$

and the transmission to the relay is illustrated in Fig. 2.12a.

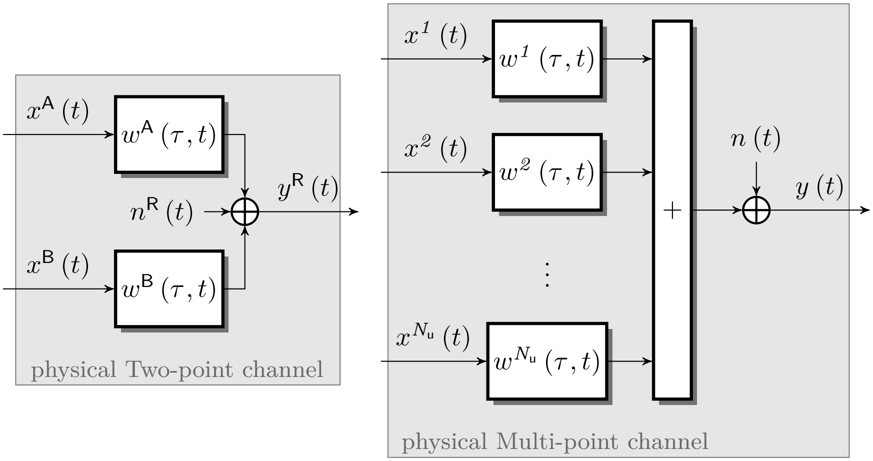

a) Two-Point Channel (Chapter 4) b) Multi-Point Channel (Chapter 5)

Figure 2.12: General multi point channel with a) Two-point channel used in the TWRC in Chapter 4 and b) massive multi-point channel in Chapter 5.

A massive MTC setup is assumed in Chapter 5, where a huge number of N_{u} devices are connected to an aggregation node as illustrated in Fig. 2.12b, the received signal at the aggregation node is given by

$$y\left(t\right)=\sum_{\mathsf{u}=1}^{N_{\mathsf{u}}}\int\limits_{-\infty}^{\infty}x^{\mathsf{u}}\left(t-\tau\right)w^{\mathsf{u}}\left(\tau,t\right)\mathrm{d}\tau+n\left(t\right)\quad . \tag{2.18}$$

2.6 Receiver Structure

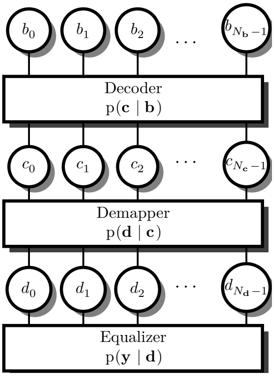

Figure 2.13: FG given by equation (2.21).

So far, we had a look at the transmitter and the transmission over a physical channel. Here, we want to focus on the receiving side, where the data $\mathbf{b}$ have to be detected. In Bayesian statistics the MAP detection is a well-known and famous procedure to recover the data by the sampled observations $\mathbf{y}$ at a destination and is given by

$$\hat{\mathbf{b}} = \underset{\mathbf{b} \in \mathcal{B}^{N_\mathbf{b}}}{\arg\max}\ \mathrm{p}(\mathbf{b} \mid \mathbf{y}) \tag{2.19a}$$

$$= \underset{\mathbf{b} \in \mathcal{B}^{N_\mathbf{b}}}{\arg\max}\ \mathrm{p}(\mathbf{y} \mid \mathbf{b}) \Pr(\mathbf{b}) . \tag{2.19b}$$

Here, $\mathrm{p}(\mathbf{b} \mid \mathbf{y})$ is the a-posteriori probability (APP) and (2.19b) is achieved by the application of Bayes' rule, where $\mathrm{p}(\mathbf{y} \mid \mathbf{b})$ is the *likelihood* function for a given observed $\mathbf{y}$ and $\Pr(\mathbf{b})$ is known as *a priori* probability. The MAP approach takes that sequence $\hat{\mathbf{b}}$ out of all possible $\mathbf{b} \in \mathcal{B}^{N_\mathbf{b}}$, which maximizes the APP. In some cases, it is infeasible to find the solution with appropriate complexity. To this end, a symbol-by-symbol MAP approach as

$$\hat{b}_\varpi = \underset{b_\varpi \in \mathcal{B}}{\arg\max}\ \mathrm{p}(\mathbf{y} \mid b_\varpi) \Pr(b_\varpi) \tag{2.20}$$

is applied. According to Appendix B, a multiple use of Bayes' rule leads to the factorization *w.r.t.* encoding, symbol mapping and channel (mapping to physical resources) resulting in

$$\mathrm{p}(b_\varpi \mid \mathbf{y}, \mathbf{d}, \mathbf{c}) = \underbrace{\mathrm{p}(\mathbf{y} \mid \mathbf{d})}_{\text{eff. Channel}} \underbrace{\mathrm{p}(\mathbf{d} \mid \mathbf{c})}_{\text{Mapping}} \underbrace{\mathrm{p}(\mathbf{c} \mid b_\varpi)}_{\text{Encoding}} \underbrace{\Pr(b_\varpi)}_{\text{a priori}} . \tag{2.21}$$

The factorization to these functions is illustrated by the FG in Fig. 2.13[4], where each function corresponds to a function node in the FG: 1) equalization, *i.e.* symbol reconstruction corresponds to the effective channel including MC scheme and physical channel, 2) symbol demapper corresponds to symbol mapper and 3) channel decoding corresponds to channel encoding. This FG is the basis for the factorization in the TWRC case in Chapter 4 and the MCSM case in Chapter 5.

2.7 Summary

In this chapter the principles of transmission via time-variant channels were presented. For this purpose, the transmitter was decomposed into an encoder, a symbol mapper and a multi-carrier scheme. To gain a deeper insight into time-variant wireless channels, four different representative functions and properties like Doppler spread, delay spread, coherence bandwidth or coherence time, *etc.* were introduced before a generalization to multipoint channels followed. A short discussion on estimation procedures for unidirectional P2P transmissions concludes the chapter and the overall FG for P2P transmission was shown.

---

[4] Note that the $\mathbf{y}$ variable and the a priori probability $\Pr(b_{\varpi})$ function nodes are not represented to facilitate the representation.

Chapter 3

Multi-Carrier Transmission Schemes

3.1 Overview

In the previous chapter we have discussed the entire transmission concept of a unidirectional P2P link between a source and a destination, including: 1) encoding 2) symbol mapping and 3) a very brief discussion about generating the transmission signal of multi-carrier (MC) transmission schemes. We will now examine the MC system in P2P in detail, including the transmitter, the receiver, and the influence of a time-variant physical channel $w(\tau, t)$, before the next chapters will extend the MC schemes to the needs of TWRC in Chapter 4 and for MTC in Chapter 5.

Structure of the Chapter Therefore, we present the basic concept of MC transmission in Section 3.2. Here the efficient mapping of the complex symbols to the available bandwidth and time duration can be implemented by the aid of filter-banks (FBs) for generating the transmit signal $y(t)$. The use of FBs at the Rx also allows data detection. Here, general waveforms that are embossed on the time-frequency plane, and their parameters will be further discussed. Important values such as the expansion in time and frequency direction are given by some important parameters, namely the Heisenberg-Gabor and the direction parameter. The expansion is illustrated by the ambiguity function for different waveform candidates. An orthogonality condition is introduced which is often used to design MC schemes with perfect reconstruction properties [Vai93, BMN11, Du08]. A general matrix description is given before a FG-based representation of the MC scheme concludes this section. Section 3.3 begins with a brief classification of properties in MC transmissions, before first orthogonal MC schemes like the famous guard interval (GI)-based CP-OFDM and zero padded-orthogonal frequency division multiplexing (ZP-OFDM) are introduced. These schemes allow orthogonal transmission within time-invariant channels with maximum delay spread captured by the GI, but they suffer from high out-of-band emissions (OoBE) due to the rectangular waveform. Windowed-orthogonal frequency division multiplexing (w-OFDM) introduces smoothing techniques to improve the spectral shape. Furthermore, the introduction of universal filtered - orthogonal frequency division multiplexing (UF-OFDM) allows for a compromise between w-OFDM and bandwidth filtered OFDM by sub-block filtering. By eliminating the limitation of complex-valued orthogonality, waveforms with a better shape in time and frequency can be used by offset quadrature amplitude modulation/orthogonal frequency division multiplexing (OQAM/OFDM) [KD18]. All these orthogonal schemes offer simple equalization techniques in synchronized systems with time-invariant channels. After introducing orthogonal MC schemes, we have a look at non-orthogonal QAM/FBMC that naturally cause interference. This property makes an equalizer indispensable even for a perfectly synchronized transmission. However, this scheme offers a robust design under offset condition, as the effective channel matrix changes only marginally. Subsequently, general frequency division multiplexing (GFDM) is discussed, which is a frame-based realization and, in contrast to QAM/FBMC, offers narrow frame boundaries. The chapter is summarized in Section 3.4.

The main own contributions of this thesis are: A common representation for all MC schemes used in this thesis is derived in a uniform context regarding time-frequency localization (TFL), lattice *i.e.* symbol and frequency spacing, used waveform, effective channel matrix, indicated interference level, which prepares the basis of the P2P system model and which are extended in Chapters 4 and 5 to the underlying needs.

3.2 Multi-Carrier Transmission

The main question of this section is “How to allocate the available resources, *i.e.*, time and frequency in the *best* fashion to achieve data detection with lowest FER?”. For this the data signal of a user should be appropriately allocated on the available resources. Usually in communication systems, we have the physical resources 1) time 2) frequency 3) code and 4) space. In this work we concentrate mainly on the first two items, but we add the code domain in Chapter 5.

We introduce subsequently robust MC transmission schemes applying general waveforms in a unidirectional P2P setup, which are known in the literature [SN96, SGA13, JK16, NSR17] to mention some and references therein. This will be the main basis in this thesis for the extension of MC schemes to two user transmission for the TWRC in Chapter 4 and for a massive number of sensor nodes with sporadic communication in Chapter 5.

3.2.1 Transmit Signal

As we have seen in Section 2.4, the overall MC scheme can be decomposed into a sub-carrier mapping block and the MC block. In this chapter we focus on the MC block as illustrated in Fig. 3.1 and assume that a symbol matrix $\mathbf{D} \in \mathbb{C}^{N_{\mathrm{SC}} \times N_{\mathrm{TS}}}$ is already available, with elements of $d_{k,\ell}$, with k as sub-carrier index and ℓ as time symbol index. Furthermore, N_{SC} denotes the number of sub-carriers and N_{TS} is the number of time symbols per frame [MBH13]. The total number of elements in one frame is $N_{\mathbf{d}} = N_{\mathrm{SC}} \cdot N_{\mathrm{TS}}$. The objective is the general description of a MC transmit signal $x(t)$ and the effective channel (*cf.* Fig. 3.1) which connects the symbols $d_{k,\ell}$ and observations $y_{k',\ell'}$ in frequency domain, getting introduced piece by piece. Therefore, we start the discussion with one arbitrary element d (omitting the indices k, ℓ) of the symbol matrix $\mathbf{D}$, before we generalize it to capture all elements of the whole frame in $\mathbf{D}$. To shift this symbol d to a physical resource in time with a delay $\tau \in \mathbb{R}$ and in frequency by a shift $\nu \in \mathbb{R}$, the

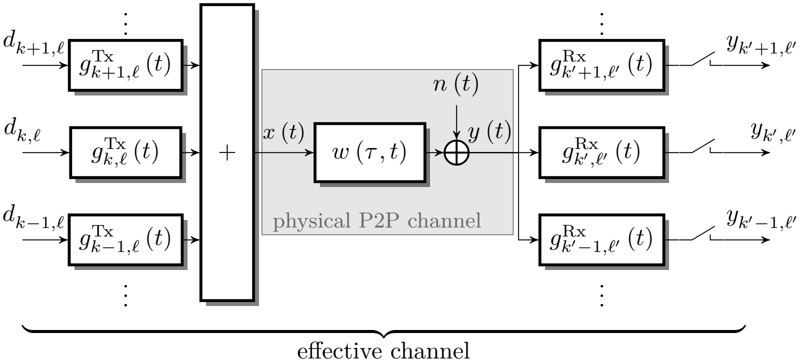

Figure 3.1: Multi-Carrier System Model (with localized sub-carrier mapping).

symbol is weighted by the impulse response of a transmit filter

$$g_{\nu,\tau}^{\mathrm{Tx}}(t) = g^{\mathrm{Tx}}(t-\tau)\, e^{j2\pi\nu t} e^{j\phi}, \tag{3.1}$$

such that the transmit signal for this symbol is $x(t) = d g_{\nu,\tau}^{\mathrm{Tx}}(t)$. This transmit filter $g_{\nu,\tau}^{\mathrm{Tx}}(t)$ is derived from the prototype filter $g^{\mathrm{Tx}}(t)$ and gets shifted by τ in time and ν in frequency direction. Additionally, a constant phase rotation ϕ may be applied, which is needed for the MC scheme OQAM later on.

The transmit filters $g_{\nu,\tau}^{\mathrm{Tx}}(t)$ are called a Gabor analysis function [Gab46, Str98, MBH13], where $g^{\mathrm{Tx}}(t)$ is the so-called Gabor atom.

Time-Frequency Grid The choice of the shifting parameters ν, τ configuring the TF plane [SK16, TJ18] plays an important role. In general, this can be done by a so-called lattice Λ, which is a subgroup of $\mathbb{R}^n$ (here with $n = 2$), describing a set of discrete locations in the TF plane $\mathbb{R}^2$. This lattice Λ can be described by a generator matrix

$$\mathbf{L} = \begin{bmatrix} x & y \\ 0 & z \end{bmatrix} \quad , \tag{3.2}$$

with parameters $x, z \in \mathbb{R} \backslash \{0\}$ and $y \in \mathbb{R}$. By choosing $x = T_0$, $z = F_0$ and $y = 0$ a rectangular lattice is achieved as illustrated in Fig. 3.2 with sub-carrier spacing $F_0 \in \mathbb{R}$ and time symbol time spacing $T_0 \in \mathbb{R}$. Each possible TF point in the lattice can be generated by the application of $\mathbf{L}$ to a vector with numbering elements. One may also note that the term lattice and time-frequency grid can be used interchangeable and the use mostly depends on the community (either communication or mathematical view). Throughout this work, we focus on the rectangular setting[1] and, therefore, the prototype filter $g_{k,\ell}^{\mathrm{Tx}}(t)$ in (3.1) is shifted to the discrete points $(\ell T_0, k F_0)$ calculated by

$$\begin{bmatrix} \ell T_0 \\ k F_0 \end{bmatrix} = \begin{bmatrix} T_0 & 0 \\ 0 & F_0 \end{bmatrix} \begin{bmatrix} \ell \\ k \end{bmatrix}. \tag{3.3}$$

As short-hand notation the index pair (k, ℓ) with $\ell \in \mathbb{Z}$, $k \in \mathbb{Z}$ are used leading to the concrete transmit filter

$$g_{k,\ell}^{\mathrm{Tx}}(t) = g^{\mathrm{Tx}}(t - \ell T_0)\, e^{j2\pi k F_0 t} e^{j\phi_{k,\ell}} \tag{3.4}$$

---

[1] Generally other types of lattices exist, *e.g.* hexagonal lattices and the interested reader is referred to [SGA13] and references therein.

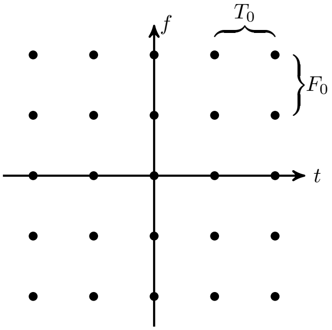

Figure 3.2: Illustration of a rectangular TF grid with sub-carrier spacing F_0 and symbol time spacing T_0.

with discrete shifts in frequency kF_0 and time ℓT_0. Thus, the overall transmit signal for all elements is given by

$$x(t) = \sum_k \sum_\ell d_{k,\ell} g_{k,\ell}^{\mathrm{Tx}}(t) \quad . \tag{3.5}$$

As this summation can be realized by bank of filters $g_{k,\ell}^{\mathrm{Tx}}(t)$, the name FBMC is often used.

Lattice Density and Bandwidth Efficiency Another question is the choice of the parameters F_0 and T_0 which determines the density of the symbols within a given TF region. One major key performance indicator (KPI) of transmission schemes is the amount of information within given resources. Thus, we want to answer the question: *How efficient is a system?* The bandwidth efficiency η is the amount of information carried on a given sub-carrier spacing F_0 and symbol time spacing T_0 and it is given by

$$\eta = \frac{\varrho}{T_0 F_0} \quad , \tag{3.6}$$

where ϱ is the number of information bits per complex symbol (*cf.* (2.5)). The bandwidth efficiency η can be seen as the amount of bits per channel use, which is a measure of Bit/s/Hz. In terms of a lattice Λ the calculation of (3.6) can be generalized to

$$\eta = \varrho \delta_{\mathrm{LD}}(\Lambda) = \frac{\varrho}{\mathrm{vol}(\Lambda)} = \frac{\varrho}{|\det(\mathbf{L})|} \quad . \tag{3.7}$$

Here, $\delta_{\mathrm{LD}}(\Lambda) = 1/\mathrm{vol}(\Lambda)$ denotes the density of the lattice, which can be calculated by the volume of the lattice $\mathrm{vol}(\Lambda)$[2]. In the case of a rectangular lattice introduced above, the lattice density is $\delta_{\mathrm{LD}}(\Lambda) = 1/(F_0 T_0)$.

The density is important: choosing the density $\delta_{\mathrm{LD}}(\Lambda)$ too small will result in an ineffective transmission. In contrast, choosing a value too large will lead to a non-unique representation of the data symbols [SK16, TJ18].

We can differ three different cases: 1) *oversampled*: $\delta_{\mathrm{LD}}(\Lambda) > 1$, this TF grid is too dense, such that no transmitter/receiver (Tx/Rx) filter pair $g_{k,\ell}^{\mathrm{Tx}}$ and $g_{k',\ell'}^{\mathrm{Rx}}$ exists that fulfills orthogonality in f and t (*cf.* (3.19) and (3.58)), 2) *critically sampled*: $\delta_{\mathrm{LD}}(\Lambda) = 1$, where an orthogonal system can only be achieved with filters of non-localized infinite shape, *e.g.* the rectangular waveform in time domain with sinc shape in frequency domain, which was proven by the Balian-Low theorem [Dau90], and 3) *under-sampled*: $\delta_{\mathrm{LD}}(\Lambda) < 1$, an orthogonal transmission is possible with well-localized filters [SB03]. All following transmission schemes will be analyzed regarding this aspect. From a communication engineering perspective, *i.e.* high bandwidth efficiency, the density should be chosen as close to one as possible to achieve a highly efficient system.

But not only the choice of the density $\delta_{\mathrm{LD}}(\Lambda)$ is important also the sub-carrier spacing F_0 and the symbol time spacing T_0 are essential. Fig. 3.3 illustrates two schemes with the same density $\delta_{\mathrm{LD}}(\Lambda) = 1/(F_0 T_0)$ and with $N_{\mathrm{SC}} = N_{\mathrm{TS}}$ but with different F_0 and T_0 configurations. On the left-hand-side the amplitudes of a time-invariant frequency selective channel transfer function $|W_{\mathrm{TF}}(f)|$ are illustrated and on the upper part the corresponding amplitudes of the channel impulse response $|w(\tau)|$ are shown. The scheme in the first plot Fig. 3.3a is mainly known as SC transmission, where only one "sub-carrier" is used occupying the whole available bandwidth $B = F_0$. Therefore, a relatively short symbol time spacing T_0 is used to achieve the density $\delta_{\mathrm{LD}}(\Lambda)$. Here, the channel $W_{\mathrm{TF}}(f)$ will have a huge impact on each symbol, due to the high frequency selectivity per symbol and the relatively long delay spread $\tau^{\max}$ of the physical time impulse response $w(\tau)$. In contrast to SC transmission, a MC transmission illustrated in Fig. 3.3b splits the available bandwidth $B = N_{\mathrm{SC}} F_0$ to many "small" sub-carriers with a nearly frequency-flat channel behavior. This highly reduces the impact of the frequency selective channel $w(\tau)$ on the subsequent symbols.

The relatively small sub-carrier spacing F_0 in Fig. 3.3b subdivides the channel transfer function $W_{\mathrm{TF}}(f)$ in small sectors with roughly constant channel gain, which can be approximated by just one channel coefficient. This behavior allows simple and low-complexity 1-tap frequency domain

---

[2] The volume of the lattice $\mathrm{vol}(\Lambda) = |\det(\mathbf{L})|$ can be calculated by the absolute value of the determinant of the generator matrix $\mathbf{L}$.

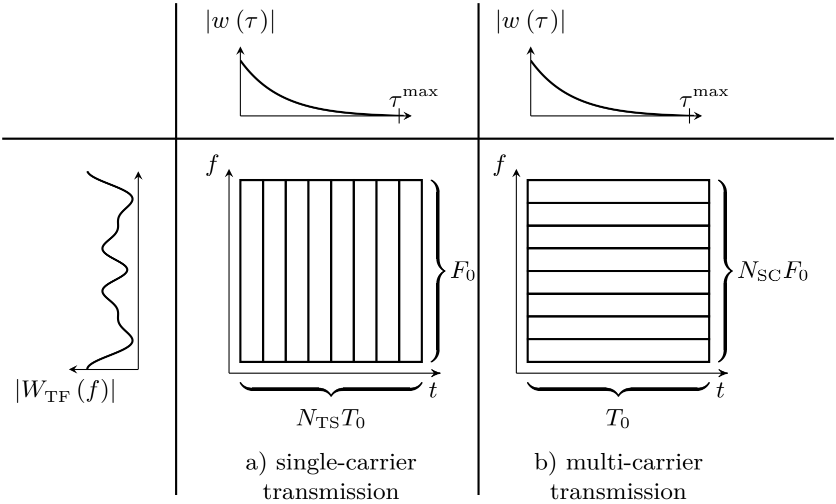

a) single-carrier transmission

b) multi-carrier transmission

Figure 3.3: Comparison of different settings for the sub-carrier spacing F_0 and symbol time spacing T_0 with $N_{\mathrm{SC}} = N_{\mathrm{TS}}$.

equalizer structures for orthogonal transmission schemes. However, this results in long symbols in time direction T_0 and the assumption of 1-tap equalization only holds for slow-fading channels within the symbol duration [Roh16].

Throughout this work, we assume time-variant channel impulse responses $w(\tau, t)$, *e.g.* due to CFO or velocity, which strongly affect the transmission.

3.2.2 Receive Signal of a Multi-Carrier Transmission

As depicted in Fig. 3.1, an *analyzing* FB is established at the receiver to observe the complex transmit symbols $d_{k,\ell}$. The prototype filters at the receiver can again be described by a Gabor synthesizing function with receive filters

$$g^{\mathrm{Rx}}_{k',\ell'}(t) = g^{\mathrm{Rx}}(t - \ell' T_0)\, e^{j2\pi k' F_0 t} e^{j\phi_{k',\ell'}} \quad , \tag{3.8}$$

where the index pair (k', ℓ') contains the corresponding lattice (TF grid) point at the receiving side. After the transmit signal $x(t)$ passes a time-variant channel $w(\tau, t)$ as in (2.7), the analysis filter for the TF point (k', ℓ') is applied to the receive signal $y(t)$ and sampled at $\iota = 0$ yielding the observations

$$y_{k',\ell'} = \left. \int\limits_{-\infty}^{\infty} y\left(t\right) g^{\mathrm{Rx}}_{k',\ell'}\left(\iota - t\right) \mathrm{d}t \right|_{\iota=0} \quad . \tag{3.9}$$

Subsequently, we use the short-hand notations $s = k + \ell N_{\mathrm{SC}}$ for the sending index and $r = k' + \ell' N_{\mathrm{SC}}$ for the receiving index. As derived in the Appendix A, the received signal can be rewritten as

$$y_r = \sum_s h_{r,s} d_s + \tilde{n}_r \quad , \tag{3.10}$$

where $\tilde{n}_r$ is a noise sample (*cf.* (A.22)). The coefficient $h_{r,s}$ is the *effective channel coefficient* including the impact of the physical channel and the used waveform and it is given by

$$h_{r,s} = e^{j\left(\phi_r + \phi_s\right)} \sum_{\gamma=0}^{N_{\mathrm{path}}-1} \varsigma_\gamma e^{j\overline{\phi}_\gamma} A^*_{g^{\mathrm{Tx}},g^{\mathrm{Rx}}}\left(\overline{\tau}_\gamma, \overline{\nu}_\gamma\right) \quad , \tag{3.11}$$

where ς_γ denotes the channel gain for path $\gamma = 0, \ldots, N_{\mathrm{path}} - 1$ given in (2.11). Furthermore, we use the frequency shift abbreviation $\overline{\nu}_\gamma = \left(k - k'\right) F_0 + \nu_\gamma$, the time shift abbreviation $\overline{\tau}_\gamma = \left(\ell - \ell'\right) T_0 + \tau_\gamma$ and the phase abbreviation $\overline{\phi}_\gamma = -\pi\left(2kF_0\tau_\gamma - \overline{\nu}_\gamma\overline{\tau}_\gamma\right)$.

The **cross ambiguity function** $A_{g_1,g_2}\left(\tau, \nu\right)$ used in (3.11) is a two-dimensional function with delay shift τ and Doppler shift ν and generally defined by

$$\begin{aligned} A_{g_1,g_2}\left(\tau, \nu\right) &= \mathcal{F}\left\{g_1\left(t + \frac{\tau}{2}\right) g_2^*\left(t - \frac{\tau}{2}\right)\right\} \\ & \int\limits_{-\infty}^{\infty} g_1\left(t + \frac{\tau}{2}\right) g_2^*\left(t - \frac{\tau}{2}\right) e^{-j2\pi\nu t} \mathrm{d}t, \end{aligned} \tag{3.12}$$

where $\mathcal{F}\left\{\cdot\right\}$ is the Fourier transformation. The cross ambiguity function describes the impact of the waveforms g_1 and g_2 under time shifts τ and frequency shifts ν. Historically, it was invented in radar research, where it is important to know if obstacles are within a specific range and at a specific speed around a radar station [Woo53].

We can define two special cases without a frequency shift, *i.e.* $\nu = 0$, giving us the time-correlation function or inner product [LAB95]

$$A_{g_1,g_2}\left(\tau, 0\right) = \int\limits_{-\infty}^{\infty} g_1\left(t + \frac{\tau}{2}\right) g_2^*\left(t - \frac{\tau}{2}\right) \mathrm{d}t \tag{3.13}$$

and without time shift ($\tau = 0$) leading to the Fourier transformation of the multiplication of both filters by

$$A_{g_1,g_2}(0,\nu) = \int_{-\infty}^{\infty} g_1(t)\, g_2^*(t)\, e^{-j2\pi\nu t} \mathrm{d}t \quad . \tag{3.14}$$

The cross ambiguity function can be interpreted as follows: *the cross ambiguity function is the Fourier transformation of the cross-instantaneous correlation between shifted transmit and receive filter*[3]*.*

The channel coefficient $h_{r,s}$ in (3.11) can be interpreted as the sum over ambiguity functions shifted in time and frequency and weighted by the corresponding channel gains ς_γ affected by an additional phase term. To further analyzed the ambiguity function as it is an important function for time and frequency shifted filters, we introduce first famous filters.

Waveform Properties

In order to gain a deeper understanding of waveform properties, different measurements like the cross ambiguity function, the direction parameter and the Heisenberg-Gabor uncertainty will be discussed in the following section for exemplary chosen waveforms, which we will first introduce.

Rectangular Waveform The rectangular waveform [KD18] of symbol length T_S is given by

$$g_\mathrm{rect}(t) = \begin{cases} 1/\sqrt{T_\mathrm{S}} & |t| \leq \frac{T_\mathrm{S}}{2} \\ 0 & \text{otherwise} \end{cases} \quad . \tag{3.15}$$

It is *limited in time* and has a constant amplitude $\frac{1}{\sqrt{T_\mathrm{S}}}$ within the symbol duration. The corresponding frequency response $G(f)$ has a broad $\mathrm{sinc}(f) = \frac{\sin(\pi f/T_\mathrm{S})}{(\pi f/T_\mathrm{S})}$ shape in frequency domain with zeros crossing at multiples of $1/T_\mathrm{S}$. The two dimensional Nyquist criterion is fulfilled by choosing $T_0 = T_\mathrm{S}$ and $F_0 = 1/T_\mathrm{S}$.

---

[3] Related to [Du08], we use the term “instantaneous” to indicate that no expectation is taken compared to the common correlation function

Root-Raised-Cosine Waveform The *frequency-limited* root-raised-cosine (RRC) waveform [KD18] given by

$$g_{\mathrm{RRC}}^{\alpha}\left(t\right)=\begin{cases}\frac{1}{\sqrt{T_{\mathrm{S}}}}\left(1-\alpha+4\frac{\alpha}{\pi}\right) & t=0\\ \frac{\alpha}{\sqrt{2T_{\mathrm{S}}}}\left[\left(1+\frac{2}{\pi}\right)\sin\left(\frac{\pi}{4\alpha}\right)+\left(1-\frac{2}{\pi}\right)\cos\left(\frac{\pi}{4\alpha}\right)\right] & t=\pm\frac{1}{4\alpha}\\ \frac{1}{\sqrt{T_{\mathrm{S}}}}\frac{\sin((1-\alpha)\pi t/T_{\mathrm{S}})+4\alpha t/T_{\mathrm{S}}\cos((1+\alpha)\pi t/T_{\mathrm{S}})}{\pi t/T_{\mathrm{S}}\left(1-(4\alpha t/T_{\mathrm{S}})^{2}\right)} & \text{otherwise}\end{cases}\tag{3.16}$$

fulfills the first Nyquist condition [KD18] in time direction, if the other symbols are placed into equidistant zero-crossings at ℓT_{S}. The filter shape can be adjusted with the roll-off factor α to find a trade-off between the used bandwidth and impulse response duration.

A special case, also used in this work [FB11, LAB95, FBY10, SSL02, Du08] is the half-cosine (in time) waveform, which is achieved by setting the roll-off factor $\alpha = 1$:

$$g_{\text{half-cosine}}\left(t\right)=g_{\mathrm{RRC}}^{\alpha=1}\left(t\right)=\frac{4\cos\left(2\pi t/T_{0}\right)}{\pi\left(1-\left(4t/T_{0}\right)^{2}\right)}\quad .\tag{3.17}$$

The dual function $g_{\text{half-cosine in freq}}\left(f\right)$ is achieved by interchanging the time index t with the frequency index f and $T_0 \rightarrow F_0$.

Gaussian Waveform The *well-localized* Gaussian waveform [KD18] is given by

$$g_{\text{Gaussian}}^{(\rho)}\left(t\right)=\left(2\rho\right)^{\frac{1}{4}}e^{-\pi\rho t^{2}}\quad ,\tag{3.18}$$

where the shape in time and frequency can be adjusted by the localization parameter $\rho \in [0, \infty)$. By choosing $\rho = 1$ the waveform has the same response in time and frequency direction.

Orthogonality An orthogonal transmission is achieved, if the inner product of two functions has the following property [Du08, SGA13, KD18]

$$\langle g_{k,\ell}^{\mathrm{Tx}},g_{k',\ell'}^{\mathrm{Rx}}\rangle=\int_{\infty}^{\infty}g_{k,\ell}^{\mathrm{Tx}}\left(t\right)g_{k',\ell'}^{*\mathrm{Rx}}\left(t\right)\mathrm{d}t=\begin{cases}1 & \text{, if } \ell'=\ell \text{ and } k'=k\\ 0 & \text{, otherwise}\end{cases}\quad .\tag{3.19}$$

Properties of Cross Ambiguity Function The orthogonality condition (3.19) can be rewritten by the sampled cross ambiguity function (*cf.* A.2

and [Du08]) at $(\ell T_0, kF_0)$ like

$$A_{g_1,g_2}(\ell T_0, kF_0) = \begin{cases} 1 & ,\ell = 0, k = 0 \\ 0 & ,\text{otherwise} \end{cases} , \tag{3.20}$$

which can be interpreted as a two-dimensional Nyquist criterion in time and frequency domain.

The ambiguity function of the **rectangular** Tx/Rx filters (3.15) of same length $T_\mathrm{S}^\mathrm{Tx} = T_\mathrm{S}^\mathrm{Rx}$ is shown in Fig. 3.4a. At the frequency shift ν-plane the projection of a cut of the ambiguity function $A(\tau = 0, \nu)$ (*cf.* (3.14)) is depicted. This can be interpreted as the Fourier transform of the Tx/Rx filters and exhibits the sinc(ν) shape typical for rectangular filters. Cutting the ambiguity function $A(\tau, \nu)$ at $\nu = 0$ equals the convolution (*cf.* (3.13)) of the two Tx/Rx filters in time domain and a triangular shape is achieved. The crossing points in Fig. 3.4a illustrate the sampling points for the TF grid (k, ℓ) by choosing $T_0 = T_\mathrm{S}$ and $F_0 = 1/T_\mathrm{S}$ to fulfill the orthogonality condition (3.20). Thus, no self-interference terms are present on the neighboring TF points. Additionally, Fig. 3.4b illustrates the ambiguity function with $T_\mathrm{S}^\mathrm{Tx} > T_\mathrm{S}^\mathrm{Rx}$ which is stretched in time domain due to the longer shape at the Tx, such that a flat plateau of length $T_\mathrm{GI} = T_\mathrm{S}^\mathrm{Tx} - T_\mathrm{S}^\mathrm{Rx}$ is generated around $\tau = 0$. This combination is used in the MC scheme CP-OFDM to improve the robustness against delay spread as introduced later on.

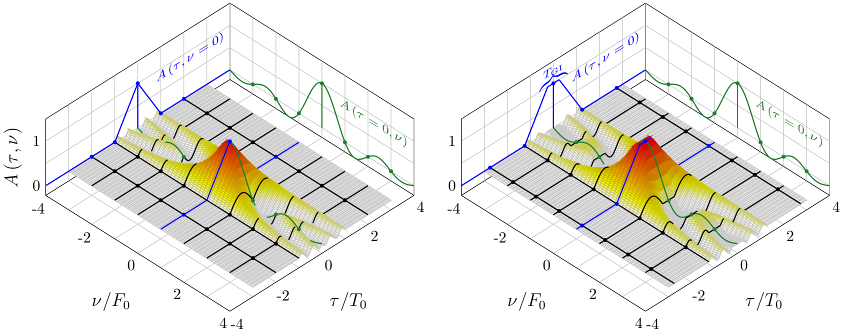

a) Rectangular Tx/Rx filter of same length $T_\mathrm{S}^\mathrm{Tx} = T_\mathrm{S}^\mathrm{Rx}$

b) Rectangular Tx/Rx filter of different length $T_\mathrm{S}^\mathrm{Tx} > T_\mathrm{S}^\mathrm{Rx}$

Figure 3.4: Ambiguity function for rectangular Tx/Rx filters.

Fig. 3.5a shows the ambiguity function of the **Gaussian** waveform with localization parameter $\rho = 1$ leading to the same shape in time and frequency domain and Fig. 3.5b shows the half-cosine waveform (3.17). The lattice is chosen with the same parameters as in the rectangular case like in Fig. 3.4a.

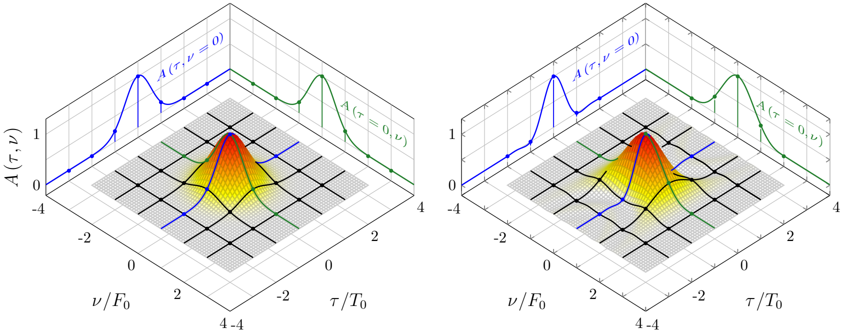

a) Gaussian Tx/Rx filter with parameter $\rho = 1$

b) Half-cosine Tx/Rx filter

Figure 3.5: Ambiguity function for a) Gaussian and b) half-cosine Tx/Rx filters.

It can be observed that each transmit signal has a considerable influence on adjacent TF grid points around the desired sampling point at $(0,0)$. However, TF grid points of larger distance to the origin are even unaffected in case of an offset shift of the TF grid in time or frequency direction.

Classification of Waveform Parameters The choice of the waveform directly determines the behavior of a transmission in time and frequency domain. So far we have illustrated the transmission with waveforms only illustratively and intuitively with the ambiguity function. Based on the ideas of Heisenberg [Hei27] and Gabor [Gab46], numerical TFL properties of a filter can be calculated either by the Heisenberg-Gabor (or only Heisenberg) uncertainty parameter given by

$$\xi = \frac{1}{4\pi\sigma_t \cdot \sigma_f} \leq 1 \quad , \tag{3.21}$$

where the product $\sigma_t \cdot \sigma_f$ is called time-bandwidth product [KD18], or by the direction parameter [DS08] given by

$$\kappa = \frac{\sigma_t}{\sigma_f}, \tag{3.22}$$

where the "width" of a function (or the dispersion in the specific domain) is calculated by the second order moment as

$$\sigma_t = \sqrt{\int_{-\infty}^{\infty} (t - \overline{\mu}_t)^2 \left|g(t)\right|^2 \mathrm{d}t} \quad , \quad \sigma_f = \sqrt{\int_{-\infty}^{\infty} \left(f - \overline{\mu}_f\right)^2 \left|G(f)\right|^2 \mathrm{d}f} \tag{3.23}$$

and the center of a function by

$$\overline{\mu}_t = \int_{-\infty}^{\infty} t\,|g(t)|\,\mathrm{d}t \quad , \quad \overline{\mu}_f = \int_{-\infty}^{\infty} f\,|G(f)|\,\mathrm{d}f \quad . \tag{3.24}$$

Waveforms with good TFL properties have a Heisenberg-Gabor parameter ξ close to 1 and are then called *well-localized.* The direction parameter indicates if the main direction of the waveform is located more in time ($\kappa > 1$) or in frequency ($\kappa < 1$) direction.

The Heisenber parameter ξ and the direction parameter κ for the rectangular, the half-cosine and the Gaussian waveform are given in Table 3.1. The rectangular waveform has a direction parameter $\kappa \to 0$ indicating that the main energy is located into frequency direction due to $\sigma_f \to \infty$ as and the Heisenberg parameter $\xi = 0$ indicates the infinite dimension [Du08]. The half-cosine waveform is “more located” in frequency direction and has a higher Heisenberg parameter denoting a better shape in frequency and time domain than the rectangular waveform. The Gaussian waveform has the best TFL property with a Heisenberg parameter $\xi = 1$ and by the choice of $\rho = 1$ the waveform gets identical in time and frequency domain (indicated by $\kappa = 1$).

Table 3.1: Waveform parameter [HB94, HB97, SR00, Du08]

	rect.[4]	half-cosine	Gaussian	Mirabbasi[5]	EGF[6]
Heisenberg ξ	0	0.8851	1	0.9769	0.8839
Direction κ	0	0.68796	$1/\rho$	0.5	0.8369

Beside the rectangular, the RRC and the Gaussian waveform, a variety of other waveforms were investigated in the past decades. We invite the interested reader to [SN96, SGA13, JK16, NSR17] and references therein. However, we want to mention two additional waveforms, the Mirabbasi waveform $g_{\text{Mirabbasi}}(t)$ (A.10) [Mar98, MM02] and the extended Gaussian function (EGF) waveform $g^{(\rho)}_{\text{EGF},F_0,T_0}(t)$ in (A.11) [RS97, SR00]. The corresponding mathematical expressions can be found in the Appendix A.3. The Mirabbasi waveform has a high efficacy on decaying in frequency direction and has been further investigated in the PHYDYAS project on FBMC [Bel10]. The EGF waveform extends the basic idea of orthogonalization like

---

[4] These are the theoretical values. However, we get $\xi = 0.1840$ and $\kappa = 0.1925$ by numerical evaluations via MATLAB, similar to [Du08]. [5] With an overlapping factor $Q = 4$ as used in Fig. 3.21b [6] These values are derived with $\rho = 2$, $T_0' = 1/2T_0$ and $F_0' = F_0$ as used in Fig. 3.21a

in the isotropic orthogonal transform algorithm (IOTA) [LAB95] procedure to general TF grids. So far, these waveforms do not fulfill the orthogonality condition (3.20), but they become more interesting in OQAM-based FBMC introduced later on.

Matrix Representation of Multi-Carrier Schemes

In this subsection we will introduce a matrix notation for the MC scheme (3.10) to simplify the notation. So far, the MC scheme is not limited in the number of sub-carriers or time instances used. This model would not result in a matrix description with finite dimension and the result could (other descriptions are possible) look like

$$\underbrace{\begin{bmatrix} \vdots \\ \begin{bmatrix} \vdots \\ y_{-1,-1} \\ y_{\pm0,-1} \\ y_{+1,-1} \\ \vdots \end{bmatrix} \\ \begin{bmatrix} \vdots \\ y_{-1,\pm0} \\ y_{\pm0,\pm0} \\ y_{+1,\pm0} \\ \vdots \end{bmatrix} \\ \begin{bmatrix} \vdots \\ y_{-1,+1} \\ y_{\pm0,+1} \\ y_{+1,+1} \\ \vdots \end{bmatrix} \\ \vdots \end{bmatrix}}_{\underline{\mathbf{y}}} = \underbrace{\begin{bmatrix} & \vdots & \\ & \mathbf{H}_{-1,-1}\mathbf{H}_{-1,\pm0}\mathbf{H}_{-1,+1} & \\ \cdots & \mathbf{H}_{\pm0,-1}\mathbf{H}_{\pm0,\pm0}\mathbf{H}_{\pm0,+1} & \cdots \\ & \mathbf{H}_{+1,-1}\mathbf{H}_{+1,\pm0}\mathbf{H}_{+1,+1} & \\ & \vdots & \end{bmatrix}}_{\underline{\mathbf{H}}} \underbrace{\begin{bmatrix} \vdots \\ \begin{bmatrix} \vdots \\ d_{-1,-1} \\ d_{\pm0,-1} \\ d_{+1,-1} \\ \vdots \end{bmatrix} \\ \begin{bmatrix} \vdots \\ d_{-1,\pm0} \\ d_{\pm0,\pm0} \\ d_{+1,\pm0} \\ \vdots \end{bmatrix} \\ \begin{bmatrix} \vdots \\ d_{-1,+1} \\ d_{\pm0,+1} \\ d_{+1,+1} \\ \vdots \end{bmatrix} \\ \vdots \end{bmatrix}}_{\underline{\mathbf{d}}} + \underbrace{\begin{bmatrix} \vdots \\ \begin{bmatrix} \vdots \\ \tilde{n}_{-1,-1} \\ \tilde{n}_{\pm0,-1} \\ \tilde{n}_{+1,-1} \\ \vdots \end{bmatrix} \\ \begin{bmatrix} \vdots \\ \tilde{n}_{-1,\pm0} \\ \tilde{n}_{\pm0,\pm0} \\ \tilde{n}_{+1,\pm0} \\ \vdots \end{bmatrix} \\ \begin{bmatrix} \vdots \\ \tilde{n}_{-1,+1} \\ \tilde{n}_{\pm0,+1} \\ \tilde{n}_{+1,+1} \\ \vdots \end{bmatrix} \\ \vdots \end{bmatrix}}_{\underline{\tilde{\mathbf{n}}}} \tag{3.25}$$

with the sub-matrices $\mathbf{H}_{\ell',\ell} \in \mathbb{C}^{N'_{\mathrm{SC}} \times N_{\mathrm{SC}}}$ given by

$$\mathbf{H}_{\ell',\ell} = \left[\begin{array}{ccccc} & & \vdots & & \\ & h_{k'-1,\ell',k-1,\ell} & h_{k'-1,\ell',k\pm 0,\ell} & h_{k'-1,\ell',k+1,\ell} & \\ \cdots & h_{k'\pm 0,\ell',k-1,\ell} & h_{k'\pm 0,\ell',k\pm 0,\ell} & h_{k'\pm 0,\ell',k+1,\ell} & \cdots \\ & h_{k'+1,\ell',k-1,\ell} & h_{k'+1,\ell',k\pm 0,\ell} & h_{k'+1,\ell',k+1,\ell} & \\ & & \vdots & & \end{array}\right] . \tag{3.26}$$

The matrix model (3.25) can be summarized as

$$\underline{\mathbf{y}} = \underline{\mathbf{H}}\,\underline{\mathbf{d}} + \underline{\tilde{\mathbf{n}}} \tag{3.27}$$

where the **frame-based effective channel matrix** $\underline{\mathbf{H}}$ has dimension $N'_{\mathrm{SC}}N'_{\mathrm{TS}} \times N_{\mathrm{SC}}N_{\mathrm{TS}}$, with N_{SC} and N_{TS} the number of sub-carriers and time symbols considered sent in one **frame**, respectively, and N'_{SC} and N'_{TS} the number of sub-carriers and time symbols, respectively, considered at the receiver. Interpreting the elements $d_{k,\ell}$ as elements of a matrix $\mathbf{D}$ of dimension $N_{\mathrm{SC}} \times N_{\mathrm{TS}}$, with N_{SC} sub-carriers and N_{TS} time-symbols, the ℓ^{th} column $\mathbf{d}_\ell = [d_{0,\ell}, d_{1,\ell}, \ldots, d_{N_{\mathrm{SC}}-1,\ell}]^{\mathsf{T}}$ of size $N_{\mathrm{SC}} \times 1$ corresponds to the ℓ **MC symbol**[7] sent at the time instance ℓT_0. Stacking all symbol vectors $\mathbf{d}_\ell$ of one frame into an overall stacked vector $\underline{\mathbf{d}} = [\mathbf{d}_0^{\mathsf{T}}, \mathbf{d}_1^{\mathsf{T}}, \ldots, \mathbf{d}_{N_{\mathrm{TS}}}^{\mathsf{T}}]^{\mathsf{T}}$ results in the **frame-based symbol vector** $\underline{\mathbf{d}}$ with size $N_{\mathrm{SC}}N_{\mathrm{TS}} \times 1$ introduced in Section 2.4. One may note that this sub-carrier mapping is realized with S/P and parallel to serial (P/S) mapping by the vectorization operator $\underline{\mathbf{d}} = \mathrm{vec}\{\mathbf{D}\}$. In the same fashion the **frame-based receive vector** $\underline{\mathbf{y}}$ with dimension $N'_{\mathrm{SC}}N'_{\mathrm{TS}} \times 1$ and the receive matrix $\mathbf{Y} \in \mathbb{C}^{N'_{\mathrm{SC}} \times N'_{\mathrm{TS}}}$ with $\underline{\mathbf{y}} = \mathrm{vec}\{\mathbf{Y}\}$ are obtained. Furthermore, the **frame-based noise vector** $\underline{\tilde{\mathbf{n}}}$ with dimension $N'_{\mathrm{SC}}N'_{\mathrm{TS}} \times 1$ is also re-presentable by $\underline{\tilde{\mathbf{n}}} = \mathrm{vec}\{\underline{\widetilde{\mathbf{N}}}\}$.

The sub-matrices $\mathbf{H}_{\ell',\ell}$ (3.26) of frame-based effective channel matrix $\underline{\mathbf{H}}$ denote the impact of a transmit MC symbol in frequency domain $\mathbf{d}_\ell$ on the receive related **MC symbol** in frequency domain $\mathbf{y}_{\ell'}$ at the receiver.

To get a finite and therefore implementable matrix description the investigation is limited to a finite number of sub-carriers N_{SC} and time instances N_{TS}. In Fig. 3.6 two windows are shown within the TF grid. Exemplary, the black filled TF grid points corresponds to the points used at the transmitter side, where N_{SC} is the number of sub-carriers and N_{TS} the number of time instances considered, respectively. A larger area within the TF grid can be

---

[7] We use here the related term MC symbol, as the vector $\mathbf{d}_\ell$ covers the coefficients of all sub-carriers in one time instance ℓT_0 in frequency domain.

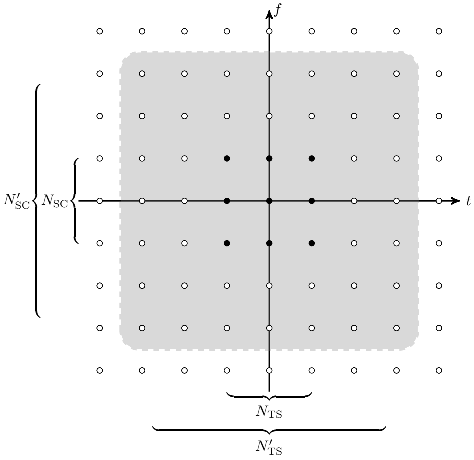

Figure 3.6: Illustration of rectangular TF grid with $N_{\mathrm{SC}}N_{\mathrm{TS}}$ transmit symbols and a receiving window considering $N'_{\mathrm{SC}}N'_{\mathrm{TS}}$ TF grid points.

affected due to the transmission over a wireless channel, even if orthogonal transmission schemes are used. To collect all spread signals within the TF grid a larger window with N'_{SC} sub-carriers and N'_{TS} time instances in gray may be used.

Factor Graph-based Representation

Based on the system model (3.27) and the derivation in the Appendix B the FG for a MC transmission can be illustrated as in Fig. 3.7, where only a part of three transmit symbols d_s and five receive signal y_r are shown [LYWM05]. It is worth noting that the entries in the effective channel matrix $\underline{\mathbf{H}}$ determine the connection in the FG. All entries unequal to zero result in an edge between the corresponding factor and variable nodes. Furthermore, by using this representation usually cycles occur between adjacent TF grid points as illustrated by the black dashed line in the figure.

Summary

This section introduced the mapping of the symbol vector $\underline{\mathbf{d}}$ to a transmit signal $x\,(t)$, which was derived for general waveforms by the help of FBs shifting the complex symbols to discrete points in the TF plane. The reception of the signal after passing a time-variant channel and the procedure at the receiver to recover the data symbols by an analyzing FB was discussed.

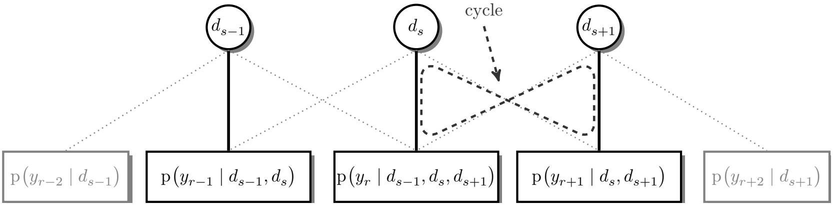

Figure 3.7: Factor graph representation with three transmit symbols and five connected receive signals. One cycle is illustratively shown by the black dashed line.

This general scheme is called FBMC. Furthermore, we derived a matrix model (3.27) capturing the general FBMC system. Finally, we gave a FG-based representation of the overall receiver procedure. The next section will introduce concrete MC schemes which are already used in standards or which were in discussion for the 5th generation (5G) and future mobile communication standards [Wun13, WJK$^+$14].

3.3 Classification of Multi-Carrier Schemes

In this section different MC schemes will be introduced, compared and the differences in terms of signal generation and signal recovery at the receiving side will be shown. The design of a MC scheme is subject to the following conditions

1) *Orthogonality*: a (complex- or real-valued) orthogonal transmission results in an interference-free reception with simple equalization techniques also called the *(near) perfect reconstruction property*. The concept of perfect reconstruction [Vai93] defines what conditions are necessary so that any signal passing through the entire MC chain (without noise and without physical channel) remains undistorted with its amplitude and phase without further processing. Another important concept is near-perfect reconstruction, where some amplitude and phase changes are allowed [BMN11].

2) *Time-frequency grid density*: the lattice density $\delta_{\mathrm{LD}}(\Lambda)$ determines the bandwidth efficiency η of a system.

3) The *waveform localization* (*i.e.* TFL property) offers control over the spectral shape and it is very important regarding the high expense of the available spectral bandwidth.

The connection of the conditions are illustrated in Fig. 3.8. Each change of one parameter has a direct influence on the other parameters. Note that a complex-valued orthogonal transmission with well-localized filters, *i.e.* good TFL properties, and a lattice density $\delta_{\mathrm{LD}}(\Lambda) = 1$ is not achievable [Gab46, Dau90, SB03].

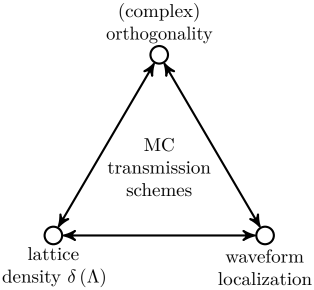

Figure 3.8: Multi-carrier conditions.

3.3.1 Orthogonal Multi-Carrier Transmissions Schemes

Within this section, we focus on orthogonal transmissions, which offer perfect symbol reconstruction at the receiver and, thus, simple 1-tap equalization techniques. The first scheme plain-OFDM uses a rectangular waveform to design an orthogonal transmission and results in flat-fading channels, where the distortion is simply equalized by one-tab divider. To mitigate the influence of multi-path fading, *i.e.* frequency-selective channels, a GI is used in the following two schemes, also based on a rectangular waveform. The high OoBE introduced by this waveform with corresponding $\mathrm{sinc}(f)$ shape in frequency domain are reduced by the additional application of a smoothing filter a the Tx in w-OFDM. Block-wise filtering is performed in UF-OFDM to achieve lower OoBE by applying filter with small filter lengths.

The last scheme considered here is OQAM-based FBMC, it offers perfect reconstruction with waveforms, like the aforementioned Mirabbasi and EGF filter with a better spectral shape by dropping the condition of complex-valued orthogonality.

Orthogonal Frequency Division Multiplexing (OFDM)

A very famous MC candidate is OFDM-based on a rectangular waveform (3.15) with symbol length T_{S}. It is important to note that for OFDM

$T_0 = T_\mathrm{S}$ holds. The rectangular shape in time domain corresponds to a sinc shape in frequency domain $X(f) = \mathcal{F}\{x(t)\}$ as illustrated in Fig. 3.9 with equidistant zeros at $1/T_\mathrm{S}$. By placing all other sub-carriers onto the zeros with sub-carrier spacing $F_0 = 1/T_\mathrm{S}$, the overall transmission will end up in an orthogonal transmission, which was already indicated by the ambiguity function in Fig. 3.4a. The OoBE also depicted in Fig. 3.9 has high amplitudes due to the sinc shape of the rectangular waveform in frequency domain with the first side-lobe level of approximate -13dB compared to the main lobe.

The resulting lattice density becomes critically sampled $\delta_\mathrm{LD}(\Lambda) = \frac{1}{T_\mathrm{S}\frac{1}{T_\mathrm{S}}} = 1$ with the ill-conditioned, *i.e.* non-localized rectangular waveform.

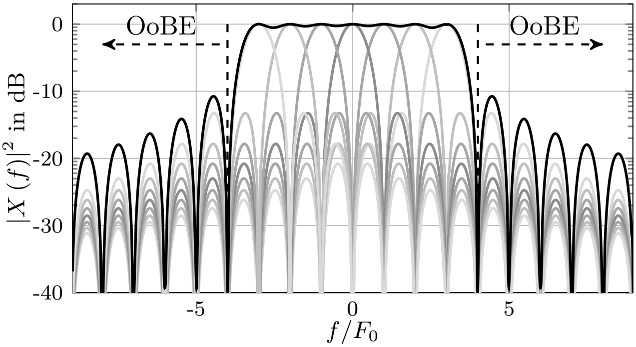

Figure 3.9: Spectrum of plain-OFDM utilizing 7 sub-carriers with a normalized sub-carrier spacing $F_0 = 1/T_\mathrm{S}$. The gray curves correspond to the sub-carriers and the black curve shows the overall transmit signal.

A discrete description by sampling with sampling time $T_\mathrm{A} = \frac{T_\mathrm{S}}{w N_\mathrm{SC}}$ is used[8]. The transmit signal (3.5) with the rectangular filter (3.15) and no additional phase rotation $\phi_s = 0$ results in $x(t)|_{t=qT_\mathrm{S}/N_\mathrm{SC}} \to x(q\frac{T_\mathrm{S}}{N_\mathrm{SC}})$ given

---

[8] Within the description we use the oversampling factor $w = 1$ and thus we skip the oversampling factor throughout our description.

by

$$x\left(q\frac{T_\mathrm{S}}{N_\mathrm{SC}}\right)=\sum_{\ell=0}^{N_\mathrm{TS}-1}\sum_{k=0}^{N_\mathrm{SC}-1}d_{k,\ell}g_\mathrm{rect}^\mathrm{Tx}\left(q\frac{T_\mathrm{S}}{N_\mathrm{SC}}-\ell T_0\right)e^{j\frac{2\pi kF_0qT_\mathrm{S}}{N_\mathrm{SC}}} \tag{3.28a}$$

$$\Leftrightarrow x\left(q\frac{T_\mathrm{S}}{N_\mathrm{SC}}\right)=\sum_{\ell=0}^{N_\mathrm{TS}-1}\sum_{k=0}^{N_\mathrm{SC}-1}d_{k,\ell}\,\underbrace{g_\mathrm{rect}^\mathrm{Tx}\left(q\frac{T_\mathrm{S}}{N_\mathrm{SC}}-\ell\frac{T_\mathrm{S}}{N_\mathrm{SC}}N_\mathrm{SC}\right)}_{g_\mathrm{rect}^\mathrm{Tx}[q-\ell N_\mathrm{SC}]}e^{j\frac{2\pi kq}{N_\mathrm{SC}}} \tag{3.28b}$$

$$\Leftrightarrow x\left[q\right]=\sum_{\ell=0}^{N_\mathrm{TS}-1}\underbrace{\sum_{k=0}^{N_\mathrm{SC}-1}d_{k,\ell}g_\mathrm{rect}^\mathrm{Tx}\left[q-\ell N_\mathrm{SC}\right]e^{j\frac{2\pi kq}{N_\mathrm{SC}}}}_{x_\ell[q-\ell N_\mathrm{SC}]}\quad. \tag{3.28c}$$

In step (3.28a) the sampling take place. In the next step (3.28b) $T_0=T_\mathrm{S}$ and $F_0=1/T_0$ are used. Finally, the shorthand notation for discrete signals $x\left[q\right]=x(q\frac{T_\mathrm{S}}{N_\mathrm{SC}})$ are used for the transmit signal $x\left[q\right]$ and the filter $g_\mathrm{rect}^\mathrm{Tx}\left[q\right]$ in (3.28c).

The rectangular shape $g_\mathrm{rect}^\mathrm{Tx}\left[q\right]$ of length T_S works like a window function and leads to the fact that each MC symbol $x_\ell\left[q-\ell N_\mathrm{SC}\right]$ can be calculated separately over all sub-carriers. Thus, the signal for each MC symbol ℓ can be generated separately for $q=0,\dots,N_\mathrm{SC}-1$ as

$$x_\ell\left[q-\ell N_\mathrm{SC}\right]=\sum_{k=0}^{N_\mathrm{SC}-1}d_{k,\ell}e^{j\frac{2\pi qk}{N_\mathrm{SC}}}. \tag{3.29}$$

Afterwards the single MC symbol $x_\ell\left[q-\ell N_\mathrm{SC}\right]$ can be summed over ℓ in (3.28c). It can be easily seen that (3.29) is similar to the inverse discrete Fourier transform (IDFT) and the calculation for a transmit symbol vector $\mathbf{d}_\ell$ can be realized by the multiplication with the inverse Fourier matrix[9] $\mathbf{F}_{N_\mathrm{SC}}^\mathsf{H}$ of size $N_\mathrm{SC}\times N_\mathrm{SC}$ yielding the ℓ^th MC transmit signal vector $\mathbf{x}_\ell$ at time slot ℓ [KD18, KK18].

$$\mathbf{x}_\ell=\mathbf{F}_{N_\mathrm{SC}}^\mathsf{H}\mathbf{d}_\ell\quad. \tag{3.30}$$

At the receiver the inverse operation is performed, *i.e.* multiplication with the Fourier matrix $\mathbf{F}\in\mathbb{C}^{N'_\mathrm{SC}\times N'_\mathrm{SC}}$, such that the effective channel sub-matrices

---

[9] The power normalized Fourier matrix $\mathbf{F}_{N_\mathrm{SC}}$ contains the elements $f_{a,b}=1/\sqrt{N_\mathrm{SC}}\exp(j\frac{2\pi ab}{N_\mathrm{SC}})$. One may note that the inverse Fourier matrix is given by the Hermitian version of the Fourier matrix $\mathbf{F}^{-1}=\mathbf{F}^\mathsf{H}$. We skip the size of the matrix to ease the notation throughout this thesis as otherwise stated.

(3.26) result in

$$\mathbf{H}_{\ell',\ell} = \mathbf{F}\mathbf{W}_{\mathrm{conv},\ell',\ell}\mathbf{F}^{\mathsf{H}} \quad . \tag{3.31}$$

As the convolution in (2.7) with the impulse response $w(\tau, t)$ (2.11) can be described by a convolutional matrix in the discrete domain [KD18], we use here the matrix description $\mathbf{W}_{\mathrm{conv},\ell',\ell} \in \mathbb{C}^{N'_{\mathrm{SC}} \times N_{\mathrm{SC}}}$ is a sub-matrix of the overall frame-based convolution matrix given by

$$\underline{\mathbf{W}}_{\mathrm{conv}} = \begin{bmatrix} \mathbf{W}_{\mathrm{conv},0,0} & \mathbf{W}_{\mathrm{conv}0,1} & \cdots & \mathbf{W}_{\mathrm{conv},0,N_{\mathrm{TS}}-1} \\ \mathbf{W}_{\mathrm{conv},1,0} & \mathbf{W}_{\mathrm{conv}1,1} & \cdots & \vdots \\ \vdots & \vdots & \ddots & \vdots \\ \mathbf{W}_{\mathrm{conv},N'_{\mathrm{TS}}-1,0} & \mathbf{W}_{\mathrm{conv},N_{\mathrm{TS}}-1,1} & \cdots & \mathbf{W}_{\mathrm{conv},N'_{\mathrm{TS}}-1,N_{\mathrm{TS}}-1} \end{bmatrix} \tag{3.32}$$

with elements $w[\text{ɿ}, q]$, which are the sampled version of the time-impulse response (2.11), with $\text{ɿ}T_{\mathrm{S}}/N_{\mathrm{SC}}$ as discrete delay step and $qT_{\mathrm{S}}/N_{\mathrm{SC}}$ denoting discrete time.

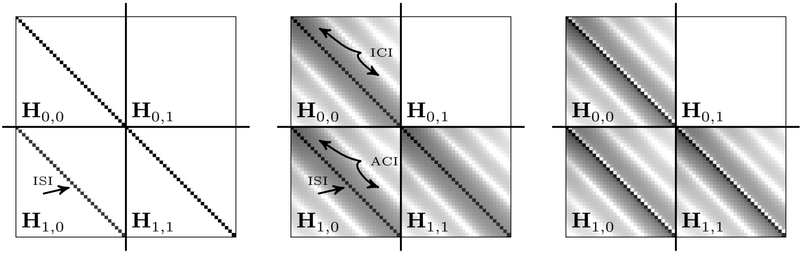

a) $\Delta\nu = 0, \Delta\tau = 0$ b) $\Delta\nu = 0, \Delta\tau = 0.1T_{\mathrm{S}}$ c) $\Delta\nu = 0.1F_0, \Delta\tau = 0.1T_{\mathrm{S}}$

Figure 3.10: Illustration of the amplitudes of the effective channel matrix $\underline{\mathbf{H}}$ for plain-OFDM. Only the first four sub-matrices (*cf.* (3.33)) are shown.

To illustrate the effect of channel impacts on the structure of the effective channel matrix $\underline{\mathbf{H}}$ (3.27) we focus on a small cutout as defined by

$$\begin{bmatrix} \mathbf{y}_0 \\ \mathbf{y}_1 \end{bmatrix} = \begin{bmatrix} \mathbf{H}_{0,0} \mathbf{H}_{0,1} \\ \mathbf{H}_{1,0} \mathbf{H}_{1,1} \end{bmatrix} \cdot \begin{bmatrix} \mathbf{d}_0 \\ \mathbf{d}_1 \end{bmatrix} + \begin{bmatrix} \mathbf{n}_0 \\ \mathbf{n}_1 \end{bmatrix} \quad . \tag{3.33}$$

Fig. 3.10 illustrates the four sub-matrices of the effective channel matrix given by (3.33) for a channel with a maximum delay spread $\tau^{\max} \approx 0.1T_0$ with Rayleigh-distributed channel coefficients of decaying power. In a perfectly synchronized system (see Fig. 3.10a), *i.e.* no TO $\Delta\tau = 0$ and no CFO

$\Delta\nu = 0$ are present (*cf.* Chapter 2), it can be observed that the effective channel matrix $\mathbf{H}_{\ell',\ell}$ results in non-zero matrices for $\ell' \neq \ell$. These diagonal elements in $\mathbf{H}_{1,0}$ producing inter-symbol interference (ISI) at the receiver. By the presence of a TO $\Delta\tau = 0.1T_\mathrm{S}$ normalized to the symbol time spacing $T_0 = T_\mathrm{S}$ (*cf.* Fig. 3.10b) or by the presence of a TO $\Delta\tau = 0.1T_\mathrm{S}$ and a CFO $\Delta\nu = 0.1F_0$ (*cf.* Fig. 3.10c), the effective channel sub-matrices are not purely diagonal anymore, *i.e.* inter-carrier interference (ICI) for $\ell' = \ell$, adjacent carrier interference (ACI) for $\ell' = \ell$, and ISI (diagonal elements $\ell' \neq \ell$) are introduced and orthogonal transmission is impossible[10]. To reduce these effects one can use equalization techniques or apply a GI as will be introduced in the next part. Therefore, this multi-carrier scheme will be named ***plain*-OFDM** throughout this work.

OFDM with Guard Interval

A main drawback of plain-OFDM is that multi-path fading channels, will destroy the orthogonality of the transmission directly as adjacent symbols overlap in time. To cope with time-invariant multi-path fading channels, a GI can be used. Fig. 3.11 shows two popular implementations of the GI namely

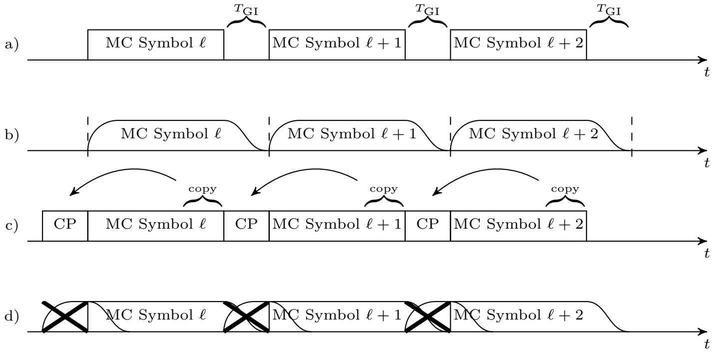

Figure 3.11: Transmission of OFDM symbols using zero padded-OFDM a) before and b) after transmission (with decay effects) and cyclic prefix-based OFDM c) before and d) after transmission (with decay effects) [KD18].

a zero padded (ZP) and a cyclic prefix (CP)-based approach [KD18]. In both cases the MC-symbols are pulled apart in time domain and an interval of length T_{GI} is inserted. It should be noted that we term the plain-OFDM

---

[10] We do not differ between ACI and ICI throughout this work and assign both as ICI, subsequently.

MC symbol as **core MC symbol**. This leads to a relaxed symbol time spacing of $T_0 = T_\mathrm{S} + T_\mathrm{GI}$ maintaining the sub-carrier spacing $F_0 = 1/T_\mathrm{S}$. After transmission over time-invariant multi-path channels with a maximum delay spread of τ^max, the symbols in Fig 3.11 are smeared over the interval. The main idea is to design the GI length $T_\mathrm{GI} \geq \tau^\mathrm{max}$ such that the impact of the channel will not affect adjacent time symbols [Roh16, STB11] and the number of observation at the receiver with $N'_\mathrm{SC} = N_\mathrm{SC}$ and $N'_\mathrm{TS} = N_\mathrm{TS}$ are sufficient to cover the overall impact of the channel.

Zero padded-OFDM (ZP-OFDM) As shown in Fig. 3.11b by relaxing the symbols in time domain, no ISI occurs and the decay time of the channel is captured by the GI. To generate the transmit signal $\mathbf{x}_\ell$ a zero-padding matrix $\mathbf{T}_\mathrm{I,ZP} = [\mathbf{I}_{N_\mathrm{SC}} \mathbf{0}_{N_\mathrm{SC} \times N_\mathrm{ZP}}]^\mathsf{T}$ can be used[11]:

$$\mathbf{x}_\ell = \mathbf{T}_\mathrm{I,ZP} \mathbf{F}^\mathsf{H} \mathbf{d}_\ell \tag{3.34}$$

inserting zeros at the end of each MC symbol. One may note that the behavior of the waveforms remains similar to plain-OFDM as the Tx/Rx filters are the same and, thus, the shape of the ambiguity function Fig. 3.4a does not change. The main difference to plain-OFDM is the change in the TF grid, where the lattice density $\delta_\mathrm{LD}(\Lambda) = \frac{1}{T_0 F_0} = \frac{T_\mathrm{S}}{T_\mathrm{S} + T_\mathrm{GI}} < 1$ gets reduced by the GI length T_GI lowering the bandwidth efficiency. Furthermore, the impact of an impulse response $w(\tau, t)$ to the effective channel coefficient (3.11) is relaxed by the change to a larger TF grid with $(\ell (T_\mathrm{S} + T_\mathrm{GI}), kF_0)$.

It can be observed in Fig. 3.11b that the receive signal is longer than the core MC-symbol ℓ introduced by the linear convolution with the physical channel. To deal with this longer influence a possible method is to use a Fourier matrix $\mathbf{F}_{2N_\mathrm{SC}}$ with double length $2N_\mathrm{SC}$ at the Rx and to pad the receive signal by zeros such that the effective channel matrix yields

$$\mathbf{H}_{\ell',\ell} = \begin{cases} \mathbf{F}_{1:2:2N_\mathrm{SC},1:N_\mathrm{SC}} \begin{bmatrix} \mathbf{W}_{\mathrm{conv},\ell',\ell} \mathbf{T}_\mathrm{I,ZP} \mathbf{F}^\mathsf{H}_{N_\mathrm{SC}} \\ \mathbf{0} \end{bmatrix} & \ell' = \ell \\ \mathbf{0}_{N_\mathrm{SC} \times N_\mathrm{SC}} & \text{otherwise} \end{cases} . \tag{3.35}$$

No ISI occurs for the synchronized case yielding the sub-matrix $\mathbf{W}_{\mathrm{conv},\ell',\ell} = \mathbf{0}$ for $\ell' \neq \ell$. Doubling the Fourier matrix size and zero padding the receive signal results in an interpolated signal of a factor of two in the frequency domain. This can be interpreted as virtually doubling the number of sub-carriers, where the data of the original transmission is carried on every second sub-carrier. The resulting dimension becomes N_SC by using only every second row of the Fourier matrix $\mathbf{F}$, denoted by $1:2:2N_\mathrm{SC}$ in (3.35).

---

[11] Instead of a zero-padding at the end of the MC symbol, one can of course also do the zero-padding at the beginning, as described in [KD18].

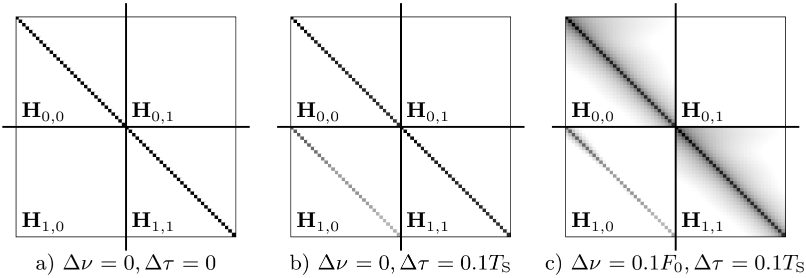

a) $\Delta\nu = 0, \Delta\tau = 0$ b) $\Delta\nu = 0, \Delta\tau = 0.1T_\mathrm{S}$ c) $\Delta\nu = 0.1F_0, \Delta\tau = 0.1T_\mathrm{S}$

Figure 3.12: Illustration of the amplitudes of four sub-matrices of the effective channel matrix $\underline{\mathbf{H}}$ in (3.33) for ZP-OFDM with $\tau^{\max} \approx 0.1T_\mathrm{S}$ and $T_\mathrm{GI} = 0.1T_\mathrm{S}$.

Consequently, the off-diagonal matrices are zero in the synchronized case as also depicted in Fig. 3.12a and no ISI occurs if the delay spread is smaller than the GI length. However, even under offset conditions, like with TO $\Delta\tau = 0.1T_\mathrm{S}$ (see Fig. 3.12b) or with CFO $\Delta\nu = 0.1F_0$ and TO $\Delta\tau = 0.1T_\mathrm{S}$ (see Fig. 3.12c) interference is introduced, which again destroys the orthogonality. Please note that the TO is normalized to the symbol time spacing of the core symbol T_S, so we can fairly compare it to plain-OFDM.

Cyclic prefix-based OFDM While in ZP-OFDM zeros are added to the signal, as illustrated in Fig. 3.11c a copy of the last N_GI samples corresponding to T_GI is inserted in front of the OFDM-symbol in CP-OFDM [ZY95]. According to the derivation in (3.28) and the changed symbol spacing $T_0 = T_\mathrm{S} + T_\mathrm{GI}$, the transmit signal of CP-OFDM is calculated for $q = -N_\mathrm{GI}, \ldots, N_\mathrm{SC} - 1$ by

$$x_\ell\left[q - \ell\left(N_\mathrm{SC} + N_\mathrm{GI}\right)\right] = \sum_{k=0}^{N_\mathrm{SC}-1} d_{k,\ell} e^{j\frac{2\pi kq}{N_\mathrm{SC}}} \tag{3.36}$$

and the addition of the cyclic prefix (CP) can be interpreted as an adopted transmit filter in contrast to plain-OFDM by

$$g_\mathrm{rect,CP}^\mathrm{Tx}(t) = \begin{cases} 1/\sqrt{T_\mathrm{S}} & |t| \leq \frac{T_\mathrm{S}+T_\mathrm{GI}}{2} \\ 0 & \text{otherwise} \end{cases}, \tag{3.37}$$

where the receive filter $g_\mathrm{rect}^\mathrm{Rx}(t)$ in CP-OFDM remains unchanged (3.15). Hence, the ambiguity function will change to Fig. 3.4b for CP-OFDM. Comparing the ambiguity functions with Fig. 3.4a, it can be observed that the shape in time domain gets broader which leads to higher robustness against delay spreads. This stretching allows a delay with a maximum spread $\tau^{\max} \leq T_{\mathrm{GI}}$ resulting in an orthogonal transmission even under time-invariant multi-path fading. Also in CP-OFDM the lattice density is reduced $\delta_{\mathrm{LD}}(\Lambda) = \frac{T_{\mathrm{S}}}{T_{\mathrm{S}}+T_{\mathrm{GI}}} < 1$ by the GI length T_{GI}.

In matrix description, the application of a CP can be realized by the multiplication with a CP insertion matrix given by

$$\mathbf{T}_{\mathrm{I,CP}} = \begin{bmatrix} \mathbf{0}_{N_{\mathrm{GI}} \times (N_{\mathrm{SC}} - N_{\mathrm{GI}})} & \mathbf{I}_{N_{\mathrm{GI}}} \\ \multicolumn{2}{c}{\mathbf{I}_{N_{\mathrm{SC}}}} \end{bmatrix} \tag{3.38}$$

such that the transmit signal changes to

$$\mathbf{x}_{\ell} = \mathbf{T}_{\mathrm{I,CP}} \mathbf{F}^{\mathsf{H}} \mathbf{d}_{\ell} \quad . \tag{3.39}$$

On the one hand, no ISI affects the MC symbols $\ell' \neq \ell$ due to the insertion of a GI with $\tau^{\max} \leq T_{\mathrm{GI}}$. On the other hand, by applying a CP, the linear convolution in (2.7) of the physical channel resulting in a cyclic convolution. The latter property is the most powerful feature of CP-OFDM in comparison to many other schemes in mobile communications. Hence, the consideration of the core symbol is sufficient and furthermore each sub-carrier is only affected by one complex channel coefficient. At the receiver the CP is removed by the rectangular receive filter by the removal matrix

$$\mathbf{T}_{\mathrm{R,CP}} = \begin{bmatrix} \mathbf{0}_{N_{\mathrm{SC}} \times N_{\mathrm{GI}}} & \mathbf{I}_{N_{\mathrm{SC}}} \end{bmatrix} \tag{3.40}$$

is applied such that the effective channel matrix changes to

$$\mathbf{H}_{\ell',\ell} = \begin{cases} \mathbf{F} \mathbf{T}_{\mathrm{R,CP}} \mathbf{W}_{\mathrm{conv},\ell',\ell} \mathbf{T}_{\mathrm{I,CP}} \mathbf{F}^{\mathsf{H}} & \ell' = \ell \\ \mathbf{0}_{N_{\mathrm{SC}} \times N_{\mathrm{SC}}} & \text{otherwise} \end{cases} . \tag{3.41}$$

An important observation is that the matrix multiplication $\mathbf{T}_{\mathrm{R,CP}} \mathbf{W}_{\mathrm{conv},\ell',\ell} \mathbf{T}_{\mathrm{I,CP}}$ results in a circulant matrix (*cf.* Appendix A.4), if the channel is time-invariant for a duration T_{S} and the condition $\tau^{\max} \leq T_{\mathrm{GI}}$ is fulfilled. From linear algebra [Str16] it is well-known that circulant matrices can easily be decomposed by the singular value decompensation (SVD) into Fourier matrices $\mathbf{F}$ and a pure diagonal matrix $\mathbf{\Sigma}_{\mathbf{H},\ell',\ell}$ with singular values on the main diagonal like

$$\mathbf{T}_{\mathrm{R,CP}} \mathbf{W}_{\mathrm{conv},\ell',\ell} \mathbf{T}_{\mathrm{I,CP}} = \mathbf{F}^{\mathsf{H}} \mathbf{\Sigma}_{\mathbf{H},\ell',\ell} \mathbf{F} \quad , \tag{3.42}$$

where the diagonal matrix is calculated by the Fourier transform of the time-invariant channel impulse response. Inserting (3.42) into the effective

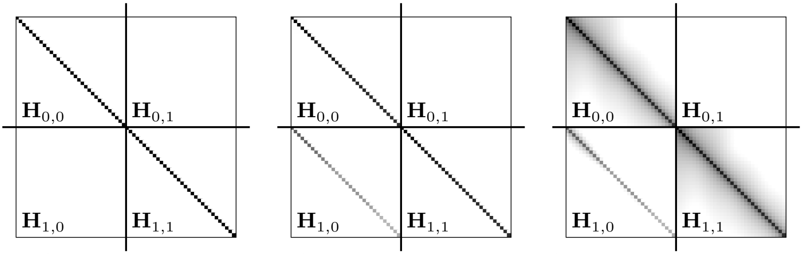

a) $\Delta\nu = 0, \Delta\tau = 0$ b) $\Delta\nu = 0, \Delta\tau = 0.1T_\mathrm{S}$ c) $\Delta\nu = 0.1F_0, \Delta\tau = 0.1T_\mathrm{S}$

Figure 3.13: Illustration of the amplitudes of the effective channel matrix of CP-OFDM applying the model (3.33) with $\tau^{\max} \approx 0.1T_\mathrm{S}$ and $T_\mathrm{GI} = 0.1T_\mathrm{S}$.

channel matrix (3.41) yields a purely diagonal matrix

$$\mathbf{H}_{\ell',\ell} = \mathbf{\Sigma}_{\mathbf{H},\ell',\ell} \quad . \tag{3.43}$$

As indicated above, each transmit symbol $d_{k,\ell}$ is only affected by one coefficient resulting in a simple equalization procedure at the receiving side for the synchronized case as indicated by Fig. 3.13a with the same model used in (3.33) Similar to ZP-OFDM the impact of offsets like TO and CFO destroys the orthogonality as indicated by Fig. 3.13b and Fig. 3.13c.

Windowed-OFDM (w-OFDM)

As introduced so far, the aforementioned plain-OFDM and GI-based OFDM schemes have a sinc shape in frequency domain based on the underlying rectangular Tx/Rx waveform, leading to high OoBE and, thus, high disturbances with other systems in adjacent frequency regions indicated by the spectrum in Fig. 3.9

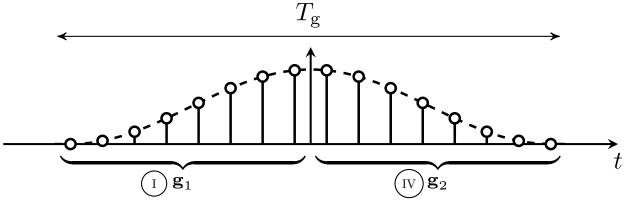

Figure 3.14: Exemplary chosen smoothing filter $g(t)$ [FB11] with a filter length $N_\mathrm{g} = 16$.

To reduce the impact on neighboring systems and maintain the advantages of orthogonal transmission, a scheme called w-OFDM (or w-CP-OFDM if a CP is applied) can be used [FBY10, FB11, Pra04, MP13, LKK14, LKK08, IEE12, JK16, ZSG^{+}16].

Here, the Tx filter can be generated by the convolution of the rectangular waveform with an additional smoothing filter $g\left(t\right)$ illustrated by Fig. 3.14 of length T_{g} like

$$g^{\mathrm{Tx}}\left(t\right) = g_{\mathrm{rect}}\left(t\right) * g\left(t\right) \quad , \tag{3.44}$$

which makes the "hard" cut of the rectangular waveform softer and reduces the OoBE. According to [FB11], we use the smoothing filter given by

$$g\left(t\right) = \frac{\pi}{2T_{\mathrm{g}}} \sin\left(\frac{\pi t}{T_{\mathrm{g}}}\right) \cdot g_{\mathrm{rect}}\left(\frac{t - \frac{T_{\mathrm{g}}}{2}}{T_{\mathrm{g}}}\right) \quad , \tag{3.45}$$

with the corresponding absolute value in frequency domain

$$\left|G\left(f\right)\right| = \left|\frac{\cos\left(\pi f T_{\mathrm{g}}\right)}{1 - \left(2fT_{\mathrm{g}}\right)^{2}}\right| \quad . \tag{3.46}$$

The convolution of the rectangular waveform with the smoothing filter $g\left(t\right)$ translates into a multiplication in frequency domain $G^{\mathrm{Tx}}\left(f\right) = G_{\mathrm{rect}}\left(f\right) \cdot G\left(f\right)$ as illustrated by Fig. 3.15 with an exemplary chosen smoothing waveform $g\left(t\right)$ with $T_{\mathrm{g}} = 0.2T_{\mathrm{S}}$ (The resulting zero crossings of the smoothing filter are at multiples of $qf = q\frac{\pi}{2T_{\mathrm{g}}} \approx q7.85F_{0},$). The positions of the zero-crossings of the combined filter remain unchanged due to the multiplication with the sinc function. Also, the ambiguity function changes the characteristic according to the used waveforms. The spectrum of the convolved filter (3.44) in Fig. 3.15c result in a lower OoBE. However, the power of the first side lobe remains roughly at a level of -13dB compared to the main lobe, which is similar to the pure rectangular waveform in Fig. 3.15a and results in a similar sensitivity to CFO as in plain-OFDM or GI-based OFDM. The better OoBE comes by the cost of a lower lattice density $\delta_{\mathrm{LD}}\left(\Lambda\right) = \frac{T_{\mathrm{S}}}{T_{\mathrm{S}}+T_{\mathrm{GI}}+T_{\mathrm{g}}} < 1$. The transmit signal can be separated into four parts as shown in Fig. 3.16, where part Ⅱ and Ⅲ are the aforementioned CP-OFDM parts. The part Ⅰ and Ⅳ are the ramp up and down parts introduced by the smoothing filter each of length $T_{\mathrm{g}}/2$, which corresponds to a sampled filter length of $N_{\mathrm{g}}/2$ for each part.

To generate the corresponding signal [Sch01] we can use the weighted overlap-add (WOLA)[Cro80, DM88, FB11, KK18] procedure as derived in

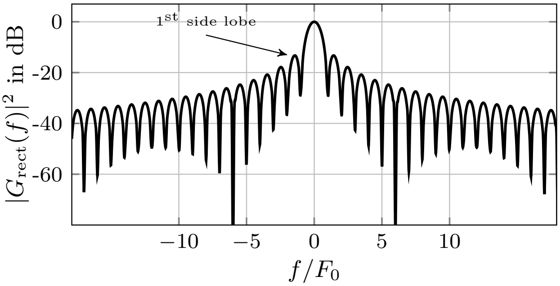

a) rectangular

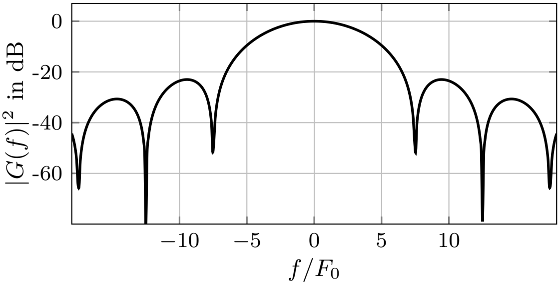

b) smoothing filter

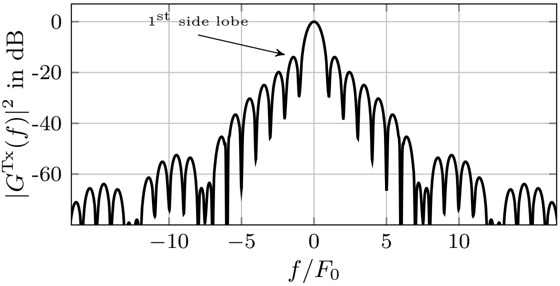

c) combined filter

Figure 3.15: Spectrum of one sub-carrier in windowed-OFDM with $T_{\mathrm{g}} = 0.2T_{\mathrm{S}}$ [FB11].

the Section A.5 like

$$\mathbf{x}_\ell = \mathbf{T}'_{\mathrm{I,win}}\mathbf{F}^{\mathsf{H}}\mathbf{d}_\ell + \mathbf{T}''_{\mathrm{I,win}}\mathbf{F}^{\mathsf{H}}\mathbf{d}_{\ell-1} \quad , \tag{3.47}$$

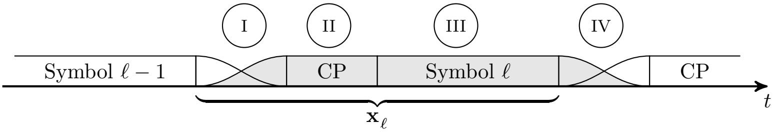

Figure 3.16: Transmit signal generation by the separation into four parts and applying WOLA algorithm in (3.47).

where the guard interval and windowing matrix reads

$$\mathbf{T}'_{\mathrm{I,win}} = \begin{bmatrix} \mathbf{0}_{N_{\mathrm{g}}/2\times(N_{\mathrm{SC}}-N_{\mathrm{g}}/2-N_{\mathrm{CP}})} & \boldsymbol{\Sigma}_{\mathbf{g}_1} & \mathbf{0}_{N_{\mathrm{g}}/2\times N_{\mathrm{CP}}} \\ \multicolumn{2}{c}{\mathbf{0}_{N_{\mathrm{GI}}\times N_{\mathrm{SC}}-N_{\mathrm{g}}/2-N_{\mathrm{CP}}}} & \mathbf{I}_{N_{\mathrm{GI}}} \\ \multicolumn{3}{c}{\mathbf{I}_{N_{\mathrm{SC}}}} \end{bmatrix} \begin{array}{c} \textcircled{\scriptsize I} \\ \textcircled{\scriptsize II} \\ \textcircled{\scriptsize III} \end{array} \quad . \tag{3.48}$$

It captures the ramp up part $\textcircled{\scriptsize I}$, the CP part $\textcircled{\scriptsize II}$ and the core symbol part $\textcircled{\scriptsize III}$ within one matrix. Matrix $\mathbf{T}''_{\mathrm{I,win}}$ is given by

$$\mathbf{T}''_{\mathrm{I,win}} = \begin{bmatrix} \boldsymbol{\Sigma}_{\mathbf{g}_2} & \mathbf{0}_{N_{\mathrm{g}}/2\times(N_{\mathrm{SC}}-N_{\mathrm{g}}/2)} \\ \multicolumn{2}{c}{\mathbf{0}_{(N_{\mathrm{SC}}+N_{\mathrm{GI}}+N_{\mathrm{g}}/2)\times N_{\mathrm{SC}}}} \end{bmatrix} \begin{array}{c} \textcircled{\scriptsize IV} \\ \end{array} \tag{3.49}$$

and contains the ramp down part for the previous MC symbol $\mathbf{d}_{\ell-1}$. The ramp up and down parts are generated by the introduction of the diagonal matrices $\boldsymbol{\Sigma}_{\mathbf{g}_1} = \operatorname{diag}\{\mathbf{g}_1\}$ and $\boldsymbol{\Sigma}_{\mathbf{g}_2} = \operatorname{diag}\{\mathbf{g}_2\}$ with the N_{g} filter coefficients derived by sampling the smoothing filter symmetrically illustrated in Fig. 3.14. Similar to CP-OFDM, where the receive filter $g^{\mathrm{Rx}}_{\mathrm{rect}}(t)$ remains unchanged (3.15) and the received signal can be generated by a cut out of the core symbol with a CP and filter removal matrix $\mathbf{T}_{\mathrm{R,win}}$ given by

$$\mathbf{T}_{\mathrm{R,win}} = \begin{bmatrix} \mathbf{0}_{N_{\mathrm{SC}}\times(N_{\mathrm{GI}}+N_{\mathrm{g}})} & \mathbf{I}_{N_{\mathrm{SC}}} \end{bmatrix} \tag{3.50}$$

and transforming the signal back into frequency domain by the Fourier matrix $\mathbf{F}$ such that the effective channel matrix results in

$$\mathbf{H}_{\ell',\ell} = \begin{cases} \mathbf{F}\mathbf{T}_{\mathrm{R,win}}\mathbf{W}_{\mathrm{conv},\ell',\ell}\mathbf{T}'_{\mathrm{I,win}}\mathbf{F}^{\mathsf{H}} & \ell' = \ell \\ \mathbf{0}_{N_{\mathrm{SC}}\times N_{\mathrm{SC}}} & \text{otherwise} \end{cases} . \tag{3.51}$$

One may note that the cross terms $\ell' \neq \ell$ will result in $\mathbf{F}\mathbf{T}_{\mathrm{R,win}}\mathbf{W}_{\mathrm{conv},\ell',\ell-1}\mathbf{T}''_{\mathrm{I,win}}\mathbf{F}^{\mathsf{H}} = \mathbf{0}$ due to the cutting performed by $\mathbf{T}_{\mathrm{R,win}}$. The w-CP-OFDM scheme is used, *e.g.*, in IEEE802.11a [IEE12] standard or in HIPERLAN/2 to achieve a lower OoBE even if most literature name it CP-OFDM.

Universal Filtered-OFDM (UF-OFDM)

Another MC candidate is UF-OFDM, which can be seen as generalization of a bandwidth filtered ZP-OFDM, where the entire band is filtered, and w-OFDM, where each sub-carrier is smoothed individually [VWS$^+$13]. In this MC scheme $N_{\mathrm{SC}}^{\mathscr{b}}$ adjacent sub-carriers are grouped to one block $\mathscr{b}$ out of N_{Blocks}, with $N_{\mathrm{SC}} = N_{\mathrm{Blocks}} N_{\mathrm{SC}}^{\mathscr{b}}$. Correspondingly, the data vector $\mathbf{d}_{\ell}$ is grouped to block vectors $\mathbf{d}_{\mathscr{b},\ell}$ with $\mathbf{d}_{\ell} = [\mathbf{d}_{0,\ell}^{\mathsf{T}}, \mathbf{d}_{1,\ell}^{\mathsf{T}}, \ldots, \mathbf{d}_{N_{\mathrm{Blocks}}-1,\ell}^{\mathsf{T}}]^{\mathsf{T}}$, where each block contains $N_{\mathrm{SC}}^{\mathscr{b}}$ data symbols. Each block of data $\mathbf{d}_{\mathscr{b},\ell}$ is transferred into time domain by a partial inverse Fourier transform $\mathbf{F}_{\mathrm{p}}^{\mathsf{H}} = \mathbf{F}^{\mathsf{H}} \mathbf{I}_{\mathrm{p}}^{\mathsf{T}} \in \mathbb{C}^{N_{\mathrm{SC}} \times N_{\mathrm{SC}}^{\mathscr{b}}}$ (similar to OFDMA, which is an access scheme using OFDM per user.) and filtered individually by a convolutional filter matrix $\mathbf{G}_{\mathscr{b}} \in \mathbb{C}^{N_{\mathrm{SC}} + N_{\mathrm{g}} \times N_{\mathrm{SC}}}$. The total transmit signal for one MC symbol ℓ is the sum over all blocks and yields

$$\mathbf{x}_{\ell} = \sum_{\mathscr{b}=0}^{N_{\mathrm{Blocks}}-1} \mathbf{G}_{\mathscr{b}} \mathbf{F}_{\mathrm{p}}^{\mathsf{H}} \mathbf{d}_{\mathscr{b},\ell}. \tag{3.52}$$

No additional GI is used as the application of the convolutional matrix $\mathbf{G}_{\mathscr{b}}$ leads to a relaxed time spacing $T_0 = T_{\mathrm{S}} + T_{\mathrm{g}}$. Fig. 3.17 shows the individual spectra of $N_{\mathrm{Blocks}} = 3$ blocks with $N_{\mathrm{SC}}^{\mathscr{b}} = 7$ sub-carriers per block with the same filter matrix $\mathbf{G}_{\mathscr{b}}, \forall_{\mathscr{b}}$ derived from the impulse response $g(t)$ in (3.45). The choice of the number of blocks N_{Blocks} and the number of sub-carriers per block $N_{\mathrm{SC}}^{\mathscr{b}}$ determine the resulting system. Many configurations are possible, here exemplary with an overall number of sub-carriers $N_{\mathrm{SC}} = 21$ given in Table 3.2 and shown in Fig. 3.18.

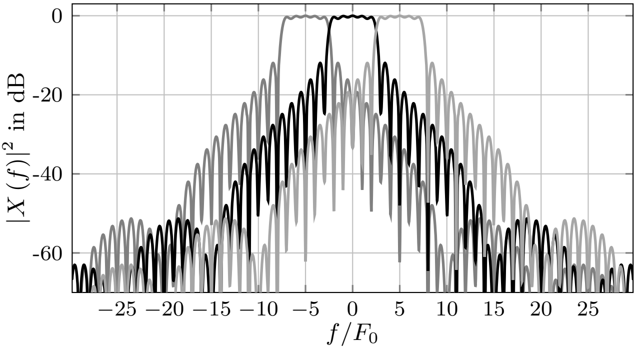

Figure 3.17: UF-OFDM spectrum with $N_{\mathrm{Blocks}} = 3$ blocks each with $N_{\mathrm{SC}}^{\mathscr{b}} = 7$ sub-carriers, with configuration listed in Table 3.2.

Table 3.2: UF-OFDM Configuration

Case	Number of Blocks	Filt. length	Resulting Scheme
Fig. 3.18a	$N_{\mathrm{Blocks}} = 1$, $N_{\mathrm{SC}}^{\beta} = 21$	$T_{\mathrm{g}} = 0$	plain-OFDM
Fig. 3.18b	$N_{\mathrm{Blocks}} = 1$, $N_{\mathrm{SC}}^{\beta} = 21$	$T_{\mathrm{g}} = 0.1T_{\mathrm{S}}$	Bandw. filt. OFDM
Fig. 3.18c	$N_{\mathrm{Blocks}} = 3$, $N_{\mathrm{SC}}^{\beta} = 7$	$T_{\mathrm{g}} = 0.1T_{\mathrm{S}}$	UF-OFDM
Fig. 3.18d	$N_{\mathrm{Blocks}} = N_{\mathrm{SC}}$, $N_{\mathrm{SC}}^{\beta} = 1$	$T_{\mathrm{g}} = 0.1T_{\mathrm{S}}$	w-OFDM

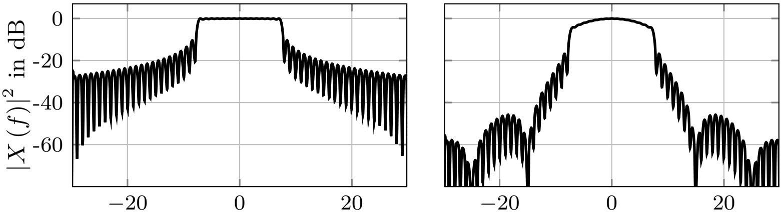

a) plain-OFDM b) Bandwidth filtered OFDM

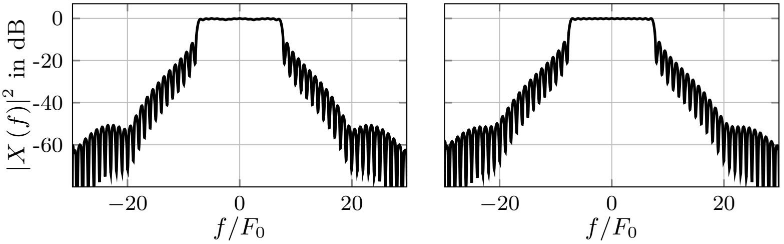

c) UF-OFDM d) w-OFDM

Figure 3.18: Spectrum of different configurations of UF-OFDM given in Tab. 3.2.

The plain-OFDM in Fig. 3.18a (*cf.* Fig. 3.9) and the w-OFDM in Fig. 3.18d (*cf.* Fig. 3.15) were already discussed and are shown as special cases from UF-OFDM. The bandwidth filtered OFDM in Fig. 3.18b is a normal plain-OFDM signal (or GI-based OFDM) that has been filtered after generation in the time domain to reduce the OoBE. UF-OFDM with a block length $N_{\mathrm{Blocks}} = 3$ and $N_{\mathrm{SC}}^{\beta} = 7$ sub-carriers each is shown in Fig. 3.18c.

All filtered schemes, *i.e.* Fig. 3.18b-Fig. 3.18d apply the same filter length $T_{\mathrm{g}} = 0.1T_{\mathrm{S}}$. Generally, it can be observed that all filtered schemes have a reduced OoBE in comparison to GI-based OFDM. The schemata behave differently with regard to their spectrum. This is due to the different use of the filters. Where in the bandwidth filtered scheme one filter is used for all sub-carriers at once, the UF-OFDM uses a filter per block for a much lower bandwidth, or even in the special case w-OFDM one filter per sub-carrier.

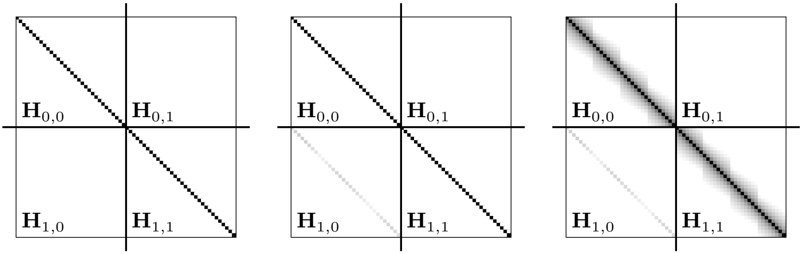

a) $\Delta\nu = 0, \Delta\tau = 0$ b) $\Delta\nu = 0, \Delta\tau = 0.1T_\mathrm{S}$ c) $\Delta\nu = 0.1F_0, \Delta\tau = 0.1T_\mathrm{S}$

Figure 3.19: Illustration of the amplitudes of the effective channel matrix of UF-OFDM applying the model (3.33) with $\tau^\mathrm{max} \approx 0.1T_\mathrm{S}$ and $T_\mathrm{g} = 0.1T_\mathrm{S}$.

Similar to ZP-OFDM the method, a discrete Fourier transformation with double length can be used to detect the desired symbols[VWS$^+$13]. The corresponding effective channel matrix leads to

$$\mathbf{H}_{\ell',\ell} = \begin{cases} \mathbf{F}_{1:2:2N_\mathrm{SC},1:N_\mathrm{SC}} \begin{bmatrix} \mathbf{W}_{\mathrm{conv},\ell',\ell} \sum_{\mathscr{b}=0}^{N_\mathrm{Blocks}-1} \mathbf{G}_{\mathscr{b}} \mathbf{F}_\mathrm{p}^\mathsf{H} \\ \mathbf{0} \end{bmatrix} & \ell' = \ell \\ \mathbf{0}_{N_\mathrm{SC}\times N_\mathrm{SC}} & \text{otherwise,} \end{cases} \tag{3.53}$$

where also the implementation of the filter with length T_g leads to a reduction of the lattice density $\delta_\mathrm{LD}(\Lambda) = \frac{T_\mathrm{S}}{T_\mathrm{S}+T_\mathrm{g}} < 1$ and therefore a reduced bandwidth efficiency η.

Similar to previous effective channel plots with (3.33), Fig. 3.19 shows the amplitudes of a UF-OFDM setup with $N_\mathrm{Blocks} = 4$ blocks and $N_\mathrm{SC}^{\mathscr{b}} = 7$ sub-carriers per block. The impact of offsets destroys the orthogonality similar to the other orthogonal schemes as indicated by Fig. 3.19b and Fig. 3.19c.

Offset QAM-based OFDM (OQAM/OFDM)

As indicated in Section 3.3 no (complex-valued) orthogonal MC design is possible applying well-localized waveforms and a lattice density $\delta_\mathrm{LD}(\Lambda) = 1$. In, [Cha66, Sal67, DS07c, FBY10, BN12, FB14, Fli94, MK97, JK16, KD18] the constraint of the lattice density $\delta_\mathrm{LD}(\Lambda) = 1$ and complex orthogonality is dropped, which would result in a too dense system with increased density $\delta_\mathrm{LD}(\Lambda) > 1$ and result in a system, where no orthogonal transmission seems to be possible. However, this drawback is solved by lattice staggering, where the main idea is to use a combination of two hexagonal TF grids with lattice density $\delta_{\mathrm{LD}}(\Lambda) = 1$ such that the overall lattice density results in $\delta_{\mathrm{LD}}(\Lambda) = 2$. The first TF plane is filled with purely real data and one with imaginary data is shifted by either $T_0' = T_0/2$ in time domain keeping $F_0' = F_0$ or by $F_0' = F_0/2$ keeping $T_0' = T_0$ in frequency domain. The staggering is indicated by Fig. 3.20 and is performed per time domain 1) proposed by [Sal67] and known as staggered multi-tone (SMT) or 2) in frequency domain by [Cha66] known as cosine modulated multi-tone (CMT). The resulting staggered TF grid can be generated by a lattice generator matrix defined in (3.2) as

$$\mathbf{L}_{\mathrm{SMT}} = \begin{bmatrix} T_0/2 & 0 \\ 0 & F_0 \end{bmatrix} \qquad \mathbf{L}_{\mathrm{CMT}} = \begin{bmatrix} T_0 & 0 \\ 0 & (F_0/2) \end{bmatrix} \quad . \tag{3.54}$$

Naturally, each complex symbol can be separated into two parts, *i.e.* the real and the imaginary part, reducing the amount of complex symbols per unit by the factor of two $\varrho^{\mathrm{SMT}} = \varrho^{\mathrm{CMT}} = \frac{1}{2}\varrho^{\mathrm{QAM}}$. Hence, the efficiency η^{SMT} for SMT and η^{CMT} for CMT in (3.7) remains equivalent even with a density $\delta_{\mathrm{LD}}(\Lambda)$ of 2 as shown by

$$\eta^{\mathrm{SMT}} = \varrho^{\mathrm{SMT}}\delta_{\mathrm{LD}}(\Lambda) = \frac{\varrho^{\mathrm{QAM}}}{2}\frac{1}{(T_0/2)F_0} = \frac{\varrho^{\mathrm{QAM}}}{T_0F_0} = \eta^{\mathrm{QAM}} \tag{3.55a}$$

$$\eta^{\mathrm{CMT}} = \varrho^{\mathrm{CMT}}\delta_{\mathrm{LD}}(\Lambda) = \frac{\varrho^{\mathrm{QAM}}}{2}\frac{1}{T_0(F_0/2)} = \frac{\varrho^{\mathrm{QAM}}}{T_0F_0} = \eta^{\mathrm{QAM}} \tag{3.55b}$$

The schemes SMT and CMT can be seen as transmission schemes with similar properties and are interchangeable [FBY10]. Throughout this work, the focus is on the SMT and it is mostly known as offset quadrature amplitude modulation/filter-bank multi-carrier (OQAM/FBMC), since the transmit signal generated by

$$x(t) = \sum_k \sum_\ell \left(d_{\mathrm{Re},k,\ell}\; g_{k,\ell}^{\mathrm{Tx}}(t) + d_{\mathrm{Im},k,\ell}\; g_{k,\ell}^{\mathrm{Tx}}\left(t - \frac{T}{2}\right)\right), \tag{3.56}$$

can be applied by OQAM mapping, with $d_{\mathrm{Re},k,\ell} = \Re\{d_{k,\ell}\}$ as real part and $d_{\mathrm{Im},k,\ell} = \Im\{d_{k,\ell}\}$ as the corresponding imaginary part of the transmit symbols. The elements $d_{k,\ell}$ ar the entries of the symbol matrix $\mathbf{D}$ introduced before [KD18, FBY10].

The realization of the transmit and receiving parts introduces a higher complexity compared to the aforementioned schemes by the extra filtering per sub-carrier. However, by utilizing a poly phase representation of discrete filters, the synthesis part at the Tx results in an IDFT and a polyphase network (PPN) component, which requires fewer computations [BD74, Hir81, HHS86, MKT99, JK16] as the direct implementation (3.56).

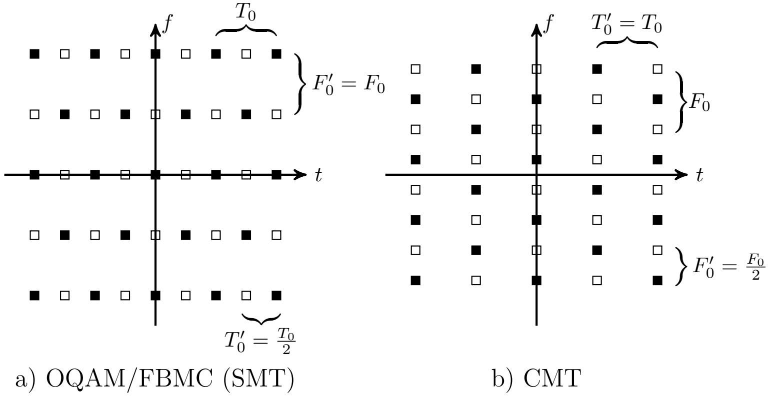

a) OQAM/FBMC (SMT) b) CMT

Figure 3.20: TF grid for a staggered lattice. Purely real data is denoted by black filled squares and purely imaginary data by white filled and black framed squares.

Table 3.3: Parameter setting for effective channel in (3.57)

scheme	condition	phase ϕ (3.1)
OFDM	$F_0 = 1/T_0$	0
OQAM-FBMC	$F_0' = F_0$ and $T_0' = \frac{T_0}{2}$	$\frac{\pi}{2}(k' - k + \ell' - \ell)$

Another possibility is the use of frequency spreading-FBMC [Bel12, DBCK14], which realizes the filtering in the frequency domain by an IDFT operation and a simple overlap-and-sum operation at the transmitter. Both implementations are out of scope of this work.

Having look to Fig. 3.20, it can be observed that symbols are alternating between pure real and pure imaginary symbols in the TF grid[DS07b, DS07c, Du08]. To generate this alternating part an additional phase shift with $\phi_s = (k + \ell)\frac{\pi}{2}$ for Tx filter in (3.4) and $\phi_r = -(k' + \ell')\frac{\pi}{2}$ for Rx filter in (3.8) is realized. As derived in the Appendix A.2, the effective channel coefficient is then given by

$$h_{r,s} = e^{j\frac{\pi}{2}\left(k-k'+\ell-\ell'\right)} \sum_{\gamma=0}^{N_{\text{path}}-1} \varsigma_\gamma e^{j\overline{\phi}_\gamma} A^*_{g^{\text{Tx}},g^{\text{Rx}}}\left(\overline{\tau}_\gamma, \overline{\nu}_\gamma\right) \tag{3.57}$$

with $\overline{\nu}_\gamma = (k - k')\,F_0 + \nu_\gamma$ and $\overline{\tau}_\gamma = (\ell - \ell')\,T_0/2 + \tau_\gamma$ and $\overline{\phi}_\gamma = -\pi\left(2kF_0\tau_\gamma - \overline{\nu}_\gamma\overline{\tau}_\gamma\right)$. Thus, the same system model as for QAM-based FBMC (3.10) can be used with the parameters given in Table 3.3. Please note that half TF spacing is inherently included in $\overline{\tau}_\gamma$ as this depends on the spacing $T_0/2$ due to the lattice staggering.

To achieve an orthogonal transmission in OQAM/FBMC schemes, the orthogonality condition is redefined [LAB95] in contrast to the orthogonality condition of QAM-based transmission schemes (3.19) like

$$\langle g_{k,\ell}^{\mathrm{Tx}}, g_{k',\ell'}^{\mathrm{Rx}} \rangle_{\mathbb{R}} = \Re\left\{ \int_{\mathbb{R}} g_{k,\ell}^{\mathrm{Tx}}(t)\, g_{k',\ell'}^{*\mathrm{Rx}}(t)\,\mathrm{d}t \right\} = \begin{cases} 1 & \text{, if } \ell' = \ell \text{ and } k' = k \\ 0 & \text{, otherwise} \end{cases} . \tag{3.58}$$

After taking the real part operator at the receiver $\Re\{y_r\}$ an orthogonal transmission for staggered TF grids is achieved, if symmetric and purely real Tx/Rx prototype filters $g(t)$ are used, which yields a pure real ambiguity function, as derived in the Appendix A.2 This restriction relaxes the requirement on the orthogonality condition to

$$A_{g_1,g_2}(2\ell T_0', 2kF_0') = \begin{cases} 1 & \ell = 0, k = 0 \\ 0 & \text{otherwise} \end{cases} \tag{3.59}$$

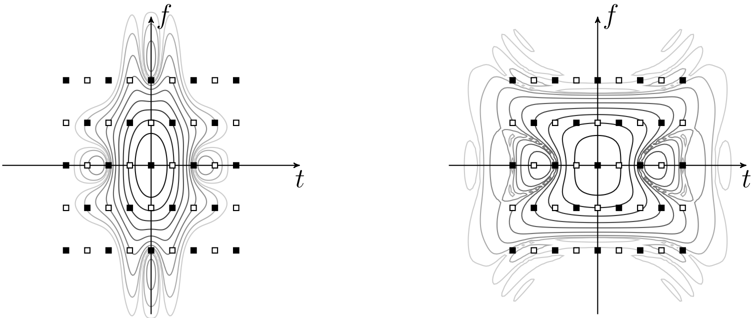

a) EGF with $T_0' = 1/2T_0$ and $F_0' = F_0$ and $\rho = 2$

b) Mirabbasi-Martin PHYDYAS with overlapping factor four

Figure 3.21: TF grid for OQAM/FBMC. The ambiguity function of the EGF and the Mirabbasi-Martin waveform are illustrated by contour lines of the amplitudes.

Waveform Design The relaxed orthogonality condition (3.59) offers a new design criterion in contrast to the QAM-based FBMC schemes with its complex-valued orthogonality condition (3.19).

An important waveform design algorithm, *i.e.* isotropic orthogonal transform algorithm (IOTA), was proposed by LeFloch in [LAB95] generating an orthogonal waveform based on the Gaussian waveform, thus is called IOTA waveform. In [RS97] this algorithm was generalized to extended Gaussian function (EGF) waveforms $g^{(\rho)}_{\mathrm{EGF},F_0,T_0}(t)$ (*cf.* (A.11)), which can be used in the OQAM/FBMC setup proposed in [SR00], illustrated by Fig. 3.21a with a filter parameter $\rho = 2$ [DS08]. This waveform fulfills the orthogonality condition (3.59) and offers better TFL parameters (*e.g.*, here $\xi = 0.9769$ and $\kappa = 0.5$) as the rectangular waveform (*cf.* Fig.3.1). In this work, we limit ourselves to this setup, $T'_0 = \frac{1}{2}T_0, F'_0 = F_0, \rho = 2$ as it offers good TFL properties [SR00]. An in-depth analysis for different settings of ρ, F_0, T_0, were done in [SR00, SSL02, DS08].

Another candidate is the Mirabbasi-Martin waveform $g_{\mathrm{Mirabbasi}}(t)$ (*cf.* (A.10)). The ambiguity function is shown on top of the TF grid in Fig. 3.21b for an overlapping factor of four. It also fulfills the real-valued orthogonality condition (3.59) and has the TFL parameters $\xi = 0.8839$ and $\kappa = 0.8369$. This waveform was further evaluated in the PHYDYAS project [Bel10] and further analyzed in the METIS project [**SPS⁺15**].

Spreading Techniques to Reduce PAPR

One challenge of OFDM is the high peak-to-average power ratio (PAPR)[12], which occurs by the basic operation, *i.e.* IDFT is a summation of many statistically independent sub-carriers. This summation results in an output signal (time signal $\underline{\mathbf{x}}$), which results in a complex-valued cyclic Gaussian random variable, due to the central limit theorem [Pro07]. A commonly used solution to reduce the PAPR in MC schemes are spreading operations, where a sub-group of independent symbols $d_{k,\ell}$ is first discrete Fourier transform (DFT) transformed and then further processed by the IDFT process in OFDM [SKJ95]. This procedure is known as DFT-*spread* OFDMA and it is used in the LTE uplink[13]. Similarly, a procedure where a group of some sub-carriers are spread by FB is proposed for OQAM/FBMC in [IVS⁺09]

Non-orthogonal OQAM-based schemes

So far, we introduced orthogonal transmission by lattice staggering and waveforms fulfilling the orthogonality condition (3.59). Lattice staggering can also be used for waveforms that do not meet the orthogonality condition (3.59). However, due to the staggering an interference reduction is never-

---

[12] The PAPR is the relation between the maximum peak power divided by the average power. [13] In LTE related literature, this procedure is named single-carrier-frequency division multiple access (SC-FDMA)

theless achieved. To differ both schemes, we will subsequently assign the name OQAM/OFDM to waveforms fulfilling the condition (3.59), whereas the name OQAM/FBMC is used for OQAM mapping with waveforms not fulfilling the orthogonality condition.

3.3.2 Non-Orthogonal Multi-Carrier Transmission Schemes

Until now, orthogonal MC schemes were discussed. These schemes offer simple symbol-wise one-tap frequency equalization techniques under mild channel conditions like linear time-invariant channels with relatively small delay spreads compared to the GI length used. However, the orthogonal schemes are sensitive to synchronization errors (*e.g. cf.* [FPT08, MSG$^+$07, SZL$^+$14, AFRFB15]) and offsets (*i.e.* TO and CFO). Even by the introduction of a GI, the CFO destroys the orthogonality and ICI terms show up. Especially for the rectangular waveform, the ICI has a huge impact [PVM95] and its power can be calculated by

$$P_{\mathrm{I}} = 1 - \operatorname{sinc}\left(\frac{\Delta\nu}{F_0}\right) \quad . \tag{3.60}$$

It is desirable to design a system which is just coarsely synchronized resulting in drastically reduced signaling overhead. Therefore, alleviating the synchronicity requirement can significantly improve operational capabilities, especially for schemes, where synchronicity cannot be guaranteed [WJK$^+$14, VT16].

In this section, we introduce *non-orthogonal* MC schemes, which offer a better spectral shape than OFDM and a robust design even under TO and CFO and are candidates for one of the next mobile communication standards [WJK$^+$14, VT16].

So far in the orthogonal schemes, the goal of the design was to achieve perfect symbol reconstruction within MC transmission schemes related to Fig. 3.8, with a high lattice density and a sharp spectral shape. We want to keep the condition of lattice density $\delta_{\mathrm{LD}}(\Lambda) \to 1$ to achieve a bandwidth efficient system.

QAM-based FBMC (QAM/FBMC)

Another possibility to achieve MC schemes with a good spectral shape, *i.e.* the application with waveforms with good TFL properties, and a dense TF grid is to drop the property of orthogonal transmission completely and allow for non-orthogonal waveform design [KM98]. On the one hand, this yields a design with more degrees of freedom in the TF grid without any restrictions on the waveforms. But on the other hand, it results in a non-orthogonal transmission, which is always affected by interference even in the synchronized case, leading to the fundamental need of equalizers of higher order than 1-tap frequency domain equalization.

The FBMC scheme was already introduced in (3.27) with the effective channel coefficients $h_{r,s}$ defined in (3.11). Similar to the TF grid representation for OQAM-based mapping (*cf.* Fig. 3.21), here we show the impact on the TF grid with the Gaussian waveform ($\rho = 1$ and TF grid density $\delta_{\mathrm{LD}}(\Lambda) = 1$) for QAM-based mapping. For comparison, we include the rectangular filter in Fig. 3.22a resulting in an orthogonal setup. As the Gaussian waveform overlay on the neighboring TF grid points, the application as Tx/Rx filter will always introduce ISI and ICI with this TF grid density. However, due to its well-localized TFL property, *i.e.* $\xi = 1$, only the direct adjacent TF grid points are affected with high amplitudes as the Gaussian waveform decay sharply in t and f.

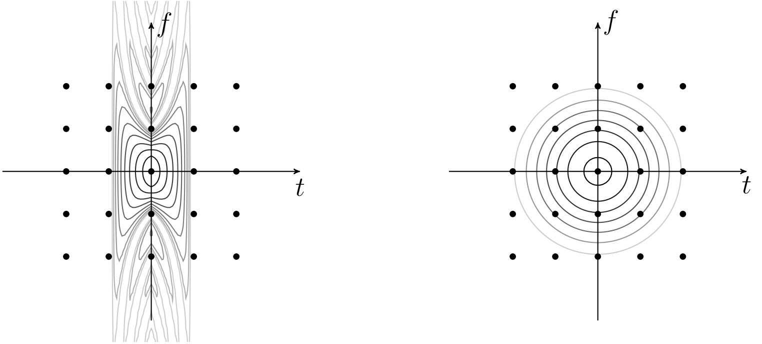

a) Rectangular filter in time domain b) Gaussian waveform with $\rho = 1$

Figure 3.22: TF grid for OQAM/FBMC at (0,0). The ambiguity function of the rectangular and the Gaussian waveform are illustrated by contour lines of the amplitudes.

The spectra of QAM/FBMC with the Gaussian waveform $g^{\mathrm{Tx}}(t) = g_{\mathrm{Gaussian}}^{(\rho=1)}(t)$ (3.18) filter parameter $\rho = 1$ is shown and the spectra of (CP)-OFDM already shown in Fig. 3.18 are shown in Fig. 3.23. As expected the spectrum of the QAM/FBMC drops drastically, and thus reaches a much lower OoBE than the orthogonal transmission scheme CP-OFDM.

The amplitudes of the effective channel matrix with (3.33) applying a Gaussian waveform are partly shown in Fig. 3.24a without offsets and with

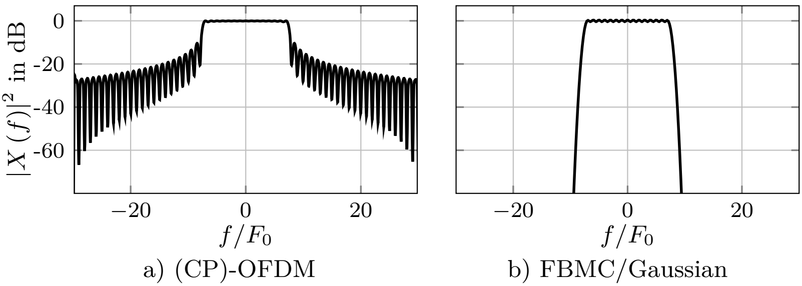

a) (CP)-OFDM b) FBMC/Gaussian

Figure 3.23: Spectrum comparison between CP-OFDM and FBMC applying Gaussian waveform with $\rho = 1$.

offsets in Fig. 3.24b and Fig. 3.24c. As already indicated, even in the synchronous case ISI and ICI are introduced and an higher order equalizer is always required. However, with both offsets, *i.e.* TO $\Delta\tau = 0.1T_\mathrm{S}$ and CFO $\Delta\nu = 0.1F_0$, the amplitudes only change marginally, and the equalizer has roughly the same structure as in the synchronized case making this scheme robust against offsets.

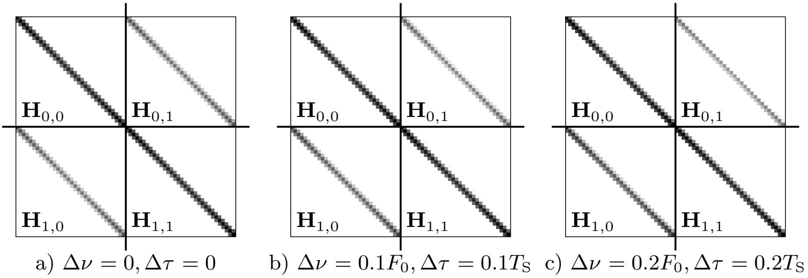

a) $\Delta\nu = 0, \Delta\tau = 0$ b) $\Delta\nu = 0.1F_0, \Delta\tau = 0.1T_\mathrm{S}$ c) $\Delta\nu = 0.2F_0, \Delta\tau = 0.2T_\mathrm{S}$

Figure 3.24: Illustration of the amplitudes of the effective channel matrix (3.33) for QAM/FBMC with Gaussian filter and filter parameter $\rho = 1$.

In contrast to OQAM/FBMC, which applies the real part operator at the Rx, we term the general FBMC scheme QAM/FBMC to distinguish between both schemes. One may note that in the literature the system is mostly analyzed with an infinite number of symbols $N_\mathrm{TS} = \infty$. Practical implementations are frame-based. Thus, the number of symbols N_TS is limited. Furthermore, as the influences between different MC symbols ℓ are not vanishing (*i.e.* $\overline{\boldsymbol{\Sigma}}_\mathbf{H} \neq \mathbf{0}$) a guard interval between two frames is used to deny inter-frame interference, which covers the rise and decay time of the waveforms as well as the impact of the channel. However, it is worth mentioning that this GI is applied only once per frame in contrast to the GI-based OFDM schemes and, hence, offers a higher spectral efficiency.

General Frequency Division Multiplexing (GFDM)

Dependent on the waveform used, QAM/FBMC has the disadvantage of long rise and decay times. To circumvent this behavior, in [FKB09, DFKH11, MMG$^+$14] the authors propose a frame-based implementation with *circular tail-biting* Tx/Rx waveforms. The idea is related to the cyclic property in CP-OFDM, where the linear convolution of the physical channel is translated into the circular convolution. The cyclic property is adopted to the waveforms such that the filters $g^{\mathrm{Tx}}[q]$ are used circularly with a period of $N_{\mathrm{SC}}N_{\mathrm{TS}}$[14], in order to facilitate a circular convolution and to shorten the rise and decay time within one frame. The generation of the transmit signal, given by

$$\underline{\mathbf{x}} = \underline{\mathbf{T}}_{\mathrm{I}}\underline{\mathbf{G}}_{\mathrm{GFDM}}\underline{\mathbf{d}} \quad , \tag{3.61}$$

is related to the general FBMC transmit signal (3.5), where $\underline{\mathbf{T}}_{\mathrm{I}}$ is the frame-based CP insertion matrix, which is used to mitigate the inter-frame interference (IFI). Fig. 3.25 shows the basic idea of the frames used in GFDM (*cf.* in Fig. 3.25a) and compares this with CP-OFDM in Fig. 3.25b (*cf.* Fig. 3.11). It can be directly observed that the frame length is considerably shorter by using only one CP than with a CP-OFDM transmission, where a MC symbol-wise CP is used. The circular shifted transmit filter can be realized by the frame-based matrix

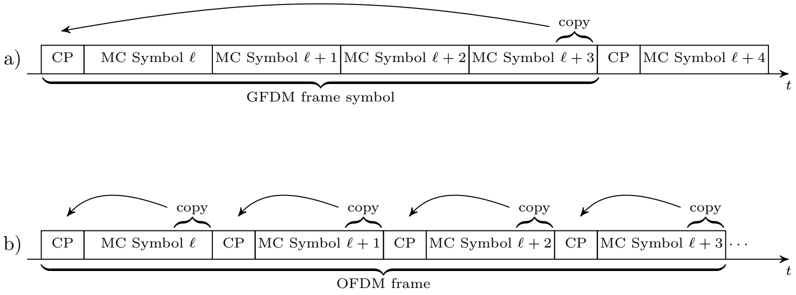

Figure 3.25: Frame structure of a) GFDM with $N_{\mathrm{TS}} = 4$ time symbols per GFDM frame and b) CP-OFDM with $N_{\mathrm{TS}} = 4$ time symbols.

$$\underline{\mathbf{G}}_{\mathrm{GFDM},q,s} = g^{\mathrm{Tx}}[(q-\ell N_{\mathrm{SC}}) \mod N_{\mathrm{SC}}N_{\mathrm{TS}}]e^{j2\pi\frac{kq}{N_{\mathrm{SC}}}} \tag{3.62}$$

---

[14] The tail-biting property is achieved by using the prototype filter with modulo operator $g^{\mathrm{Tx}}[(q-\ell N_{\mathrm{SC}}) \mod N_{\mathrm{SC}}N_{\mathrm{TS}}]$

with the sending index $s = k + \ell N_{\mathrm{SC}}$ and time discrete index $q = 0, \ldots, N_{\mathrm{Resources}}^{\mathrm{Frame}} - 1$. The GFDM frame size is given by $N_{\mathrm{Resources}}^{\mathrm{Frame}} = N_{\mathrm{TS}} N_{\mathrm{SC}}$. More efficient implementations are discussed in [GMN+13, MGK+12, FBM15].

For the circular half-cosine waveform and for the corresponding Gaussian waveform the amplitudes of the matrices $\underline{\mathbf{G}}_{\mathrm{GFDM}}$ are illustrated in Fig. 3.26a and Fig. 3.26b, respectively, with $N_{\mathrm{TS}} = 4$ time symbols and $N_{\mathrm{SC}} = 12$ sub-carriers. Despite the cyclic property of the tail-biting waveform, the boundary symbols of a frame suffer from the hard cut and result to a high OoBE [MGK+12, MMG+14]. Inserting guard symbols (GSs), *i.e.* setting N_{GS} border symbols to zero, or using a smoothing filter comparable to w-CP-OFDM, reduces this impact.

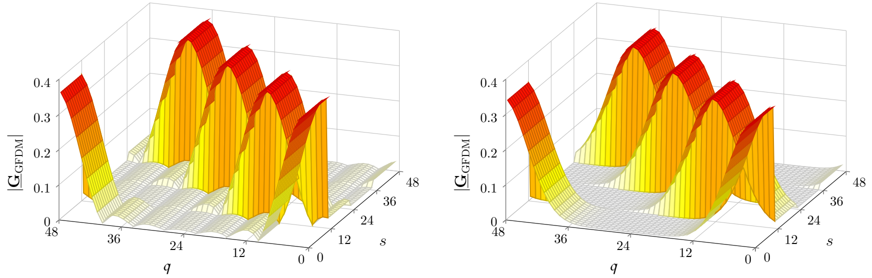

a) Half-cosine in time direction

b) Gaussian with $\rho = 1$

Figure 3.26: GFDM generator matrix $\underline{\mathbf{G}}_{\mathrm{GFDM}}$ with $N_{\mathrm{TS}} = 4$ time symbols and $N_{\mathrm{SC}} = 12$ sub-carriers.

After removing the CP with the removal matrix $\underline{\mathbf{T}}_{\mathrm{R}}$, the matched filter (MF) is applied by $\underline{\mathbf{G}}_{\mathrm{GFDM}}^{\mathsf{H}}$ yielding the frame-based receive signal

$$\underline{\mathbf{y}} = \underbrace{\underline{\mathbf{G}}_{\mathrm{GFDM}}^{\mathsf{H}} \underline{\mathbf{T}}_{\mathrm{R}} \underline{\mathbf{W}}_{\mathrm{conv}} \underline{\mathbf{T}}_{\mathrm{I}} \underline{\mathbf{G}}_{\mathrm{GFDM}}}_{\text{eff. Channel } \underline{\mathbf{H}}} \underline{\mathbf{d}} + \underline{\mathbf{G}}_{\mathrm{GFDM}}^{\mathsf{H}} \underline{\mathbf{T}}_{\mathrm{R}} \underline{\mathbf{n}} \tag{3.63}$$

where $\underline{\mathbf{W}}_{\mathrm{conv}}$ is the frame-based convolutional matrix (3.32). According to [MMG+14], Fig. 3.27 illustrates the spectra of plain-GFDM ((3.61)), windowed-GFDM (w-GFDM) with different filter length, *i.e.* $N_{\mathrm{g}} = 16, N_{\mathrm{g}} = 32$, and GS-GFDM applying $N_{\mathrm{GS}} = 2$. Exemplary, all GFDM implementations are realized with the half-cosine filter, further filter design for GFDM can be found in [HSL17]. The smoothing filter $g(t)$ for w-GFDM is given in (3.45) sampled to achieve $N_{\mathrm{g}} = 16$ or $N_{\mathrm{g}} = 32$.

In addition to the GFDM schemes, the spectra of QAM/FBMC with half-cosine waveform and CP-OFDM are shown as a benchmark. It can be

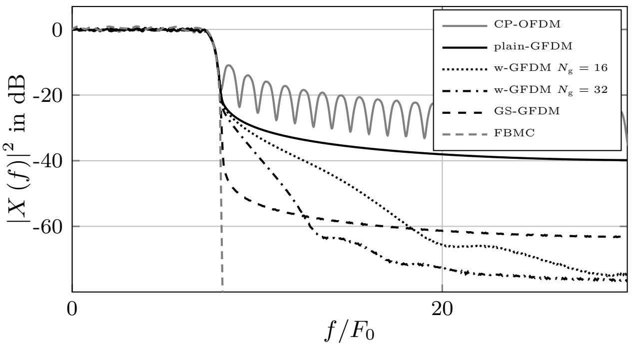

Figure 3.27: Spectrum comparison of GFDM applying different OoBE reducing techniques[MGK+12, MMG+14].

observed that both techniques, *i.e.* smoothing in w-GFDM and inserting GSs in GS-GFDM, can improve the spectral shape. However, this is bought at the expanse of a reduced lattice density $\delta_{\mathrm{LD}}(\Lambda)$. The mean lattice density per frame for w-GFDM is

$$\bar{\delta}_{\mathrm{LD}}(\Lambda) = \frac{1}{\left(T_0 + \frac{T_{\mathrm{g}}+T_{\mathrm{GI}}}{N_{\mathrm{TS}}}\right) F_0} \tag{3.64}$$

and for GS-GFDM it is

$$\bar{\delta}_{\mathrm{LD}}(\Lambda) = \frac{1}{\left(T_0 + \frac{T_{\mathrm{GI}}}{N_{\mathrm{TS}}}\right) F_0} \left(1 - \frac{N_{\mathrm{GS}}}{N_{\mathrm{TS}}}\right) \quad . \tag{3.65}$$

Table 3.4 summarizes the densities for an LTE like setup with $N_{\mathrm{SC}} = 72$ sub-carriers, $N_{\mathrm{TS}} = 14$ symbols, a CP length of $T_{\mathrm{GI}} = 0.07T_0$ with the assumption of no additional guard band or guard symbol[15]. The filter lengths are set to $T_{\mathrm{g}} = 16/72T_0$ or $T_{\mathrm{g}} = 32/72T_0$ corresponding to a number of filter coefficients $N_{\mathrm{g}} = 16$ or $N_{\mathrm{g}} = 32$, respectively.

For further information on GFDM the reader of interest is referred to the Ph.D. thesis [Mic15] from Michailow and references therein.

Special Cases of GFDM GFDM can be seen as a generalization of most of the MC schemes introduced above. Hence, applying the rectangular waveform (3.15) yields the frame-based matrix $\underline{\mathbf{G}}_{\mathrm{GFDM}}$ for OFDM. If additionally

---

[15] One may note that in the QAM/FBMC the assumption of timely infinite long transmission is performed. Assuming guard band and guard symbols would reduce the lattice density.

Table 3.4: Lattice density comparison for MC transmission schemes

MC schemes	$\delta_{\mathrm{LD}}(\Lambda)$ or $\overline{\delta}_{\mathrm{LD}}(\Lambda)$	Orthogonal
CP-OFDM	0.93	✓
GFDM	0.995	✗
w-GFDM$_1$	0.979	✗
w-GFDM$_2$	0.965	✗
GS-GFDM	0.853	✗
QAM/FBMC	1	✗

also a GI introduction matrix is introduced, CP-OFDM or ZP-OFDM is introduced.

Exemplary for **CP-OFDM** the resulting generation matrix $\underline{\mathbf{G}}_{\mathrm{GFDM}}$ contains the inverse Fourier matrices $\mathbf{F}_{N_{\mathrm{SC}}}^{\mathsf{H}}$ per MC time symbol ℓ and the MC symbol-wise guard insertion matrix $\mathbf{T}_{\mathrm{I}}$ from (3.38) and is generated by

$$\underline{\mathbf{G}}_{\mathrm{GFDM}} = \mathbf{I}_{N_{\mathrm{TS}}} \otimes \left(\mathbf{T}_{\mathrm{I}}\mathbf{F}_{N_{\mathrm{SC}}}^{\mathsf{H}}\right) \quad . \tag{3.66}$$

By the application of symbol-wise guard insertion matrix $\mathbf{T}_{\mathrm{I}}$, no frame-based guard insertion matrix is required and, hence, it is $\underline{\mathbf{T}}_{\mathrm{I}} = \mathbf{I}$.

Furthermore, a non-orthogonal scheme with symbol-wise CP was already introduced by Vogeler in [Vog06], which was therein called **CP-FBMC**. It is achieved by truncating the waveform with $\pm T_0/2$ and protected each MC symbol ℓ by a CP. The resulting matrix is

$$\underline{\mathbf{G}}_{\mathrm{GFDM}} = \mathbf{I}_{N_{\mathrm{TS}}} \otimes \left(\mathbf{T}_{\mathrm{I}}\mathbf{\Sigma}_{\mathbf{g}}\mathbf{F}_{N_{\mathrm{SC}}}^{\mathsf{H}}\right) \quad , \tag{3.67}$$

where $\mathbf{\Sigma}_{\mathbf{g}}$ is a diagonal matrix containing the truncated waveform coefficients.

A OQAM-based version of GFDM was introduced in [GMM$^+$15], which allows the reduction of interference by adjacent symbols in the TF grid with an additional application of a real part operator at the receiver side. The OQAM/GFDM can be seen as frame-based implementation of OQAM/FBMC with an additional frame-based CP to reduce IFI.

Colored Noise

Finally, it should be noted that for the non-orthogonal transmission schemes, the noise term is colored by the receive filter and is not uncorrelated anymore as in the orthogonal schemes. In the appendix A the different auto-correlation functions $\Psi_{\tilde{\mathbf{n}}\tilde{\mathbf{n}}}$ are discussed. The receiver algorithm used in this thesis is based on the Forney receiver [For73], which is based on a linear prewhitening

MF at the Rx side like

$$\underline{\tilde{\mathbf{y}}} = \mathbf{P}\underline{\mathbf{y}} \tag{3.68}$$

with a prewhitening matrix $\mathbf{P}$. This decorrelation property is important for the message passing algorithm mainly used in this work. The possible implementations for the different MC schemes are discussed in Appendix B. It should be noted that the prewhitening filter matrix is always applied in the subsequent chapters. However, it is not mentioned within the formulas to keep the notation simpler.

3.3.3 Multi-Carrier Schemes Summary

Finally, Table 3.5 summarizes all mentioned MC schemes. All schemes have the same sub-carrier spacing with $F_0 = 1/T_\mathrm{S}$ based on the symbol duration time of the rectangular waveform and the bandwidth efficiency η is considered in terms of the amount of information bits per complex symbol in QAM with ϱ^{QAM} (2.5) to have a fair comparison.

Table 3.5: Classification of different multi-carrier schemes, with $F_0 = 1/T_\mathrm{S}$

Scheme	Channel equation	Tx filter $g^\mathrm{Tx}(t)$	Rx filter $g^\mathrm{Rx}(t)$	Symbol spacing T_0	bandwidth efficiency η	ortho-gonal
plain-OFDM	(3.31)	$g_\mathrm{rect}(t)$	$g_\mathrm{rect}(t)$	T_S	ϱ^QAM	✓
ZP-OFDM	(3.35)	$g_\mathrm{rect}(t)$	$g_\mathrm{rect}(t)$	$T_\mathrm{S} + T_\mathrm{GI}$	$\frac{\varrho^\mathrm{QAM} T_\mathrm{S}}{T_\mathrm{S}+T_\mathrm{GI}}$	✓
CP-OFDM	(3.41)	$g_\mathrm{rect,CP}(t)$	$g_\mathrm{rect}(t)$	$T_\mathrm{S} + T_\mathrm{GI}$	$\frac{\varrho^\mathrm{QAM} T_\mathrm{S}}{T_\mathrm{S}+T_\mathrm{GI}}$	✓
w-CP-OFDM	(3.51)	$(g_\mathrm{rect,CP} * g)(t)$	$g_\mathrm{rect}(t)$	$T_\mathrm{S} + T_\mathrm{GI} + T_\mathrm{g}$	$\frac{\varrho^\mathrm{QAM} T_\mathrm{S}}{T_\mathrm{S}+T_\mathrm{GI}+T_\mathrm{g}}$	✓
UF-OFDM	(3.53)	$g_\mathrm{rect}(t)$ & block filter	$g_\mathrm{rect}(t)$	$T_\mathrm{S} + T_\mathrm{g}$	$\frac{\varrho^\mathrm{QAM} T_\mathrm{S}}{T_\mathrm{S}+T_\mathrm{g}}$	✓
OQAM/OFDM	(3.57)	well-local. $g(t)$	$g^*(-t)$	$T_\mathrm{S}/2$ (2 used Λ)	ϱ^QAM	✓
OQAM/FBMC	(3.57)	well-local. $g(t)$	$g^*(-t)$	$T_\mathrm{S}/2$ (2 used Λ)	ϱ^QAM	✗
QAM/FBMC	(3.11)	well-local. $g(t)$	$g^*(-t)$	T_S	ϱ^QAM	✗
GFDM	(3.63)	cyc. well-local. $g(t)$	$g^*(-t)$	$T_\mathrm{S} + \frac{T_\mathrm{GI}}{N_\mathrm{TS}}$	$\varrho^\mathrm{QAM} \overline{\delta}_\mathrm{LD}(\Lambda)$	✗

3.4 Chapter Summary

In this chapter the basics of multi-carrier systems were introduced. For this purpose, a generic multi-carrier system model has been derived, which serves as the basis for more complex setups, which are considered in Chapter 4 and Chapter 5. First, in Section 3.2, multi-carrier transmission through a system model was introduced, along with design criteria for the time-frequency grid and bandwidth efficiency related to the waveform based ambiguity function. Finally, a factor graph-based representation of multi-carrier schemes based on the matrix model was derived.

Section 3.3 then dealt with the classification of various multi-carrier schemes. After a brief overview of classification criteria, concrete multi-carrier implementations known from literature were given, which have been used or proposed in the recent decades for the fifth mobile communication generation and beyond. Besides orthogonal schemes such as OFDM, CP-OFDM, w-OFDM, UF-OFDM or OQAM/OFDM, which offer simple equalization techniques, the non-orthogonal schemes QAM/FBMC, OQAM/FBMC and CP-FBMC were also introduced. The latter offer a robust design against timing and frequency offsets, which is important in transmissions scenarios where these impacts cannot be directly mitigated.

The generation of the transmit signal and the receive signal was given and all multi-carrier schemes were compared with respect to the effective channel matrix in a synchronized transmission and under offset conditions due to timing inaccuracies or frequency shifts.

Chapter 4

Transmissions over Two-Way Relaying Channels

4.1 Overview

Modern radio communication systems aim to improve data rate, reliability and robustness even under difficult channel conditions.

In wireless mobile communication, performance is limited primarily by multi-path propagation, fading, shadowing, and path loss. Recently, *Cooperative Communication* has been extensively discussed, exploiting spatial diversity techniques that combat fading and other channel effects, even though the terminals are equipped with only a single antenna. The cooperation with a relay has become a promising technique to improve throughput, reliability and coverage of wireless networks. Two-way relaying channel (TWRC) can be implemented in a variety of scenarios, such as in satellite communication or in an underwater scenario. As TWR can be set in completely different scenarios as 1) phone to phone, 2) car to car [HLL14], 3) boat to boat [WHZW13], 4) plane to plane, 5) submarine to submarine and many more, a wide range on different impacts can be assumed. In many wireless communication standards, the concept of *cooperative communication* is available, such as: *e.g.*, WLAN, LTE and WiMax (defined in IEEE802.16j). Especially in TWRCs, where a number of users want to exchange information about a support relay, the reduction of communication overhead is of utmost importance.

A relay can generally communicate in *full-duplex* or *half-duplex* mode. Using a full-duplex relay provides greater spectral efficiency [ZCL$^+$15]. However, the power levels of transmit and receive signals make the implementation difficult [SSG$^+$14, RW06, RW07]. Due to orthogonal multiplexing, however, the realization of a half-duplex relay is much easier and is therefore used in this chapter. In [RW07, PY06a, PY07, PKA09] the authors discuss various half-duplex TWR protocols that also establish a bidirectional connection between two terminals with a half-duplex relay. We usually consider the following approaches in TWR: 1) *Four-phase approach*, 2) *Three-phase approach*, and 3) *Two-phase approach*, which gets introduced in Section 4.2. The two-phase approach is the main topic of this chapter and offers the highest spectral efficiency. However, it is also the most challenging approach due to the superposition in the first phase (multiple access (MA) phase).

Several physical layer network coding (PLNC) detection approaches for the first phase, such as separate channel decoding (SCD) [ZLL06b], joint channel decoding and physical-layer network coding (JCNC) [ZLL06b, PY07] and generalized joint channel decoding and physical-layer network coding (GJCNC) [Wüb10] have been introduced in the literature for estimating the relay message in single-carrier (SC) transmissions over synchronous frequency flat channels.

Under these mild channel conditions, the transmission can be described by a one-tap channel per symbol transmitted, offering simple one-tap a-posteriori probability (APP) detection techniques. In contrast, these simple techniques are inadequate under severe channel conditions and result in degraded performance at the relay and thus overall transmission [ZLL06a, ZLW13, XXX12, WLW$^+$16a, WLW$^+$16b].

A commonly used alternative to reduce the receiver complexity for these severe channels are MC approaches introduced in Chapter 3. In particular, the use of CP-OFDM for TWRC has been extensively analyzed, *e.g.* [Wüb10, XXX12, WWD13b, LLZ15, WLW$^+$16a, WLW$^+$16b, Wu17]. However, as indicated by theoretical investigations [ZLL06a, ZLW13, XXX12] and demonstrated by corresponding hardware implementations [LWLZ13] and [**WLW$^+$14**], CP-OFDM in TWRC is very sensitive to node asynchrony such as CFO or TO, resulting in ISI and ICI at the receiver. For unidirectional P2P transmissions, these offsets can be estimated and post-compensated in the receiver so that a one-tap frequency domain equalizer is still sufficient [Pro07, KD18]. Nevertheless, the signals of a pair of users are superimposed and the compensation of the user-specific offsets can not be realized for both users signals in a TWR system [LLZ15], but only an average compensation achieves better performance than other strategies [LWLZ13, HLL14, Wu17], and [**WLW$^+$14**].

Besides cooperative communication, the need for more devices has stimulated discussions about new MC schemes (see Chapter 3) for the next generation of mobile radio systems and beyond [Bel10, WJK$^+$14] and **[SPS$^+$15]**.

Central Question

With regard to the limitations mentioned above, the main questions in this chapter are: *Which MC schemes offer a robust design for a wide range of timing and frequency offsets in a two-phase TWRC transmission, and how to design the estimation of the data at the relay?*

Structure of this Chapter This chapter is organized as follows: This section is the general overview of this chapter. In Section 4.2 the general scenario of four, three and two-phase TWR and the generation for the relay messages are illustrated. In Section 4.3, we introduce the system model of the MA phase and discuss briefly the mapping of information bits to physical resources according to the MC schemes from Chapter 3. Here also, the three aforementioned PLNC detection schemes are introduced. The structure of all PLNC detection schemes are drawn by means of factor graphs (FGs) for a synchronized orthogonal transmission scheme, *e.g.* CP-OFDM.

In Section 4.4, we generalize the channel properties step by step from simple one-tap affects to time-variant channels, which mostly introduce interference as already indicated by the effective channel matrices in Chapter 3.

Subsequently, an exhaustive interference analysis for TWRC with different MC schemes is provided. It is shown that the well-localized Gaussian waveform offers a lower spread on the time-frequency (TF) grid for a wide range of offsets. The main energy is concentrated only on the adjacent TF grid points. Thus, the author introduced a factor graph-based equalizer (FGE) in **[WWD16, WWD18]** taking in the first instance the whole TF grid into account, which is illustrated in Section 4.5, wherein the focus is on the utilization of general multi-carrier transmission schemes applied to TWRCs and the utilization of FGE at the relay in order to mitigate the impacts of the physical channels, offsets, and the non-orthogonal waveforms. In combination with the subsequent physical-layer network coding detection/decoding scheme, this combination allows for a flexible design of the waveforms and the FGE to meet the complexity-performance trade-off at the relay Further, we introduces a concept of reducing the complexity of the underlying algorithm by taking only neighboring TF grid points into consideration with the highest power. A further complexity reduction is achieved by the additional application of a linear equalizer (LE) at the receiver based on minimum mean square error (MMSE) criterion utilizing the full effective channel matrix [**SWW+14, WWD15a**] and a reduced version [**WWD+15b**] leading to a smaller neighborhood in the FG and a further performance improvement can be achieved by sIC [**WWD15a, WSW+16**]. A performance analysis in Section 4.6 concludes the chapter and shows the advantage of the combination of well-localized waveforms in TWRC with a proper designed equalizers structures. Finally, Section 4.7 summaries the chapter.

The main contributions of this thesis are: The main contributions of this thesis lie in a combination of the already published conference proceedings [**WLW+14, SWW+14, SPS+15, WWD15a, WWD+15b, WWD15a, WSW+16, WWD16**] and the journal article [**WWD18**]. Therefore a common system model based on the MC schemes mentioned in the previous chapter was developed, which contains all equalizers types and TWRC detection types mentioned above. In addition, a joint analysis and comparison of the methods applied will be carried out, which have not yet been published.

4.2 TWRC: General Scenarios

As discussed above, a pair of two users want to communicate with each other by the help of a relay positioned in the surrounding area. We concentrate here on the communication over a single relay with one receiving antenna to open the general concepts concerning offsets and multi-carrier procedures. For the interested reader we refer to [WWD14b, WWD14a] for distributed relays. Fig. 4.1 shows the generic setup, where a user A wants to transmit some information via a relay R to the user B and vice versa. The figure shows the possible communication links, in particular A → B, A → R, B → A, B → R, R → A and finally R → B. Within this work we assume that both users have no direct link to each other due to shadowing or high distance such that the links $A \not\to B$ and $B \not\to A$ have considerable low signal-to-noise ratio (SNR).

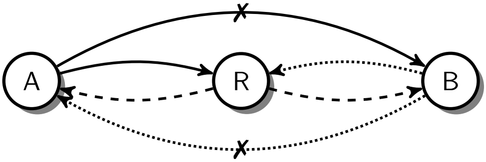

Figure 4.1: Generic setup of two users communicating via a relay.

Four Phase Scenario The first scheme allows four different phases illustrated on the information word level by Fig. 4.2. The exchange of information of a user pair is multiplexed into four orthogonal phases, where two phases are needed per user to transmit via the relay to the other user. Related to Chapter 3 and the multi-carrier system mode (3.27) the four phases are listed below:

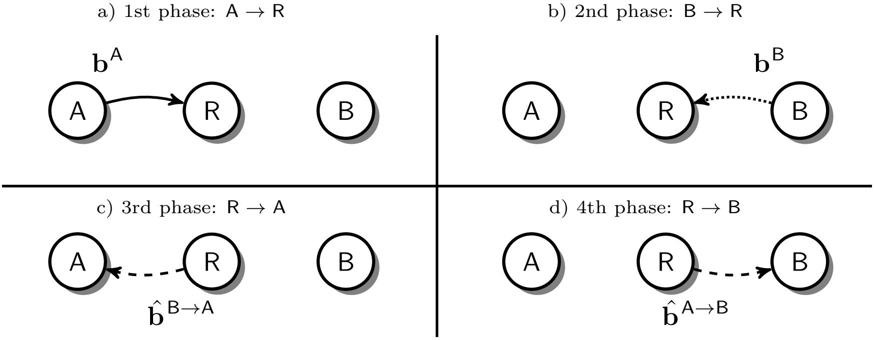

Figure 4.2: Four phase scenario based on the information word level.

- 1st phase (P2P): A → R, signal at relay: $\underline{\mathbf{y}}^{\mathsf{A}\to\mathsf{R}} = \underline{\mathbf{H}}^{\mathsf{A}\to\mathsf{R}}\underline{\mathbf{d}}^{\mathsf{A}} + \underline{\mathbf{n}}^{\mathsf{A}\to\mathsf{R}}$
- 2nd phase (P2P): B → R, signal at relay: $\underline{\mathbf{y}}^{\mathsf{B}\to\mathsf{R}} = \underline{\mathbf{H}}^{\mathsf{B}\to\mathsf{R}}\underline{\mathbf{d}}^{\mathsf{B}} + \underline{\mathbf{n}}^{\mathsf{B}\to\mathsf{R}}$
- 3rd phase (P2P): R → A, signal at user A: $\underline{\mathbf{y}}^{\mathsf{R}\to\mathsf{A}} = \underline{\mathbf{H}}^{\mathsf{R}\to\mathsf{A}}\underline{\tilde{\mathbf{d}}}^{\mathsf{B}} + \underline{\mathbf{n}}^{\mathsf{R}\to\mathsf{A}}$
- 4th phase (P2P): R → B, signal at user B: $\underline{\mathbf{y}}^{\mathsf{R}\to\mathsf{B}} = \underline{\mathbf{H}}^{\mathsf{R}\to\mathsf{B}}\underline{\tilde{\mathbf{d}}}^{\mathsf{A}} + \underline{\mathbf{n}}^{\mathsf{R}\to\mathsf{B}}$,

where a user $\mathsf{u} \in \{\mathsf{A}, \mathsf{B}\}$ encodes its information word $\mathbf{b}^{\mathsf{u}}$ by an encoder yielding the code word $\mathbf{c}^{\mathsf{u}} = \mathcal{C}\left(\mathbf{b}^{\mathsf{u}}\right)$ with rate R_{c}. The coded bits are mapped to complex transmit symbol frame $\underline{\mathbf{d}}^{\mathsf{u}} = \mathcal{M}\left(\mathbf{c}^{\mathsf{u}}\right)$, that are transmitted by an access scheme to the destination. The notation R → B describes the path from an entity R to an entity B.

As we introduced in Chapter 3, we focus on MC schemes, where the overall bandwidth efficiency (3.6) is defined as $\eta = \varrho\delta_{\mathrm{LD}}\left(\Lambda\right)$, where ϱ and $\delta_{\mathrm{LD}}\left(\Lambda\right)$ are the information bits per symbol and the TF grid density, respectively. The phases could be implemented as different time slots or as different frequency bands. Hence, in all implementations the bandwidth efficiency η gets reduced by a factor of the number of phases used [ZLL06b]. The user rate per resource used is $\varrho^{\mathsf{u}} = \log_2\left(M^{\mathsf{u}}\right) R_{\mathrm{c}}^{\mathsf{u}}$. Assuming the same encoding scheme and the same mapping for both users, it results in an overall bandwidth efficiency for four slots of $\eta^{\text{4Phase}} = (\varrho^{\mathsf{A}} + \varrho^{\mathsf{B}})\delta_{\text{LD}}\,(\Lambda) = \frac{2\log_2(M)R_{\text{c}}}{4T_0F_0} = \frac{1}{2}\frac{\varrho^{\text{P2P}}}{T_0F_0} = \frac{1}{2}\eta^{\text{P2P}}$, which is half of the bandwidth efficiency of a unidirectional P2P transmission. Here, ϱ^{P2P} (*cf.* (2.5)) and η^{P2P} (*cf.* (3.6)) denotes the information bits per symbol and the bandwidth efficiency in the P2P case.

The relay signal for the third and fourth phase can be generated by different relaying techniques. Beside amplify and forward (AF) that amplifies the received signal without any additional processing on the data, decode and forward (DF) techniques estimates the underlying information bits and perform re-encoding to generate the relay transmit symbols. In this work, we focus on DF. Other schemes are investigated for example in [Wu17].

Three Phase Scenario This scenario is also known as straightforward NC [ZL10]. A reduction to three phases is achieved by the idea of NC, which was proposed by Ahlswede *et al.*in 2000 [ACLY00] and further discussed in [LYN03, Yeu08]. NC changed the way of communication in networks by the combination of information from multiple sources in order to increase the overall system throughput. Hence, the first two phases remain orthogonal. However, the third phase uses a NC frame broadcast to the users in the so-called broadcast (BC) phase. The procedure is illustrated in Fig. 4.3 and the receive signals in each phase are given by

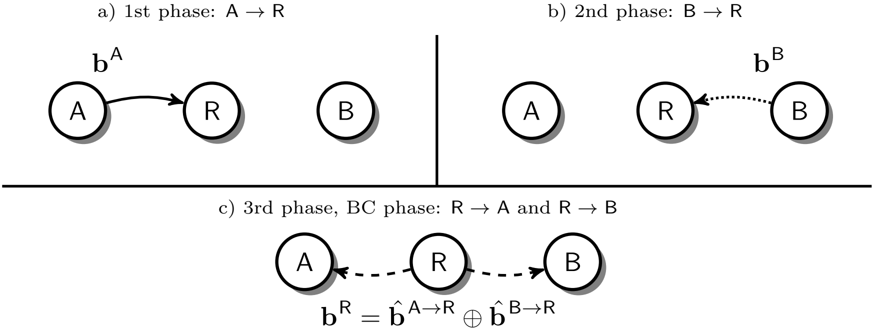

Figure 4.3: Three phase scenario based on the information word level.

- 1st phase (P2P): A → R, signal at relay: $\underline{\mathbf{y}}^{\mathsf{A}\to\mathsf{R}} = \underline{\mathbf{H}}^{\mathsf{A}\to\mathsf{R}}\underline{\mathbf{d}}^{\mathsf{A}} + \underline{\mathbf{n}}^{\mathsf{A}\to\mathsf{R}}$
- 2nd phase (P2P): B → R, signal at relay: $\underline{\mathbf{y}}^{\mathsf{B}\to\mathsf{R}} = \underline{\mathbf{H}}^{\mathsf{B}\to\mathsf{R}}\underline{\mathbf{d}}^{\mathsf{B}} + \underline{\mathbf{n}}^{\mathsf{B}\to\mathsf{R}}$

- BC Phase (2×P2P): $\mathsf{R} \rightarrow \mathsf{A}$ and $\mathsf{R} \rightarrow \mathsf{B}$, Rx signal at A: $\underline{\mathbf{y}}^{\mathsf{R}\rightarrow\mathsf{A}} = \underline{\underline{\mathbf{H}}}^{\mathsf{R}\rightarrow\mathsf{A}}\underline{\mathbf{d}}^{\mathsf{R}} + \underline{\mathbf{n}}^{\mathsf{R}\rightarrow\mathsf{A}}$ and Rx signal at B: $\underline{\mathbf{y}}^{\mathsf{R}\rightarrow\mathsf{B}} = \underline{\underline{\mathbf{H}}}^{\mathsf{R}\rightarrow\mathsf{B}}\underline{\mathbf{d}}^{\mathsf{R}} + \underline{\mathbf{n}}^{\mathsf{R}\rightarrow\mathsf{B}}$.

Similar to the four phase scenario, first, the information words are estimated $\hat{\mathbf{b}}^{\mathsf{u}\rightarrow\mathsf{R}} = \mathbf{b}^{\mathsf{u}} \oplus \mathbf{e}^{\mathsf{u}\rightarrow\mathsf{R}} \in \mathbb{F}_2^{N_{\mathsf{b}}}$, $\mathsf{u} \in \{\mathsf{AB}\}$ separately at the relay, where $\mathbf{e}^{\mathsf{u}\rightarrow\mathsf{R}}$ is the user specific error vector from a user u to R. The task at the relay is to generate one joint message $\mathbf{b}^{\mathsf{R}\rightarrow\mathsf{u}} = f_{\mathrm{BC}}(\hat{\mathbf{b}}^{\mathsf{A}\rightarrow\mathsf{R}}, \hat{\mathbf{b}}^{\mathsf{B}\rightarrow\mathsf{R}})$ based on the estimated information words $\hat{\mathbf{b}}^{\mathsf{u}\rightarrow\mathsf{R}}$ needed for the third phase. The NC approach considered in this thesis to generate the BC message is based on the bit-wise XOR combination of the underlying information word bits (or code word bits by using linear encoding schemes) such that the BC information word is generated[1] by $\mathbf{b}^{\mathsf{R}} = f_{\mathrm{BC}}(\hat{\mathbf{b}}^{\mathsf{A}\rightarrow\mathsf{R}}, \hat{\mathbf{b}}^{\mathsf{B}\rightarrow\mathsf{R}}) = \hat{\mathbf{b}}^{\mathsf{A}\rightarrow\mathsf{R}} \oplus \hat{\mathbf{b}}^{\mathsf{B}\rightarrow\mathsf{R}}$. After estimating the BC signal $\hat{\mathbf{b}}^{\mathsf{R}\rightarrow\mathsf{u}} = \mathbf{b}^{\mathsf{R}} \oplus \mathbf{e}^{\mathsf{R}\rightarrow\mathsf{u}}$, user A performs self-interference cancellation with the knowledge of its own data $\mathbf{b}^{\mathsf{A}}$ of the transmission in the first phase by

$$\begin{aligned}
\hat{\mathbf{b}}^{\mathsf{B}} &= \hat{\mathbf{b}}^{\mathsf{R}\rightarrow\mathsf{A}} \oplus \underbrace{\mathbf{b}^{\mathsf{A}}}_{\substack{\text{self interference}\\ \text{cancellation}}} \\
&= \mathbf{b}^{\mathsf{R}} \oplus \mathbf{b}^{\mathsf{A}} \oplus \mathbf{e}^{\mathsf{R}\rightarrow\mathsf{u}} \\
&= \hat{\mathbf{b}}^{\mathsf{A}\rightarrow\mathsf{R}} \oplus \hat{\mathbf{b}}^{\mathsf{B}\rightarrow\mathsf{R}} \oplus \mathbf{b}^{\mathsf{A}} \oplus \mathbf{e}^{\mathsf{R}\rightarrow\mathsf{A}} \\
&= \mathbf{b}^{\mathsf{B}} \oplus \underbrace{\mathbf{b}^{\mathsf{A}} \oplus \mathbf{b}^{\mathsf{A}}}_{=\mathbf{0}} \oplus \underbrace{\mathbf{e}^{\mathsf{A}\rightarrow\mathsf{R}} \oplus \mathbf{e}^{\mathsf{B}\rightarrow\mathsf{R}} \oplus \mathbf{e}^{\mathsf{R}\rightarrow\mathsf{A}}}_{\mathbf{e}^{\text{total}}} \\
&= \mathbf{b}^{\mathsf{B}} \oplus \mathbf{e}^{\text{total}}
\end{aligned} \tag{4.1}$$

In the same way user B can estimate the data of user A. If no error occurs on the transmission chain, *i.e.* the individual errors $\mathbf{e}^{\mathsf{u}} = \mathbf{0}$ result in a $\mathbf{e}^{\text{total}} = \mathbf{0}$, user A and B are able to receive the data of the other user successfully, making the BC message

$$\mathbf{b}^{\mathsf{R}} = \hat{\mathbf{b}}^{\mathsf{A}\rightarrow\mathsf{R}} \oplus \hat{\mathbf{b}}^{\mathsf{B}\rightarrow\mathsf{R}} \tag{4.2}$$

a good choice for the third phase. And even if errors occur, proper channel encoding techniques will be able to allow for an error free transmission as subsequently shown. Other mappings are possible, but are not topic of this thesis, and we refer to [HS11, Hek13] and references therein.

For the Three-Phase approach, the effective transmission rate is reduced to 2 frames per 3 resources, thus, the bandwidth efficiency $\eta^{\text{3Phase}} = \frac{2}{3}\frac{\varrho^{\text{P2P}}}{T_0 F_0}$ is 2/3 of a unidirectional P2P transmission.

Two-Phase Scenario One step further is the idea of Zhang, Liew and

---

[1] By using a linear encoding scheme the relay code word can be represented by $\mathbf{c}^{\mathsf{R}} = \mathcal{C}(\mathbf{b}^{\mathsf{A}} \oplus \mathbf{b}^{\mathsf{B}})$ or $\mathbf{c}^{\mathsf{R}} = \mathcal{C}(\mathbf{b}^{\mathsf{A}}) \oplus \mathcal{C}(\mathbf{b}^{\mathsf{B}})$ as in both cases a valid code word is generated.

a) 1. phase, MA phase: $\mathsf{A} \rightarrow \mathsf{R}$ and $\mathsf{B} \rightarrow \mathsf{R}$

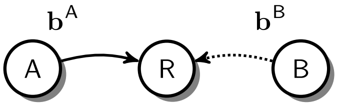

b) 2. phase, BC phase: $\mathsf{R} \rightarrow \mathsf{A}$ and $\mathsf{R} \rightarrow \mathsf{B}$

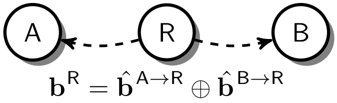

Figure 4.4: Two-phase scenario on an information word level

Lam in 2006 [ZLL06b] and at the same time by Popovski and Yomo in [PY06a, PY06b] with the idea of PLNC, where the overall transmission is done in a MA phase and a BC phase. This reduction of the effective transmission rate to two frames per two resources can be done by also reducing the first and second phase to a mutual MA phase, where user A and B transmit simultaneously[2] to the relay as illustrated in Fig. 4.4. The basic idea of this approach is the underlying additive nature of arriving electromagnetic waves on the same physical resource at the relay, which can be interpreted as an equivalent summation of the underlying coding operation. The additive signal is called PLNC as the NC is inherently done by the physical channel. The PLNC signal is estimated at the relay and broadcast to the users in the second phase. This procedure results in a bandwidth efficiency $\eta^{\text{2Phase}} = \frac{\varrho^{\text{P2P}}}{T_0 F_0}$ which is equal to the bandwidth efficiency of a unidirectional P2P transmission. However, in contrast to the 3 phase approach, where two separate unidirectional P2P channels are used in the first two phases, we use here a TWRC where the uplink is introduced in Section 2.5 as two-point channel. The phases can be given by

- MA phase (TWRC): $\mathsf{A} \rightarrow \mathsf{R}$ and $\mathsf{B} \rightarrow \mathsf{R}$ with receive signal at the relay:

$$\underline{\mathbf{y}}^{\mathsf{AB}\rightarrow\mathsf{R}} = \underline{\mathbf{H}}^{\mathsf{A}\rightarrow\mathsf{R}}\underline{\mathbf{d}}^{\mathsf{A}} + \underline{\mathbf{H}}^{\mathsf{B}\rightarrow\mathsf{R}}\underline{\mathbf{d}}^{\mathsf{B}} + \underline{\mathbf{n}}^{\mathsf{AB}\rightarrow\mathsf{R}}$$

- BC phase (2×P2P): $\mathsf{R} \rightarrow \mathsf{A}$ and $\mathsf{R} \rightarrow \mathsf{B}$ with receive signals:

$$\begin{aligned} \text{Rx signal at } \mathsf{A}: \quad & \underline{\mathbf{y}}^{\mathsf{R}\rightarrow\mathsf{A}} = \underline{\mathbf{H}}^{\mathsf{R}\rightarrow\mathsf{A}}\underline{\mathbf{d}}^{\mathsf{R}} + \underline{\mathbf{n}}^{\mathsf{R}\rightarrow\mathsf{A}} \\ \text{Rx signal at } \mathsf{B}: \quad & \underline{\mathbf{y}}^{\mathsf{R}\rightarrow\mathsf{B}} = \underline{\mathbf{H}}^{\mathsf{R}\rightarrow\mathsf{B}}\underline{\mathbf{d}}^{\mathsf{R}} + \underline{\mathbf{n}}^{\mathsf{R}\rightarrow\mathsf{B}} \end{aligned}$$

---

[2] In this setup, *simultaneously* means that we use the same resources, *i.e.* time, and frequency and only one receive antenna at the relay.

This approach is the most challenging one due to the superposition of the two user frames at the relay on the same physical resources resulting in an *interference* affected system. We just get one observation per two unknowns. Most communication systems avoid this kind of multi-user interference (MUI), however, by embracing this interference, we are able to increase the bandwidth efficiency and, thus, the overall performance is improved.

The relay has the task to generate a joint BC message $\underline{\mathbf{d}}^{\mathsf{R}}$ based on the superposition MA frame $\underline{\mathbf{y}}^{\mathsf{AB}\rightarrow\mathsf{R}}$ like

$$\textit{broadcast frame} = f_{\mathrm{MA}\rightarrow\mathrm{BC}}\left(\textit{superpostion frame}\right), \tag{4.3}$$

where $f_{\mathrm{MA}\rightarrow\mathrm{BC}}\left(\cdot\right)$ is some function mapping the received MA frame to a BC frame. The questions are: *How does this function look like and what is it based on?* Different detection schemes are proposed in [ZLL06b, Wüb10, WL10], based on the idea that the relay directly estimates the joint BC message $f_{\mathrm{MA}\rightarrow\mathrm{BC}}(\underline{\mathbf{y}}^{\mathsf{AB}\rightarrow\mathsf{R}}) \rightarrow \mathbf{b}^{\mathsf{A}} \oplus \mathbf{b}^{\mathsf{B}}$ related to the three-phase scenario. This is one reasonable interpretation as the superposition of two symbol vectors $\underline{\mathbf{d}}^{\mathsf{A}}$ and $\underline{\mathbf{d}}^{\mathsf{B}}$ can be interpreted as the transmission of the XOR combination of the underlying bits $\mathbf{b}^{\mathsf{A}} \oplus \mathbf{b}^{\mathsf{B}}$.

In general more than one pair of users can interact over one relay, *e.g.* in [Len16] the author investigates interleaved division multiple access (IDMA) as multiplexing technology in a multiple pair bidirectional relaying scenario and [CY09] also discusses CDMA as a multiplexing techniques.

To show the principle ideas and properties of MC transmission schemes with general waveforms in a TWRC under offset conditions, we investigate the application of one pair of users, only, without any additional multiplexing procedure. However, the combination of the aforementioned multiplexing techniques (*i.e.* IDMA and CDMA) or others with general MC schemes are further implementable, but the combination is out of scope of this thesis. Furthermore, we limit the discussion to the MA phase, as the transmission in the BC phase can be seen as two P2P transmissions from the relay to each user.

One may note that, we will subsequently omit the indices *e.g.* like $\underline{\mathbf{H}}^{\mathsf{u}} = \underline{\mathbf{H}}^{\mathsf{u}\rightarrow\mathsf{R}}$, $\mathbf{y}^{\mathsf{u}} = \mathbf{y}^{\mathsf{u}\rightarrow\mathsf{R}}$ or $\underline{\mathbf{d}}^{\mathsf{u}} = \underline{\mathbf{d}}^{\mathsf{u}\rightarrow\mathsf{R}}$ as it is obvious from or to which node the signal “comes from” or “goes to” and it makes the equations more readable and shorter.

Subsequently, in Section 4.3, we will introduce a detailed system model for the transmission of two user signals to a relay station applying general MC transmissions based on the basic concepts of Chapter 2 and 3. We then focus on three detection schemes based on different ideas for the detailed mapping function $f_{\mathrm{MA}\rightarrow\mathrm{BC}}\left(\cdot\right)$. The estimation of the BC message at the relay is rested on a FG-based approach, such that the mapping function $f_{\mathrm{MA}\rightarrow\mathrm{BC}}\left(\cdot\right)$

will be represented as FG later on. The following sections presuppose the general knowledge of the concept of FGs and the message exchange within these entities. To focus on the general concepts *w.r.t.* TWRC detection, the introduction of a FGE for P2P transmissions is briefly given in Appendix B. Furthermore, the interested reader is invited to the references (without any claim to completeness) [KFL01, Loe03, Loe04, Wym07], which give a great overview on FGs and the SPA in general.

4.3 System Model and Detection Methods of Two-Phase TWRC Transmissions

4.3.1 Overview

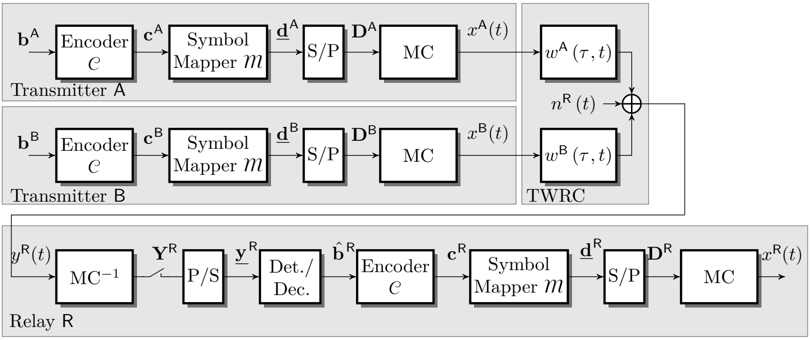

Figure 4.5: Overall system model for the multiple access phase. The upper three blocks show the transmission to the relay and the lower block illustrates the signal generation for the broadcast phase.

In this section we first focus on the description of the system model. To further give insights on the basic detection concept, *i.e.* on the, so far, general function $f_{\mathrm{MA}\rightarrow\mathrm{BC}}(\cdot)$, we introduce a detailed mapping of the information to the physical resources to generate the individual transmit signals at each user, illustrated as "Transmitter u", $\mathsf{u} \in \{\mathsf{A}, \mathsf{B}\}$ in Fig. 4.5. We discuss the TWRC, which superimposes the two user signals $x^{\mathsf{A}}(t)$ and $x^{\mathsf{B}}(t)$, and furthermore, the detection at the relay is described and discussed in detail. We limit ourselves to a single antenna setup, *i.e.* each node is only equipped with a single antenna.

User Transmit Signal The binary information sequence $\mathbf{b}^{\mathsf{u}} \in \mathbb{F}_2^{N_{\mathbf{b}}}$ with length $N_{\mathbf{b}}$ is encoded by a linear encoding scheme, such that a code word is generated with an encoder $\mathcal{C}$ by $\mathbf{c}^{\mathsf{u}} = \mathcal{C}\left(\mathbf{b}^{\mathsf{u}}\right) \in \mathbb{F}_2^{N_{\mathsf{c}}}$ with a code rate $R_{\mathrm{c}} = \frac{N_{\mathsf{b}}}{N_{\mathsf{c}}}$.

The symbol mapper $\mathcal{M}$ maps $\log_2(M)$ code bits to a complex symbol symbols $\underline{\mathbf{d}}^{\mathsf{u}}$. This symbol vector $\underline{\mathbf{d}}^{\mathsf{u}}$ is a user specific stacked data symbol vector and after a serial to parallel (S/P)^{3} conversion, the symbol matrix $\mathbf{D}^{\mathsf{u}} \in \mathbb{C}^{N_{\mathrm{SC}} \times N_{\mathrm{TS}}}$, with $\underline{\mathbf{d}}^{\mathsf{u}} = \mathrm{vec}\{\mathbf{D}^{\mathsf{u}}\}$ is achieved.

Each symbol element $d^{\mathsf{u}}_{k,\ell}$ of matrix $\mathbf{D}^{\mathsf{u}}$ is mapped on a sub-carrier kF_0 and a time instance ℓT_0 by a MC scheme introduced in Chapter 3, implemented by the MC block in Fig. 4.5 resulting in the time signal $x^{\mathsf{u}}(t)$ and transmitted to the relay. As also discussed in Chapter 2, a TWRC channel is used to describe the transmission of both user signals A and B to the relay R. In general, we assume time-variant channels $w^{\mathsf{u}}(\tau, t)$ additionally affected by AWGN $n^{\mathsf{R}}(t)$ with zero mean and variance σ_{n}^2.

Two-Way Relaying Channel At the relay the analysis part and sampling generates the observation matrix $\mathbf{Y}^{\mathsf{R}} \in \mathbb{C}^{N'_{\mathrm{SC}} \times N'_{\mathrm{TS}}}$ containing the observation $y^{\mathsf{R}}_{k',\ell'}$ at the TF grid point (k', ℓ'). After P/S conversion with $\underline{\mathbf{y}}^{\mathsf{R}} = \mathrm{vec}\{\mathbf{Y}^{\mathsf{R}}\}$, the overall receive signal at the relay is given in matrix notation by

$$\underline{\mathbf{y}}^{\mathsf{R}} = \underline{\mathbf{H}}^{\mathsf{A}}\underline{\mathbf{d}}^{\mathsf{A}} + \underline{\mathbf{H}}^{\mathsf{B}}\underline{\mathbf{d}}^{\mathsf{B}} + \tilde{\mathbf{n}}^{\mathsf{R}} \quad , \tag{4.4}$$

where $\underline{\mathbf{H}}^{\mathsf{u}}$ is the frame-based effective channel matrix introduced and discussed in Chapter 3 (3.27) and a noise vector $\tilde{\mathbf{n}}^{\mathsf{R}}$ at the relay.

The received signal can be separated into three parts: the desired signal ①, the interference part ② and noise ③ like

$$\underline{\mathbf{y}}^{\mathsf{R}} = \underbrace{\boldsymbol{\Sigma}_{\mathbf{H}}^{\mathsf{A}}\mathbf{d}^{\mathsf{A}} + \boldsymbol{\Sigma}_{\mathbf{H}}^{\mathsf{B}}\mathbf{d}^{\mathsf{B}}}_{\textcircled{1}\ \text{PLNC signal}} + \underbrace{\left(\overline{\boldsymbol{\Sigma}}_{\mathbf{H}}^{\mathsf{A}}\mathbf{d}^{\mathsf{A}} + \overline{\boldsymbol{\Sigma}}_{\mathbf{H}}^{\mathsf{B}}\mathbf{d}^{\mathsf{B}}\right)}_{\textcircled{2}\ \text{common interference}} + \underbrace{\tilde{\mathbf{n}}^{\mathsf{R}}}_{\textcircled{3}\ \text{noise}} \quad , \tag{4.5}$$

where the effective channel matrix $\underline{\mathbf{H}}^{\mathsf{u}} = \boldsymbol{\Sigma}_{\mathbf{H}}^{\mathsf{u}} + \overline{\boldsymbol{\Sigma}}_{\mathbf{H}}^{\mathsf{u}}$ can be split into a desired matrix $\boldsymbol{\Sigma}_{\mathbf{H}}^{\mathsf{u}}$, which contains only the main diagonal elements and an interference matrix $\overline{\boldsymbol{\Sigma}}_{\mathbf{H}}^{\mathsf{u}}$ containing all off-diagonal elements. The matrix representation corresponds in scalar form to

$$y_r^{\mathsf{R}} = \underbrace{h_{r,r}^{\mathsf{A}} d_r^{\mathsf{A}} + h_{r,r}^{\mathsf{B}} d_r^{\mathsf{B}}}_{\textcircled{1}\ \text{PLNC signal}} + \underbrace{\sum_{s \neq r} \left(h_{r,s}^{\mathsf{A}} d_s^{\mathsf{A}} + h_{r,s}^{\mathsf{B}} d_s^{\mathsf{B}}\right)}_{\textcircled{2}\ \text{common interference}} + \underbrace{\tilde{n}_r^{\mathsf{R}}}_{\textcircled{3}\ \text{noise}} \quad , \tag{4.6}$$

---

[3] The S/P as well as the parallel to serial (P/S) conversion can be mathematically described by the vectorization operator $\underline{\mathbf{a}} = \mathrm{vec}\{\mathbf{A}\}$, stacking the columns of a matrix $\mathbf{A} \in \mathbb{C}^{N_{\mathrm{rows}} \times N_{\mathrm{columns}}}$ into a frame vector $\underline{\mathbf{a}} \in \mathbb{C}^{N_{\mathrm{columns}} N_{\mathrm{rows}} \times 1}$, and vice versa with $\mathbf{A} = \mathrm{vec}\{\underline{\mathbf{a}}\}$.

where $d_s^{\mathsf{u}} \in \{\mathsf{A}, \mathsf{B}\}$ denotes the transmit symbols per user, y_r the observation at the relay and $\tilde{n}_r^{\mathsf{R}}$ the noise at the relay. The receiving index $r = k' + \ell' N'_{\mathrm{SC}}$ with $0 \leq r \leq N'_{\mathrm{TS}} N'_{\mathrm{SC}} - 1$ and sending index $s = k + \ell N_{\mathrm{SC}}$ with $0 \leq s \leq N_{\mathrm{TS}} N_{\mathrm{SC}} - 1$ is used. The signal in ① of both equation is the so-called interference-free PLNC signal, forming the basis of the detection of the BC message (4.2).

Impact of Timing Offset and Carrier Frequency Offset Before we analyze the impact on the different PLNC detection schemes, we focus on the common ISI, ICI and ACI in ② (4.6). For this, we analyze two influences, namely the TO and the CFO regarding the amount of interference introduced as published by the author in parts in [**WZWD16, WWD16, WWD18**]. Certainly, the results can be generalized to delay spread and Doppler spread as they can be described by multiple TOs and CFOs, respectively. *It is of utmost importance how the useful power of one symbol is spread over the Rx-TF grid, and, is it sufficient to consider a limited number of neighboring TF grid points?*

The answer to this question is important for the design of the FGE in the next section, as it controls the number of connection within the FG. Many elements $h_{r,s}^{\mathsf{u}}$ unequal to zero result in a dense adjacency matrix and thus in a highly connected FGE, resulting in a high computational complexity for the SPA. Thus, we analyze the influence of the introduced interference at the relay considering the following MC transmission schemes 1) QAM-based OFDM (w/o guard interval), 2) OQAM/OFDM with EGF waveform ($\rho = 2$), 3) CP-OFDM, 4) QAM-based MC schemes, with half-cosine, and Gaussian waveform with $\rho = 1$, 5) OQAM-based FBMC schemes, with half-cosine, and Gaussian waveform with $\rho = 2$. We analyze the introduced interference power dispersed over the Rx-TF grid (k', ℓ') at the relay transmitting only one fixed transmit symbol d_s at sending TF grid (k, ℓ). The transmit symbol power per user is normalized (*i.e.* symbol variance $\sigma_{\mathrm{d}}^2 = 1$) to compare QAM and OQAM mapping. The underlying physical channels are assumed to be affected by constant TO $\Delta\tau$ and constant CFO $\Delta\nu$ and result in a one-tap delay-Doppler function

$$s^{\mathsf{u}}(\tau, \nu) = e^{j\phi^{\mathsf{u}}} \delta(\tau - \Delta\tau^{\mathsf{u}}) \, \delta(\nu - \Delta\nu^{\mathsf{u}}) \tag{4.7}$$

per user with the connection of the delay-Doppler function $s(\tau, \nu)$ and the corresponding channel coefficient $h_{r,s}^{\mathsf{u}}$ in (3.11). We focus on symmetric compensation of all effects and, thus, an average compensation is assumed yielding $\Delta\tau^{\mathsf{B}} = -\Delta\tau^{\mathsf{A}}$ for TO, $\Delta\nu^{\mathsf{B}} = -\Delta\nu^{\mathsf{A}}$ for the CFO and a symmetric phase difference of $\phi^{\mathsf{B}} = -\phi^{\mathsf{A}}$.

Let us recall the TF grid in Fig. 3.6, the power used at N_{N} TF grid points and ignoring the residue is then defined as

$$P_{d_s}^{\mathrm{QAM}}(N_{\mathrm{N}}) = \sum_{r \in \mathcal{N}_{d_s^{\mathsf{A}}}^{\mathrm{QAM}}(N_{\mathrm{N}})} \left|h_{r,s}^{\mathsf{A}}\right|^2 + \sum_{r \in \mathcal{N}_{d_s^{\mathsf{B}}}^{\mathrm{QAM}}(N_{\mathrm{N}})} \left|h_{r,s}^{\mathsf{B}}\right|^2 \tag{4.8}$$

for QAM-based schemes, where the sets $\mathcal{N}_{d_s^{\mathsf{u}}}^{\mathrm{QAM}}(N_{\mathrm{N}})$ are user specific sets of receive indices r according to the N_{N} largest amplitudes squared $\left|h_{r,s}^{\mathsf{u}}\right|^2$. The signal power $P_{d_s}^{\mathrm{QAM}}(N_{\mathrm{N}})$ accumulates the N_{N} neighbors with the highest power of a column $\underline{\mathbf{H}}_{1:\mathrm{end},s}^{\mathsf{u}}$ for a fixed sending symbol s.

The OQAM-based FBMC transmission schemes achieve only orthogonality by applying the real part operator on the relay received signal $y_r^{\mathsf{R},\mathrm{OQAM}} = \Re\{y_r^{\mathsf{R}}\}$ [**WZWD16**]. Hence, the useful power yields

$$P_{d_s}^{\mathrm{OQAM}}(N_{\mathrm{N}}) = \sum_{r \in \mathcal{N}_{d_s^{\mathsf{A}}}^{\mathrm{OQAM}}(N_{\mathrm{N}})} \Re\left\{h_{r,s}^{\mathsf{A}}\right\}^2 + \sum_{r \in \mathcal{N}_{d_s^{\mathsf{B}}}^{\mathrm{OQAM}}(N_{\mathrm{N}})} \Re\left\{h_{r,s}^{\mathsf{B}}\right\}^2 \quad , \tag{4.9}$$

where the sets $\mathcal{N}_{d_s^{\mathsf{u}}}^{\mathrm{OQAM}}(N_{\mathrm{N}})$ are generated according to the N_{N} largest real parts squared $\Re\{h_{r,s}^{\mathsf{u}}\}^2$. Eq. (4.8) and (4.9) give an indication on the amount of useful power spread over a number of N_{N} TF grid points at the relay. The set $\mathcal{N}_{d_s^{\mathsf{u}}}^{\mathrm{scheme}}(N_{\mathrm{N}})$ can be interpreted as the *neighborhood* of a symbol d_s with N_{N} neighbors, which is the important design parameter for the FGE in the next section. We further define the normalized power loss

$$\gamma(N_{\mathrm{N}}) = \frac{P_{\mathrm{Total}} - P_{d_s}(N_{\mathrm{N}})}{P_{\mathrm{Total}}} = \frac{\text{unused power}}{P_{\mathrm{Total}}} \tag{4.10}$$

giving the amount of signal power ignored by considering only N_{N} samples, where P_{Total} collects the overall available power at the relay, *i.e.* (4.8) or (4.9) with $N_{\mathrm{N}} \to \infty$. The curves in Fig. 4.6 show the normalized power loss $\gamma(N_{\mathrm{N}})$ *w.r.t.* a different TO $\Delta\tau^{\mathsf{u}}$ for an increasing number of neighbors $N_{\mathrm{N}} = 1, 4, 7, 10, 13$ and the different MC transmission schemes discussed above without CFO ($\Delta\nu^{\mathsf{u}} = 0$). In this analysis, the underlying channels are fully aligned such that the phase difference is $\phi^{\mathsf{AB}} = 0$. If no TO (*i.e.* at $\Delta\tau^{\mathsf{u}} = 0$) is present or in other words the system is perfectly synchronized, the power loss already vanishes for the orthogonal schemes with just one neighbor $N_{\mathrm{N}} = 1$. Hence, the effective matrix $\underline{\mathbf{H}}^{\mathsf{u}}$ in (4.4) results in a purely diagonal structure (*i.e.* $\overline{\mathbf{\Sigma}}_{\mathbf{H}}^{\mathsf{u}} = \mathbf{0}$). Thus, a one-tap equalizer is sufficient and similar frame error rate (FER) performance like in Fig. 4.14 are achievable. As expected, the orthogonal CP-OFDM scheme does not suffer from a power

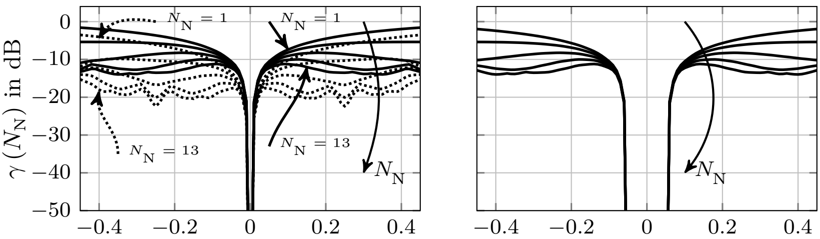

a) OFDM

b) CP-OFDM, $T_\mathrm{GI}=0.1T_\mathrm{S}$

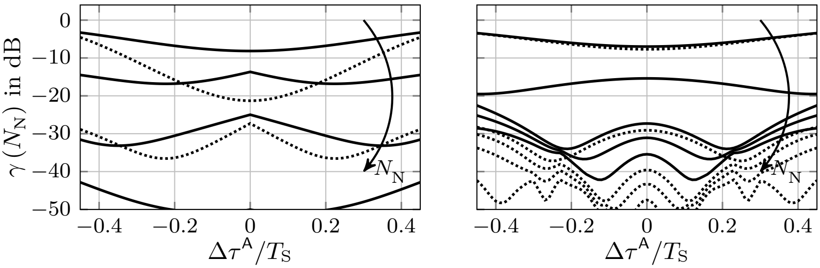

c) FBMC, Gaussian

d) FBMC, half-cosine

Figure 4.6: Normalized power loss in logarithmic scale for the QAM-based schemes (——) and OQAM-based schemes (········) with $N_\mathrm{N} = 1, 4, 7, 10, 13$ applying TWRC, w/ different normalized TO $\Delta\tau^\mathsf{A}/T_\mathrm{S}$, without CFO $\Delta\nu^\mathsf{u}=0$ and without phase difference $\phi^\mathsf{AB}=0$.

loss as long as the TO is within the guard interval length, which would be similar to ZP-OFDM and w-CP-OFDM. In contrast, for the non-orthogonal schemes all neighbors and, thus, P_Total is required to achieve a completely vanishing power loss $\gamma(N_\mathrm{N})$. All schemes suffer from spreading over the TF grid with the presence of TO. However, by collecting more neighbors N_N the loss $\gamma(N_\mathrm{N})$ decreases. The Gaussian waveform achieves the lowest loss among all schemes collecting fewer neighbors N_N over a wide range of offsets. The OQAM-based schemes outperform the corresponding QAM schemes due to the better separation in the TF grid and the reduced interference power in the imaginary domain if no phase difference ϕ^AB occur between the users.

Fig. 4.7 shows the normalized power loss $\gamma(N_\mathrm{N})$ for a varying CFO $\Delta\nu^\mathsf{u}$ without a TO $(\Delta\tau^\mathsf{u}=0)$[4]. Contrarily to the setup of Fig. 4.6, a symmetric but misaligned phase difference between the users of $\phi^\mathsf{AB}=\pi/2$ is applied.

---

[4] One may note that the curves for OFDM and CP-OFDM with $N_\mathrm{N}=1$ can be calculated with (3.60).

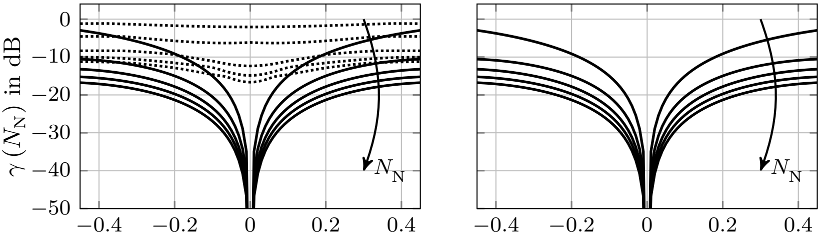

a) OFDM

b) CP-OFDM, $T_{\mathrm{GI}} = 0.1T$

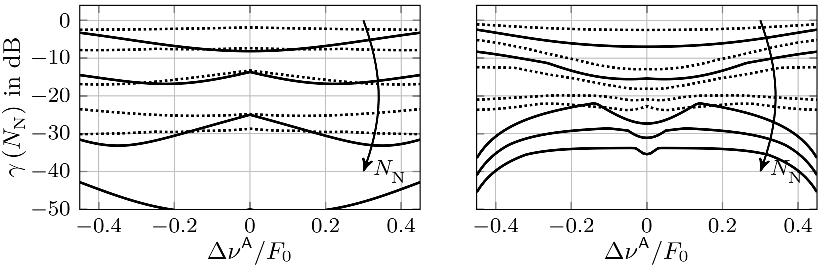

c) FBMC, Gaussian

d) FBMC, half-cosine

Figure 4.7: Normalized power loss for the QAM-based schemes (——) and OQAM-based schemes (········) with $N_{\mathrm{N}} = 1, 4, 7, 10, 13$ applying TWRC, different normalized CFO $\Delta\nu^{\mathsf{A}}/F_0$, without TO $\Delta\tau^{\mathsf{u}} = 0$ and with a fixed phase difference $\phi^{\mathsf{AB}} = \pi/2$.

This phase shift destroys the real-valued orthogonality of OQAM/OFDM ($\Re\{$②$\} \neq 0$) and the reduced interference of the OQAM/FBMC ($\Re\{$②$\} \gg 0$) as it fully aligns the interference from one user to the useful power of the other user and vice versa. Correspondingly, a huge degradation in $\gamma\left(N_{\mathrm{N}}\right)$ can be observed. Hence, it should be noted that the OQAM-based schemes introduce a high spread of the useful power in the TF grid, even if this scheme is orthogonal in an unidirectional P2P transmission. More neighbors would be required (also in the FGE in the next section) to collect the same amount of power. The interference terms are not vanishing by the real part operator in (4.34) such that an equalizer should consider the full effective channel matrix without any real part operation at the receiver side.

Finally, Fig. 4.8 indicates the influence on the different MC schemes for different number of neighbors N_{N} with a varying phase shift ϕ^{AB} and fixed TO and CFO ($\Delta\tau^{\mathsf{A}} = 0.1T_{\mathrm{S}}$ and $\Delta\nu^{\mathsf{A}} = 0.1F_0$). Generally, the more neighbors used, the lower the loss $\gamma\left(N_{\mathrm{N}}\right)$. The lowest loss is achieved by the Gaussian waveform in both mapping schemes due to the good localization properties.

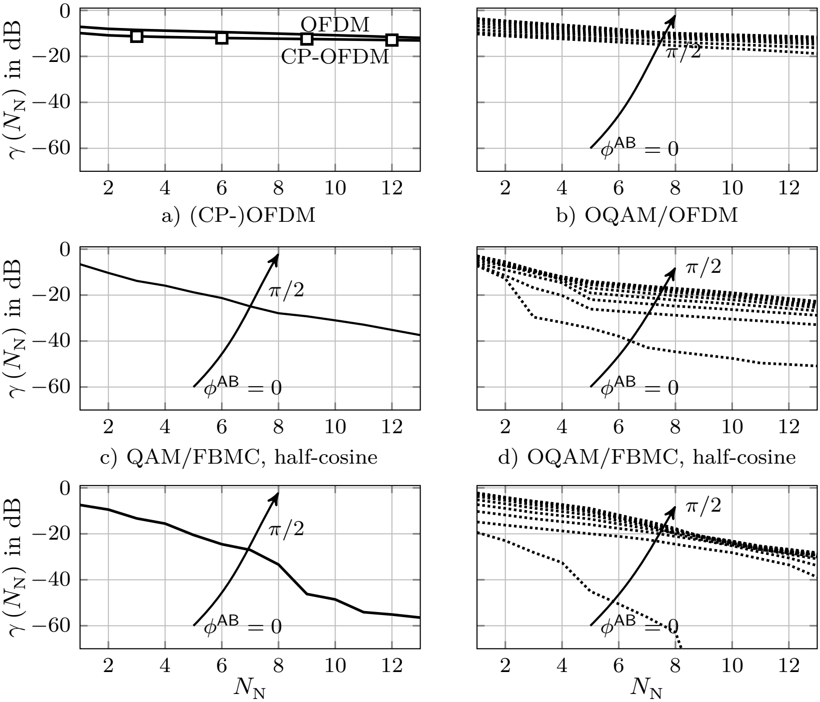

a) (CP-)OFDM b) OQAM/OFDM

c) QAM/FBMC, half-cosine d) OQAM/FBMC, half-cosine

e) QAM/FBMC, Gaussian f) OQAM/FBMC, Gaussian

Figure 4.8: Normalized power loss applying TWRC with the QAM-based (——) and OQAM-based (- - -) FBMC schemes with varying number of N_{N}. Fixed normalized TO $\Delta\tau^{\mathsf{A}}/T_{\mathrm{S}} = 0.1$ and CFO $\Delta\nu^{\mathsf{A}}/F_0 = 0.1$ for varying phase differences $\phi^{\mathsf{AB}} = 0, \frac{1}{10}\frac{\pi}{2}, \frac{2}{10}\frac{\pi}{2}, \ldots, \frac{\pi}{2}$.

It can further be observed, that the QAM-based schemes are independent of the affected phase ϕ^{AB}, thus, all curves are indistinguishable, whereas the OQAM schemes only achieve a low loss with phases differences ϕ^{AB} close to zero. The real-valued orthogonality of OQAM-based MC schemes destroys the good properties in a TWRC. The sensitivity to the unresolvable phase shifts in a TWRC concludes that OQAM-based schemes are not well suited with just one receive antenna at the relay and, thus, not recommended in this setup.

4.3.2 TWRC Detectors

Let us remember the separate signal description (4.5) and (4.6) on page 85, we ask for the connection between the desired PLNC signal part in ① and the joint BC message for the broadcast phase, defined in (4.2) resulting in the mapping function $f_{\mathrm{MA}\rightarrow\mathrm{BC}}(\cdot)$ in (4.3). So, we first focus on the detection of the BC message based on different detection strategies within an **interference-free scenario** besides AWGN, *i.e.* $\overline{\mathbf{\Sigma}}_{\mathbf{H}}^{\mathsf{u}} = \mathbf{0}$, $\mathsf{u} \in \{\mathsf{A}, \mathsf{B}\}$, before we generalize the schemes considering ISI and ICI. The transmission can be seen as synchronized GI-based OFDM transmission without any TO or CFO such that the receive signal per sub-carrier (4.6) can be simplified to

$$y^{\mathsf{R}} = h^{\mathsf{A}} d^{\mathsf{A}} + h^{\mathsf{B}} d^{\mathsf{B}} + \tilde{n}^{\mathsf{R}} \quad , \tag{4.11}$$

omitting the indices of the TF grid to introduce the principle ideas of the detection schemes based on MAP estimation. The focus for finding the MA to BC message function $f_{\mathrm{MA}\rightarrow\mathrm{BC}}(\cdot)$ lies on three different PLNC detection schemes:

I) **Separate channel decoding (SCD)**: The SCD detector first estimates the information streams $\hat{\mathbf{b}}^{\mathsf{A}}$ and $\hat{\mathbf{b}}^{\mathsf{B}}$ of each user separately by considering the other user as interference [WL10]. Afterwards, the relay performs a XOR mapping $\mathbf{b}^{\mathsf{R}} = \hat{\mathbf{b}}^{\mathsf{A}} \oplus \hat{\mathbf{b}}^{\mathsf{B}}$ to generate the BC message.

II) **Joint channel decoding and physical-layer network coding (JCNC)**: Contrarily to SCD, JCNC is a scheme directly estimating the XOR combination by exploiting the linearity of the applied channel codes $\mathbf{b}^{\mathsf{R}} = \hat{\mathbf{b}}^{\mathsf{A}\oplus\mathsf{B}}$ without having any interest on the individual signals of the specific users [ZLL06b].

III) **Generalized joint channel decoding and physical-layer network coding (GJCNC)**: Furthermore, GJCNC is an extension of JCNC interpreting the messages of both users as a joint information tuple $\mathbf{b}^{\mathsf{AB}}$ in a higher Galois field and uses a non-binary decoder [Wüb10, WL10, LW10]. This scheme offers the best performance by the utilization of the fully available underlying information. The message for the BC phase is generated by simply mapping the estimated tuple $\hat{\mathbf{b}}^{\mathsf{AB}}$ to the relay message $\mathbf{b}^{\mathsf{R}}$. The decoder and demapper have to work in higher fields, contrarily to SCD and JCNC.

The block diagrams of all relay processing schemes are given in Fig. 4.9. All schemes share the same first block, *i.e.* the equalizer for the symbol tuple, and differ mainly in the generation of the signals fed to the symbol de-mapper. The gray box determines the detection depending equalizer and will be discussed, subsequently. To clearly understand the different detection schemes, we first identify the principles of the first block, which is the same for all schemes, and then we point out the major differences of SCD, JCNC and GJCNC. We further assume an BPSK mapping with $d^{\mathsf{u}} = (-1)^{c_c^{\mathsf{u}}}$ with code bit index c and set $\mathcal{D}^{\mathsf{u}}_{\mathrm{BPSK}} \in \{1, -1\}$ and cardinality $|\mathcal{D}| = M = 2$ such we can label each symbol by a decimal index $i \in \{0, \ldots, M-1\}$[5]. All possible combinations of the separate code bits c^{A} and c^{B} are given in Table 4.1. It should be noted that also the XORed version $c^{\mathsf{A}\oplus\mathsf{B}} = c^{\mathsf{A}} \oplus c^{\mathsf{B}}$. Furthermore, the code word combination $c^{\mathsf{AB}} = c^{\mathsf{A}} + c^{\mathsf{B}} D$ for BPSK is defined with indeterminate D in a polynomial description as a short hand notation for the four different combination of c^{A} and c^{B} living in the extension field $c^{\mathsf{AB}} \in \mathbb{F}_{2^{N_{\mathsf{u}} \log_2(M)}}$ needed later [Wüb10, WL10, Wu17]. Additionally, all corresponding symbols d^{A}, d^{B}, $d^{\mathsf{A}\oplus\mathsf{B}}$ and an extended symbol tuple d^{AB} are

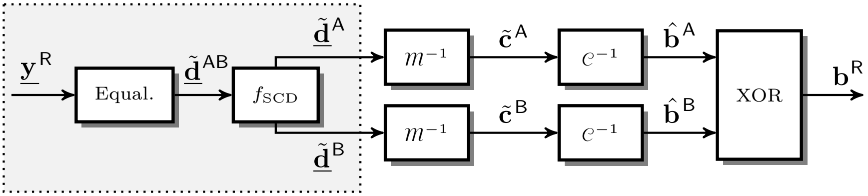

a) SCD

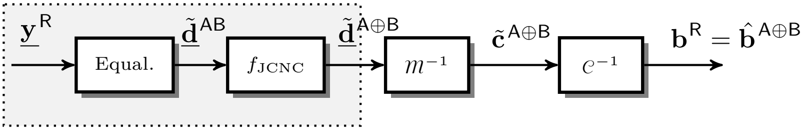

b) JCNC

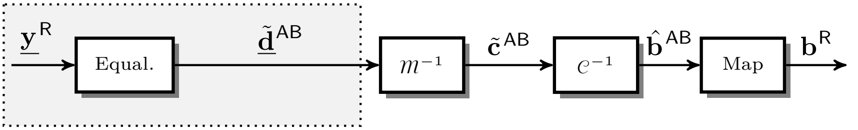

c) GJCNC

Figure 4.9: Relay processing chains for SCD, JCNC and GJCNC related to the mapping function $f_{\mathrm{MA}\to\mathrm{BC}}\left(\underline{\mathbf{y}}^{\mathsf{R}}\right) \to \mathbf{b}^{\mathsf{R}}$. The gray box determines the detection depending equalizer.

---

[5] The corresponding signals and sets for QPSK mapping are given in Appendix C.1

Table 4.1: Possible combinations of code bits, symbols and noise & interference-free receive signals for BPSK with omitted indices.

i	c^{A}	c^{B}	$c^{\mathsf{A}\oplus\mathsf{B}}$	c^{AB}	d^{A}	d^{B}	$d^{\mathsf{A}\oplus\mathsf{B}}$	d^{AB}	noise/interference-free receive signal
0	0	0	0	0	1	1	1	$(1,1)$	$h^{\mathsf{A}} + h^{\mathsf{B}}$
1	1	0	1	1	-1	1	-1	$(-1,1)$	$-h^{\mathsf{A}} + h^{\mathsf{B}}$
2	0	1	1	D	1	-1	-1	$(1,-1)$	$h^{\mathsf{A}} - h^{\mathsf{B}}$
3	1	1	0	$D+1$	-1	-1	1	$(-1,-1)$	$-h^{\mathsf{A}} - h^{\mathsf{B}}$

listed. The superposition of a pair of two M-ary symbols d^{u} result in M^2 different combinations at the relay. This resulting symbol tuple can be read as Cartesian product with $\mathcal{D}^{\mathsf{AB}} = \mathcal{D}^{\mathsf{A}} \times \mathcal{D}^{\mathsf{B}}$ with all pairs

$$\mathcal{D}^{\mathsf{AB}} = \left\{ \left(d^{\mathsf{A}}, d^{\mathsf{B}}\right) \mid d^{\mathsf{A}} \in \mathcal{D}^{\mathsf{A}}, d^{\mathsf{B}} \in \mathcal{D}^{\mathsf{B}} \right\} \quad . \tag{4.12}$$

with cardinality $\left|\mathcal{D}^{\mathsf{AB}}\right| = \left|\mathcal{D}^{\mathsf{A}}\right| \cdot \left|\mathcal{D}^{\mathsf{B}}\right|$. The variable tuple d^{AB} is from the extended set $\mathcal{D}^{\mathsf{AB}}$. The Fig. 4.9 shows the estimates instead of the variables, whereby the variables with tilde, *i.e.* $\tilde{\mathbf{d}}^{\mathsf{u}}$, $\tilde{\mathbf{d}}^{\mathsf{A}\oplus\mathsf{B}}$, $\tilde{\mathbf{d}}^{\mathsf{AB}}$ for the different symbol vectors, $\tilde{\mathbf{c}}^{\mathsf{u}}$, $\tilde{\mathbf{c}}^{\mathsf{A}\oplus\mathsf{B}}$, and $\tilde{\mathbf{c}}^{\mathsf{AB}}$ for the code vectors, correspond to soft estimates and the variables with hat, *i.e.* $\hat{\mathbf{b}}^{\mathsf{u}}$, $\hat{\mathbf{b}}^{\mathsf{A}\oplus\mathsf{B}}$, and $\hat{\mathbf{b}}^{\mathsf{AB}}$ for the information bit vectors, correspond to hard estimates.

Considering the interference-free signal (4.11), the signal plane of an example of the possible transmissions is illustrated in Fig. 4.10. Each filled circle determines one of the possible noise/interference-free receive signal i assuming complex channel coefficients h^{A} and h^{B} also given in Table 4.1 for BPSK. These noise/interference-free receive signal serve as hypotheses in the subsequent detection schemes. The receive signal y^{R} is denoted by a cross ×. The lines in Fig. 4.10a illustrates the Euclidean distance between a hypothesis i and the receive signal y^{R}.

Based on the hypotheses and the receive signal, the task of the detector is to generate a proper choice of the BC message. In the following, we discuss the three different strategies by means of FG-based detection in an interference-free scenario illustrated in Fig. 4.11 to achieve this goal. It should be noted, that in Appendix B the general concept of FG based detection/equalization is briefly discussed and is the basis of the following part.

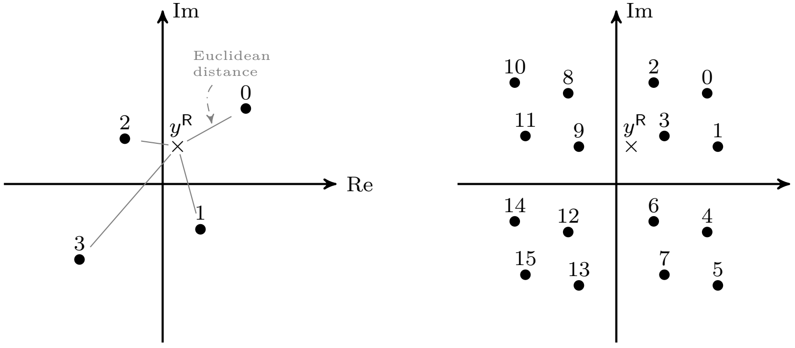

a) BPSK b) QPSK

Figure 4.10: Receive signal plane, with possible hypotheses corresponding to the labels i in Table 4.1 for BPSK and Table C.1 for QPSK.

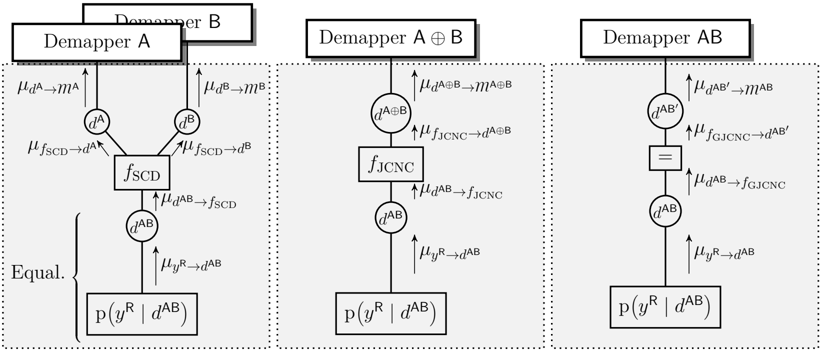

a) SCD b) JCNC c) GJCNC

Figure 4.11: Factor graphs for interference-free transmission of all detection schemes considered [HZ11, WHZW13] with just a few important messages displayed for simplicity's sake. Furthermore, the argument and the indices are omitted due to readability.

I) Separate Channel Decoding

Within SCD the basic idea already drawn in Fig. 4.9 is to detect the individual streams for each user $\hat{\mathbf{b}}^{\mathsf{u}}, \mathsf{u} \in \{\mathsf{A}, \mathsf{B}\}$ separately and perform an XOR combination afterwards such that a joint information word $\mathbf{b}^{\mathsf{R}} = \hat{\mathbf{b}}^{\mathsf{A}} \oplus \hat{\mathbf{b}}^{\mathsf{B}}$ is generated. This BC information word is then encoded with an encoding scheme $\mathcal{C}$ and mapped to a complex symbol by a mapping scheme $\mathcal{M}$ and further processed by a MC scheme such that a BC transmit signal

$x^{\mathsf{R}}(t) = \mathrm{MC}(\mathcal{M}(\mathcal{C}(\mathbf{b}^{\mathsf{R}})))$ is generated. In this work, a bit-by-bit MAP detection for each bit b^{u}_{ϖ}, $\varpi = 0, \ldots, N_{\mathbf{b}} - 1$ given by

$$\hat{b}^{\mathsf{u}}_{\varpi} = \arg\max_{b^{\mathsf{u}}_{\varpi}\in\mathbb{F}_2} \mathrm{p}\left(b^{\mathsf{u}}_{\varpi} \mid \underline{\mathbf{y}}^{\mathsf{R}}\right) \tag{4.13}$$

is used. As we will introduce in the Appendix B, we use the SPA working on a FG to solve the marginalization needed for (4.13). According to Section B.2.1, the MAP detector (4.13) can be factorized into

$$\begin{aligned}\hat{b}^{\mathsf{u}}_{\varpi} = \arg\max_{b^{\mathsf{u}}_{\varpi}\in\mathbb{F}_2} \underbrace{\Pr\left(b^{\mathsf{u}}_{\varpi}\right)}_{\text{a priori}} \Bigg[\sum_{\sim\{b^{\mathsf{u}}_{\varpi}\}} & \underbrace{\mathrm{p}\left(\underline{\mathbf{y}}^{\mathsf{R}}|\underline{\mathbf{d}}^{\mathsf{AB}}\right)\mathrm{p}\left(\underline{\mathbf{d}}^{\mathsf{AB}}|\underline{\mathbf{d}}^{\mathsf{u}}\right)}_{\text{Equalizer}} \\ \cdot \underbrace{\mathrm{p}(\underline{\mathbf{d}}^{\mathsf{u}}|\mathbf{c}^{\mathsf{u}})}_{\text{Mapping}} \underbrace{\mathrm{p}(\mathbf{c}^{\mathsf{u}}|b^{\mathsf{u}}_{\varpi})}_{\text{Encoding}} & \underbrace{\prod_{\iota\backslash\varpi} \Pr\left(b^{\mathsf{u}}_{\iota}\right)}_{\mu_{b^{\mathsf{u}}_{\iota}\to\mathrm{Est.}}(b^{\mathsf{u}}_{\iota})} \Bigg].\end{aligned} \tag{4.14}$$

The equalizer part in (4.14) is factorized into the relation between observation and superimposed symbol tuple d^{AB} by $\mathrm{p}(\underline{\mathbf{y}}^{\mathsf{R}}|\underline{\mathbf{d}}^{\mathsf{AB}})$ and the likelihood $\mathrm{p}(\underline{\mathbf{d}}^{\mathsf{AB}}|\underline{\mathbf{d}}^{\mathsf{u}})$ connects the superimposed symbol d^{AB} with the user specific symbol d^{u} for a user u. The corresponding FGE is drawn in Fig. 4.11a for an interference-free transmission (4.11) [**WWD16, WWD18**]. Similar to the approach in Appendix B with the factorization of the equalizer in (B.12), the underlying structure of the function blocks are opened. The message from the observation factor node to the variable node $\mu_{y^{\mathsf{R}}\to d^{\mathsf{AB}}}\left(d^{\mathsf{AB}}\right)$ is an extension of (B.17) defined for the unidirectional P2P case. Here, the variable tuple d^{AB} is used with the larger set $\mathcal{D}^{\mathsf{AB}}$ in comparison to a unidirectional P2P transmission. Thus, without any interference, this message can be calculated like[6]

$$\mu_{y^{\mathsf{R}}\to d^{\mathsf{AB}}}\left(d^{\mathsf{AB}}\right) \propto \mathrm{p}\left(y^{\mathsf{R}} \mid d^{\mathsf{AB}}\right) \tag{4.15}$$

where the likelihood is related like

$$\mathrm{p}\left(y^{\mathsf{R}} \mid d^{\mathsf{AB}}\right) \propto \exp\left(\frac{\left|y^{\mathsf{R}} - h^{\mathsf{A}}d^{\mathsf{A}} - h^{\mathsf{B}}d^{\mathsf{B}}\right|^2}{\sigma_{\mathrm{n}}^2}\right) \quad . \tag{4.16}$$

Hence, this detection scheme is directly related to the APP-based schemes applied in [Wüb10, WL10, WWD13b].

---

[6] This calculation is a special case of an interference-free transmission with AWGN, the general equation (4.6) is related to (B.12)

As introduced in Appendix B, the dimension of a message is related to the cardinality of the variable connected, *e.g.* for a discrete M-ary modulated symbol, describable by an M-ary vector with M entries. From a connected node perspective, each entry in this vector denotes the probability of the specific symbol transmitted. The message dimension of $\mu_{d^{\mathsf{AB}}\to f_{\mathrm{SCD}}}\left(d^{\mathsf{AB}}\right)$ is related to the variable d^{AB} and, thus, of cardinality M^2. We introduce a PLNC helping factor node f_{SCD}, generating the symbol tuple $d^{\mathsf{AB}} = \left(d^{\mathsf{A}}, d^{\mathsf{B}}\right)$, also given in Fig. 4.11a. Related to the notation in [Wym07], this function can be expressed by $f_{\mathrm{SCD}}\left(D^{\mathsf{A}} = d^{\mathsf{A}}, D^{\mathsf{B}} = d^{\mathsf{B}}\right) = \delta(D^{\mathsf{A}} - d^{\mathsf{A}})\delta(D^{\mathsf{B}} - d^{\mathsf{B}})$. The mapping gets more important in the interference afflicted case and will be discussed later on. To extract the useful part needed for user A, we calculate the marginal distribution $\mathrm{p}(\underline{\mathbf{d}}^{\mathsf{AB}}|\underline{\mathbf{d}}^{\mathsf{A}})$ related to (4.14) *w.r.t.* user A. This marginalization is done by the introduced helping function node f_{SCD} and works for user A like

$$\begin{aligned}\mu_{f_{\mathrm{SCD}}\to d^{\mathsf{A}}}\left(d^{\mathsf{A}}\right) =& \sum_{\sim\{d^{\mathsf{A}}\}} \Big[\delta(D^{\mathsf{A}} - d^{\mathsf{A}})\delta(D^{\mathsf{B}} - d^{\mathsf{B}}) \\ &\qquad \cdot \mu_{d^{\mathsf{AB}}\to f_{\mathrm{SCD}}}\left((d^{\mathsf{A}}, d^{\mathsf{B}})\right)\mu_{d^{\mathsf{B}}\to f_{\mathrm{SCD}}}\left(d^{\mathsf{B}}\right)\Big] \qquad (4.17a)\\ =& \sum_{i\in\mathcal{D}_{\mathrm{SCD}}^{D^{\mathsf{A}}=d^{\mathsf{A}}}} \mu_{d^{\mathsf{AB}}\to f_{\mathrm{SCD}}}\left(D^{\mathsf{AB}} \equiv i\right)\mu_{d^{\mathsf{B}}\to f_{\mathrm{SCD}}}\left(d^{\mathsf{B}}\right) \quad , \qquad (4.17b)\end{aligned}$$

The message in (4.17a) can be rewritten to (4.17b), where $\mathcal{D}_{\mathrm{SCD}}^{D^{\mathsf{A}}=d^{\mathsf{A}}}$ is the set of indices for a fixed realization $D^{\mathsf{A}} = d^{\mathsf{A}}$ and all possible realizations of the symbol of the other user defined by

$$\mathcal{D}_{\mathrm{SCD}}^{D^{\mathsf{A}}=d^{\mathsf{A}}} = \left\{i \mid D^{\mathsf{A}} = d^{\mathsf{A}}\right\} \quad . \qquad (4.18)$$

The expression “$D^{\mathsf{AB}} \equiv i$” in (4.17) corresponds to that symbol tuple of line i in Table 4.1 on page 93. For example, by the application of BPSK, the $M = 2$ available sets for user A are $\mathcal{D}_{\mathrm{SCD}}^{D^{\mathsf{A}}=1} = \{0, 2\}$ for $D^{\mathsf{A}} = 1$ and $\mathcal{D}_{\mathrm{SCD}}^{D^{\mathsf{A}}=-1} = \{1, 3\}$ for $D^{\mathsf{A}} = -1$. Equation (4.17) is equivalent for user B. For $D^{\mathsf{B}} = 1$ the set is $\mathcal{D}_{\mathrm{SCD}}^{D^{\mathsf{B}}=1} = \{0, 1\}$ and for $D^{\mathsf{B}} = -1$ the set is $\mathcal{D}_{\mathrm{SCD}}^{D^{\mathsf{B}}=-1} = \{2, 3\}$. Corresponding sets for QPSK can be found in Appendix C.1. The messages for user A and B are further processed by single-user SotA demapping and decoding strategies in $\mathbb{F}_2$. After estimating $\hat{\mathbf{b}}^{\mathsf{A}}$ and $\hat{\mathbf{b}}^{\mathsf{B}}$, the BC message $\mathbf{b}^{\mathsf{R}} = \hat{\mathbf{b}}^{\mathsf{A}} \oplus \hat{\mathbf{b}}^{\mathsf{B}}$ is generated and broadcast to the users.

II) Joint Channel Decoding and Physical-Layer Network Coding

Ultimately, the relay's goal is to generate one common message for the BC phase. Thus, it is not interested in the individual messages of each user, but in the joint PLNC message. Zhang *et al.*proposed to simplify the detection to just one single stream directly based on the XOR combination $\mathbf{b}^{\mathsf{A}\oplus\mathsf{B}}$ in [ZLL06b]. Or, in other words, the relay directly detects the BC message

$$\mathbf{b}^{\mathsf{R}} = \mathbf{b}^{\mathsf{A}\oplus\mathsf{B}} = \mathbf{b}^{\mathsf{A}} \oplus \mathbf{b}^{\mathsf{B}} \quad . \tag{4.19}$$

We use the terminology $\mathbf{b}^{\mathsf{A}\oplus\mathsf{B}}$ to distinguish from SCD and GJCNC. The corresponding symbol set is described by

$$\mathcal{D}^{\mathsf{A}\oplus\mathsf{B}} = \left\{\mathcal{M}(c^{\mathsf{A}} \oplus c^{\mathsf{B}}) \mid \mathcal{M}(c^{\mathsf{A}}) \in \mathcal{D}^{\mathsf{A}}, \mathcal{M}(c^{\mathsf{B}}) \in \mathcal{D}^{\mathsf{B}}\right\}, \tag{4.20}$$

with the XOR symbol $d^{\mathsf{A}\oplus\mathsf{B}} = \mathcal{M}(c^{\mathsf{A}} \oplus c^{\mathsf{B}})$ (also given in Table 4.1 and Table C.1) which lies also in the set of $\mathcal{D}^{\mathsf{A}\oplus\mathsf{B}} = \mathcal{D}^{\mathsf{u}}$ of a single user due to its linearity. This approach leads to a reduced structure compared to SCD in the relay by only one processing chain for the combined data stream as illustrated in Fig. 4.9b. In the AWGN case, *i.e.* $h^{\mathsf{A}} = 1$ and $h^{\mathsf{B}} = 1$ (*i.e.* in the time continuous domain $w^{\mathsf{A}}(\tau) = w^{\mathsf{B}}(\tau) = \delta(\tau)$), this detection scheme leads to a receive signal (4.11) with a reduced number of hypotheses, *e.g.* with BPSK the hypotheses are -2,0,2 as illustrated in Fig. 4.12a (in other words the hypotheses $i = 1$ and $i = 2$ overlay in the signal plane). Without detecting the separate signals, the BC message can be directly estimated.

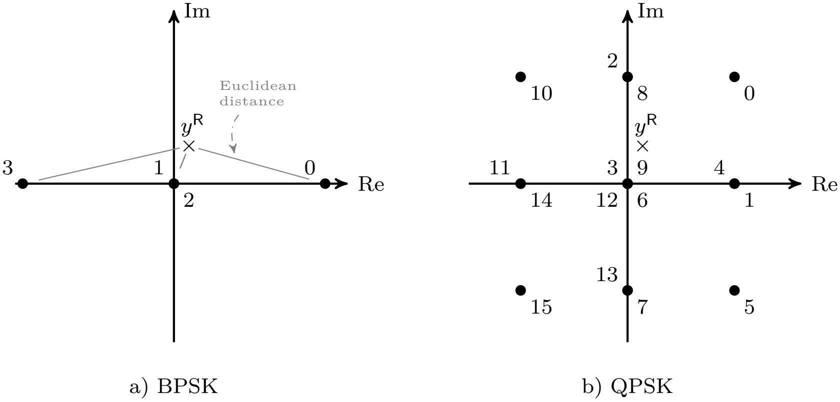

a) BPSK b) QPSK

Figure 4.12: Receive signal plane, with possible hypotheses corresponding to the labels i in Table 4.1 for BPSK and Table C.1 for QPSK with a AWGN channel, *i.e.* $h^{\mathsf{A}} = 1$ and $h^{\mathsf{B}} = 1$.

So, if the receive signal y_r^{R} is close in terms of Euclidean distance to the hypotheses $i = 0, i = 3$ it is highly probable that the underlying XOR code bit is $c^{\mathsf{A}\oplus\mathsf{B}} = 0$ and close to $i = 1, i = 2$ the joint code is $c^{\mathsf{A}\oplus\mathsf{B}} = 1$ (see Tab. 4.1). This principle works similarly for QPSK as illustrated in Fig. 4.12b with the related code bits listed in Table C.1. However, with more general channels (phase shift, TO, *etc.*) more hypotheses are possible, *cf.* Fig. 4.10b, which reduces the detection performance of JCNC. The corresponding MAP approach reads

$$\hat{b}_{\varpi}^{\mathsf{A}\oplus\mathsf{B}} = \underset{b_{\varpi}^{\mathsf{A}\oplus\mathsf{B}} \in \mathbb{F}_2}{\arg\max}\ \mathrm{p}\left(b_{\varpi}^{\mathsf{A}\oplus\mathsf{B}} \mid \underline{\mathbf{y}}^{\mathsf{R}}\right) \tag{4.21}$$

with information bit index $\varpi = 0, \ldots, N_{\mathbf{b}} - 1$ and can be factorized into

$$\begin{aligned}\hat{b}_{\varpi}^{\mathsf{A}\oplus\mathsf{B}} = \underset{b_{\varpi}^{\mathsf{A}\oplus\mathsf{B}} \in \mathbb{F}_2}{\arg\max}\ \underbrace{\mathrm{Pr}\left(b_{\varpi}^{\mathsf{A}\oplus\mathsf{B}}\right)}_{\text{a priori}} \Bigg[\sum_{\sim\left\{b_{\varpi}^{\mathsf{A}\oplus\mathsf{B}}\right\}} \underbrace{\mathrm{p}\left(\underline{\mathbf{y}}^{\mathsf{R}} | \underline{\mathbf{d}}^{\mathsf{A}\oplus\mathsf{B}}\right) \mathrm{p}\left(\underline{\mathbf{d}}^{\mathsf{AB}} | \underline{\mathbf{d}}^{\mathsf{A}\oplus\mathsf{B}}\right)}_{\text{Equalizer}} \\ \cdot \underbrace{\mathrm{p}\left(\underline{\mathbf{d}}^{\mathsf{A}\oplus\mathsf{B}} | \mathbf{c}^{\mathsf{A}\oplus\mathsf{B}}\right)}_{\text{Demapper}} \underbrace{\mathrm{p}\left(\mathbf{c}^{\mathsf{A}\oplus\mathsf{B}} | b_{\varpi}^{\mathsf{A}\oplus\mathsf{B}}\right)}_{\text{Decoder}} \prod_{\iota \backslash \varpi} \mathrm{Pr}\left(b_{\iota}^{\mathsf{A}\oplus\mathsf{B}}\right) \Bigg] \quad . \end{aligned} \tag{4.22}$$

Similar to SCD, where the processing in the symbol demapper and decoder are based on the message dimension of $|M|$, the JCNC detection scheme also works in this domain. Thus, it has to perform a marginalization on the equalizer messages to reduce the signal space to allow further processing. According to [**WWD18**], this can be done by a function $f_{\mathrm{JCNC}} = \delta\left(D^{\mathsf{A}\oplus\mathsf{B}} - d^{\mathsf{A}\oplus\mathsf{B}}\right)$ (related to $\mathrm{p}(\underline{\mathbf{d}}^{\mathsf{AB}} | \underline{\mathbf{d}}^{\mathsf{A}\oplus\mathsf{B}})$ in (4.22)), which maps the variable tuple set $\mathcal{D}^{\mathsf{AB}}$ to the XORed combined space $\mathcal{D}^{\mathsf{A}\oplus\mathsf{B}}$. The function is illustrated in Fig. 4.11b as block f_{JCNC} between d^{AB} and $d^{\mathsf{A}\oplus\mathsf{B}}$. The message from the function f_{JCNC} to the XORed symbol $d^{\mathsf{A}\oplus\mathsf{B}}$ is calculated by

$$\mu_{f_{\mathrm{JCNC}} \to d^{\mathsf{A}\oplus\mathsf{B}}}\left(d^{\mathsf{A}\oplus\mathsf{B}}\right) = \sum_{\sim\left\{d^{\mathsf{A}\oplus\mathsf{B}}\right\}} \delta\left(D^{\mathsf{A}\oplus\mathsf{B}} - d^{\mathsf{A}\oplus\mathsf{B}}\right) \mu_{d^{\mathsf{AB}} \to f_{\mathrm{JCNC}}}\left(\left(d^{\mathsf{A}}, d^{\mathsf{B}}\right)\right) \tag{4.23a}$$

$$= \sum_{q \in \mathcal{D}_{\mathrm{JCNC}}^{D^{\mathsf{A}\oplus\mathsf{B}} = d^{\mathsf{A}\oplus\mathsf{B}}}} \mu_{d^{\mathsf{AB}} \to f_{\mathrm{JCNC}}}\left(D^{\mathsf{A}\oplus\mathsf{B}} \equiv q\right) \quad . \tag{4.23b}$$

Similar to the SCD case (4.17), the message from the JCNC function to the in (4.23a) can be rewritten to (4.23b), where the set $\mathcal{D}_{\mathrm{JCNC}}^{D^{\mathsf{A}\oplus\mathsf{B}} = d^{\mathsf{A}\oplus\mathsf{B}}}$ is given by

$$\mathcal{D}_{\mathrm{JCNC}}^{D^{\mathsf{A}\oplus\mathsf{B}} = d^{\mathsf{A}\oplus\mathsf{B}}} = \left\{ i \mid D^{\mathsf{A}\oplus\mathsf{B}} = d^{\mathsf{A}\oplus\mathsf{B}} \right\} \quad . \tag{4.24}$$

and contains all possible combinations i for a fixed $D^{\mathsf{A}\oplus\mathsf{B}} = d^{\mathsf{A}\oplus\mathsf{B}}$ from Table 4.1 for BPSK or Table C.1 for QPSK.

For instance, for $D^{\mathsf{A}\oplus\mathsf{B}} = 1$ the set is $\mathcal{D}_{\text{JCNC}}^{D^{\mathsf{A}\oplus\mathsf{B}}=1} = \{0, 3\}$ and for $D^{\mathsf{A}\oplus\mathsf{B}} = -1$ the set is $\mathcal{D}_{\text{JCNC}}^{D^{\mathsf{A}\oplus\mathsf{B}}=-1} = \{1, 2\}$. For the corresponding QPSK mapping we refer to Appendix C.1. The message (4.23) is further processed by just one joint SotA demapper and decoder in $\mathbb{F}_2$ as introduced in Chapter 2. The estimate $\hat{\mathbf{b}}^{\mathsf{A}\oplus\mathsf{B}}$ is directly mapped as BC message $\mathbf{b}^{\mathsf{R}} = \hat{\mathbf{b}}^{\mathsf{A}\oplus\mathsf{B}}$ and transmitted in the BC phase.

III) Generalized Joint Channel Decoding and Physical-Layer Network Coding

Both schemes, *i.e.* SCD and JCNC, reduce the possible variable space $\mathcal{D}^{\mathsf{AB}}$ in an early state of the detection process, *i.e.* directly after the equalizer either to $\mathcal{D}^{\mathsf{u}}$ or to $\mathcal{D}^{\mathsf{A}\oplus\mathsf{B}}$. This leads to the loss of information[LLZ15]. Especially, the aforementioned detection schemes are not fully able to utilize the underlying information by this reduction. The authors in [ZL09, LWK10, LW10] propose as solution the extension with a “virtual decoder” (an adopted decoder) at the relay based on the arithmetic-sum algorithm for AWGN channels with just three hypotheses for BPSK or nine for QPSK. The authors in [WL10, Wüb10] further generalize this idea by the use the virtual decoder with the “hypotheses” mentioned in Table 4.1 and Table C.1 working on the noise/interference-free receive signals as hypotheses, which offers the decoding also in Rayleigh fading channels. Therefore, the method mentioned in [WL10, Wüb10] extends the virtual decoder working on variable tuples like c^{AB} in extension fields to the Galois field $\mathbb{F}_{2^{2\log_2(M)}}$.

The corresponding MAP approach is

$$\hat{b}_{\varpi}^{\mathsf{AB}} = \underset{b_{\varpi}^{\mathsf{AB}} \in \mathbb{F}_{2^{N_{\mathsf{u}} \log_2(M)}}}{\arg\max} \; \mathrm{p}\left(b_{\varpi}^{\mathsf{AB}} \mid \mathbf{y}^{\mathsf{R}}\right) \tag{4.25}$$

with information bit index $\varpi = 0, \ldots, N_{\mathbf{b}} - 1$ and it can be factorized into

$$\begin{aligned} \hat{b}_{\varpi}^{\mathsf{AB}} = \underset{b_{\varpi}^{\mathsf{AB}} \in \mathbb{F}_{2^{N_{\mathsf{u}} \log_2(M)}}}{\arg\max} \; & \underbrace{\Pr\left(b_{\varpi}^{\mathsf{AB}}\right)}_{\text{a priori}} \Bigg[\sum_{\sim\{b_{\varpi}^{\mathsf{AB}}\}} \underbrace{\mathrm{p}\left(\underline{\mathbf{y}}^{\mathsf{R}} | \underline{\mathbf{d}}^{\mathsf{AB}}\right)}_{\text{Equalizer}} \\ & \cdot \underbrace{\mathrm{p}\left(\underline{\mathbf{d}}^{\mathsf{AB}} | \mathbf{c}^{\mathsf{AB}}\right)}_{\text{Demapping}} \underbrace{\mathrm{p}\left(\mathbf{c}^{\mathsf{AB}} | b_{\varpi}^{\mathsf{AB}}\right)}_{\text{Decoder}} \prod_{\iota \setminus \varpi} \Pr\left(b_{\iota}^{\mathsf{AB}}\right) \Bigg] \end{aligned} \tag{4.26}$$

The advantage of this detection scheme is the direct use of the message $\mu_{y^{\mathsf{R}} \to d^{\mathsf{AB}}}\left(d^{\mathsf{AB}}\right)$ in the demapping and decoding process such that no marginalization function f_{GJCNC} is required as illustrated in Fig. 4.11c. Furthermore, in GJCNC each code bit tuple c^{AB} is directly related to just one symbol d^{AB} due to the extension to a higher Galois field as exemplary illustrated in Tab. 4.1 for the BPSK mapping. Nevertheless, we introduce the mapping function f_{GJCNC} to unify the description of the SPA *w.r.t.* all other detection schemes later on. The mapping function should not change the properties of the connected variables so we introduce the mapping function f_{GJCNC} as equal factor node denoted by $\boxed{=}$ which can be described by $f_{\mathrm{GJCNC}} = \delta(D^{\mathsf{AB}'} - d^{\mathsf{AB}'})\delta(D^{\mathsf{AB}} - d^{\mathsf{AB}})$, where $\delta(\cdot)$ is the dirac distribution [KK18]. By the application of this node the messages from and to this node results in $\mu_{f_{\mathrm{GJCNC}} \rightarrow d^{\mathsf{AB}'}}(d^{\mathsf{AB}'}) = \mu_{d^{\mathsf{AB}} \rightarrow f_{\mathrm{GJCNC}}}(d^{\mathsf{AB}})$ [Wym07].

TWRC Detector Summary

Table 4.2: Overview of different detection schemes

	SCD	JCNC	GJCNC
Detection	separate	joint	joint
Complexity	➵	➴	➶
Set	$\mathcal{D}^{\mathsf{A}}$ & $\mathcal{D}^{\mathsf{B}}$	$\mathcal{D}^{\mathsf{A}\oplus\mathsf{B}}=\mathcal{D}^{\mathsf{u}}$	$\mathcal{D}^{\mathsf{AB}}$
Symbols	d^{A} & d^{B}	$d^{\mathsf{A}\oplus\mathsf{B}}$	d^{AB}
Code bits	c^{A} & c^{B}	$c^{\mathsf{A}\oplus\mathsf{B}}$	c^{AB}
Info bits	b^{A} & b^{B}	$b^{\mathsf{A}\oplus\mathsf{B}}$	b^{AB}
Broadcast Mes.	$b^{\mathsf{R}} = b^{\mathsf{A}} \oplus b^{\mathsf{B}}$	$b^{\mathsf{R}} = b^{\mathsf{A}\oplus\mathsf{B}}$	$b^{\mathsf{AB}} \rightarrow b^{\mathsf{R}}$
Field	$N_{\mathsf{u}} \times \mathbb{F}_2$	$N_{\mathsf{u}}/2 \times \mathbb{F}_2$	$N_{\mathsf{u}}/2 \times \mathbb{F}_{2^{N_{\mathsf{u}}\log_2(M)}}$
Marginalization	✓	✓	✗

So far, we have seen that we can use three different PLNC detection schemes ($f_{\mathrm{MA}\rightarrow\mathrm{BC}}\left(\mathbf{y}^{\mathsf{R}}\right) \rightarrow \mathbf{b}^{\mathsf{R}}$) in the **interference-free scenario** based on the PLNC signal part ① in (4.6). The main differences are illustrated in Fig. 4.9 and Fig. 4.11 and are summarized in Table 4.2. We need two detection chains for SCD and have a reduction to one for JCNC. However, in both cases, we marginalize the available information to match the message dimension needed. Contrarily, the full available message space can be used by GJCNC, but a decoder working in extension fields is necessary.

In the next section, we first give the KPIs for the performance measurements in a TWRC setup. Then, we show first results related to the considered detection schemes with AWGN channels and with phase affected channels to show the impact related to the PLNC detection schemes, before we adapt the FG to general MC schemes and general channels.

4.4 Channel Impacts on TWRC Detectors

Before we generalize the two-phase TWRC system *w.r.t.* general channels, we want to have a deeper understanding of the underlying challenges of a TWR communication. Thus, we start the performance analysis of the TWRC detectors in a synchronous setup by means of numerical simulations. Thereafter, we look at asynchronous setup and provide an analysis *w.r.t.* the introduced interference power.

Key Performance Indicators The MA phase is the crucial part in the two-phase TWRC communication and we restrict ourselves on the inference of the relay message $\hat{b}^{\mathsf{R}}$ at the relay. Thus, we focus on the instantaneous bit error rate (BER) of frame q at the relay like

$$\mathrm{BER}_{\mathrm{Relay}}\left(q\right)=\frac{N_{\text{Bit-Errors}}\left(q\right)}{N_{\mathbf{b}}}, \tag{4.27}$$

where

$$N_{\text{Bit-Errors}}\left(q\right)=\sum_{\substack{\hat{b}^{\mathsf{R}}_{\varpi}\neq b^{\mathsf{A}}_{\varpi}\oplus b^{\mathsf{B}}_{\varpi}\\ \varpi=0}}^{N_{\mathbf{b}}-1}1 \tag{4.28}$$

is the number of errors of a transmission of $N_{\mathbf{b}}$ bits per user in frame q. Furthermore, the mean BER at the relay is defined like

$$\overline{\mathrm{BER}}_{\mathrm{Relay}}=\frac{1}{N_{\mathrm{Frames}}}\sum_{q=1}^{N_{\mathrm{Frames}}}\mathrm{BER}_{\mathrm{Relay}}\left(q\right) \tag{4.29}$$

and the mean FER at the relay is defined as

$$\overline{\mathrm{FER}}_{\mathrm{Relay}}=\frac{N_{\text{Frame-Errors}}}{N_{\mathrm{Frames}}}, \tag{4.30}$$

where

$$N_{\text{Frame-Errors}}=\sum_{\substack{\mathrm{BER}_{\mathrm{Relay}}(q)>0\\ q=0}}^{N_{\mathrm{Frames}}-1}1 \tag{4.31}$$

is the number of frames with errors.

Finally, the effective throughput assuming a selective-repeat automatic repeat request (ARQ) [**WWD+13, WWD+14**] protocol is defined as

$$\eta_{\mathrm{eff}}=\eta\left(1-\overline{\mathrm{FER}}_{\mathrm{Relay}}\right)\quad . \tag{4.32}$$

with the bandwidth efficiency η defined in (3.6) depending on MC, mapping and encoding schemes. In contrast to the bandwidth η to the effective throughput considers also the success of the transmission.

Table 4.3: Overview of the basic setup parameters

Name	variable	value
# sub-carriers	N_{SC}	72
# time symbols	N_{TS}	14
# complex symbols per user	$N_{\mathbf{d}}$	1008
Mapping scheme cardinality	M	2 (BPSK), 4 (QPSK)
# code bits per frame	$N_{\mathbf{c}}$	1008, 2016
# info bits per frame	$N_{\mathbf{b}}$	302, 605
# guard interval symbols	N_{GI}	8
Code rate	R_{c}	0.3
Bandwidth efficiency	η^{scheme}	0.27, 0.54
Encoding scheme	LDPC	regular check degree of 3, parity-check matrix by [HEA05]

Basic Setup The basic setup in this chapter is related to the parameters in Table 4.3. We use a MC scheme with $N_{\mathrm{SC}} = 72$ sub-carriers and $N_{\mathrm{TS}} = 14$ time symbols. This configuration is related to the $B = 1.4\mathrm{MHz}$ configuration of an LTE setup [STB11]. In contrast to LTE, here we use an LDPC encoding scheme with a code rate of $R_{\mathrm{c}} = 0.3$. The mapping is either BPSK with $M = 2$ different symbols or QPSK with $M = 4$ different symbols per user. Initially, we assume the application of CP-OFDM with a GI length $T_{\mathrm{GI}} = 0.1T_{\mathrm{S}}$ resulting in a bandwidth efficiency $\eta = \varrho\delta_{\mathrm{LD}}(\Lambda)$, of either $\eta^{\mathrm{BPSK}} = 0.27$ for BPSK or $\eta^{\mathrm{QPSK}} = 0.54$ for QPSK.

4.4.1 Performance Analysis of the PLNC Detection Schemes in Orthogonal Transmissions

An analysis with an AWGN channel ($w^{\mathsf{A}}(\tau) = w^{\mathsf{B}}(\tau) = \delta(\tau)$) was done in [ZLL06b]. It was shown that SCD and JCNC suffer from the superposition in (4.11) resulting in only three different hypotheses, *i.e.* -2,0,2, whereas GJCNC outperforms the others in this case. Assuming the controllability over the phase terms per user similar to the analysis in [WWD13a] and [WL10], the effective channels coefficients results in $h^{\mathsf{A}} = e^{j\phi^{\mathsf{A}}}$ and $h^{\mathsf{B}} = e^{j\phi^{\mathsf{B}}}$ which results in an effective phase difference $\phi^{\mathsf{AB}} = \phi^{\mathsf{A}} - \phi^{\mathsf{B}}$ at the relay.

Here, we recap these results already presented in the mentioned publications as benchmark for asynchronous analysis, hereafter.

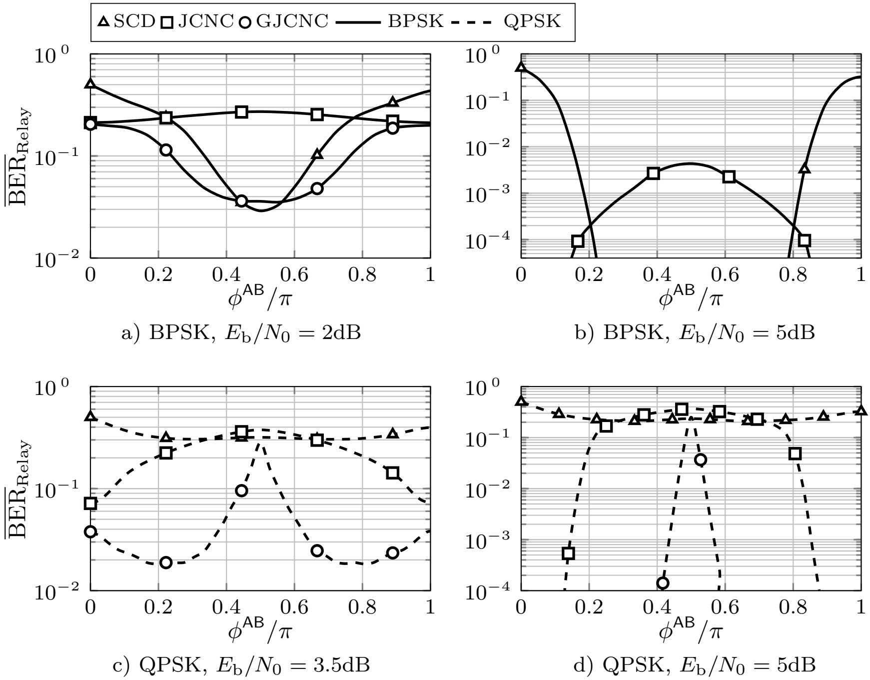

a) BPSK, $E_\mathrm{b}/N_0 = 2\mathrm{dB}$

b) BPSK, $E_\mathrm{b}/N_0 = 5\mathrm{dB}$

c) QPSK, $E_\mathrm{b}/N_0 = 3.5\mathrm{dB}$

d) QPSK, $E_\mathrm{b}/N_0 = 5\mathrm{dB}$

Figure 4.13: BER performance at the relay over the phase difference ϕ^{AB} with an LDPC encoding scheme with $R_\mathrm{c} = 0.3$.

Analysis of Channel Phase Differences Fig. 4.13 shows the mean BER performance $\overline{\mathrm{BER}}_{\mathrm{Relay}}$ over the phase difference ϕ^{AB} for all schemes with an SNR of $E_\mathrm{b}/N_0 = 2\mathrm{dB}$ and $E_\mathrm{b}/N_0 = 5\mathrm{dB}$ for BPSK and $E_\mathrm{b}/N_0 = 3.5\mathrm{dB}$ and $E_\mathrm{b}/N_0 = 5\mathrm{dB}$ for QPSK at the relay also considered in [WL10, Wu17, Min15] and [**WZWD16**]. It can be observed, that all three schemes are sensitive to phase rotations as indicated above. JCNC has the best performance, if no phase rotation takes place due to direct mapping to the BC message as mentioned in Section 4.3.2. But, it suffers from the rotation leading to an increased number of possible hypotheses and, hence, an ambiguous mapping. Especially with BPSK and a phase rotation of $\phi^{\mathsf{AB}} = \frac{1}{2}\pi$, $\frac{3}{2}\pi$ JCNC performs worst. In these cases, SCD and GJCNC have a better BER performances at the relay, since the hypotheses of the symbol tuples do not overlap in the signal plane (*cf.* Fig. 4.12 and Fig. 4.10). The separation of both users is easier for the SCD case and also GJCNC works significantly better than JCNC due to the good separation of all different hypotheses. If the users use higher order symbol mapping like QPSK, the possible hypotheses superimpose also to a reduced set (from 16 possible symbols to 9). Here, JCNC works well, if the phase rotation is $\phi^{\mathsf{AB}} = 0$ or $\phi^{\mathsf{AB}} = \pi$, but degrades with a phase rotation up to $\phi^{\mathsf{AB}} = \pi/2$. GJCNC suffers also from the phase rotation. However, it performs best for a broad range of phase differences.

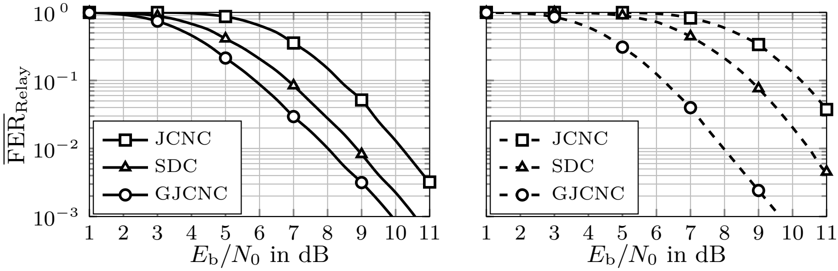

a) BPSK b) QPSK

Figure 4.14: Average FER performance at the relay for BPSK and QPSK for a synchronized CP-OFDM transmission with a delay spread fully captured in the CP.

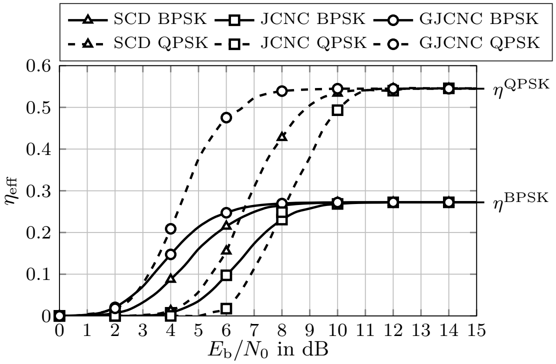

Figure 4.15: Throughput performance relay for BPSK and QPSK.

Performance Analysis In general, the phases of channels h^{u} cannot be controlled. Assuming typically Rayleigh fading channels (2.13), the phase are usually uniformly distributed within $\phi^{\mathsf{u}} \in [0, 2\pi[$, [XCT$^+$11, WWD13a, Wu17]. In Fig. 4.14 the average FER performance at the relay is shown for the three different detection schemes. It can be observed that SCD and GJCNC outperforms the JCNC detection scheme in both symbol mappings over the whole SNR range. This result is directly related to the uniform distribution of the phases ϕ^{u} and their BER performance indicated by Fig. 4.13. The throughput η_{eff} over the SNR for these scenarios is illustrated by Fig. 4.15. As expected, GJCNC offers the highest throughput over the whole SNR range and JCNC offers the worst performance. In [Wüb10, WL10, WWD13b, HLL14] TWRCs are analyzed within CP-OFDM with synchronized reception, leading to fully diagonal channel and thus to similar conditions as in the analysis in Fig. 4.14a and Fig. 4.14b. Finally, these curves should be the benchmark for the MC schemes analyzed in the sequel.

4.4.2 Performance Analysis of the PLNC Detection Schemes in Interference-Affected Transmissions

So far, we assumed synchronized CP-OFDM with a maximum delay spread fully caught by the CP. No additional channel impacts introduced in Chapter 2 like TO, CFO or Doppler spread are present, resulting in a pure diagonal effective channel matrix and thus the application of the simplified FGE in Fig. 4.11 and the simple APP detection in (4.16) can be used. However, the impact of CFO within TWRC is analyzed in [Wüb10, WL10, HLL14], and [**WLW$^+$14**] and even small offsets lead to a severe degradation.

In contrast to an unidirectional P2P transmission, where the individual impact of offsets like CFO or TO can be compensated at the Rx or pre-compensated at the Tx [LLZ15], here the compensation at the relay (Rx) is not directly possible. The received signal at the relay contains the effect of both users. Fig. 4.16 illustrates the impact on the receive signal for unidirectional P2P transmissions and TWRC transmissions at the relay.

On the upper part the separate receive signal of user A in Fig. 4.16a and user B in Fig. 4.16b affected without any offset, delay or Doppler spread is depicted in terms of a TF grid by the transmission with the Gaussian waveform as an example. The cross × and the circle ○ denote the optimal sampling point for a maximum signal energy. In the Fig. 4.16c the superposition of both signals is shown, leading to the maximum energy at the sampling points $(k'F_0, \ell' T_0)$. The impact of a CFO $\Delta\nu^{\mathsf{A}} = 0.2F_0$ for user A and TO $\Delta\tau^{\mathsf{B}} = 0.2T_0$ for user B is illustrated in Fig. 4.16d resulting in shifted ambiguity functions. In this case, the TF grid point $(k'F_0, \ell' T_0)$

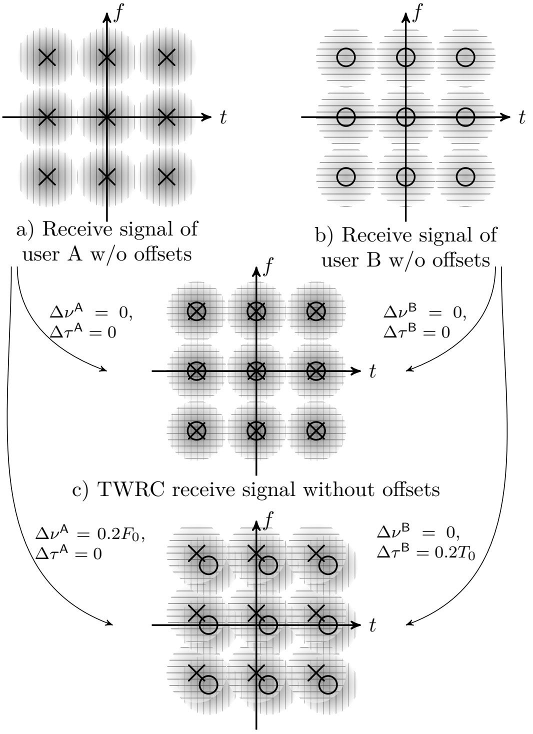

a) Receive signal of user A w/o offsets

b) Receive signal of user B w/o offsets

c) TWRC receive signal without offsets

d) TWRC receive signal with offsets

Figure 4.16: Time frequency grid with filter affected by different channels.

won't lead to the optimal sampling points in terms of maximum energy detection due to the shifts introduced by the offsets. Furthermore, no mutual observation point exists covering the optimum in terms of maximum signal power for both receive signals together. Usually, a common approach is to pre-compensate such impacts at the Tx side. However, within a time-variant channel, where the channel gains change quickly or in bursty, sporadic traffic, pre-compensation at the Tx side is impractical, due to missing or too fast changing channel state information (CSI)-Tx [LZL13, LLZ15]. Hence, in [SJ09, LWLZ13, Wu17, LLZ15], and [**WLW$^+$14**] the proposed solution is to compensate the *mean* impact of CFO, TO, delay or Doppler spread at the relay, only. However, this leads to a residual interference affected system, where the interference matrix $\overline{\mathbf{\Sigma}}^{\mathsf{u}}_{\mathbf{H}} \neq \mathbf{0}$ does not vanish even with an orthogonal MC scheme. To this end we further ask: *If offsets like TO and CFO are always present (unable to prevent or compensate), does it make sense* *to restrict to orthogonal transmissions? Or, do non-orthogonal multi-carrier schemes offer more robustness against channel impacts in general?*

Interference Analysis Before answering this question, we first focus on the amount of *residual* interference introduced by different waveform candidates under fixed offsets, delay, and Doppler conditions. Thus, we separate the power of the received signal corresponding to (4.6) like

$$\mathrm{E}\{|y_r^{\mathsf{R}}|^2\} = \underbrace{\sigma_\mathrm{d}^2\left(\left|h_{r,r}^{\mathsf{A}}\right|^2 + \left|h_{r,r}^{\mathsf{B}}\right|^2\right)}_{①P_{\mathrm{d},r}^{\mathrm{QAM}}} + \underbrace{\sigma_\mathrm{d}^2\sum_{s\neq r}\left(\left|h_{r,s}^{\mathsf{A}}\right|^2 + \left|h_{r,s}^{\mathsf{B}}\right|^2\right)}_{②P_{\mathrm{I},r}^{\mathrm{QAM}}} + \underbrace{\sigma_\mathrm{n}^2}_{③P_{\tilde{\mathrm{n}},r}^{\mathrm{QAM}}} \tag{4.33}$$

with the desired part ①, the interference part ② and the noise part ③ at the TF grid point r. Further, the corresponding received signal power for the OQAM-based transmission schemes is extended with (3.58) is given by

$$\begin{aligned}\mathrm{E}\{|y_r^{\mathsf{R}}|^2\} = &\underbrace{\sigma_\mathrm{d}^2\left(\Re\left\{h_{r,r}^{\mathsf{A}}\right\}^2 + \Re\left\{h_{r,r}^{\mathsf{B}}\right\}^2\right)}_{①P_{\mathrm{d},r}^{\mathrm{OQAM}}} \\ &+ \underbrace{\sigma_\mathrm{d}^2\sum_{s\neq r}\left(\Re\left\{h_{r,s}^{\mathsf{A}}\right\}^2 + \Re\left\{h_{r,s}^{\mathsf{B}}\right\}^2\right)}_{②P_{\mathrm{I},r}^{\mathrm{OQAM}}} + \underbrace{\sigma_\mathrm{n}^2}_{③P_{\tilde{\mathrm{n}},r}^{\mathrm{OQAM}}} \quad ,\end{aligned} \tag{4.34}$$

as the useful power is located in the real part.

Analysis of Channel Phase Differences Similar to the phase analysis *w.r.t.* the different TWRC detection schemes, we now focus on the analysis of the introduced interference ② $P_{\mathrm{I},r}$ *w.r.t.* different waveforms introduced in Chapter 3. In particular, the QAM and OQAM-based FBMC schemes applying the time-limited rectangular, the frequency-limited half-cosine and the "well-localized" Gaussian waveform[7], as well as the Mirabbasi-Martin and the EGF with $\rho = 2$ are considered for an effective lattice density $\delta_{\mathrm{LD}}(\Lambda) = 1$.

Fig. 4.17 shows the interference term $P_{\mathrm{I},r}$ for these schemes with fixed one-tap channels $h^{\mathsf{A}} = e^{j\phi^{\mathsf{A}}}$ and $h^{\mathsf{B}} = e^{j\phi^{\mathsf{B}}}$ for user A and user B, respectively. Here, only a phase difference $\phi^{\mathsf{AB}} = \phi^{\mathsf{A}} - \phi^{\mathsf{B}}$ is investigated. We first

---

[7] with parameter $\rho = 1$ for QAM and $\rho = 2$ for OQAM. With the OQAM mapping, the localization parameter should be chosen $\rho = 2$ to introduce less interference [Min15] due to the staggered TF grid.

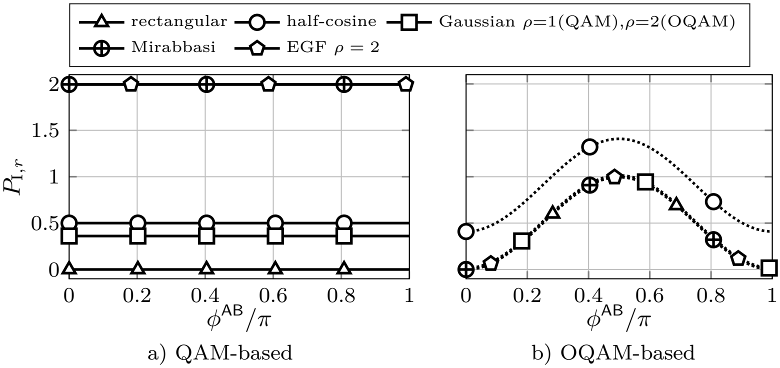

a) QAM-based b) OQAM-based

Figure 4.17: Interference introduced by phase differences.

look at the QAM-based schemes in Fig. 4.17a. As expected, the rectangular waveform results in an interference-free, *i.e.* orthogonal transmission, whereas the both "OQAM" waveforms (*i.e.* Mirabbasi-Martin and EGF) are affected by a severe amount of interference, since they were designed for a staggered lattice (*cf.* Fig. 3.21) and here abusively used with a TF lattice density $\delta_{\mathrm{LD}}(\Lambda) = 1$ are used. The non-orthogonal waveforms (Gaussian and half-cosine) are also affected by interference, but with comparable lower level. As expected due (4.33), we can observe that in the QAM-based schemes, no change of the interference power $P_{\mathrm{I},r}$ is observed by a modified phase term ϕ^{AB}. In contrast, the OQAM-based schemes are phase sensitive as illustrated in Fig. 4.17b. As expected without a phase difference $\phi^{\mathsf{AB}} = 0$ (or $\phi^{\mathsf{AB}} = \pi$ as the rotation by π leads to the same situation, since the usable energy returns to the real part.), the interference part is purely orthogonal to the signal power and, hence, a simple real part operation in (4.34) suppresses fully the interference power resulting in an overall orthogonal transmission. The presence of phase differences $\phi^{\mathsf{AB}} \neq 0$ severely increase the interference power. In the special cases of $\phi^{\mathsf{AB}} = \frac{\pi}{2}$ (or $\phi^{\mathsf{AB}} = \frac{3\pi}{2}$, not shown in the figure), the interference term of one user is completely aligned to the useful signal power of the other user and vice versa. The severe phase sensitivity is contra productive for the before mentioned phase sensitivity of the different detection schemes (SCD, JCNC and GJCNC *cf.* Fig. 4.13).

Fig. 4.18 shows the mean BER performance at the relay *w.r.t.* the different mappings (QAM and OQAM) and the different detection schemes. The solid lines correspond to the BER performance by the CP-OFDM scheme already illustrated in Fig. 4.13. The dotted lines determine OQAM/OFDM applying exemplary the EGF waveform, both schemes with a fixed SNR of

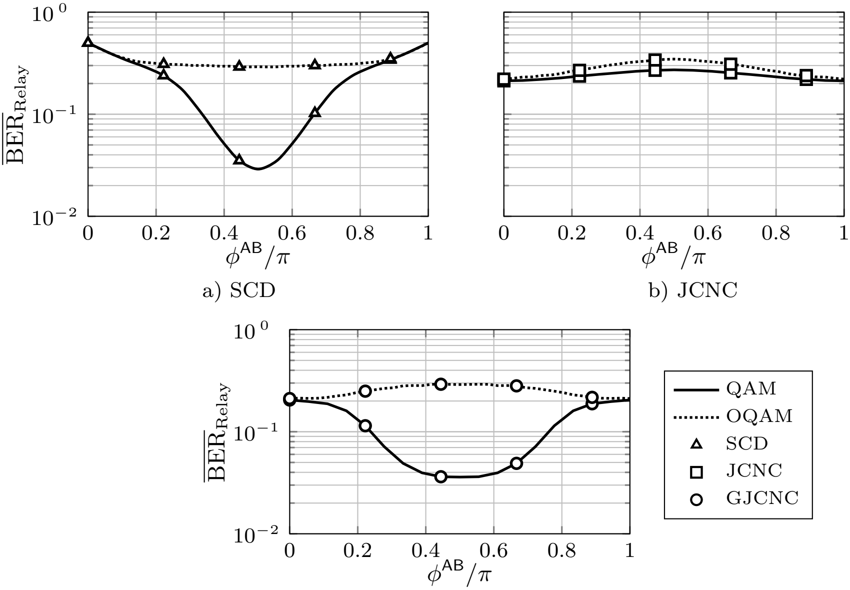

a) SCD

b) JCNC

c) GJCNC

Figure 4.18: Average BER performance at the relay with $E_\mathrm{b}/N_0 = 2\mathrm{dB}$ over the phase difference ϕ^{AB} with an LDPC encoding scheme and code rate $R_\mathrm{c} = 0.3$ for QAM with CP-OFDM and OQAM symbol mapping with EGF waveform $\rho = 2$.

$E_\mathrm{b}/N_0 = 2\mathrm{dB}$. We use BPSK for QAM. However, to compare both schemes, we have to use QPSK in OQAM resulting in BPSK symbols per used TF grid point due to the lattice staggering. To fairly compare both schemes, we used a normalized power with both mappings.

Both mappings result in the same BER performance without a phase difference ($\phi^{\mathsf{AB}} = 0$ or $\phi^{\mathsf{AB}} = \pi$), because no interference is introduced and both schemes are noise limited, only. However, by the presence of phase rotations in a TWRC, the OQAM-based schemes suffer from the separation of useful power in the real domain and the interference power in the other domain. The separation of useful power and the interference power is impossible by simple real part operation in this under-determined system like TWRC in contrast to a unidirectional P2P transmission.

4.5 Equalizer

So far we introduced the TWRC detectors based on the interference-free model (4.11). This system model is only valid for an orthogonal and perfectly synchronized reception at the relay. The presence of phase differences (for OQAM-based schemes), TO (larger than the GI), CFO, delay spread (without any GI) or Doppler spread introduces interference terms spread more or less over the whole TF grid at the relay. *E.g.* in [**WLW⁺14**] TWRC was analyzed regarding an LTE-like setting (CP-OFDM) on a hardware demonstration setup. The results verify the high sensitivity to CFO. Instead of performing compensation algorithms, fully applicable for unidirectional P2P users, only, the relay is not able to simply perform individual compensation on the superposition of all impacts. To deal with these impacts, we will introduce equalizer algorithms *w.r.t.* TWRC to handle the impact of general channels and compare the BER/FER performance at the relay regarding the BC message $\mathbf{b}^{\mathsf{R}}$. For TWRC, equalization techniques like linear filtering based on least squares (LS) or on an MMSE criterion as introduced in [**SWW⁺14, WWD⁺15b, WSW⁺16**], non-linear approaches like sIC (*cf.* [**WWD15a, WSW⁺16**]) or FGE (*cf.* [**WWD16, WWD18**]) avoid, mitigate or utilize the introduced interference terms. In the upper mentioned publications, TWRC with multi-carrier and general waveform are proposed and a flexible estimation framework is achieved, which in contrast to the rigid CP-OFDM, can be flexible adapted to changing channel conditions or other requirements like a higher demand on data rate, *etc.* For that, we generalize the aforementioned APP-based methods to a general FGE framework taking advantage of the underlying physical channel and the selectable waveform introduced by general MC schemes. We also discuss complexity reduction techniques, which will give a trade-off between FER performance and computational complexity at the relay. Thus, we address a linear equalizer technique for TWRC-based on a MMSE criterion. The computational complexity can further be reduced by the application of windowing techniques utilizing again the knowledge of the waveform used. Moreover, by the knowledge of already decided symbols, a sIC approach is implemented to improve further the overall performance.

4.5.1 Factor Graph-based Equalizer

Over the past decade factor graphs (FGs) and the underlying sum-product algorithm (SPA) have been used intensively for a variety of applications like error correction decoding, Kalman filtering, and iterative detection [KFL01, Loe03, Loe04, Wym07, WS01]. For SC transmission over time-invariant channels the factor graph-based equalizer (FGE) has been proposed in [CG05, Col06, ACC$^+$07, GP08] and has been extended for time-variant channels in [DS07a]. Further extensions for MIMO antenna systems [KDK05, LYWM05, KDK07, HD08], single-input single-output (SISO)-OFDM with time-variant channels [OWM$^+$12], and MIMO-OFDM [HTH11, XM10] indicated the excellent performance of FG-based detection/equalization similar to the corresponding optimal algorithms (even if the FGs have a small girth due the present ISI or ICI). Even for unidirectional P2P transmissions, the application of a FGE in OQAM based schemes offer good performances [FZCC16]. First applications of FGE for SC-TWRC has been proposed for the time and phase asynchronous case in [LL12], whereas for CP-OFDM modulated TWRC for time-variant (doubly-dispersive) channels in [HZ11, XXX12, WHZW13, SG12].

In the Appendix B, we briefly introduce the general concept of FGs by means of an unidirectional P2P communication system. In this subsection, we generalize this idea to TWRCs with MC and general waveforms according to the publications [**WWD16, WWD18**]. The main goal is to estimate the BC message $\mathbf{b}^{\mathsf{R}}$. We have already seen a special case of the FGE in the interference-free case (4.11) resulting in a simplified message calculation (see (4.15) and (4.16)) and a FGE with a single edge between observation node and desired variable node. However, in the presence of offsets, *e.g.* TO, CFO, delay spread and Doppler spread, this simplified model is not accurate anymore. In addition, the application of non-orthogonal MC transmission schemes leads also to a spread of the useful power in the Rx-TF grid and, thus, to more connections in the FG. Nevertheless, the application of general waveform offers the adaption of the effective channel and, hence, the amount of connection in the FG resulting in a controllable equalizer. The considered FG in this work is given in the conventional notation [KFL01] and the general structure of the FGE is based on the Forney approach [For72a] (see Appendix B for a detailed description).

Generation of the FGE

The FGE can be directly derived by the corresponding effective channel matrices (see Appendix B). Given the channel matrices $\underline{\mathbf{H}}^{\mathsf{u}}$, the adjacency matrix $\mathbf{A}^{\mathsf{u}}$ is derived with elements

$$a^{\mathsf{u}}_{r,s} = \begin{cases} 1 & , \text{ if } h^{\mathsf{u}}_{r,s} \neq 0 \\ 0 & , \text{ otherwise} \end{cases} , \tag{4.35}$$

similar to the unidirectional P2P case (B.13). Each “1” in the adjacency matrix determines one edge between variable and factor node, *e.g.* $a^{\mathsf{u}}_{r,s} = 1$ means that the observation y^{R}_r is connected by an edge with variable d^{u}_s.

However, we focus on the TWRC setup where we use the symbol tuple d_s^{AB}. So we define the neighborhood for this tuple d_s^{AB} as

$$\mathcal{N}_{d_s^{\mathsf{AB}}} = \left\{ r \mid a_{r,s}^{\mathsf{A}} = 1 \vee a_{r,s}^{\mathsf{B}} = 1 \right\} \tag{4.36}$$

and the neighborhood of a factor node $\mathrm{p}(y_r^{\mathsf{R}} \mid \underline{\mathbf{d}}^{\mathsf{AB}})$ connected to observation y_r^{R} is given by

$$\mathcal{N}_{y_r^{\mathsf{R}}} = \left\{ s \mid a_{r,s}^{\mathsf{A}} = 1 \vee a_{r,s}^{\mathsf{B}} = 1 \right\} \quad . \tag{4.37}$$

We can observe that, if the frame-based effective channel matrix $\underline{\mathbf{H}}^{\mathsf{u}}$ is purely diagonal, *i.e.* $\underline{\mathbf{H}}^{\mathsf{u}} = \mathbf{\Sigma}_{\mathbf{H}}^{\mathsf{u}}$ and $\overline{\mathbf{\Sigma}}_{\mathbf{H}}^{\mathsf{u}} = \mathbf{0}$, the adjacency matrix result in an identity matrix $\mathbf{A}^{\mathsf{u}} = \mathbf{I}$. This matches with the FGs for the interference-free system model (4.11).

FGE for TWRC: An Example Here, we go through a simple example to show the procedure of generating a FG for the symbol tuple part common to all TWRC detection approaches. Hence, if the channel matrices are exemplary

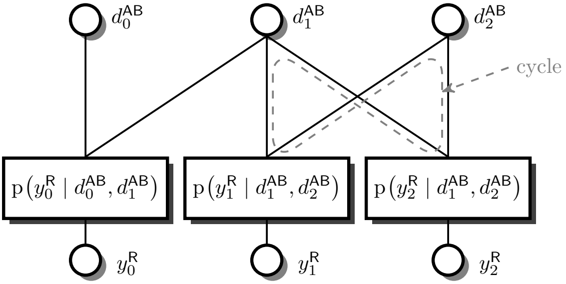

Figure 4.19: An example of a factor graph with three symbols d_s^{AB} and three observations y_r^{u}.

$$\underline{\mathbf{H}}^{\mathsf{A}} = \begin{bmatrix} 1+j & 0.1j & 0 \\ 0 & 0.7+0.9j & 0.02 \\ 0 & 0.1+0.1j & 0.8j \end{bmatrix} \quad \underline{\mathbf{H}}^{\mathsf{B}} = \begin{bmatrix} -1 & 1+j & 0 \\ 0 & -0.9+0.1j & 0 \\ 0 & -0.2+0.1j & -0.7j \end{bmatrix} \tag{4.38}$$

the resulting adjacency matrices with elements defined by (4.35) are

$$\mathbf{A}^{\mathsf{A}} = \begin{bmatrix} 1 & 1 & 0 \\ 0 & 1 & 1 \\ 0 & 1 & 1 \end{bmatrix} \quad \mathbf{A}^{\mathsf{B}} = \begin{bmatrix} 1 & 1 & 0 \\ 0 & 1 & 0 \\ 0 & 1 & 1 \end{bmatrix} . \tag{4.39}$$

The symbol tuple neighborhoods are in this case: $\mathcal{N}_{d_0^{\mathsf{AB}}} = \{0\}$, $\mathcal{N}_{d_1^{\mathsf{AB}}} = \{0,1,2\}$ and $\mathcal{N}_{d_2^{\mathsf{AB}}} = \{1,2\}$ and the observation neighborhoods: $\mathcal{N}_{y_0^{\mathsf{R}}} = \{0,1\}$, $\mathcal{N}_{y_1^{\mathsf{R}}} = \{1,2\}$ and $\mathcal{N}_{y_2^{\mathsf{R}}} = \{1,2\}$. The resulting FG is illustrated in Fig. 4.19. Note that we focus in this work on the sub-optimal FGE, which represent the per path FG of the effective channel. Thus, we fully open the factor nodes, which result in a loopy FG with influence of the direct neighbors in the TF grid. Nonetheless, the analysis in [LYWM05] indicates the excellent performance similar to the optimal algorithms. In contrast to this model, the BCJR algorithm offers the optimal solution without any loops based on the trellis representation of the channel memory. However, its computational complexity is exponentially related to the number of channel taps.

General FGE for TWRC Similar to the example, we can generate the neighborhoods depending on the used MC scheme and the corresponding effective channel matrices $\underline{\mathbf{H}}^{\mathsf{u}}$ as given in Chapter 3. In Fig. 4.11, we have seen the FGs for all detection schemes in the interference-free scenario. Based on these neighborhoods, the corresponding FGs gets extended and are illustrated in Fig. 4.20 for SCD, Fig. 4.21 for JCNC and Fig. 4.22 for GJCNC are generated[8].

The FGs describe the whole estimation process for the underlying bits. The part below the dashed line corresponds to the equalizer part. The special case of interference-free transmission are denoted by the gray box (without cross terms) and are related to the interference-free system model in Fig. 4.11

General Messages on the FGE

As we generalize the FG to tackle the introduction of interference terms, the messages exchanged over the edges in the FGE have to be adopted.

---

[8] The number of iterations $N_{\mathrm{It}}^{\mathrm{FGE}}$ for the equalizer and the number of iterations $N_{\mathrm{It}}^{\mathrm{outer}}$ for the complete system are already included in these images, but will be used later in the performance analysis.

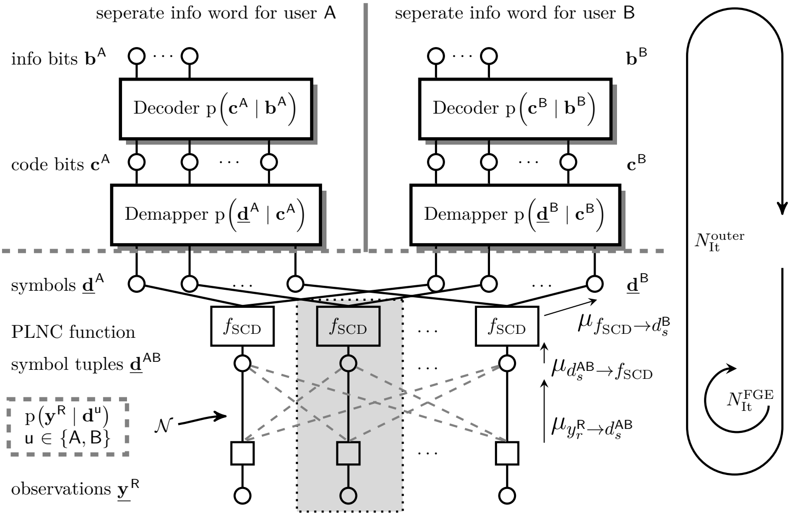

Figure 4.20: FG for the transmission of user A and B to relay R applying SCD detection. The part below the horizontal line consists of the equalizer part $\mathrm{p}\left(\underline{\mathbf{y}}^{\mathsf{R}} \mid \underline{\mathbf{d}}^{\mathsf{u}}\right)$. The PLNC function f_{SCD} performs tuple generation $\underline{\mathbf{d}}^{\mathsf{AB}} = \left(\underline{\mathbf{d}}^{\mathsf{A}}, \underline{\mathbf{d}}^{\mathsf{B}}\right)$.

- **Message $\mu_{y_r^{\mathsf{R}}\to d_s^{\mathsf{AB}}}$ from Observation Node to Symbol Tuple Node**

The message from a factor node connected to an observation y_r^{R} to a variable tuple node[9] is calculated as

$$\mu_{y_r^{\mathsf{R}}\to d_s^{\mathsf{AB}}}\left(d_s^{\mathsf{AB}}\right) = \sum_{\sim\{d_s^{\mathsf{AB}}\}} \mathrm{p}\left(y_r^{\mathsf{R}} \mid d^{\mathsf{AB}} \in \mathcal{N}_{y_r^{\mathsf{R}}}\right) \prod_{q\in\mathcal{N}_{y_r^{\mathsf{R}}}\setminus s} \mu_{d_q^{\mathsf{AB}}\to y_r^{\mathsf{R}}}\left(d_q^{\mathsf{AB}}\right) \quad , \tag{4.40}$$

where $\mathrm{p}(y_r^{\mathsf{R}} \mid d^{\mathsf{AB}} \in \mathcal{N}_{y_r^{\mathsf{R}}})$ is the likelihood function given by

$$\mathrm{p}\left(y_r^{\mathsf{R}} \mid d^{\mathsf{AB}} \in \mathcal{N}_{y_r^{\mathsf{R}}}\right) \propto \exp\left(-\frac{1}{\tilde{\sigma}_{\mathrm{n},r}^2}\left|y_r^{\mathsf{R}} - \sum_{s\in\mathcal{N}_{y_r^{\mathsf{R}}}}\left(h_{r,s}^{\mathsf{A}} d_s^{\mathsf{A}} - h_{r,s}^{\mathsf{B}} d_s^{\mathsf{B}}\right)\right|^2\right) . \tag{4.41}$$

It should be noted that the calculation (4.40) takes all incoming messages from connected variables d_q^{AB} with $q \in \mathcal{N}_{y_r^{\mathsf{R}}} \setminus s$ into consideration, without that message (*i.e.* $\mu_{d_s^{\mathsf{AB}}\to y_r^{\mathsf{R}}}(d_s^{\mathsf{AB}})$) coming from the desired variable d_s^{AB}.

---

[9] We abbreviate the $\mu_{\mathrm{p}\left(y_r^{\mathsf{R}} \mid d^{\mathsf{AB}} \in \mathcal{N}_{y_r^{\mathsf{R}}}\right)\to d_s^{\mathsf{AB}}} = \mu_{y_r^{\mathsf{R}}\to d_s^{\mathsf{AB}}}$ to ease the notation.

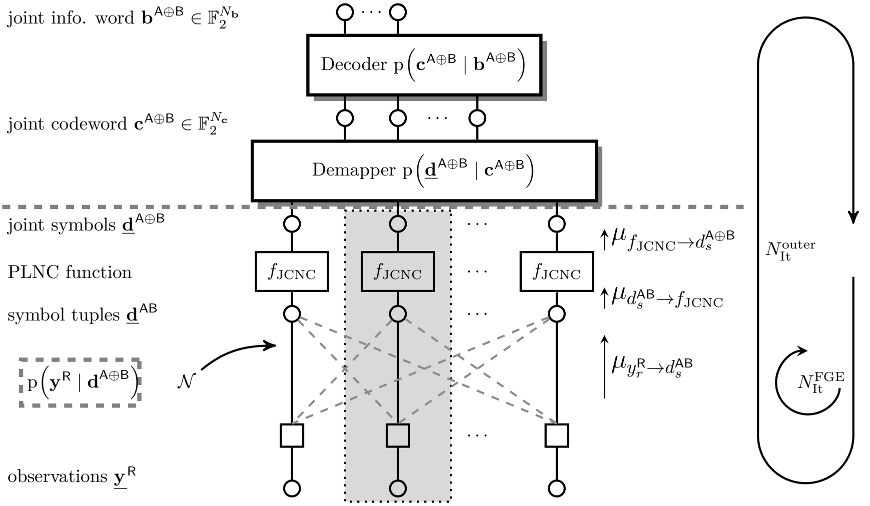

Figure 4.21: FG for the JCNC detection scheme to estimate BC message $\mathbf{b}^{\mathsf{R}} = \hat{\mathbf{b}}^{\mathsf{A}\oplus\mathsf{B}}$. The PLNC function performs marginalization from symbol tuple $\mathbf{d}^{\mathsf{AB}}$ to the joint symbol $\mathbf{d}^{\mathsf{A}\oplus\mathsf{B}}$.

- **Message $\mu_{d_s^{\mathsf{AB}} \to y_r^{\mathsf{R}}}$ from Symbol Tuple Node to Observation Node** The incoming messages from connected variable tuple nodes are calculated like[10]:

$$\mu_{d_s^{\mathsf{AB}} \to y_r^{\mathsf{R}}}\left(d_s^{\mathsf{AB}}\right) = \mu_{f_\mathrm{PLNC} \to d_s^{\mathsf{AB}}}\left(d_s^{\mathsf{AB}}\right) \prod_{q \in \mathcal{N}_{d_s^{\mathsf{AB}}} \backslash r} \mu_{y_r^{\mathsf{R}} \to d_q^{\mathsf{AB}}}\left(d_q^{\mathsf{AB}}\right) \tag{4.42}$$

and contains the a priori message $\mu_{f_\mathrm{PLNC} \to d_s^{\mathsf{AB}}}\left(d_s^{\mathsf{AB}}\right)$ from the PLNC function block.

- **Message $\mu_{d_s^{\mathsf{AB}} \to f_\mathrm{PLNC}}$ from Symbol Tuple Node to PLNC Function Node** The message from the symbols tuple to the corresponding function nodes f_PLNC (*i.e.* f_SCD, f_JCNC or f_GJCNC) is calculated by

$$\mu_{d_s^{\mathsf{AB}} \to f_\mathrm{PLNC}}\left(d_s^{\mathsf{AB}}\right) = \prod_{q \in \mathcal{N}_{d_s^{\mathsf{AB}}}} \mu_{y_r^{\mathsf{R}} \to d_q^{\mathsf{AB}}}\left(d_q^{\mathsf{AB}}\right) \quad . \tag{4.43}$$

taking all connections of the FGE into consideration.

---

[10] To describe the procedure, generally, we use here the term PLNC instead of the specific terms SCD, JCNC or GJCNC.

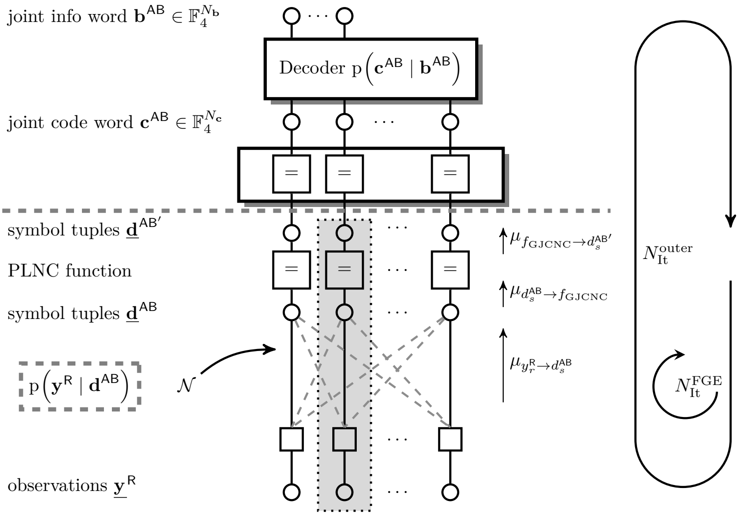

Figure 4.22: FG for the GJCNC detection scheme estimating the info word tuple $\mathbf{b}^{\mathsf{AB}}$. Here, the PLNC function is a simple equality node for a unified calculation.

• Message $\mu_{f_{\mathrm{PLNC}} \to d_s^{\mathsf{AB}}}$ from PLNC Function Node to Symbol Tuple

The upper introduced message $\mu_{f_{\mathrm{PLNC}} \to d_s^{\mathsf{AB}}}\left(d_s^{\mathsf{AB}}\right)$ coming from the PLNC function node is an important message as it contains the a priori information of the upper symbol demapping block and it depends on the chosen detection scheme. In Section 4.3.2 we introduced the different marginalization functions f_{SCD}, f_{JCNC} needed to handle the set size reduction of the symbol tuple needed for the further processing in the symbol demapper and decoder. The message from the demapper to the equalizer needs to be “demarginalized” for the further processing using the SCD and JCNC scenario.

I) SCD In case of SCD, the calculation of the a priori message $\mu_{f_{\mathrm{SCD}} \to d_s^{\mathsf{AB}}}\left(d_s^{\mathsf{AB}}\right)$ is the multiplication of the user specific incoming messages $\mu_{d_s^{\mathsf{B}} \to f_{\mathrm{SCD}}}\left(d_s^{\mathsf{u}}\right)$ with $\mathsf{u} \in \{\mathsf{A}, \mathsf{B}\}$:

$$\mu_{f_{\mathrm{SCD}} \to d_s^{\mathsf{AB}}}\left(d_s^{\mathsf{AB}}\right) = \mu_{d_s^{\mathsf{A}} \to f_{\mathrm{SCD}}}\left(d_s^{\mathsf{A}}\right) \cdot \mu_{d_s^{\mathsf{B}} \to f_{\mathrm{SCD}}}\left(d_s^{\mathsf{B}}\right) \quad . \tag{4.44}$$

The multiplication of the a priori messages coming from the demapper to the corresponding variables can be justified by the independent symbols of the users. Furthermore, they extend the message space $(M \to M^2)$.

II) JCNC Contrarily, the JCNC suffers from the marginalization of the message space $\mathcal{D}^{\mathsf{A}\oplus\mathsf{B}}$ in (4.20). However, reducing the message space in the upper part of the FG to the combined symbol $d_s^{\mathsf{A}\oplus\mathsf{B}}$ leads to an ambiguous assignment of the a priori message coming back from the decoder and demapper to the equalizer at the PLNC function block. Hence, we can only use the *ambiguous mapping* (*i.e.* changing the dimension from $M \to M^2$) by

$$\mu_{f_{\text{JCNC}} \to d_s^{\mathsf{AB}}}\left(d_s^{\mathsf{AB}}\right) = \frac{1}{M}\mu_{d_s^{\mathsf{A}\oplus\mathsf{B}} \to f_{\text{JCNC}}}\left(d_s^{\mathsf{A}\oplus\mathsf{B}}\right). \tag{4.45}$$

The factor $\frac{1}{M}$ is also justifiable by the independence of the symbols of the users, whereby here however no unambiguous assignment of the respective symbols is possible and thus the same probability of the symbols is assumed.

III) GJCNC With GJCNC the decoder directly provide the full feedback message such that it can directly be used

$$\mu_{f_{\text{GJCNC}} \to d_s^{\mathsf{AB}}}\left(d_s^{\mathsf{AB}}\right) = \mu_{d_s^{\mathsf{AB}} \to f_{\text{GJCNC}}}\left(d_s^{\mathsf{AB}}\right) \tag{4.46}$$

- **Message from PLNC function node to upper nodes** These messages are calculated in the same way as in the interference-free calculation given in (4.17) for SCD and (4.23) for JCNC or directly used for GJCNC.

Sum Product Algorithm for the Equalizer in TWRC

In Alg. 4.1 the algorithm for the FGE is shown. The FG is initialized by the matrices $\mathbf{A}^{\mathsf{A}}$ and $\mathbf{A}^{\mathsf{B}}$ from (4.35). Usually this kind of FG has loops between neighboring variable tuples and factors [XM10], hence the calculation within the equalizer is done iteratively. Furthermore, the overall FG containing decoder, symbol demapper and equalizer is processed iteratively. If the demapper stage provides a priori information based on the upper part of the overall FG, these messages are initialized as in line 5 for SCD, line 7 for JCNC or line 9 for GJCNC (Alg. 4.1). However, if no a priori information is available (*e.g.*, in the first iteration) the messages are initialized as equally distributed (line 12 in Alg. 4.1). After some iterations the messages are fed to the demapper and the decoder detects the information words depending on the PLNC approach and the relay message is generated and transmitted in the BC phase.

Algorithm 4.1 SPA Equalizer

```
#Initialize factor graph # setup the edges based on the adjacency matrix like in (4.35)
#Initialize#
if a priori information available then
    if Detection scheme == SCD then
        calculate $\mu_{f_{\mathrm{SCD}} \to d_s^{\mathsf{AB}}}\left(d_s^{\mathsf{AB}}\right)$ like in (4.44)
    else if Detection scheme == JCNC then
        calculate $\mu_{f_{\mathrm{JCNC}} \to d_s^{\mathsf{AB}}}\left(d_s^{\mathsf{AB}}\right)$ like in (4.45)
    else if Detection scheme == GJCNC then
        calculate $\mu_{f_{\mathrm{GJCNC}} \to d_s^{\mathsf{AB}}}\left(d_s^{\mathsf{AB}}\right)$ like in (4.46)
    end if
else
    $\mu_{f_{\mathrm{PLNC}} \to d_s^{\mathsf{AB}}}\left(d_s^{\mathsf{AB}}\right) = 1/M^2$
end if
#Start Calculation of SPA#
repeat
    #Calculate variable to factor message#
    for $s = 0, s \leq N_{\mathrm{SC}} N_{\mathrm{TS}} - 1, s = s + 1$ do
        calculate $\mu_{d^{\mathsf{AB}} \to y_r^{\mathsf{R}}}\left(d_s^{\mathsf{AB}}\right)$ like in (4.42)
    end for
    #Calculate factor to variable message#
    for $r = 0, r \leq N'_{\mathrm{SC}} N'_{\mathrm{TS}} - 1, r = r + 1$ do
        calculate $\mu_{y_r^{\mathsf{R}} \to d_s^{\mathsf{AB}}}\left(d_s^{\mathsf{AB}}\right)$ like in (4.40) and (4.41)
    end for
until Any stopping criterion is met
#calculate equalizer output message#
calculate $\mu_{d_s^{\mathsf{AB}} \to f_{\mathrm{PLNC}}}\left(d_s^{\mathsf{AB}}\right)$ like in (4.43)
# Calculate the messages to the demappers/decoders #
if Detection scheme == SCD then
    $\mu_{f_{\mathrm{SCD}} \to d_s^{\mathsf{A}}}\left(d_s^{\mathsf{A}}\right)$ and $\mu_{f_{\mathrm{SCD}} \to d_s^{\mathsf{B}}}\left(d_s^{\mathsf{B}}\right)$ like in (4.17)
else if Detection scheme == JCNC then
    $\mu_{f_{\mathrm{JCNC}} \to d_s^{\mathsf{A} \oplus \mathsf{B}}}\left(d_s^{\mathsf{A} \oplus \mathsf{B}}\right)$ like in (4.23)
else if Detection scheme == GJCNC then
    $\mu_{f_{\mathrm{GJCNC}} \to d_s^{\mathsf{AB}}}\left(d_s^{\mathsf{AB}}\right) = \mu_{d_s^{\mathsf{AB}} \to f_{\mathrm{GJCNC}}}\left(d_s^{\mathsf{AB}}\right)$ like in (4.46)
end if
```

Complexity Reduction

The complexity of the SPA working on the FG is mainly influenced by the number of edges as this is directly related to the number of messages exchanged within the FG (*cf.* Appendix Fig. B.8). In this subsection, we want to reduce the amount of edges with considerable small effective channel amplitudes to lower the complexity maintaining the performance. This results in an inaccurate structure of FGE, however, as the messages of these edges only contributes marginally to the overall probability the performance will only decrease insignificantly. According to the interference analysis *w.r.t.* the number of neighbors N_{N} in Section 4.4.2, we can define the reduced adjacency matrix $\mathbf{A}^{\mathsf{u},\text{reduced}}$ with elements given by

$$a^{\mathsf{u},\text{reduced}}_{r,s} = \begin{cases} 1 & \text{, if } r \in \mathcal{N}_{d^{\mathsf{u}}_s}(N_{\mathrm{N}}) \\ 0 & \text{, otherwise} \end{cases} , \tag{4.47}$$

The number of neighbors N_{N} is a trade-off parameter concerning the computational complexity and the accuracy of the algorithm. On the one hand, by setting $N_{\mathrm{N}} = N_{\mathrm{SC}} N_{\mathrm{TS}}$ (yielding the full matrix (4.35)), even small amplitudes $\left|h^{\mathsf{u}}_{r,s}\right|$ lead to an edge in the FG. However, these connections will only have a small impact on the overall performance at cost of a huge message exchange. On the other hand, the choice of a too small number of neighbors N_{N} producing only some connections within the FG and therefore decreasing the complexity could lead to a performance degradation of the equalizer in case of a high number of interference terms ② in (4.6) not considered in the FG. This modification leads to a different view on the FG and corresponds to the rewritten system model from (4.6) as

$$\begin{aligned} y^{\mathsf{R}}_r = & \underbrace{h^{\mathsf{A}}_{r,r} d^{\mathsf{A}}_r + h^{\mathsf{B}}_{r,r} d^{\mathsf{B}}_r}_{\text{① desired signal}} + \underbrace{\sum_{s \in \mathcal{N}^{\text{reduced}}_{y^{\mathsf{R}}_r}} \left(h^{\mathsf{A}}_{r,s} d^{\mathsf{A}}_s + h^{\mathsf{B}}_{r,s} d^{\mathsf{B}}_s \right)}_{\text{②a considered interference}} \\ & + \underbrace{\sum_{s \notin \mathcal{N}^{\text{reduced}}_{y^{\mathsf{R}}_r}} \left(h^{\mathsf{A}}_{r,s} d^{\mathsf{A}}_s + h^{\mathsf{B}}_{r,s} d^{\mathsf{B}}_s \right)}_{\text{②b unconsidered interference}} + \underbrace{\tilde{n}_r}_{\text{③ noise}} \quad . \end{aligned} \tag{4.48}$$

with also reduced neighborhoods $\mathcal{N}^{\text{reduced}}_{d^{\mathsf{AB}}_s} \subseteq \mathcal{N}_{d^{\mathsf{AB}}_s}$ (4.36) and $\mathcal{N}^{\text{reduced}}_{y^{\mathsf{R}}_r} \subseteq \mathcal{N}_{y^{\mathsf{R}}_r}$ (4.37).

Similar to the analysis in Fig. 4.6 and 4.7 the corresponding interference powers related to (4.33) for QAM and (4.34) for OQAM can be given as the overall interference power which can be separated into a considered $P_{\mathrm{I},2\mathrm{a},r}$ and unconsidered $P_{\mathrm{I},2\mathrm{b},r}$ interference power in the FGE. The considered power ②a is simply spoken handled by the structure of the FG. Whereas, the unconsidered interference power is modeled as independent and identically distributed (iid) complex variable with Gaussian distribution $\mathcal{N}(0, P_{\mathrm{I,2b},r})$ with $P_{\mathrm{I,2b},r} = \mathrm{E}\{②b\}$. This additive interference term is used in the calculation of the likelihood function (4.41) as combined noise term $\tilde{\sigma}^2_{\mathrm{n},r} = \sigma^2_{\mathrm{n}} + P_{\mathrm{I,2b},r}$.

The choice of the used waveforms and the channel also influences the number of edges within the FG. It is obvious that these interference terms are defined by the chosen waveform, the effective channel, and TO/CFO.

In case of an orthogonal MC scheme, *e.g.* plain-OFDM, with a channel $s^{\mathsf{A}}(\tau, \nu) = s^{\mathsf{B}}(\tau, \nu) = \delta(\tau)\,\delta(\nu)$, the adjacency matrix is the identity matrix (as indicated by Fig. 3.10) leading to the solid lines in Fig. 4.20 and, thus, to the interference-free structure in Fig. 4.11. In contrast, by the presence of CFO, delay spread, TO or Doppler effect a huge amount of off-diagonals will lead to cross edges between the function and variable nodes.

4.5.2 Additional Linear Pre-Equalizer

In Chapter 3 we have seen that by the presence of a time-variant channel the effective channel matrix has many entries unequal to zero for CP-OFDM resulting in a densely connected FGE. However, the dense connection is reduced by the application of other waveforms or a FGE with reduced adjacency matrix. In this part we want to further reduce the number of edges in the FG by the application of a LE before performing the FGE [LYWM05]. The goal is to reduce the off-diagonals in the effective channel matrix and, thus, the amount of edges in the FG.

In the following, we focus on a frame-based LE for TWRC according to an MMSE criterion [BD12]. The computational complexity of the inversion of a large frame-based matrix is still high, so we also stress techniques to reduce the complexity by windowing according to the underlying waveform used.

TWRC-based Linear Pre-Equalizer

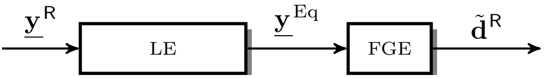

Figure 4.23: Linear equalizer for TWRC.

The authors in [BD12] propose a LE for the relay receive signal, which reduces the mean square error (MSE) between the superposition $\underline{\mathbf{d}}^{\mathsf{R}} = \underline{\mathbf{d}}^{\mathsf{A}} + \underline{\mathbf{d}}^{\mathsf{B}}$ (the undisturbed PLNC signal) and the estimated relay symbols $\tilde{\underline{\mathbf{d}}}^{\mathsf{R}}$ by the application of a linear filter $\underline{\mathbf{G}}$ on the receive signal $\underline{\mathbf{y}}^{\mathsf{R}}$. Using the MMSE criterion, the linear TWRC filter matrix based on the superposition can be achieved solving

$$\underline{\mathbf{G}}^{\mathsf{R}}_{\mathrm{TWRC}} = \arg\min_{\underline{\mathbf{G}}} \mathrm{E}\{\|\underline{\tilde{\mathbf{d}}}^{\mathsf{R}} - \underline{\mathbf{d}}^{\mathsf{R}}\|^2\} \tag{4.49}$$

and with some mathematical steps [**SWW⁺14**] the mutual linear filter matrix yields

$$\underline{\mathbf{G}}^{\mathsf{R}}_{\mathrm{TWRC}} = \left(\left(\underline{\mathbf{H}}^{\mathsf{A}}\right)^{\mathsf{H}} + \left(\underline{\mathbf{H}}^{\mathsf{B}}\right)^{\mathsf{H}}\right)\left(\underline{\mathbf{H}}^{\mathsf{A}}\left(\underline{\mathbf{H}}^{\mathsf{A}}\right)^{\mathsf{H}} + \underline{\mathbf{H}}^{\mathsf{B}}\left(\underline{\mathbf{H}}^{\mathsf{B}}\right)^{\mathsf{H}} + \frac{1}{\sigma_{\mathrm{d}}^2}\Psi_{\tilde{\mathbf{n}}\,\tilde{\mathbf{n}}}\right)^{-1} , \tag{4.50}$$

where $\Psi_{\tilde{\mathbf{n}}\,\tilde{\mathbf{n}}}$ is the correlation matrix of the noise defined in Appendix A.6, which is in this case of uncorrelated noise terms $\Psi_{\tilde{\mathbf{n}}\,\tilde{\mathbf{n}}} = \sigma_{\mathrm{n}}^2\mathbf{I}$.

The corresponding block diagram for this approach is illustrated in Fig. 4.23 with the resulting system model:

$$\underline{\mathbf{y}}^{\mathrm{Eq}} = \underbrace{\underline{\mathbf{G}}^{\mathsf{R}}_{\mathrm{TWRC}}\underline{\mathbf{H}}^{\mathsf{A}}}_{\underline{\widetilde{\mathbf{H}}}^{\mathsf{A}}}\underline{\mathbf{d}}^{\mathsf{A}} + \underbrace{\underline{\mathbf{G}}^{\mathsf{R}}_{\mathrm{TWRC}}\underline{\mathbf{H}}^{\mathsf{B}}}_{\underline{\widetilde{\mathbf{H}}}^{\mathsf{B}}}\underline{\mathbf{d}}^{\mathsf{B}} + \underline{\mathbf{G}}^{\mathsf{R}}_{\mathrm{TWRC}}\underline{\mathbf{n}}^{\mathsf{R}} \tag{4.51}$$

Two modifications have to be made to the FGE with the afore introduced Forney-based FG approach. On the one hand, we have to calculate new neighborhoods $\mathcal{N}_{d_s^{\mathsf{u}}}$, $\mathcal{N}_{y_r^{\mathsf{R}}}$, $\mathcal{N}_{d_s^{\mathsf{AB}}}$ *w.r.t.* the modified effective channel matrix $\underline{\widetilde{\mathbf{H}}}^{\mathsf{u}}$ and on the other hand, the likelihood function used in (4.40) changes *w.r.t.* (4.51) like

$$\mathrm{p}\left(y_r^{\mathsf{R}} \mid d^{\mathsf{AB}} \in \mathcal{N}_{y_r^{\mathsf{R}}}\right) \propto \exp\left(-\frac{1}{\tilde{\sigma}_{\mathrm{n},r}^2}\left|y_r^{\mathsf{R}} - \sum_{s\in\mathcal{N}_{y_r^{\mathsf{R}}}}\left(\tilde{h}_{r,s}^{\mathsf{A}}d_s^{\mathsf{A}} - \tilde{h}_{r,s}^{\mathsf{B}}d_s^{\mathsf{B}}\right)\right|^2\right) . \tag{4.52}$$

It should be noted that many off-diagonals are of very low amplitude, such that the application of a reduced neighborhood with the reduced adjacency matrix (4.47) is preferable.

TWRC-based Linear Pre-Equalizer by Windowing

In the last section, we dealt with the frame-based LE performing a full inversion of the effective channel matrix of size $N_{\mathrm{TS}}N_{\mathrm{SC}} \times N_{\mathrm{TS}}N_{\mathrm{SC}}$ in (4.51), which can be of significant computational complexity. As we introduced in Chapter 3, the effective channel matrix has a band diagonal structure,

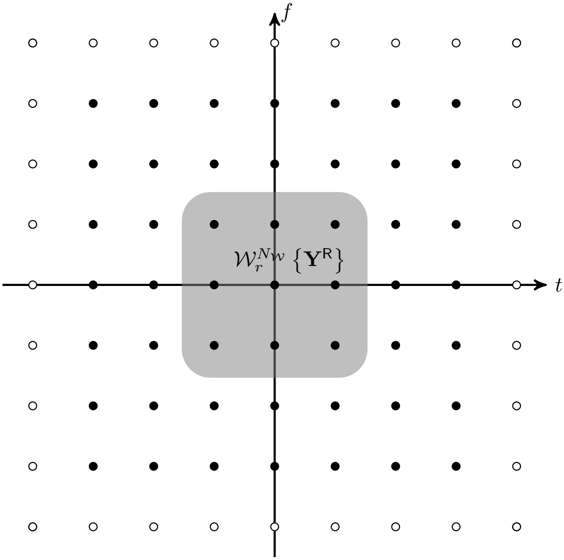

Figure 4.24: TF grid area used for the linear pre-equalizer with windowing. Here, with a window size of $N_\mathcal{W} = 1$, leading to $N_\mathrm{N} = 9$ neighbors considered.

dependent on the physical channel, the chosen waveform and the MC scheme used, which is the main motivation of the reduction to a limited number of neighbors. Similar to the adjacency matrix (4.35), we focus only on the adjacent symbols in the TF grid to perform the linear equalization. Let us define a window operator

$$\mathcal{W}_{k',\ell'}^{N_\mathcal{W}}\left\{\mathbf{Y}\right\} := \mathrm{vec}\{[\mathbf{Y}]_{k'-N_\mathcal{W}:k'+N_\mathcal{W},\ell'-N_\mathcal{W}:\ell'+N_\mathcal{W}}\} \tag{4.53}$$

that selects $N_\mathcal{W}$ neighboring elements in a window of size $(2N_\mathcal{W}+1) \times (2N_\mathcal{W}+1)$ around a lattice point (k',ℓ') of frame $\mathbf{Y}$ **[WWD⁺15b]**[SK15] as illustrated in Fig. 4.24. In this figure the black filled circles denote the TF grid points, which are affected by a symbol transmitted at the TF grid point (0,0).

Without loss of generality, we assume that the window is square. The operator can be extended easily to a window that uses different number of neighbors in time and frequency direction. By applying the window operator in (4.53) to the received signal with receive index $r = \ell' + k'N_\mathrm{SC}$, the signal

$$\underline{\mathbf{y}}_r^{\mathsf{R},\mathcal{W}} = \mathcal{W}_r^{N_\mathcal{W}}\left\{\mathbf{Y}^\mathsf{R}\right\} \quad . \tag{4.54}$$

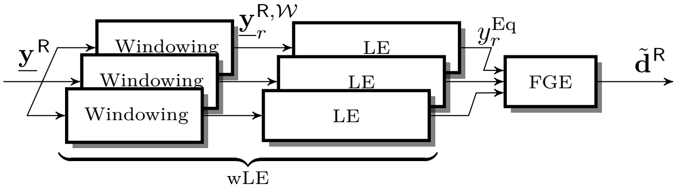

Figure 4.25: Several branches for the linear equalizer with windowing.

is generated, which selects a subset of $N_{\mathrm{N}} = (2N_{\mathcal{W}} + 1)^2$ neighboring signals around a specific lattice point (k', ℓ') as well as the desired signal for the LE. By a window size of $N_{\mathcal{W}} = 1$ in Fig. 4.24, the number of neighbors considered yield in total $N_{\mathrm{N}} = 9$. The restriction to neighboring symbols was motivated by the sampled auto-ambiguity function $A(\ell' T_0, k' F_0)$ for the Tx/Rx filters given in Chapter 3 and the interference analysis in Section 4.4.2. So, it highly depends on the offset and spread condition how large a window should be chosen. Even in the case of a rectangular Tx/Rx the main energy is located around the desired symbol and thus a window can be used. However, the analysis in Section 4.4.2 has shown that the window should be chosen considerable larger for the rectangular waveform in comparison to the Gaussian waveform. The altered block diagram is depicted in Fig. 4.25.

The windowed receive signal $\underline{\mathbf{y}}_r^{\mathsf{R},\mathcal{W}}$ is used as equalizer input and applying the window operator (4.54) on the receive signal (4.4) yields a reduced system model

$$\underline{\mathbf{y}}_r^{\mathsf{R},\mathcal{W}} = \underline{\mathbf{H}}^{\mathsf{A},\mathcal{W}} \underline{\mathbf{d}}^{\mathsf{A}} + \underline{\mathbf{H}}^{\mathsf{B},\mathcal{W}} \underline{\mathbf{d}}^{\mathsf{B}} + \tilde{\underline{\mathbf{n}}}_r^{\mathcal{W}} \quad , \tag{4.55}$$

per branch r, where $\underline{\mathbf{H}}^{\mathsf{A},\mathcal{W}}$ and $\underline{\mathbf{H}}^{\mathsf{B},\mathcal{W}}$ are corresponding matrices matching the data $\underline{\mathbf{d}}^{\mathsf{u}}$ to the received signal $\underline{\mathbf{y}}_r^{\mathsf{R},\mathcal{W}}$, and $\tilde{\underline{\mathbf{n}}}_r^{\mathcal{W}}$ is the windowed noise vector. The dimension per branch of the reduced effective channel matrices is $N_{\mathcal{W}} \times (N_{\mathrm{TS}} N_{\mathrm{SC}})$.

After windowing, a reduced LE $\underline{\mathbf{G}}_{\mathrm{TWRC}}^{\mathsf{R},\mathcal{W}}$ is applied and the output of this windowed linear equalizer (wLE) for the symbol at $r = \ell' + k' N'_{\mathrm{SC}}$ is given by

$$y_r^{\mathrm{Eq}} = \left(\mathbf{g}_r^{\mathcal{W}}\right)^{\mathsf{T}} \underline{\mathbf{y}}_r^{\mathsf{R},\mathcal{W}} \quad , \tag{4.56}$$

where vector $\mathbf{g}_r^{\mathcal{W}} = \mathbf{i}^{\mathsf{T}} \underline{\mathbf{G}}_{\mathrm{TWRC}}^{\mathsf{R},\mathcal{W}}$ contains the coefficients of the wLE. The vector $\mathbf{i} = [0, \ldots, 0, 1, 0, \ldots, 0]^{\mathsf{T}}$ selects the row that corresponds to the desired symbol at (k', ℓ'). The inversion for the filter matrix $\underline{\mathbf{G}}_{\mathrm{TWRC}}^{\mathsf{R},\mathcal{W}}$ is of smaller dimension as $\underline{\mathbf{G}}_{\mathrm{TWRC}}^{\mathsf{R}}$, however, has to be done for each element r, separately.

As the complexity is mainly influenced by the inversion of matrices we focus here on the complexity of inversions in the LE exploiting the full receive signal (4.4) and the reduced signal (4.55) by wLE. Considering a smaller number of neighbors reduces the complexity. The impact of the interference is directly connected to the window size. If $N_{\mathcal{W}}$ adjacent neighbors are used by the equalizer, the influence caused by the $N_{\mathrm{N}} = (2N_{\mathcal{W}} + 1)^2$ symbols around lattice point (k', ℓ') will be taken in to account. The interference of TF grid points that are more than $N_{\mathcal{W}} + 1$ symbols away, are not considered by the equalizer and are modeled again as Gaussian noise terms. In (4.56) an inversion of a matrix with dimension $(2N_{\mathcal{W}} + 1)^2 \times (2N_{\mathcal{W}} + 1)^2$ has to be applied for each symbol at (k', ℓ'). The larger $N_{\mathcal{W}}$, the smaller the impact of the residual interference. For a frame size of $N_{\mathrm{Resources}}^{\mathrm{Frame}} = N_{\mathrm{TS}} N_{\mathrm{SC}}$ symbols, the complexity of a full inversion in (4.50) is $\mathcal{C}_{\mathrm{full}} \sim \mathcal{O}((N_{\mathrm{Resources}}^{\mathrm{Frame}})^3)$, whereas a reduced equalizer requires $N_{\mathrm{Resources}}^{\mathrm{Frame}}$ inversions of a matrix with size N_{N} which is $\mathcal{C}_{\mathrm{reduced}} \sim \mathcal{O}\left(N_{\mathrm{Resources}}^{\mathrm{Frame}} \cdot N_{\mathrm{N}}^3\right)$. Note, that the windowed equalizer scales with the number of neighbors.

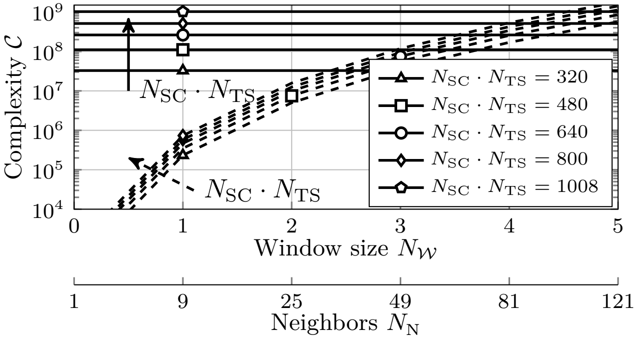

Figure 4.26: Complexity of a full inversion (solid), and inversion of reduced size matrix (dashed) for different frame sizes.

Fig. 4.26 shows the complexity of applying a LE which uses the full signal (4.4) and the windowed version (4.55) considering only a small window $N_{\mathcal{W}} = 1, \ldots, 5$. Taking only a few neighbors N_{N} into account the complexity is reduced. If more neighbors are taken into account, the complexity increases strongly. For a frame of size $N_{\mathrm{Resources}}^{\mathrm{Frame}} = 320$ elements, complexity can be reduced only if $N_{\mathcal{W}} \leq 3$, resulting in up to $N_{\mathrm{N}} = 25$ within the TF grid. In our setup, with a frame size $N_{\mathrm{Resources}}^{\mathrm{Frame}} = 1008$ elements, the window size can be chosen up $N_{\mathcal{W}} \approx 4$ to achieve less complexity.

4.5.3 Soft Interference Cancellation

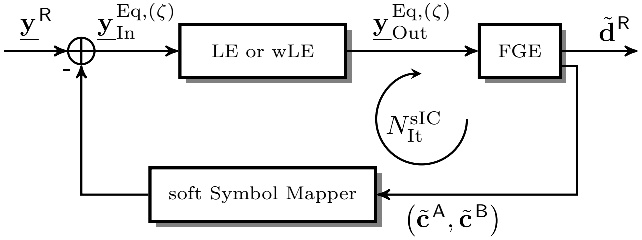

Figure 4.27: Equalizer with soft interference cancellation.

So far, we have introduced the concept of linear pre-equalization to reduce the complexity of the subsequent FGE. In order to further improve the estimation performance, the equalizer is extended with a feedback path [**WWD$^+$15b**], where the interference terms of already estimated data symbols $\underline{\tilde{\mathbf{d}}}^{\mathsf{A}}$ and $\underline{\tilde{\mathbf{d}}}^{\mathsf{B}}$ from the FGE block are fed back in a soft manner, which is commonly called soft interference cancellation (sIC). In addition to the estimation of the relay code word, SCD and GJCNC provide also soft estimates of the source code words $\tilde{\mathbf{c}}^{\mathsf{A}}$ and $\tilde{\mathbf{c}}^{\mathsf{B}}$, which can be used to generate soft symbol [WV99] and [**WLW$^+$14**] for the feedback link. The ability of providing soft symbols is essential for iterative detection of TWRC systems [**WLW$^+$14**]. Thus, in contrast to SCD and GJCNC, which provides these signals, the JCNC detection scheme, which directly estimates the relay code word without providing separate estimates for the source code words $\mathbf{c}^{\mathsf{A}}$ and $\mathbf{c}^{\mathsf{B}}$, cannot be used with sIC [ZLL06b] and thus will not be considered in the performance analysis *w.r.t.* sIC. A block diagram of sIC is shown in Fig. 4.27. One may note that in the iterative sIC structure the window operator introduced in (4.55) can be used to reduce the complexity in the equalizing step, but it is omitted here for the sake of simplicity. In the ζ^{th} iteration, with $\zeta = 1, \ldots, N_{\text{It}}^{\text{sIC}}$, the signal at the equalizer input is given by

$$\begin{aligned}
\underline{\mathbf{y}}_{\text{In}}^{\text{Eq},(\zeta)} =& \underline{\mathbf{y}}^{\mathsf{R}} - \left(\overline{\boldsymbol{\Sigma}}_{\mathbf{H}}^{\mathsf{A}} \underline{\tilde{\mathbf{d}}}^{\mathsf{A},(\zeta-1)} + \overline{\boldsymbol{\Sigma}}_{\mathbf{H}}^{\mathsf{B}} \underline{\tilde{\mathbf{d}}}^{\mathsf{B},(\zeta-1)} \right) \\
=& \underbrace{\boldsymbol{\Sigma}_{\mathbf{H}}^{\mathsf{A}} \underline{\mathbf{d}}^{\mathsf{A}} + \boldsymbol{\Sigma}_{\mathbf{H}}^{\mathsf{B}} \underline{\mathbf{d}}^{\mathsf{B}}}_{\text{PLNC signal}} + \underbrace{\underline{\mathbf{n}}^{\mathsf{R}}}_{\text{noise}} \\
& + \underbrace{\overline{\boldsymbol{\Sigma}}_{\mathbf{H}}^{\mathsf{A}} \left(\underline{\mathbf{d}}^{\mathsf{A}} - \underline{\tilde{\mathbf{d}}}^{\mathsf{A},(\zeta-1)} \right) + \overline{\boldsymbol{\Sigma}}_{\mathbf{H}}^{\mathsf{B}} \left(\underline{\mathbf{d}}^{\mathsf{B}} - \underline{\tilde{\mathbf{d}}}^{\mathsf{B},(\zeta-1)} \right)}_{\text{residual common interference}}
\end{aligned} \tag{4.57}$$

where $\underline{\mathbf{y}}^{\mathsf{R}}$ denotes the separable received signal (4.5). The matrix $\boldsymbol{\Sigma}_{\mathbf{H}}^{\mathsf{u}}$ is a main diagonal matrix and corresponds to the interference-free PLNC signal. The corresponding off-diagonal matrix $\overline{\boldsymbol{\Sigma}}^{\mathsf{u}}_{\mathbf{H}}$ is responsible for the interference part ② in (4.5). The vectors $\underline{\tilde{\mathbf{d}}}^{\mathsf{A},\zeta-1}$ and $\underline{\tilde{\mathbf{d}}}^{\mathsf{B},\zeta-1}$ denote the estimates for the transmitted signals achieved in the previous iteration $\zeta - 1$. Please note that for the first iteration $\zeta = 1$ the feedback symbols are initialized by $\underline{\tilde{\mathbf{d}}}^{\mathsf{u},\zeta=0} = \mathbf{0}$ yielding the LE (4.50). Assuming the estimates of $\underline{\tilde{\mathbf{d}}}^{\mathsf{u},\zeta-1}$ are tight, the residual interference terms get close to zero. Hence, only the diagonal parts of the effective channel matrix $\boldsymbol{\Sigma}^{\mathsf{u}}_{\mathbf{H}}$ will remain.

In comparison to the use of the pure LE in (4.51), we have to change the following during the iterations:

$\zeta = 1$ iteration: The neighborhood has to be adapted and the likelihood function in (4.52) has to be used.

$\zeta > 1$ iteration: Assuming that the estimation was tight to transmitted symbols, this yields a roughly vanishing interference part resulting in the FG of Fig. 4.11 with just the connections $r = s$. The variance of residual interference term is estimated and modeled by a Gaussian distribution.

After $N_{\mathrm{It}}^{\mathrm{sIC}}$ iterations, the output of the equalizer $\underline{\tilde{\mathbf{d}}}^{\mathsf{R}}$ is fed to the symbol demapper and channel decoder, which provides the estimated relay information word $\hat{\mathbf{b}}^{\mathsf{R}}$, which is mapped to the relay symbol vector $\underline{\mathbf{d}}^{\mathsf{R}}$ and transmitted in the BC phase.

4.6 Performance Analysis

In this section we investigate simulation results for a selection of MC schemes introduced in Chapter 3 applied for TWRC with the basic parameter set given by Tab. 4.3 on page 102. The focus at the beginning of this analysis is the performance in the synchronized time-invariant case with sufficiently large GI (if this option is used). Especially, the number of neighbors N_{N} in the FGE and the number of inner and outer iterations are important, namely $N_{\mathrm{It}}^{\mathrm{FGE}}$ and $N_{\mathrm{It}}^{\mathrm{outer}}$, respectively. If the sIC is used also the number of iterations of the sIC $N_{\mathrm{It}}^{\mathrm{sIC}}$ is used. Afterwards, the robustness against offsets is analyzed by means of FER and throughput performance analysis.

Generally, we assume a multi-path fading channel (2.12) generated by overall $N_{\mathrm{path}} = 300$ Rayleigh fading coefficients for each user resulting in the effective channel coefficients $h^{\mathsf{u}}_{r,s}$, (3.11) [Vog06, Sch01]. The path specific time delay spread $\tau^{\mathsf{u}}_{\gamma}$ and the Doppler spread $\nu^{\mathsf{u}}_{\gamma}$ are equally distributed within $[0, \tau^{\max}]$ and $[-\nu^{\max}, \nu^{\max}]$, respectively, in this analysis. For these analyses, we consider the following different MC schemes:

I) plain-OFDM,
II) CP-OFDM with $T_{\mathrm{GI}} = 0.1T_{\mathrm{S}}$,
III) ZP-OFDM with $T_{\mathrm{GI}} = 0.1T_{\mathrm{S}}$,
IV) w-CP-OFDM with $T_{\mathrm{GI}} = 0.1T_{\mathrm{S}}$ and $T_{\mathrm{g}} = 0.05T_{\mathrm{S}}$,
V) UF-OFDM, with $T_{\mathrm{g}} = 0.1T_{\mathrm{S}}$,
“complex orthogonal”
VI) QAM/FBMC with Gaussian waveform (3.18) and $\rho = 1$, and
VII) OQAM/FBMC with Gaussian waveform and $\rho = 2$.

and focus on the KPI mentioned in the beginning of Section 4.4 on page 101, like the average FER at the relay $\overline{\mathrm{FER}}_{\mathrm{Relay}}$ in (4.30) and the effective throughput at the relay η_{eff} in (4.32).

1. Scenario: Synchronized, Time-invariant Multi-path Channel

In this first scenario, we assume a time and frequency synchronous multi-path fading channel setup per user with a maximum delay spread $\tau^{\max} = 0.1T_{\mathrm{S}}$, *i.e.* no TO ($\Delta\tau = 0$), no CFO ($\Delta\nu = 0$) and no Doppler spread ($\nu^{\max} = 0$)[11]. One may directly note that this scenario is tailored to the orthogonal MC transmission schemes II)-V) as the channel influence is fully captured by the GI or smoothing filter. Hence, a pure diagonal effective matrix is achieved per user, *cf.* Chapter 3. In contrast to that, the FBMC schemes are non-orthogonal and non-diagonal elements show up in the effective channel matrix, *i.e.* $\overline{\mathbf{\Sigma}}_{\mathbf{H}} \neq 0$.

One-Tap Equalizer $N_{\mathbf{N}} = 1$ Fig. 4.28 shows the FER and throughput performance of the three PLNC detection schemes at the relay with BPSK symbol mapping and the schemes I)-VI). In all MC schemes the FGE with $N_{\mathrm{N}} = 1$ is used yielding the 1-tap frequency domain equalizer mostly used in CP-OFDM throughout the literature [KD18, Pro07]. Consequently, by the use of the FGE (4.47) with $N_{\mathrm{N}} = 1$, the use of plain-OFDM and QAM/FBMC results unconsidered interference terms, *cf.* (4.48). In Fig. 4.28a, it can be observed that QAM/FBMC and plain-OFDM suffers drastically from this unconsidered interference terms for all three PLNC schemes. Unexpectedly, the plain-OFDM scheme achieves a better FER performance than the QAM/FBMC, although, the effective channel matrix suggest a lower performance due to the higher number of interference terms,

---

[11] We use a maximum delay spread $\tau^{\max}$ related to the symbol duration T_{S} of the rectangular waveform to compare all schemes in a fair manner.

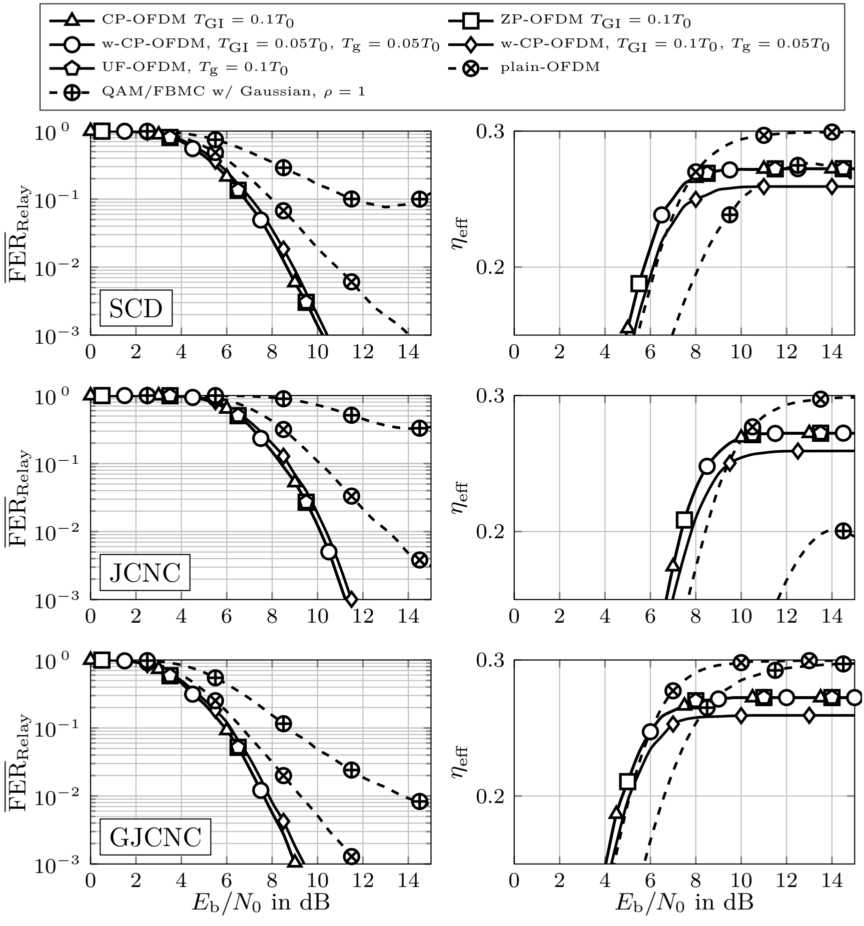

a) FER performance b) Throughput performance

Figure 4.28: FER and throughput performance at the relay with FGE and $N_N = 1$. Setup: $\Delta\tau = 0$, $\Delta\nu = 0$, $\nu^{\max} = 0$, BPSK.

cf. Fig. 3.10 and Fig. 3.24. However, these large amount of unconsidered interference terms are of smaller amplitude and the modeling as Gaussian noise term is more accurate than the few unconsidered interference terms with larger amplitude in QAM/FBMC with Gaussian waveform. The application of either a sufficiently large GI or a smoothing filtering avoids the ISI completely, and thus, the simple one-tap equalizer structure, used here, is sufficient and outperforms the non-orthogonal schemes.

Analyzing the FER performance *w.r.t.* the PLNC detection schemes shows that the GJCNC scheme outperforms all other detection schemes by the full utilization of the available information from the equalizer to the demapper in the FG, which coincides with the analysis in Fig. 4.14.

Fig. 4.28b shows the effective throughput η_{eff} of all considered MC schemes. As stated above, the ISI-free property of the "orthogonal" MC schemes comes by the expense of a GI or a smoothing filter, which reduces the effective throughput $\eta_{\mathrm{eff}} \propto \delta_{\mathrm{LD}}(\Lambda)$. The w-CP-OFDM scheme achieves the lowest throughput as the TF grid density $\delta_{\mathrm{LD}}(\Lambda) = 0.8696$ is the smallest of all schemes. In contrast to that, plain-OFDM and QAM/FBMC use a TF grid density of $\delta_{\mathrm{LD}}(\Lambda) = 1$ and have the potential to benefit of a higher throughput. Nevertheless, as the unconsidered interference terms are modeled by a Gaussian process in the FGE in (4.41), the FER performance runs into an error floor in the high SNR region or even growth as this approximation is not tight.

In Fig. 4.29, we change the symbol mapping to QPSK (4-QAM), which allows the comparison to VII) OQAM/FBMC. As already indicated by interference analysis in Section 4.4, the FER performance of OQAM suffers drastically by the high amount of interference and only the GJCNC detection scheme achieve a small improvement over the considered SNR region. In general, the phase sensitivity and the additional impact of ISI and ICI cannot be handled sufficiently by a simple 1-tap equalization such that the loss for plain-OFDM and QAM/FBMC is significantly higher than for the "orthogonal" counterparts. The GJCNC detection scheme is more robust against this kind of impacts. However, the need for a better performance requires the consideration of more neighbors in the FGE: $N_{\mathrm{N}} > 1$.

Equalizer considering $N_{\mathbf{N}} > 1$ In the following analysis we increase the number of considered neighbors in the FGE, but the other parameters are identical to the previous analysis. By increasing the number of neighbors N_{N} in the FGE, we have first to consider two important values: 1) the number of iterations within the FGE $N_{\mathrm{It}}^{\mathrm{FGE}}$, and 2) the number of iterations $N_{\mathrm{It}}^{\mathrm{outer}}$ exchanging messages between decoder, demapper and equalizer. In Fig. 4.30 the FER performance for QAM/FBMC with Gaussian waveform $\rho = 1$ *w.r.t.* the number of inner iterations $N_{\mathrm{It}}^{\mathrm{FGE}}$ with a fixed $N_{\mathrm{N}} = 5$ are illustrated on the left. The analysis *w.r.t.* the outer number of iterations $N_{\mathrm{It}}^{\mathrm{outer}}$ with $N_{\mathrm{N}} = 3$ and $N_{\mathrm{N}} = 5$ are shown on the right. The analysis is done for a fixed SNR working point of $E_{\mathrm{b}}/N_0 = 5\mathrm{dB}$ and BPSK mapping. In this figure, three types of curves are drawn:

1. *No a priori knowledge*: In this case the number of outer iterations is

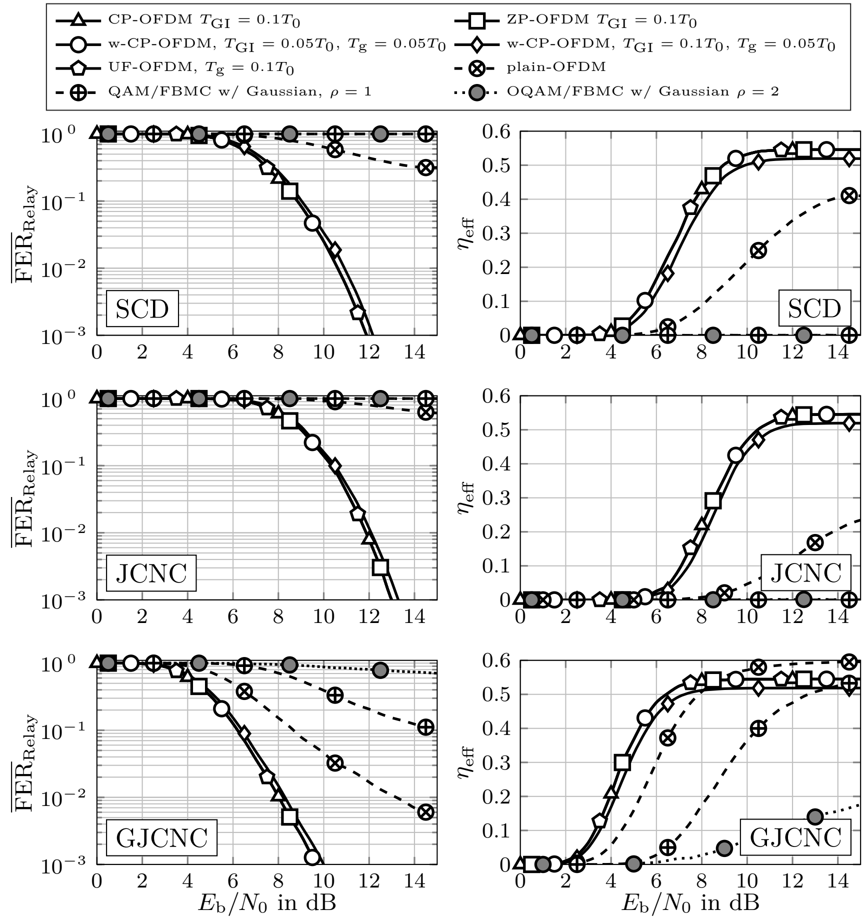

a) FER performance b) Throughput performance

Figure 4.29: FER and throughput performance at the relay with FGE and $N_{\mathrm{N}} = 1$. Setup: $\Delta\tau = 0$, $\Delta\nu = 0$, $\nu^{\max} = 0$, QPSK.

set to $N_{\mathrm{It}}^{\mathrm{outer}} = 0$ and no a priori information is available within the FGE and the *no a priori assumption* in Alg. 4.1 line 12 on page 118 is used.

2. *Iterative*: This type is realized by either a fixed number of outer iterations $N_{\mathrm{It}}^{\mathrm{outer}} = 4$ and variable number of inner iterations $N_{\mathrm{It}}^{\mathrm{FGE}} =$

$1, 2, 3, 4$ for Fig. 4.30a, or a variable number of outer iterations $N_{\mathrm{It}}^{\mathrm{outer}} = 1, \ldots, 6$ and a fixed number of inner iterations $N_{\mathrm{It}}^{\mathrm{FGE}} = 3$. This configuration is the practical interesting scheme.

3. *Perfect a priori knowledge*: The perfect a priori knowledge of the symbols d_s^{AB} is available at the equalizer input, which is only analytically possible and serves as a best-case benchmark.

In Fig. 4.30a it can be observed that the FER performance converge with just 2-3 inner iterations and further iterations will not achieve a better performance. This result is meaningful as the interference is well-located around the desired symbol yielding cycles in the FG with a small girth of four.

In Fig. 4.30b the convergence behavior is slightly different *w.r.t.* the outer number of iterations with a fixed number of inner iterations $N_{\mathrm{It}}^{\mathrm{FGE}} = 3$. Here again, the iterations help to improve the FER performance at the relay. However, a saturation is achieved with roughly 4 - 5 outer iterations and the performance approaches almost the a priori bound.

For the further analysis, we set the iterative structure to $N_{\mathrm{It}}^{\mathrm{FGE}} = 3$ and $N_{\mathrm{It}}^{\mathrm{outer}} = 4$ based on this analysis.

Fig. 4.31 shows the FER performance of the PLNC detection schemes considering a varying number of neighbors $1 \leq N_{\mathrm{N}} \leq 6$ used per node in the FGE with perfect a priori knowledge and the iterative structure. The QAM/FBMC with Gaussian waveform $\rho = 1$ is compared to CP-OFDM for SNR working point of 5dB and 7dB. In all three PLNC detection schemes, CP-OFDM achieves a constant performance *w.r.t.* the number of neighbors due to the orthogonality, *i.e.* cycle freeness, in this synchronized time-invariant channel. Here, no message exchange occurs in the FGE and the symbol-by-symbol MAP solutions (4.13), (4.21) and (4.25) for the equalizer are exact. In contrast, QAM/FBMC starts with a higher FER at the relay with $N_{\mathrm{N}} = 1$, due to the unconsidered interference terms. Nevertheless, it achieves a high improvement utilizing only a few neighbors and the a priori feedback message in the FGE. It is worth mentioning that due to the well localized waveform about 4-5 neighbors are sufficient to outperform CP-OFDM. However, this is only valid for SCD and GJCNC as these schemes can fully exploit the underlying feedback message (4.44) and (4.46) within the inner iterations in contrast to the ambiguous mapping in the JCNC scheme (4.45). JCNC only outperforms CP-OFDM in the perfect a priori case.

A similar analysis is drawn in Fig. 4.32 *w.r.t.* the number of neighbors for OQAM/FBMC with QPSK symbol mapping for two SNR working points, *i.e.* $E_{\mathrm{b}}/N_0 = 5$dB and $E_{\mathrm{b}}/N_0 = 12$dB. This analysis confirm our

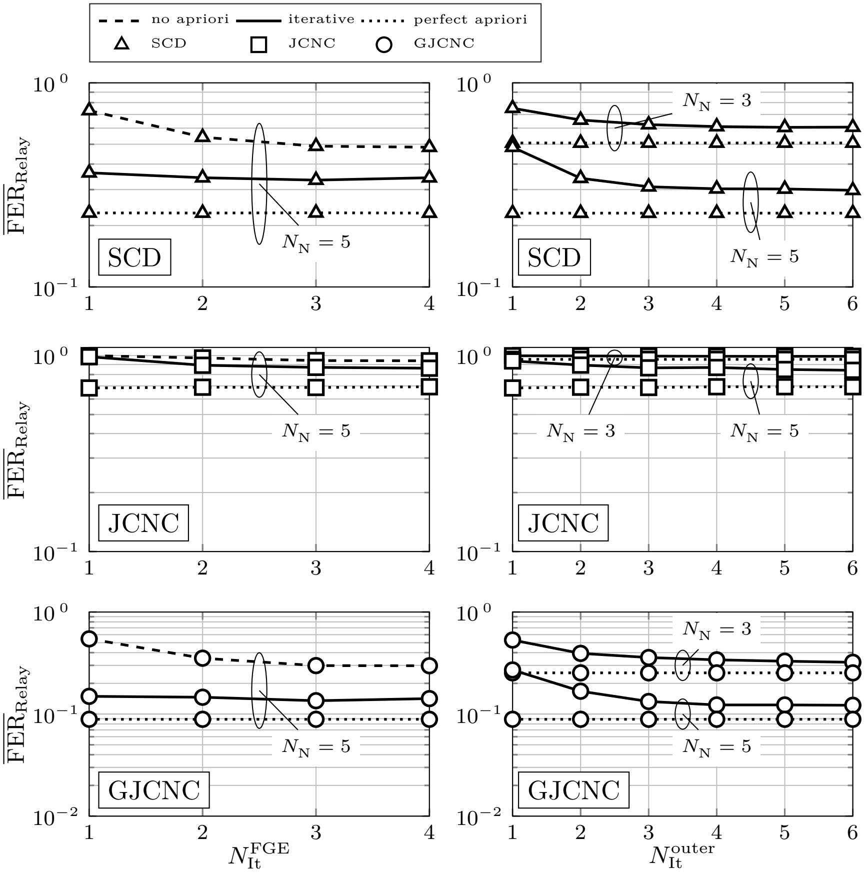

a) Inner Iterations $N_{\mathrm{It}}^{\mathrm{outer}} = 4$

b) Outer Iterations $N_{\mathrm{It}}^{\mathrm{FGE}} = 3$

Figure 4.30: FER performance at the relay for a different number of iterations a) in the FGE with $N_{\mathrm{It}}^{\mathrm{FGE}} = 3$ and b) outer iterations with $N_{\mathrm{It}}^{\mathrm{outer}} = 4$ at a $E_\mathrm{b}/N_0 = 5\mathrm{dB}$. Setup: $\Delta\tau = 0$, $\Delta\nu = 0$, $\nu^{\max} = 0$, QAM/FBMC with Gaussian waveform $\rho = 1$, BPSK.

expectation drawn in the interference analysis, *cf.* Section 4.4.2, with the need of a larger number of neighbors N_N in the FGE for OQAM based schemes. However, with the considered number of up to $N_\mathrm{N} = 7$, no gain is achieved compared to CP-OFDM in this synchronized setup. In

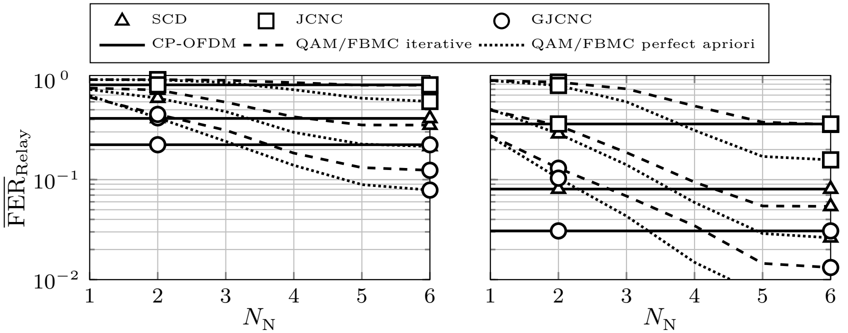

a) $E_{\mathrm{b}}/N_0 = 5\mathrm{dB}$ b) $E_{\mathrm{b}}/N_0 = 7\mathrm{dB}$

Figure 4.31: FER performance at the relay with different number of neighbors N_{N} in the FGE with perfect a priori information and the iterative structure and a BPSK symbol mapping.

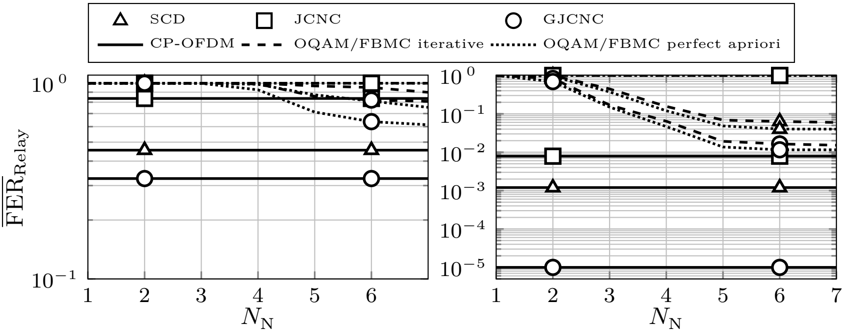

a) $E_{\mathrm{b}}/N_0 = 5\mathrm{dB}$ b) $E_{\mathrm{b}}/N_0 = 12\mathrm{dB}$

Figure 4.32: FER performance at the relay with different number of neighbors N_{N} in the FGE with perfect a priori information and the iterative structure and a QPSK symbol mapping.

contrast to QAM/FBMC with QPSK symbol mapping, the complexity of OQAM/FBMC is significantly lower as the symbol mapping can be seen as a BPSK mapping. Comparing the complexity consideration in the Appendix B, Fig. B.8, shows that QPSK with a number of neighbors N_{N} yield the same number of additions or multiplication than $N_{\mathrm{N}} + 2$ with BPSK. Nevertheless, even with $N_{\mathrm{N}} = 7$, OQAM/FBMC performs worse than CP-OFDM, which concludes that OQAM-based MC schemes are not suitable for TWRC with a single antenna at the relay [Min15] and [**WZWD16**]. Subsequently, we skip the OQAM-based scheme and we refer to [**WZWD16**] for a deeper analysis of OQAM/FBMC in TWRC. Therein, a second antenna at the relay is used, which allows resolving the phase problems and offers an improved FER performance as CP-OFDM and QAM/FBMC in a TWRC by the cost of a second receiver branch. However, a second antenna at the relay is out of scope of this thesis.

So far, we have seen that QAM/FBMC requires an equalizer with roughly 4-5 neighbors to outperform CP-OFDM. Fig. 4.33 shows the performance curves for the FBMC schemes with $N_{\mathrm{N}} = 3$ and $N_{\mathrm{N}} = 5$ over the SNR at the relay with the number of iterations $N_{\mathrm{It}}^{\mathrm{FGE}} = 3$ and $N_{\mathrm{It}}^{\mathrm{outer}} = 4$. The curves for CP-OFDM with $T_{\mathrm{GI}} = 0.1T_{\mathrm{S}}$ and $N_{\mathrm{N}} = 1$ are shown as benchmark. In all cases, the application of more neighbors yields a significant improvement in the FER performance already for $N_{\mathrm{N}} = 3$, and $N_{\mathrm{N}} = 5$ fully outperforms the CP-OFDM scheme as the system is more effective, which can also be seen in the throughput performance curves. The gain in performance, however, is bought by the higher complexity considering more neighbors in the FGE as will be indicated in the analysis in the appendix in Fig. B.8.

2. Scenario: Time Synchronized Multi-path Channel with CFO

For this analysis, we focus on the GJCNC detection scheme, only. The orthogonal MC schemes exploit their benefit of 1-tap frequency equalization in the synchronized scenario without any offset. However, as introduced in the interference analysis in Section 4.4, the FER performance of the schemes based on the rectangular waveform degrades in case of TO and CFO from the sinc shape in frequency domain. Here for clarity CP-OFDM with $T_{\mathrm{GI}} = 0.1T_{\mathrm{S}}$ and w-CP-OFDM with $T_{\mathrm{GI}} = 0.1T_{\mathrm{S}}$ and $T_{\mathrm{g}} = 0.05T_{\mathrm{S}}$ are shown, representatively.

Fig. 4.34 shows the FER performance of all considered schemes *w.r.t.* a varying normalized CFO $\Delta\nu$ with a 1-tap equalizer, *i.e.* $N_{\mathrm{N}} = 1$, and an FGE with $N_{\mathrm{N}} = 3$ and $N_{\mathrm{N}} = 5$ neighbors with the number of iterations $N_{\mathrm{It}}^{\mathrm{FGE}} = 3$ and $N_{\mathrm{It}}^{\mathrm{outer}} = 4$. As expected, by the application of a simple 1-tap equalizer the performance of the orthogonal schemes degrades extremely over the CFO. This result is highly related to the interference analysis in Fig. 4.7 *w.r.t.* CFOs as the additional introduced interference is unconsidered in the FGE, beside the Gaussian approximation. Considering more neighbors in the FGE achieve a high improvement for all MC schemes. Although many interference terms show up in the effective channel matrix for the “orthogonal” transmission schemes, also these schemes achieve a high improvement in error performance. Nevertheless, the Gaussian waveform with its robust shape allows even for high offsets roughly the same performance over a wide range of offsets. Especially, for higher offsets already $N_{\mathrm{N}} = 3$ in QAM/FBMC

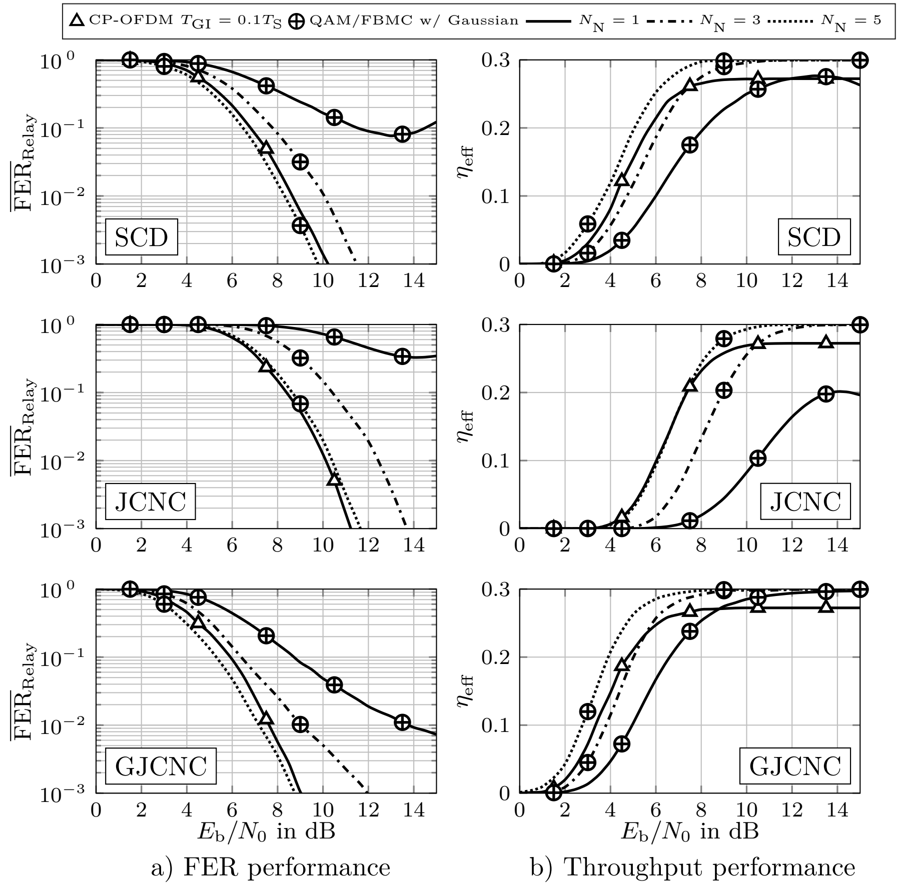

a) FER performance b) Throughput performance

Figure 4.33: FER and throughput performance at the relay for QAM/FBMC with a varying number of neighbors N_N and BPSK symbol mapping.

fully outperforms the other MC schemes in throughput due to its good localization property. Furthermore, QAM/FBMC outperforms all schemes in FER and throughput performance, even in the low offset region and serves as most robust scheme among all considered ones.

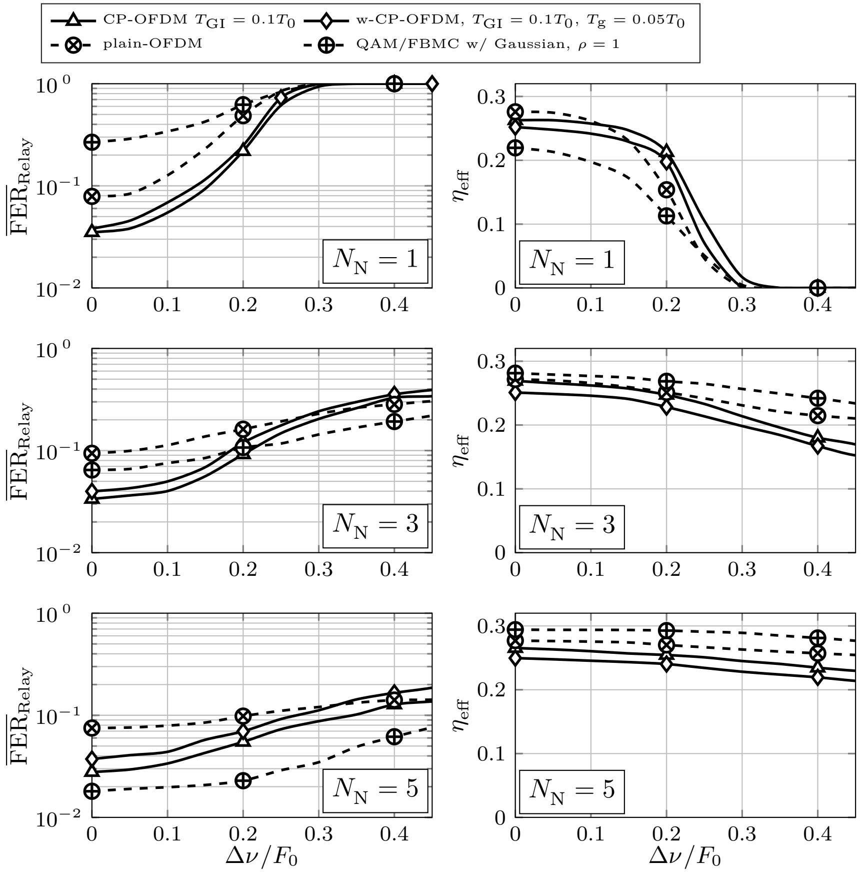

a) FER performance b) Throughput performance

Figure 4.34: FER performance at the relay over the normalized CFO at a fixed SNR of 7dB with the GJCNC detection scheme at the relay.

3. Scenario: Moving users in an LTE-like Setup

Beside CFO due to inaccuracy of the crystal oscillator (XO), also movement of the transmitter or receiver are a potential challenge in a communication scenario. So far, we have concentrated on TO and CFO values normalized to the symbol spacing in the time and frequency domain without explicit physical meaning. However, in this subsection we have a brief look on realistic offset values. Therefore, we fix the carrier frequency to $f_0 = 2.4\text{GHz}$

and focuses on devices with a relative speed $v_0 = 200\text{km/h}$ into the direction of the relay. Furthermore, a fixed CFO is assumed generated by a XO with an inaccuracy of roughly ±1parts per million (ppm) to ±10ppm resulting in an LTE like setup with a sub-carrier spacing $F_0 = 15\text{kHz}$ to a relative offset of $\Delta\nu = \pm 0.16F_0, \ldots \pm 1.6F_0$ and a maximum Doppler spread of $\nu^{\max} = 0.03F_0$[Wan12][12]. In this scenario, we analyze QAM/FBMC with Gaussian waveform $\rho = 1$ with the aforementioned complexity reduction techniques by the LE, wLE, with or without the sIC structure in Fig. 4.35 and compare the performance to CP-OFDM with the number of iterations $N_{\text{It}}^{\text{FGE}} = 3$ and $N_{\text{It}}^{\text{outer}} = 4$. The application of the LE and the wLE without

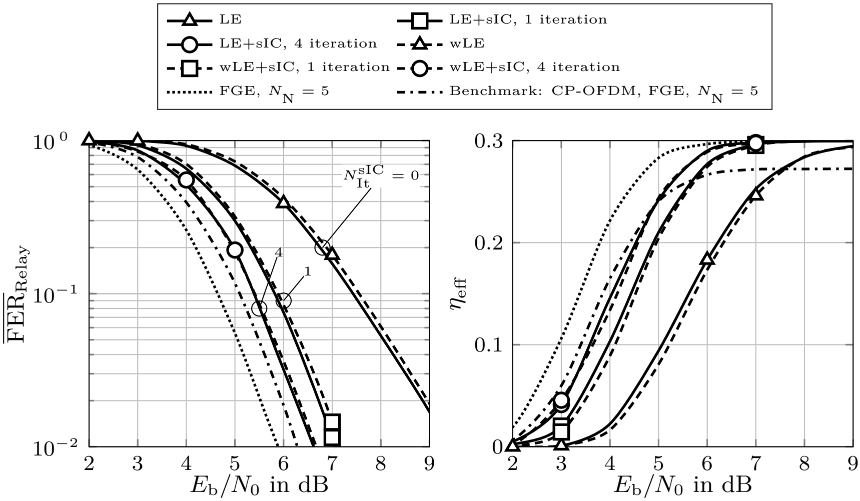

a) FER performance b) Throughput performance

Figure 4.35: FER and throughput performance using GJCNC decoding at the relay with FGE, wLE, wLE + sIC for time-variant channel with a maximum delay spread of $\tau^{\max} = 0.1T_{\text{S}}$, and maximum Doppler spread $\nu^{\max} = 0.03F_0$ and a CFO $\Delta\nu = 0.1F_0$ and no additional TO with BPSK symbol mapping for QAM/FBMC with Gaussian waveform $\rho = 1$. As benchmark CP-OFDM with FGE and $N_{\text{N}} = 5$ is also shown.

sIC has the worst performance. However, it can be observed that the application of just $N_{\mathcal{W}} = 1$ (or $N_{\text{N}} = 9$) roughly has the same performance

---

[12] *E.g.*, the inaccuracy of WLAN is allowed to be roughly ±20ppm for the 20MHz and ±10ppm for the 5MHz [IEE12]. In LTE the inaccuracy has to be strictly lower than ±0.1ppm [3GP11].

compared to the full inversion of the effective channel matrices with LE. By the additional application of the sIC algorithm, here with $N_{\mathrm{It}}^{\mathrm{sIC}} = 1$ and $N_{\mathrm{It}}^{\mathrm{sIC}} = 4$ a huge gain of up to 2dB is achieved. Nonetheless, the application of the sIC structure leads roughly to a pure diagonal structure, where the a priori information cannot be exploited by the subsequent FGE. Still, the best performance is achieved by the FGE using $N_{\mathrm{N}} = 5$ neighbors with QAM/FBMC with the iterations $N_{\mathrm{It}}^{\mathrm{FGE}} = 3$ and $N_{\mathrm{It}}^{\mathrm{outer}} = 4$.

Finally, the properties of the aforementioned equalizer structures are summarized in Table 4.4. It should be noted that we cover here the full FGE (fFGE) considering all occurring neighboring terms in the FG or the reduced FGE (rFGE) covering only N_{N} neighbors in the FG.

Table 4.4: Overview Equalizers

	LE	LE+sIC	wLE	wLE+sIC	fFGE	rFGE
problem	MMSE	MMSE	MMSE	MMSE	MAP	MAP
window.	✗	✗	✓	✓	✗	✓
feedback	(✗)	✓	(✗)	✓	✓	✓
scalable	✗	✗	✓	✓	✗	✓
iterativ.	✗	✓	✗	✓	✓	✓
complex.	➴	➶	↓	➵	↑	➵(N_{N})
perform.	✓	✓✓	✓	✓✓	✓✓✓	✓✓✓

4.7 Chapter Summary

This chapter summarizes the publications that have already been published, *i.e.* [**WLW+14, SWW+14, SPS+15, WWD15a, WWD+15b, WWD15a, WSW+16, WWD16, WWD18**]. Furthermore, this chapter provides a detailed overview of the combination of a two-phase TWRC, PLNC detection schemes and general non-orthogonal waveforms. It has been shown that the main performance driver is a suitable combination of MC scheme with general waveforms, relay word detection algorithm, and receiver architecture. For this we have introduced the FGE at the relay, which meets the high requirements of TWRC. The interpretation of the entire transmission by a FG and in particular the equalizer provides a deeper insight into the structure of the TWR transmission. The structure of the FGE is mainly controlled by the effective channel matrix and the chosen PLNC detection scheme and can be controlled by the introduced neighbor parameter N_{N}. Especially under strong channel influences, the effective channel matrix of the well-known CP-OFDM is influenced by strong amplitude variations. In contrast, the use of general waveforms in QAM/FBMC offers robustness to these variations. In a synchronous transmission, CP-OFDM outperforms the QAM/FBMC with the application of a simple one-tap frequency domain equalizer, *i.e.* using only one neighbor within the equalizer. And in QAM/FBMC, more neighbors N_{N} are needed to perform better than CP-OFDM. However, synchronous reception cannot be assumed in TWRCs as it cannot be guaranteed to synchronize both users exactly. For asynchronous transmission, the non-orthogonal QAM/FBMC with Gaussian waveform outperforms the orthogonal CP-OFDM for a wide range of offsets with only $N_{\mathrm{N}} = 3$, and it completely outperforms the other scheme with $N_{\mathrm{N}} = 5$ neighbors. Nevertheless, QAM/FBMC is always favorable by means of spectrum shaping and spectral efficiency, even in synchronized transmission, since it waives a GI by the expanse of a higher order equalizer. The complexity in the FGE was reduced by an MMSE-based linear filter and additional windowing, resulting in lower computational complexity in the FGE. Nevertheless, this gain in performance and spectral shape is carried at the expense of complexity. The performance gain depends on the scenario, *i.e.* on the signal power and the physical channel, but also on the desired data rate, and a system designer must decide to what extent the receiver is willing to implement this complexity to recover the data. All simulation results indicate the good properties of MC transmissions in TWRC, especially in asynchronous reception at the relay.

Chapter 5

Multi-Carrier Compressed Sensing Multi-User Detection

5.1 Overview

In recent decades, the high data rate has been a driver for the design of mobile communication systems. The research community has been focusing on technology components to meet the needs of communication systems for human to human communication. Recently, however, the focus has increasingly been on communication between machines of the so-called MTC. MTC is one of the big drivers for future communication systems. Keywords such as IoT in the private sector or Industry 4.0 (I4.0) for industrial applications are being used more and more. However, the demands placed on MTC are fundamentally different from those placed on human communication with regard to the type of communication. Where humans are more concerned with high data rates, e.g. when watching videos or playing games, MTC communication is mostly concerned with small data packets that are reliably exchanged between two autonomous entities.

If one continues to assume that, as predicted by Cisco [Cis19], MTC communication will soon make up a considerably large part of communication, *i.e.* from 2017 11% to 2022 31% of the global mobile devices with a total traffic portion of 2.2% in 2021, one must ask oneself whether the current communication systems such as LTE or wireless-fidelity (WI-FI) for this massive MTC are at all still tailored to the current requirements. IoT and I4.0 refer to the explosive growth of devices such as sensors measuring physical values like temperature, pressure, the status of a switch *etc.* [NO16, She16].

Nevertheless, existing communication systems such as Bluetooth (IEEE 802.15.1), Zigbee (IEEE 802.15.4), WI-FI (IEEE 802.11b) or NB-IoT in LTE (LTE-A Release 13 [3GP17]) try to incorporate the new requirements into the standardization process [LCL11, 3GP13, BPN^{+}16, BPW^{+}18, SW19].

Among the numerous use cases for MTC ranging from high data rate services to low data rate services, sporadic MTC raises special demands on existing communication systems. This class describes nodes that are not always active. Many MTC applications such as sensor networks, smart meters or medical applications have a very low data rate and MTC devices are mostly inactive, resulting in sporadic traffic [FFK^{+}11] This type of communication is called sporadic MTC communication. However, if one assumes that a huge number of nodes are present in the network, one speaks of sporadic massive MTC. Integrating sporadic traffic with short packets into existing systems is challenging, as the overhead used for signaling may be too large. Existing system rely on access reservation as shown in Fig. 5.1a, where before transmitting data a handshake between a node and a base-station takes place to negotiate free physical resources. The small packet size in sporadic MTC leads to ineffective communication, where the communication part consists more of signaling than data. Furthermore, if one assumes that

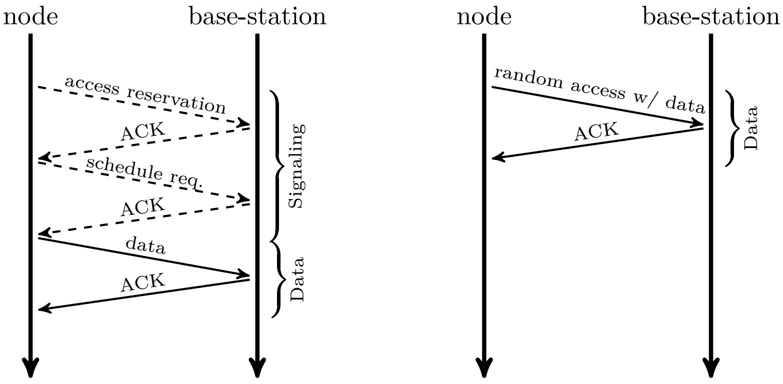

a) access reservation b) direct random access

Figure 5.1: Medium access reservation protocol versus direct random access protocol.

a massive number of devices are present in the system, this can lead to a collapse of the communication, since the communication consists only of signaling[CW10, RMGV14].

As possible solution DRA was considered as a PHY layer candidate technology in METIS [OMM16], which reduces the signaling effort for sporadic MTC. The medium access reservation and the DRA are shown in Fig. 5.1. In contrast to medium access reservation, the nodes send their data packets directly and without prior signaling in DRA.

With this access method, as shown in Fig. 5.1b, a device sends when it has something to send without prior signaling. The challenge of this approach is to shift the complexity to the base-station, which has to resolve the interference, *i.e.* multi-user interference (MUI), of the nodes in the system. Here we achieve that the signaling is almost completely omitted, but buy this with the uncertainty of when a node was active and which one. Furthermore, collisions cannot be avoided, as two nodes could transmit at the same time.

Central Question

With regard to the system mentioned above, the main questions in this chapter are: *Which concepts are necessary for a robust data transmission of many simple sporadically active nodes to a base station without much signaling?*

Structure of this Chapter This chapter is organized as follows: In Section 5.2 the general setup and system model of a massive number of nodes transmitting sporadically data to a base station is presented. A slotted random access is used for the transmission of this data. Recent developments uses compressed sensing-multi-user detection (CS-MUD) to solve the problem of activity and data estimation at the base station. This concept is based on compressed sensing (CS) used for multi-user detection (MUD), both CS and CS-MUD will be briefly introduced.

In Section 5.3, we take the advantage of CS-MUD and introduce a multi-carrier narrow band system that addresses key aspects such as massive access, flexible resource allocation and bandwidth efficiency. This MCSM system efficiently combines three PHY layer technologies to achieve a simple system model [**MWBD15b**]. We describe the processing at the MTC terminals and the multiplexing of MTC nodes in the frequency domain and concentrate on various MC schemes. In order to flexibly allocate MTC traffic to radio resources, MCSM uses a combination of multi-carrier concepts and CDMA in the TF grid. This allows to multiplex MTC traffic within the coherence bandwidth of the channel. Here we can use non-coherent symbol mapping and receiver concepts that reduce the need for pilot overhead for channel estimation while providing a certain degree of robustness in terms of minor time/frequency offsets. We specify the detection model that describes a so-called multiple measurement vector-compressed sensing (MMV-CS) problem [CREKD05] and give a brief view on a recovery algorithm known from literature. Finally, CS-MUD also allows to efficiently detect MTC traffic while only a small number of radio resources are used. This can overload systems in the classical sense. In [**MWBD15b**] we introduced the general MCSM system concept and evaluated the performance in an uncoded setup. Additionally, we demonstrated MCSM in a hardware setup that includes a line of sight and a non line of sight connection. The results were presented in [**BMWD15, WMBD16**] and [Wil16].

The main own contributions of this thesis are: New transmission concepts components for MCSM that have not yet been published, such as 1. the use of non-orthogonal pilots for mean channel estimation, 2. the introduction of weighted spread sequences for more robust detection under time offsets, 3. resource efficient mapping in time-frequency grids, and 4. general multi-carrier techniques for robust detection under frequency offsets, will be introduced in Section 5.4. Section 5.5 focuses on new receiver concepts at the base station that represent multi-user transmission as FG and a data detection is done by the famous SPA and it beats the error rate of SotA MCSM data detection by 10-30dB. Finally, we prove the feasibility of MCSM in a realistic propagation environment including frequency selectivity and asynchronism in Section 5.6.

5.2 System Scenario

The scenario we have in mind is shown in Fig. 5.2, where a large number of N_u wants to transmit some data to a BS.

When using DRA, the base station is not aware of which nodes are currently active and sending data, so in addition to the usual data detection which is basically a multi-user detection (MUD) problem, the base station now also has the task of estimating the activity of the nodes. Recent research [BSD13, SD11, MBWD12, Sch15] has proposed a novel PHY layer technology that combines DRA and CS to estimate both: the activity of a sporadic active nodes **and** the data of the nodes. This approach exploits the sporadic structure of the MTC multi-user signal by using algorithms from sparse signal processing and CS [CT06] to establish a PHY layer approach based on CS and DRA and is called CS-MUD. With the matrix notation

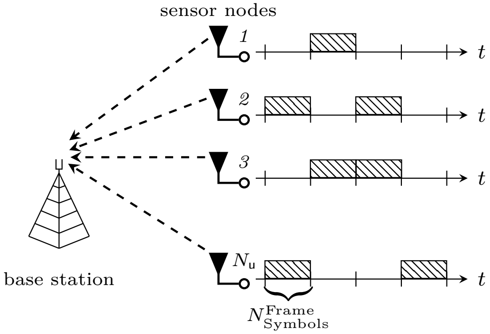

Figure 5.2: Machine to machine uplink scenario with N_{u} nodes transmitting frames of length $N^{\text{Frame}}_{\text{Symbols}}$ to a central BS assuming a slotted ALOHA (ALOHA) protocol as random access protocol.

introduced in Chapter 3, the total receive signal at the BS in Fig. 5.2 of N_{u} sporadically active sensor nodes can be written as

$$\mathbf{y} = \sum_{\mathsf{u}\in\mathcal{A}} \mathbf{M}^{\mathsf{u}}\mathbf{d}^{\mathsf{u}} + \mathbf{n} = \sum_{\mathsf{u}=1}^{N_{\mathsf{u}}} \mathbf{M}^{\mathsf{u}}\mathbf{d}^{\mathsf{u}} + \mathbf{n} \tag{5.1}$$

$$= \underbrace{\left[\mathbf{M}^{1}\ \mathbf{M}^{2} \cdots \mathbf{M}^{N_{\mathsf{u}}}\right]}_{\underline{\mathbf{M}}} \underbrace{\begin{bmatrix} \mathbf{d}^{1} \\ \mathbf{d}^{2} \\ \vdots \\ \mathbf{d}^{N_{\mathsf{u}}} \end{bmatrix}}_{\underline{\mathbf{d}}} + \mathbf{n} \quad , \tag{5.2}$$

where $\mathbf{M}^{\mathsf{u}}$ capture all impacts of the medium access such as general waveforms, effective channel impacts, synchronization errors *etc.*. In recent research [Sch15] different medium access schemes such as CDMA, OFDMA or multi-carrier-code division multiple access (MC-CDMA)[Kai98, FK00, Dek01, FK08, Kai02] were discussed. A further assessment of multiple access schemes used together with CS-MUD can be found in [Sch15]. In this work we limit ourselves to MC-CDMA, which will be presented in detail in Section 5.3.2. As the shaded frames in Fig. 5.2 indicate, only some sensor nodes are active. The traffic model is assumed to be Bernoulli distributed with an activity probability of $\mathrm{p_a} = \Pr(\mathbf{d} \neq \mathbf{0}) \ll 1$, and an inactivity probability of $\Pr(\mathbf{d} = \mathbf{0}) = 1 - \mathrm{p_a}$. However, most of the sensor nodes are assumed to be inactive, which can be described by the set of active users $\mathcal{A} = \{\mathsf{u} \mid \mathsf{u} \text{ is active}\}$ with $\mathsf{u} \in \{1, 2, 3, \ldots, N_{\mathsf{u}}\}$. If a node is inactive, *i.e.* it is quiet during a time slot, we can model this inactivity of a node mathematically by sending a frame $\mathbf{d}^{\mathsf{u}}$ of zeros. This results to an augmented symbol set $\mathcal{D}_0 = \mathcal{D} \cup \{0\}$ that if a user is active, the Tx symbol vector is $\mathbf{d}^{\mathsf{u}} \neq \mathbf{0}$ or the user is inactive with $\mathbf{d}^{\mathsf{u}} = \mathbf{0}$. The vector $\underline{\mathbf{d}}$ in (5.2) collects all user data vectors $\mathbf{d}^{\mathsf{u}}$. Hence, the stacked vector $\underline{\mathbf{d}}$ is called *block-sparse* for a low activity probability $\mathrm{p_a}$.

Subsequently, we give a brief introduction to the basics of CS-MUD jointly estimating the activity set $\hat{\mathcal{A}}$ **and** the data $\tilde{\underline{\mathbf{d}}}^{\mathsf{u}}$ of the nodes. Therefore, we will start with the general concept of a single measurement vector-compressed sensing (SMV-CS) problem and some mathematical measurement that provide a more detailed insight into the properties of CS. In addition, there is the MMV-CS problem which enables a compact representation especially for block-sparse systems.

5.2.1 Basics of CS-MUD

Previous works on CS-MUD [SBD13a, SBD13b, Sch15, Mon17, KD18] assumed a PHY layer-based setup in which several nodes transfer data to a BS. Although the nodes should be as simple as possible key components of communication technologies, *e.g.*, channel coding, multiplexing techniques *etc.* must be implemented to ensure a successful transmission. Concepts for estimating activity and data at the BS are based on sparse signal processing and CS. Before going into the details of the MCSM system using the general concept of CS-MUD in the Section 5.3, we will briefly introduce in this subsection the general concept of CS with a SMV-CS and a MMV-CS representative. For a further detailed description of CS-MUD the reader is referred to [Sch15, Mon17, KD18] and references therein. Afterwards, we take a look at the famous group orthogonal matching pursuit (GOMP) recovery algorithm An error classification and the connection of the general CS mathematics to CS-MUD complete this subsection, before we connect the CS mathematics with the MUD problem statement.

Compressive Sensing

SMV-CS Problem By assuming a mathematical linear vector model, the SMV-CS problem can be generally described by

$$\mathbf{y} = \mathbf{M} \underbrace{\boldsymbol{\Phi}\mathbf{d}}_{\mathbf{x}} + \mathbf{n} \quad , \tag{5.3}$$

where $\mathbf{M} \in \mathbb{R}^{N_\mathbf{y} \times N_\mathrm{x}}$ is the measurement matrix (also called sensing matrix) that models the relationship between the observations $\mathbf{y} \in \mathbb{R}^{N_\mathbf{y}}$ with length $N_\mathbf{y}$ and the signal $\mathbf{x} \in \mathbb{R}^{N_\mathrm{x}}$ of length N_x. An additional distortion by an AWGN vector $\mathbf{n}$ is assumed. The equation in (5.3) is illustrated in Fig. 5.3. The dimension of the observation $\mathbf{y}$ is much smaller than the dimension of $\mathbf{x}$, *i.e.* $N_\mathbf{y} \ll N_\mathrm{x}$ such that the matrix $\mathbf{M}$ is a **fat** matrix and that we have much fewer observations than unknowns. In linear algebra, the left inversion of a fat matrix does not exist, making it impossible to uniquely recover $\mathbf{x}$ from $\mathbf{y}$ without additional side information. One of the main assumptions in CS is that $\mathbf{x}$ is *compressible*. This means that a sparsity transformation matrix $\mathbf{\Phi}$ exists, so that $\mathbf{x} = \mathbf{\Phi d}$ is *sparse*. A signal, here $\mathbf{d}$, is $\mathscr{s}$-sparse when the number of non-zero elements is smaller than $\mathscr{s}$, or in other words $\mathbf{x}$ is compressible via $\mathbf{d}$. For example, the Joint Photographic Experts Group (JPEG) compression is based on the observation that a change of the basis by discrete cosine transform (DCT) or a wavelet basis to a spectral domain produces a sparse signal representation of most pictures. In some cases, the vector $\mathbf{d} = \mathbf{x}$ is directly sparse. In this case the sparsity transformation matrix is $\mathbf{\Phi} = \mathbf{I}$.

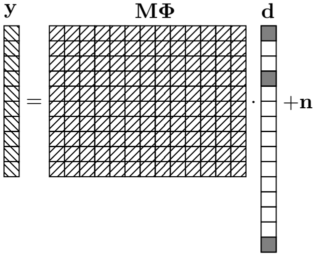

Figure 5.3: SMV-CS problem statement.

The aim of CS is twofold: on the one hand, we want to have good recovery properties and, on the other hand, recovery should be possible with as few measurements as possible. These properties depend on the dimension $N_\mathrm{x}, N_\mathbf{y}$ and on the sparsity $\mathscr{s}$, *i.e.* the number of non-zero elements $\mathscr{s} = \|\mathbf{d}\|_0$ measured by the ℓ^0-*"norm"*[1].

The recovery of $\mathbf{d}$ or $\mathbf{x}$ (if $\mathbf{\Phi}$ is known) from $\mathbf{y}$ is the basic CS reconstruction problem and it can be solved in the noiseless case like

$$\tilde{\mathbf{d}} = \arg\min_{\mathbf{d} \in \mathbb{R}^{N_\mathbf{d}}} \|\mathbf{d}\|_0 \quad \text{subject to} \quad \mathbf{Mx} = \mathbf{y} \quad . \tag{5.4}$$

---

[1] The ℓ^0-*"norm"* is neither a norm in a mathematical sense nor a pseudo norm. In the context of CS, however, the term "norm" is often used.

The complexity of finding the sparsest solution $\tilde{\mathbf{d}}$ in (5.4) of an under determined system is non-deterministic polynomial-time (NP)-hard [HV02]. Principally, three main different methods are known used in CS: the optimization method *e.g.* (5.4) with a relaxation of the ℓ^0-*"norm"* to ℓ^1-norm, greedy methods and thresholding methods. We focus on greedy algorithms in this work, but we invite the reader to [EK12, FR13] for a good overview of the other CS recovery methods. At this point the questions arises: *Are there some quantities to indicate the recovery performance?*

The answer to this question is not easy and also to show performance guarantees are not trivial [EK12, FR13, Sch15], but there are conditions to the matrix $\mathbf{M}$, which lead to the fact that a unique solution of the detection problem exists in the noise free environment. Therefore, we introduce the term of mutual incoherence property (MIP) [MZ93, DH01] defined as

$$m_{\mathrm{i}} = \max_{q \neq \iota} \frac{|\langle \mathbf{M}_{:,q}, \mathbf{M}_{:,\iota} \rangle|}{\|\mathbf{M}_{:,q}\|_2 \|\mathbf{M}_{:,q}\|_2} \leq 1 \quad . \tag{5.5}$$

The MIP compares a pair of columns in the measurement matrix $\mathbf{M}$ *w.r.t.* the correlation in a normalized manner and obviously is upper bounded by one. The lower bound is given by the *Welch bound* [EK12, FR13, Sch15] with

$$\underbrace{\sqrt{\frac{N_{\mathrm{x}} - N_{\mathbf{y}}}{N_{\mathbf{y}} \left(N_{\mathrm{x}} - 1\right)}}}_{\text{Welch bound}} \leq m_{\mathrm{i}} \leq 1 \tag{5.6}$$

and depends only on the dimensions of the measurement matrix $\mathbf{M}$. Furthermore, if the sparsity of $\mathbf{d}$ fulfills

$$\mathscr{s} = \|\tilde{\mathbf{d}}\|_0 \leq \underbrace{\frac{1}{2}\left(1 + m_{\mathrm{i}}^{-1}\right)}_{\text{RHS}} \quad , \tag{5.7}$$

the sparse estimation $\tilde{\mathbf{d}}$ is a unique solution of the SMV-CS recovery problem in the noiseless case, *i.e.* $\mathbf{n} = \mathbf{0}$ [EK12, FR13]. If the maximum correlation m_{i} is sufficiently small, the MIP states that an exact recovery is very likely and in some cases can even be guaranteed *e.g.* [Tro04].

Fig. 5.4 shows the MIP and the right-hand-side (RHS) of (5.7) for an *w.l.o.g.* exemplary fixed value of $N_{\mathrm{x}} = 120$ for a different number of measurements $N_{\mathbf{y}}$. Especially, for the right plot, where the solid curve fulfill equation (5.7) with equality, it can be observed that a significant small sparsity is needed to guarantee a unique solution ($\mathscr{s} \ll N_{\mathbf{y}}$). As expected, with a "sparsity" of $\mathscr{s} = N_{\mathrm{x}}$ a unique solution exists only with full-determined system, *i.e.*

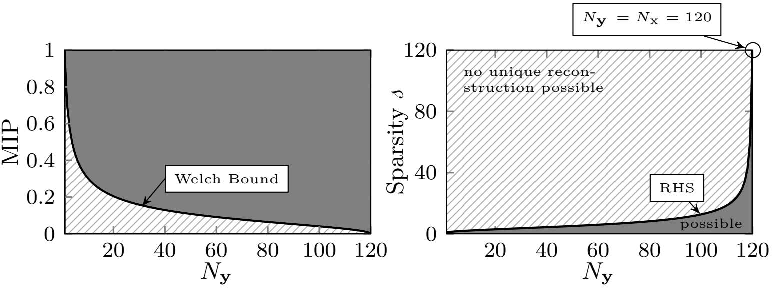

Figure 5.4: MIP and the sparsity of system with $N_{\mathrm{x}} = 120$ and different number of observations.

$N_{\mathbf{y}} = N_{\mathrm{x}} = 120$. Note, that these results are only valid in the noiseless case, furthermore, the quantities of MIP and (5.7) give no design rules on the structure of the measurement matrix $\mathbf{M}$.

MIP is a simple tool because it reflects only the most extreme relationships in the dictionary. However, the lower bound on the coherence, *i.e.* the Welch bound in (5.6) limits the performance analysis of recovery algorithms to rather small sparsity levels. A better measurement to overcome this limitation gives the so-called restricted isometric property (RIP), which consider not only pairs of columns of a matrix, but also all $\mathcal{s}$-tuples of columns and is therefore more suited to assess the quality of a matrix $\mathbf{M}$. However, the calculation of the RIP for a given matrix is very complex and we limit ourselves in this work on this short introduction of MIP and invite the reader to [EK12, FR13, KD18, Sch15] for further recovery properties.

MMV-CS Problem A system, where the sparsity pattern is the same for N_{Frames} measurements, is called MMV-CS. The same sparsity structure means that the indices of the non-zero elements in the vector $\mathbf{d}$ are the same for several measurements, the MMV-CS formulation

$$\mathbf{Y} = \mathbf{M}\mathbf{\Phi}\mathbf{D} + \mathbf{N} \tag{5.8}$$

can be used, also illustrated in Fig. 5.5. The observation matrix $\mathbf{Y} \in \mathbb{R}^{N_{\mathbf{y}} \times N_{\mathrm{Frames}}}$ and the symbol matrix $\mathbf{D} \in \mathbb{R}^{N_{\mathbf{y}} \times N_{\mathrm{Frames}}}$ are still connected by the measurement matrix $\mathbf{M}$ and $\mathbf{\Phi}$ like in the SMV-CS case. The matrix $\mathbf{Y}$ contains multiple measurements of the same sparsity structure. The sparsity can be redefined in terms of row-wise sparsity $\mathcal{s}_{\mathrm{B}}$, which counts the number of non-zeros rows in $\mathbf{D}$. One may note that each MMV-CS problem can be also rewritten as SMV-CS problem with a block-sparse

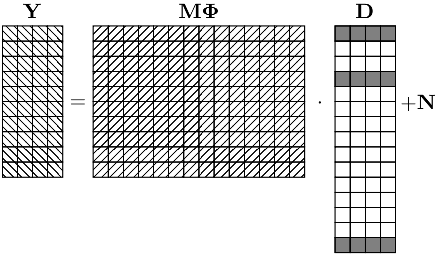

Figure 5.5: CS problem statement.

vector $\underline{\mathbf{d}}$ and a block-diagonal measurement matrix $\mathbf{M}$, but in general not vice versa.

As will be shown in Section 5.3.4 the The MMV-CS problem (5.8) can be used to model sporadic MTC transmissions to a BS.

Recovery Algorithm After stating the mathematical problem in SMV-CS or MMV-CS, the question of recovering the vector $\mathbf{d}$ and the matrix $\mathbf{D}$ arises. In [EK12, CREKD05, FR13, MBD14] some recovery algorithms are presented, which can deal with this problem. Furthermore, in [Sch15, Mon17] recovery algorithms in the context of CS-MUD are deeply discussed. One famous algorithm is the GOMP algorithm, which is an extension of the orthogonal matching pursuit (OMP) algorithm utilizing the group structure in the MMV-CS statement (5.8). Both algorithms, the OMP for SMV-CS and GOMP for MMV-CS are very similar, thus, we only introduce the GOMP algorithm in Alg. 5.1 and refer to [Sch15] for the OMP. This iterative greedy algorithm starts with an empty set of non-zero elements, which is filled per iteration with the supposedly non-zero entries[2]. After the decision of an non-zero position, the corresponding data is subtracted and the residuum is used for the next iteration.

---

[2] With regard to the CS-MUD concept that we have in mind, we will non-zero element and activity are interchangeable.

Algorithm 5.1 MMV-GOMP algorithm

```
# Initialize
$\mathcal{A}^{(0)} = \emptyset,\ q = 0,\ \mathbf{R}^{(0)} = \mathbf{Y},\ \widetilde{\mathbf{D}} = \mathbf{0}_{N_\mathrm{s} \times N_\mathrm{Symbols}^\mathrm{Frame}}$
# Start calculations
repeat
    $q = q + 1$
    # Find column with the highest correlation to residuum
    $\tilde{\mathsf{u}} = \arg\max_{\mathsf{u}} \sum_{\ell=0}^{N_\mathrm{Symbols}^\mathrm{Frame}-1} \left| \mathbf{M}_{:,\mathsf{u}}^\mathsf{H} \mathbf{R}_{:,\ell}^{(q-1)} \right|$
    # Update active and inactive set
    $\mathcal{A}^{(q)} = \mathcal{A}^{(q-1)} \cup \tilde{\mathsf{u}}$
    # Estimate data of active nodes
    $\widetilde{\mathbf{D}}_{\mathcal{A}^{(q)},:} = \mathbf{M}_{:,\mathcal{A}^{(q)}}^\dagger \mathbf{Y}$
    # Update residuum
    $\mathbf{R}^{(q)} = \mathbf{Y} - \mathbf{M}\widetilde{\mathbf{D}}_{\mathcal{A}^{(q)},:}$
until $q = N_\mathrm{act}$
# Output
$\hat{\mathcal{A}} = \mathcal{A}^{(q)}$ and $\widetilde{\mathbf{D}} = \widetilde{\mathbf{D}}_{\mathcal{A}^{(q)},:}$
```

For further details on the recovery algorithm the reader is referred to [CREKD05] and references therein.

The application of the GOMP on the system model (5.2) needs the full knowledge of $\mathbf{M}$. One may note that to fully recover the data and the activity, the GOMP needs the knowledge of the measurement matrix $\mathbf{M}$, the sensing matrix $\mathbf{\Phi}$ and the sparsity level $\mathscr{s}$.

Connection of CS to solve MUD: CS-MUD

In the previous section we looked at the signal structure of a general mathematical under-determined equation system, describing the structure of an SMV-CS and an MMV-CS problem. As recovery algorithm we looked at the GOMP, which can find a solution for the non-zero positions and their values under the condition of a block-sparse data signal. If we once again recapitulate the mMTC setup in (5.2), which generates a receive signal from a massive number of nodes using a DRA for transmission, it has already been shown in [ZG11, SD11, BSD13] that this MUD problem can be solved by interpreting this as SMV-CS at the base station. Furthermore, it was shown that if the signal has a block structure, the signal can be described as MMV-CS problem. The detection for MUD solved with the help of a CS approach is then called CS-MUD. By the interpretation as CS-MUD problem, the measurement matrix $\underline{\mathbf{M}}$ captures now all medium access effects of all users, including the effective channel, and the stacked symbol vector $\underline{\mathbf{d}}$ contains the data of active nodes and zeros for inactive nodes. The sparsity mentioned in CS is directly linked to the number of active users as the inactive users are modeled as transmitting zeros. By using CS reconstruction techniques, the BS is able to reconstruct the activity and data information, even if the system (5.2) is under-determined, *i.e.* $N_{\mathbf{y}} \ll N_{\mathbf{d}}$. In this case we have a system load $\beta = \frac{N_{\mathbf{d}}}{N_{\mathbf{y}}} > 1$. Other media access methods do not permit a system load of more than one directly, so that when sporadic activity is exploited, more users can be in the system than resources are available, which is a huge advantage of CS-MUD taking the advantage of the low activity of the user nodes in the system.

A big challenge at the BS applying the GOMP algorithm in Alg. 5.1 is to obtain the full knowledge of the medium access matrix $\mathbf{M}^{\mathsf{u}}$ per user, which is necessary to recover the data. This is a difficult task, as the medium access also includes the each user's physical channel and estimating a massive number of channel coefficients seems impossible due to the immense amount of signaling overhead [SBD13b].

In the next section we show a possible realization of (5.2) using MC-CDMA and a sub-carrier allocation within the coherence bandwidth with good approximations about the medium access matrix $\underline{\mathbf{M}}$. This simplification transfers the SMV-CS (5.3) into an MMV-CS problem (5.8) with a fully known measurement matrix at the BS.

5.2.2 Error Classification

Unlike scheduled access reservation protocols, where a user's activity is perfectly known and the data estimation errors are based on the data detection, there are other possible sources of error in DRA. Due to the activity detection in DRA also activity errors are possible. Fig. 5.6 illustrates all error events in a DRA system related to [Sch15, Mon17]. The following errors may occur during a recovery at the BS for separated data and activity detection:

1. *No error:* No error occurs, *i.e.*, the activity is decided correctly, *i.e.* the estimated user index is in $\mathsf{u} \in \mathcal{A}$ and $\mathsf{u} \notin \hat{\mathcal{A}}$. And after decoding the correct information is achieved $\hat{\mathbf{b}}^{\mathsf{u}} = \mathbf{b}^{\mathsf{u}}$.

2. *Bit error:* The event of a symbol or bit error is the classical error

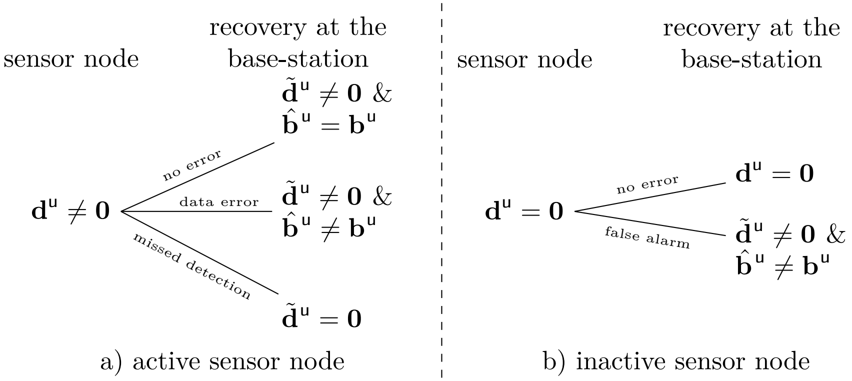

Figure 5.6: Possible Error Events.

in a communication system, where the activity for a user $\mathsf{u} \in \mathcal{A}$ is estimated correctly $\mathsf{u} \in \mathcal{A}$, but the underlying bit vector is erroneous $\hat{\mathbf{b}}^{\mathsf{u}} \neq \mathbf{b}^{\mathsf{u}}$.

3. *Missed detection (MD):* The MD is the event of detecting an active sensor node $\mathsf{u} \in \mathcal{A}$ as inactive. Such that the estimated activity set $\hat{\mathcal{A}}$ at the BS does not contain u, and thus the data vector is estimated as $\mathbf{d}^{\mathsf{u}} = \mathbf{0}$ yielding no useful information.

4. *False alarm (FA):* The event of detecting an inactive sensor node as active, *i.e.* $\mathsf{u} \notin \mathcal{A}$ and $\mathsf{u} \in \hat{\mathcal{A}}$, is called FA leading to a symbol vector-based on noise.

In the error event (bit error), the underlying channel coding scheme may be able to detect or even correct the bit errors. However, if the correction fails, the BS can detect such error events by applying a CRC code so that a retransmission can be requested. The most severe error event is MD causing a total data loss and, even worse, without indicating an error event, since the symbol vector $\tilde{\mathbf{d}}^{\mathsf{u}} = \mathbf{0}$ is a valid vector of the augmented alphabet $\mathcal{D}_0^{N_{\mathsf{d}}}$. For a FA event, the data symbol can be estimated as valid symbol vector. However, since the user is not active, the received signal does not contain any useful information of user u. This event can be efficiently detected by applying a CRC code, resulting in a detectable error event at the BS. However it has been shown in [Mon17] that by the occurrence of an FA the system suffers an SNR loss if the FA rate increases. The severe impact of the two activity errors (MD and FA) lead to serious effects on overall performance. To deal with this impact the authors in [MBD15, Mon17] propose a balancing algorithm to control both error events. Note that, these concrete algorithms do not fall within the scope of this thesis.

5.3 Multi-Carrier Compressed Sensing Multi-User Detection: The Concept

5.3.1 General Idea

Within the framework of MTC-based communication, we identified the following challenges: In contrast to human driven communication, where a small number of users usually require a large amount of data, the nature of machine-based communication differs completely. For example, a sensor node that measures the current temperature and the relative humidity and transmits it to a BS. Inside buildings or production halls, the temperature does not change too quickly, such that this transmission can be considered a **regularly-based** transmission. In addition, the amount of information is rather small compared to human communication. Simply mapping the temperature value to a **small packet** usually works with just 1 % of the capable WI-FI frame size or with 1 % of the corresponding LTE frame size. The big difference lies in the **massive** number of sensors to be expected within such a setup (as indicated above). In LTE usually 10-100 users can be served within one band at a BS simultaneously. With Bluetooth version 5.0[Gro16] (and also the older versions), up to 255 nodes can be connected to a master in different state modes, but only a maximum of seven slaves can communicate simultaneously in the CONNECTION state to the master. Both communication systems mentioned suffer from a high number of users and can only operate a limited number of devices which will not fit the new challenges.

Another characteristic of sensor nodes is the type of **sporadic** communication. If we take as an example the sensor node that measures the temperature within a production hall: For example, if the temperature jumps over a certain threshold, the sensor sends an **event-based** message, which in turn is a small packet, to the BS. Through this observation alone, exclusive and thus orthogonal physical resources lead to a large amount of unused physical resources. Therefore, DRA can be used to enable efficient use of physical resources. Unlike WI-FI, the physical random access channel (PRACH) in LTE or other schemes, in which DRA is also partly implemented, we do not assume here that collision avoidance methods are used for active users. We assume a DRA where each sensor node sends whenever it has something to send, so we could have a number of simultaneously active users N_{act} per frame. The BS then performs **activity detection** to estimate the data afterwards. In TWRC we assumed full knowledge of CSI for equalization and detection at the assisting relay. Contrary to the transmission of unidirectional P2P or TWRC, the **channel estimation** by a massive number of users would lead to enormous pilot overhead. In LTE we have a pilot overhead per user of about 15 or 48% to fully describe the CSI, which means a huge reduction in effective throughput on the one hand, and an **orthogonal allocation of pilots** is not feasible for a massive number of nodes even if only a low number of users is active (due to the scheduling of orthogonal pilots) [JKL$^+$16]. Another challenge is the allocation of data symbols to physical resources beside existing systems. Thus, **flexible allocation** on the TF grid is favorable, leading to multi-carrier schemes as introduced in Chapter 3 in combination with CDMA concepts. Especially the use of proper designed waveform can lead to a high reduction of the OoBE radiation, which makes it also applicable within white spaces in the spectrum. To serve a flexible and thus **scaleable** amount of users, CDMA concepts with non-orthogonal spreading sequences are used, which makes the system adaptive to higher loads. For wirelessly connected sensor nodes, a **cost-efficient and energy-efficient design** is important to achieve long battery life, leading to dump sensors. The algorithm used should be **robust** against influences of TO or CFO.

In the next section we first introduce the general idea of MCSM. The basic concept uses MC-CDMA with CP-OFDM within the coherence bandwidth of the channel and differential modulation to simplify the system model and provide a simple transmission scheme.

After the description of the general MCSM concept, further promising approaches such as non-orthogonal MC transmission schemes for node processing and factor graph-based estimation algorithms at the base station are presented which lead to an improvement of the performance especially in asynchronous scenarios.

5.3.2 The MCSM Concept

MCSM identifies three key components to cope with the above requirements and provide a flexible PHY layer solution as illustrated in Fig. 5.7.

1. *Multi-carrier Processing*: Multi-carrier (MC) schemes offer a flexible and scaleable possibility to assign symbols to a TF grid and serve here as first key component. Especially under “mild channel conditions”, each symbol on an orthogonal sub-carrier is only affected by one unknown channel coefficient and no additional interference term disturbs the

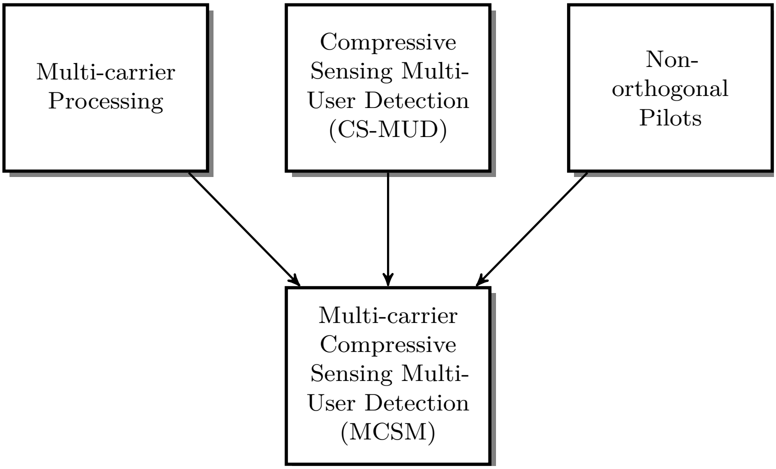

Figure 5.7: MCSM key components.

transmission. Furthermore, by requiring low data rate, the available spread data symbols can be allocated within the channel's coherence bandwidth, resulting in a single channel coefficient for a set of subcarriers within a small bandwidth. This property greatly simplifies the amount of channel estimation.

2. *Compressed Sensing-Multi-User Detection*: The second key component, as already introduced above, is CS-MUD exploiting the MUI of all users. Due to the sporadic nature of the transmission - whether event-driven or regular - fewer resources can be used than nodes exist in the system. Processing complexity is shifted to the BS, which requires algorithms (such as GOMP) to detect the activity and the data information of the nodes.

3. *Non-orthogonal pilots*: Data detection at the aggregation node demands either a non-coherent reception of the data symbols by, *e.g.* differential symbol mapping, or coherent reception. For the latter, the channel has to be known for all active nodes. The original approach of MCSM in [**MWBD15b**] requires differential symbol mapping. In the context of this work we also take a look at the average estimation of the channel, which offers soft values for the code bits and thus a better FER performance may be expected.

The following section introduces the general MCSM system concept including node processing and TF grid mapping. While MCSM offers the possibility to multiplex several narrow band MCSM subsystems simultaneously, we limit ourselves to the description of a certain MCSM subsystem with N_{u} nodes without loss of generality. The multiplexing of several MCSM subsystems will be explained later on. The general system topology is shown in Fig. 5.2 on page 145. Here, N_{u} nodes transmit frames with $N_{\text{Symbols}}^{\text{Frame}}$ symbols to a central BS for further processing. Fig. 5.2 also shows that not all nodes are permanently active but sporadically transmit frames to the BS. The traffic model is assumed to be Bernoulli distributed and determined by the node specific activity probability $\mathrm{p_a} = \Pr(\mathbf{d} \neq \mathbf{0}) \ll 1$, which we assume is the same for all the nodes in the system. With probability $\mathrm{p_a}$ a node is active and transmits a data frame to the BS, while $1 - \mathrm{p_a}$ specifies the probability that the node is inactive. Adaptations of the underlying CS-MUD algorithms for other traffic models have been investigated in [JBD15]. Furthermore, we assume a slotted ALOHA scheme [Abr70] as random access protocol, where the time is divided into slots and active nodes transmit only for the duration of a slot.

As already mentioned above, we use MC-CDMA with direct sequence spreading as medium access. For this reason, the matrix $\mathbf{M}^{\mathsf{u}}$ in (5.2) can be decomposed into two parts for a user u, such as

$$\mathbf{M}^{\mathsf{u}} = \underline{\mathbf{H}}^{\mathsf{u}}\underline{\mathbf{S}}^{\mathsf{u}} \quad , \tag{5.9}$$

where the MC transmission can be described by the effective channel matrix $\underline{\mathbf{H}}^{\mathsf{u}}$ capturing all effects of the physical channel and the underlying waveforms introduced by (3.25) and (3.26) in the MC Chapter 3.

User separation in this setup is based on CDMA with non-orthogonal spreading sequences, where each user is assigned a user-specific spreading sequence $\mathbf{s}^{\mathsf{u}}$.

The CDMA part of MC-CDMA can be modeled by the multiplication of a user specific stacked spreading matrix $\underline{\mathbf{S}}^{\mathsf{u}}$ with the user data vector $\mathbf{d}$.

All spreading sequences of all users can be stored in the columns of a spreading sequence matrix $\mathbf{S} \in \mathbb{C}^{N_{\mathrm{s}} \times N_{\mathsf{u}}}$, whereby the spreading sequence length is shorter than the number of users $N_{\mathrm{s}} \ll N_{\mathsf{u}}$. In a classical CDMA context, this system is referred to as resource efficient or in mathematical context under-determined, because we use fewer resources than users in the system.

5.3.3 MCSM Node Processing

In the following we describe the MCSM transmit signal generation at node u as shown in Fig. 5.8. To illustrate the basic idea of MCSM, we limit ourselves to a pure sub-carrier mapping of general M-PSK symbols. A realization with D-M-PSK as in the original work **[MWBD15b]** is presented later. We describe the signal generation at a specific node that is assumed to be active. First, a data stream of $N_{\mathbf{b}}$ bits $\mathbf{b}^{\mathsf{u}} \in \mathbb{F}_2^{N_{\mathbf{b}}}$ is encoded by an encoder $\mathcal{C}$ into a stream of code bits $\mathbf{c}^{\mathsf{u}} \in \mathbb{F}_2^{N_{\mathbf{c}}}$ with code rate $R_{\mathrm{c}} = \frac{N_{\mathbf{b}}}{N_{\mathbf{c}}}$, here $\mathbb{F}_2$ denotes the binary field. Subsequently, the stream of code bits $\mathbf{c}^{\mathsf{u}}$ is interleaved and further mapped with a modulator $\mathcal{M}$ to a symbol vector $\mathbf{d}^{\mathsf{u}} \in \mathbb{C}^{N_{\mathbf{d}}}$ via a M-PSK or M-QAM, leading to a user specific rate $\varrho^{\mathsf{u}} = \frac{N_{\mathbf{b}}}{N^{\text{Frame}}_{\text{Symbols}}} = \frac{N_{\mathbf{c}}\,R_{\mathrm{c}}}{N^{\text{Frame}}_{\text{Symbols}}} = \frac{N_{\mathbf{d}}\log_2(M)R_{\mathrm{c}}}{N^{\text{Frame}}_{\text{Symbols}}}$.

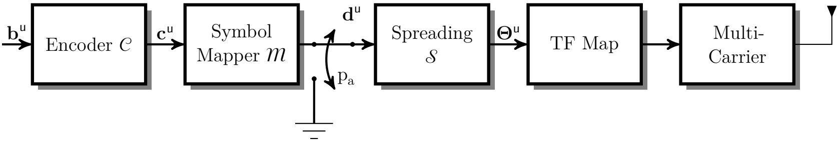

Figure 5.8: Block diagram of signal generation at MCSM node.

The next stage (Spreading $\mathcal{S}$) spreads the symbols $\mathbf{d}^{\mathsf{u}}$ to chips via a unique node specific spreading sequence $\mathbf{s}^{\mathsf{u}} \in \mathbb{C}^{N_{\mathrm{s}}}$ by

$$\boldsymbol{\theta}_i^{\mathsf{u}} = \mathbf{s}^{\mathsf{u}} d_i^{\mathsf{u}} \tag{5.10}$$

resulting in a user specific chip matrix $\mathbf{\Theta}^{\mathsf{u}}$ with columns $\boldsymbol{\theta}_i^{\mathsf{u}}$. Note, the latter matrix can also be generated by the Kronecker product with $\mathbf{\Theta}^{\mathsf{u}} = \mathrm{vec}\{\mathbf{d}^{\mathsf{u}} \otimes \mathbf{s}^{\mathsf{u}}\} = \mathrm{vec}\{\underline{\mathbf{S}}^{\mathsf{u}}\mathbf{d}^{\mathsf{u}}\} = \mathbf{s}^{\mathsf{u}}\mathbf{d}^{\mathsf{u}\mathsf{T}}$.

The last step in the MCSM signal generation is to multiplex the chips to physical resources, *i.e.*, to the TF grid and the generation of the MC signal. Here, we start the description based on CP-OFDM, which is generalized later on. The set $\mathcal{S}_i$ determines the sub-carriers that are allocated for transmission. Without loss of generality, we assume $|\mathcal{S}_i| = N_{\mathrm{s}}$, $\forall i$, *i.e.* the spreading factor matches the number of sub-carriers allocated (which we term pure sub-carrier mapping). We multiplex the weighted chip matrix $\mathbf{\Theta}^{\mathsf{u}}$ to $\mathcal{S}_i \subseteq \{0, \ldots, N_{\mathrm{IFFT}} - 1\}$ consecutive sub-carriers of the overall N_{IFFT} sub-carriers by using a partial power normalized IDFT matrix $\mathbf{F}^{\mathsf{H}}\mathbf{I}_{\mathcal{S}_i}^{\mathsf{T}} \in \mathbb{C}^{N_{\mathrm{IFFT}} \times |\mathcal{S}_i|}$ at the transmitter, which is related to a narrow band OFDMA transmission. Adding a CP as GI of length N_{CP} via the CP insertion matrix $\mathbf{T}_{\mathrm{I}} \in \mathbb{F}_2^{N_{\mathrm{CP}}+N_{\mathrm{IFFT}} \times N_{\mathrm{IFFT}}}$ yields the following description of the baseband transmit signal $\mathbf{x}_i^{\mathsf{u}}$ in vector notation for node u per symbol i

$$\mathbf{x}_i^{\mathsf{u}} = \mathbf{T}_{\mathrm{I}}\mathbf{F}^{\mathsf{H}}\mathbf{I}_{\mathcal{S}_i}^{\mathsf{T}}\boldsymbol{\theta}_i^{\mathsf{u}} \quad . \tag{5.11}$$

5.3.4 MCSM Detection Model

The following section mathematically formalizes the MCSM system model and states the detection model at the BS. The first processing step at the BS is to remove the guard interval via the CP removal matrix $\mathbf{T}_{\mathrm{R}} \in \mathbb{F}_2^{N_{\mathrm{IFFT}} \times (N_{\mathrm{IFFT}}+N_{\mathrm{CP}})}$. Afterwards, the time domain signal is transformed into frequency domain by the application of the partial DFT matrix $\mathbf{I}_{\mathcal{S}_i}\mathbf{F} \in \mathbb{C}^{N_{\mathrm{s}} \times N_{\mathrm{IFFT}}}$ selecting only the $|\mathcal{S}_i|$ sub-carriers used. The noise free user specific received signal for a frame can be written in the same way as the model in Chapter 3 by

$$\underline{\mathbf{y}}^{\mathsf{u}} = \underline{\mathbf{H}}^{\mathsf{u}}_{\mathcal{S}_i} \underline{\boldsymbol{\theta}}^{\mathsf{u}} \quad , \tag{5.12}$$

where $\underline{\boldsymbol{\theta}}^{\mathsf{u}} = \operatorname{vec}\{\boldsymbol{\Theta}\} = \mathbf{d}^{\mathsf{u}} \otimes \mathbf{s}^{\mathsf{u}}$ is the stacked weighted chip vector of user u. The partial frame-based effective channel matrix $\underline{\mathbf{H}}^{\mathsf{u}}_{\mathcal{S}_i}$ according to (3.41) and (3.43) contains only the sub-carriers used with the sub-carrier set $\mathcal{S}_i$

$$\mathbf{H}^{\mathsf{u}}_{\mathcal{S}_i,i',i} = \begin{cases} \mathbf{I}_{\mathcal{S}_i} \boldsymbol{\Sigma}^{\mathsf{u}}_{h,i',i} \mathbf{I}^{\mathsf{T}}_{\mathcal{S}_i} & i' = i \\ \mathbf{0}_{N_{\mathrm{s}} \times N_{\mathrm{s}}} & \text{otherwise} \end{cases} \quad . \tag{5.13}$$

Under mild channel conditions, *i.e.*, no frequency offset and timing offset and a channel length within the GI, the effective channel matrix (5.13) is purely diagonal and restricted to the set of sub-carriers used, illustrated by Fig. 3.13.

As stated above, the received signal at the BS can be described via the superposition of N_{u} user specific signals. Assuming that all nodes transmit frames of length $N^{\mathrm{Frame}}_{\mathrm{Symbols}}$, we obtain the multi-user (MU)-signal received at the BS

$$\underline{\mathbf{y}} = \sum_{\mathsf{u}=1}^{N_{\mathsf{u}}} \underline{\mathbf{y}}^{\mathsf{u}} + \underline{\mathbf{n}} = \sum_{\mathsf{u}=1}^{N_{\mathsf{u}}} \underline{\mathbf{H}}^{\mathsf{u}}_{\mathcal{S}_i} \underbrace{(\mathbf{d}^{\mathsf{u}} \otimes \mathbf{s}^{\mathsf{u}})}_{\underline{\boldsymbol{\theta}}^{\mathsf{u}}} + \underline{\mathbf{n}} \quad , \tag{5.14}$$

where $\underline{\mathbf{n}}$ is an AWGN vector.

As we pointed out in the MCSM concept that we allocate the spreading sequence along the sub-carriers within the coherence bandwidth, we can roughly assume that the channel is constant among the sub-carriers (*cf.* Fig. 5.9 with bandwidth 1) B_{MCSM}). With the channel coefficient h^{u}_i for the i^{th} MC symbol the diagonal parts in (5.13) can be approximated $\boldsymbol{\Sigma}_{\mathbf{H}} \approx h^{\mathsf{u}}_i \mathbf{I}_{N_{\mathrm{s}} \times N_{\mathrm{s}}}$. Therefore the partial frame-based effective channel matrix is given by $\underline{\mathbf{H}}^{\mathsf{u}}_{\mathcal{S}_i} \approx \operatorname{diag}\{\mathbf{h}\} \otimes \mathbf{I}_{N_{\mathrm{s}} \times N_{\mathrm{s}}}$, where $\mathbf{h}^{\mathsf{u}} = [h^{\mathsf{u}}_0, h^{\mathsf{u}}_1, \ldots, h^{\mathsf{u}}_i, \ldots, h^{\mathsf{u}}_{N^{\mathrm{Frame}}_{\mathrm{Symbols}}}]^{\mathsf{T}}$ is a vector collecting all channel elements over a frame. Hence, the overall

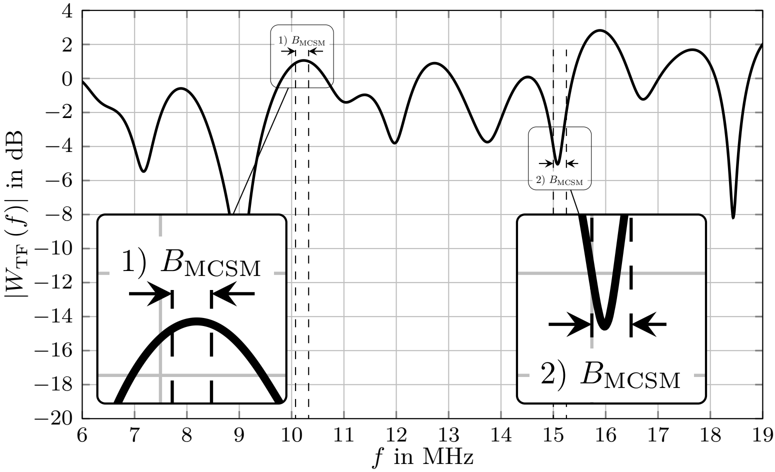

Figure 5.9: Possible channel realization with a maximum delay spread $\tau^{\max} = 1\mu s$, sampling rate of $T_{\mathrm{A}} = \frac{1}{26\mathrm{MHz}}$ and $N_{\mathrm{FFT}} = 2048$.

received signal can be then approximated by

$$\begin{aligned}\underline{\mathbf{y}} &\approx \sum_{\mathsf{u}=1}^{N_\mathsf{u}} \left(\mathrm{diag}\left\{\mathbf{h}^\mathsf{u}\right\} \otimes \mathbf{I}_{N_\mathrm{s}\times N_\mathrm{s}}\right) \cdot \left(\mathbf{d}^\mathsf{u} \otimes \mathbf{s}^\mathsf{u}\right) + \underline{\mathbf{n}} \\ &= \sum_{\mathsf{u}=1}^{N_\mathsf{u}} \underbrace{\left(\mathrm{diag}\left\{\mathbf{h}^\mathsf{u}\right\} \mathbf{d}^\mathsf{u}\right)}_{\tilde{\mathbf{d}}^\mathsf{u}} \otimes \underbrace{\left(\mathbf{I}_{N_\mathrm{s}\times N_\mathrm{s}} \mathbf{s}^\mathsf{u}\right)}_{\mathbf{s}^\mathsf{u}} + \underline{\mathbf{n}} \end{aligned} \tag{5.15}$$

where the vector $\tilde{\mathbf{d}}^\mathsf{u}$ contains the symbols of user u weighted by the channel coefficients $\tilde{d}_i^\mathsf{u} = h_i^\mathsf{u} d_i^\mathsf{u}$. Note that $\tilde{\mathbf{d}}^\mathsf{u} \otimes \mathbf{s}^\mathsf{u} = \mathrm{vec}\{\mathbf{s}^\mathsf{u} \tilde{\mathbf{d}}^{\mathsf{u}\mathsf{T}}\}$.

By further applying the vectorization operator on $\mathbf{Y} = \mathrm{vec}\{\underline{\mathbf{y}}\}$ the receive signal can be approximated by

$$\mathbf{Y} \approx \mathbf{S}\widetilde{\mathbf{D}} + \mathbf{N} \tag{5.16}$$

with $\mathbf{N} = \mathrm{vec}\{\underline{\mathbf{n}}\} \in \mathbb{C}^{N_\mathrm{s} \times N_{\mathrm{Symbols}}^{\mathrm{Frame}}}$, where the summation over all users in (5.15) can be realized by a matrix multiplication after applying the vectorization operator with spreading matrix $\mathbf{S} \in \mathbb{C}^{N_\mathrm{s} \times N_\mathsf{u}}$ containing the spreading sequences $\mathbf{s}^\mathsf{u}$ of all active and inactive nodes in the columns. The matrix $\widetilde{\mathbf{D}} \in \mathbb{C}^{N_\mathsf{u} \times N_{\mathrm{Symbols}}^{\mathrm{Frame}}}$ contains the modulated symbols from the N_u nodes weighted with the individual frequency domain channel tab, *i.e.* for user u the entries $\widetilde{\mathbf{D}}_{\mathsf{u},i} = h_i^\mathsf{u} d_i^\mathsf{u}$ contain the weighted symbol of node u at time instance i. $\mathbf{Y} \in \mathbb{C}^{N_\mathrm{s} \times N^\mathrm{Frame}_\mathrm{Symbols}}$ contains the $N^\mathrm{Frame}_\mathrm{Symbols}$ received chips as column vectors. Recovering $\widetilde{\mathbf{D}}$ from $\mathbf{Y}$ can be interpreted as MMV-CS problem introduced in (5.8) and can be solved by the GOMP in Alg. 5.1 or other algorithms from the literature.

By the application of the three basic concepts of MCSM, the SMV-CS problem (5.2) with "unknown" measurement matrix $\underline{\mathbf{M}}$ results in a MMV-CS problem with known measurement matrix $\mathbf{S}$ and row-sparse matrix $\widetilde{\mathbf{D}}$. Note that (5.16) is under-determined due to the fact that we use less radio resources than nodes resulting in a **fat** matrix $\mathbf{S} \in \mathbb{C}^{N_\mathrm{s} \times N_\mathsf{u}}$ with $N_\mathrm{s} \ll N_\mathsf{u}$. The load of this system can directly be given as $\beta = \frac{N_\mathsf{u}}{N_\mathrm{s}}$.

The overall BS processing is given in Fig. 5.10. After estimating the activity set $\hat{\mathcal{A}}$ and symbol matrix $\widetilde{\mathbf{D}}$, the BS is able to delete the unimportant rows of $\widetilde{\mathbf{D}}$ in the node sorting block and perform classical symbol demapping and decoding to obtain the underlying information of each user.

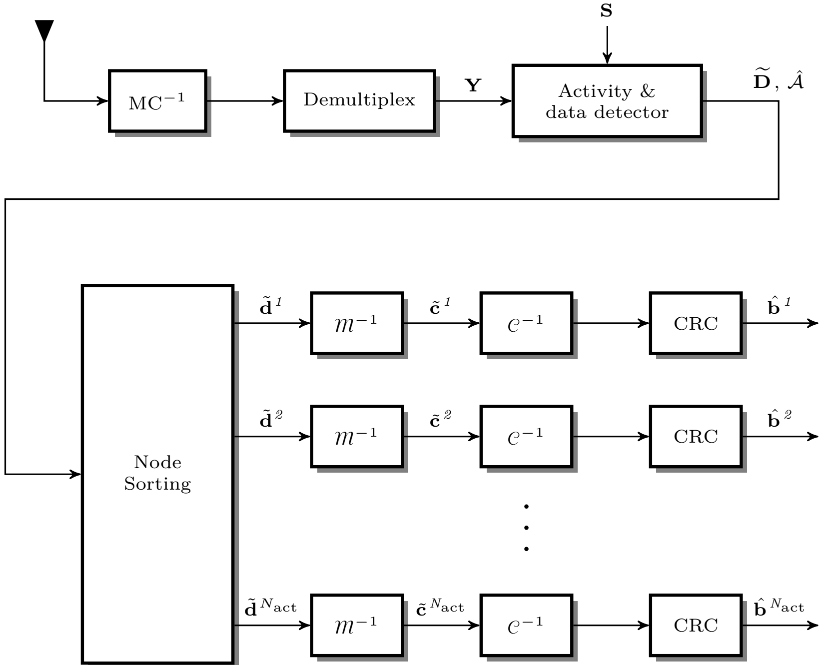

Figure 5.10: BS processing of N_act active user data streams.

5.3.5 Frequency Hopping and Channel Coding

The assignment of all spreading sequences $\mathbf{s}^{\mathsf{u}}$ to the same set of sub-carriers $\mathcal{S}_{i} = \mathcal{S}\ \forall i$ leads to a marginal change of the average channel coefficients h_{i}^{u} over time, particularly in a static channel scenario. Especially if the sub-carrier set is coincides a notch as shown in Fig. 5.9 (*cf.* Fig. 5.9 with bandwidth 2) B_{MCSM}), this overall effective channel cannot be described by a 1-path Rayleigh fading transmission.

To gain diversity, we define a changing sub-carrier allocation set $\mathcal{S}_{i}$, which changes according to a predefined pattern and results in frequency hopping. This method enables frequency diversity gains through reallocating the sub-carriers of each N_{hop} MC symbol and can be used when several MCSM systems are multiplexed to a certain bandwidth. The changing channel coefficient can be exploited by the channel decoding, which gains diversity.

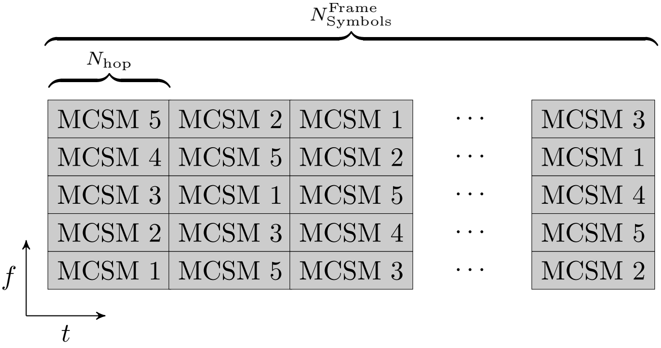

Figure 5.11: Illustration of possible scheduling. Each MCSM systems changes its sub-carrier allocation each N_{hop} symbols to gain frequency diversity.

Figure 5.11 illustrates this reallocation exemplary in a setup with 5 MCSM systems in which each MCSM system changes its sub-carrier allocation according to N_{hop} transmit symbols and thus gains in frequency diversity through encoding and interleaving via time symbols with $N_{\mathrm{pilots}} = \lceil \frac{N_{\mathrm{Symbols}}^{\mathrm{Frame}}}{N_{\mathrm{hop}}} \rceil$. Assuming that each MC symbol carries one symbol d_{i}^{u}, this reallocation result in a rate loss of $\frac{N_{\mathrm{pilots}}}{N_{\mathrm{Symbols}}^{\mathrm{Frame}}} R_{\mathrm{c}} \log_{2}(M)$, which is caused by the insertion of pilots or start phase symbols through differential symbol mapping that does not carry information as introduced in (5.17). Complex scheduling algorithms can be avoided by implementing a static hopping pattern that is repeated each frame.

Especially in combination with channel coding, hopping leads to a diversity gains that improves the overall performance shown in [**MWBD15a**].

5.3.6 Spreading Sequences

It has been shown in [EK12, FR13, Sch15, CT05, RV08] that the choice of the spreading sequences in $\mathbf{S}$, and thus, the choice of the measurement matrix highly changes the performance of the underlying CS algorithm. Since $\mathbf{S}$ only contains the spreading sequences $\mathbf{s}^{\mathrm{u}}$, the question arises: *How to choose good spreading sequences?* Within this work, we restrict ourselves on three different types of sequences:

1. Pseudo noise (PN) sequences-based on maximum length sequence (MLS) [Ver98]
2. Complex Gaussian sequences
3. Random phase (RP) sequences

motivated by good average correlation properties even under asynchronous reception. It should be noted, that the PN and RP sequences have constant amplitudes, whereas the Gaussian distributed sequence have non-constant amplitudes. For a fair comparison the spreading sequences are normalized to the same power. The interested reader is referred to [Sch15, Wil16] for a deeper analysis *w.r.t.* different implementations.

5.4 New Concepts for MCSM

In addition to the already described concepts, which were already described in the publications [**MWBD15b, MWBD15a, BMWD15, WMBD16**], and [Mon17], we now present further concepts. These concepts have not yet been published and represent the most innovative part of this chapter. Fig. 5.12 shows again the node processing, furthermore the new concepts,

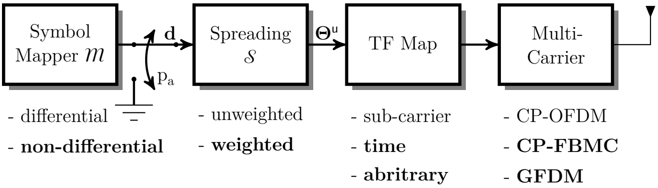

Figure 5.12: Block diagram of signal generation at MCSM node.

which we will present below, are shown in bold font.

5.4.1 Differential vs. Non-differential Symbol Mapping

In this subsection we give a brief insight into the third technology component of MCSM: “non-orthogonal pilots”. So far we have assumed that the channel knowledge is perfectly known, so that the base station does not have to estimate the channel. As we have seen, MCSM “shifts” the knowledge of the channel from the measurement matrix **M** including the effective channel impact to the MCSM approximation of a fully known spreading matrix **S** and to the symbols $\widetilde{\mathbf{D}}_{\mathsf{u},i} = h_i^{\mathsf{u}} d_i^{\mathsf{u}}$ with the influence of a one-tap channel per user as given in (5.16). Complete estimation of the CSI for all users with an orthogonal pilot design seems not feasible. However, a *non-orthogonal* channel estimation, where the pilots are introduced before spreading within the coherence bandwidth leads to a reasonable approach. Since we are shifting the channel estimation problem to the symbol matrix $\widetilde{\mathbf{D}}$ affected by a one-tap channel, we can use any mapping such as M-PSK, M-QAM or other mappings with additional pilots. The pilots, however, cannot be freely assigned in the TF grid, since the pilot is inserted before spreading illustrated by Fig. 5.13a. The estimated pilots at the BS reflect only an average de-spread channel coefficient per pilot.

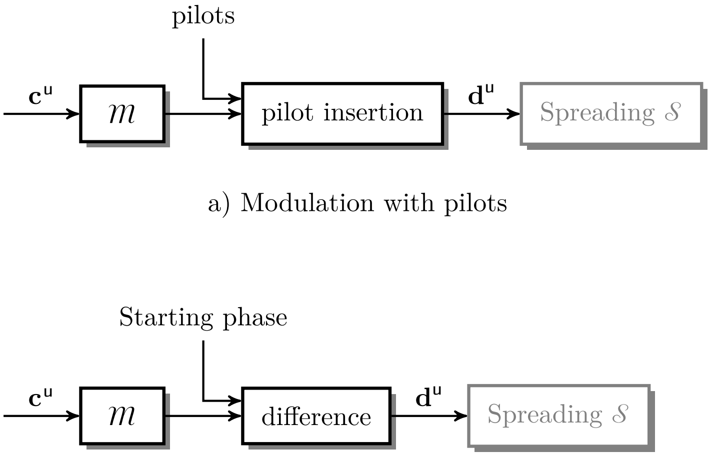

a) Modulation with pilots

b) Differential modulation

Figure 5.13: Block diagram of pilot insertion versus differential symbol mapping per active user u.

By contrast, the use of differential symbol mapping, as in the original work [**MWBD15b**], provides incoherent detection based on the differences of symbols without the need of an additional channel estimation. We use differential symbol mapping and the ith symbol reads $\mathring{d}_i^{\mathsf{u}} = d_{i-1}^{\mathsf{u}} \mathring{d}_{i-1}^{\mathsf{u}}$ for $i = 1, \ldots, N_{\mathbf{d}}$ with an arbitrary known starting phase, *e.g.* $\mathring{d}_0^{\mathsf{u}} = 1$ as illustrated in Fig. 5.13b.

The number of symbols $N_{\text{Symbols}}^{\text{Frame}}$ per frame is given by

$$N_{\text{Symbols}}^{\text{Frame}} = N_{\mathbf{d}} + N_{\text{pilots}} \tag{5.17}$$

where N_{pilots} is the number of pilots used in one frame. If D-M-PSK is initialized only once, the number of “pilots” is $N_{\text{pilots}} = 1$ for the starting phase. Note that the starting phase symbol and the pilot symbols carry no information. Hence, the bandwidth efficiency gets reduced.

5.4.2 MCSM with Timing and Carrier Frequency Offsets

In a scenario where a massive number of sensor nodes transmit to a BS, the receive signal gives a sum over this huge number of transmit signals affected by multi-path channels. Different runtimes due to different distances of the sensor nodes to the BS, low-cost local oscillator (LO) and imprecise synchronization at the sensor nodes are some reasons for TO. In this part we want to demonstrate the impacts of practical limitations such as TO and CFO in CP-OFDM-based MCSM systems. At essence, MCSM uses CS-MUD techniques, which in turn have proven their robustness against asynchronicity. As shown in [SBD13a], the CS-MUD detector can be extended by delay hypothesis, which drastically increase the complexity of the detection. In contrast, MCSM can inherently handle asynchronous transmissions without increasing the detection complexity, as long as the maximum delay is limited to the length of the CP in time domain, *i.e.* the CP must correspond to the length of the channel impulse response **and** the expected time shift from asynchronous transmissions. The performance gracefully degrades under asynchronicity as shown in [**MWBD15a**]. Nevertheless, the extension of the CP to cope with asynchronicity clearly leads to a loss in spectral efficiency.

Timing Offsets As mentioned above, we assume a slotted ALOHA protocol, in which a sensor has to synchronize to a slot basis if it wants to transmit a data packet. An asynchronous reception of packets at the BS might occur, as illustrated in Fig. 5.14. In contrast to a unidirectional P2P transmission and similar to the transmission via a TWRC, even if the offsets $\Delta\tau^{\mathsf{u}}$ are perfectly known, individual post-compensation at the BS is not possible as only the sum of all user signals affected by the physical channel are available. However, an average compensation is possible. We distinguish two cases:

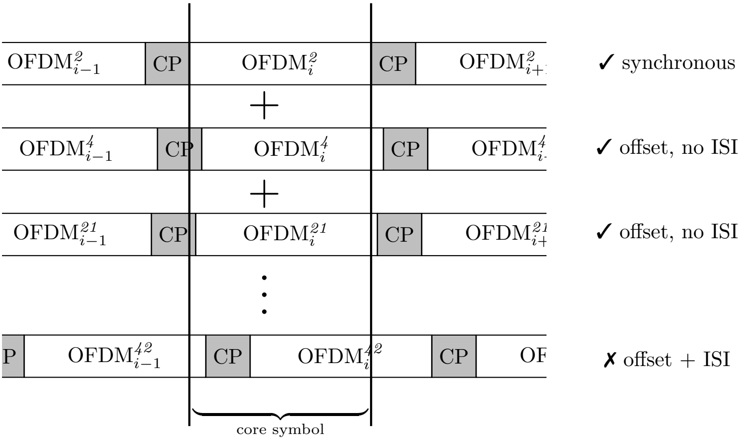

Figure 5.14: Illustration of possible asynchronous reception of CP-OFDM symbols from some active sensor nodes.

- *Case a:* the user specific delay $\Delta\tau^{\mathsf{u}} \leq T_{\mathrm{GI}}$ is within the GI time and
- *Case b:* the delay $\Delta\tau^{\mathsf{u}} > T_{\mathrm{GI}}$ is larger than the GI length.

Particularly, in *case b* the overall transmission is affected by ISI. We focus on *case a* and assume that the GI is well-designed to match an overall ISI-free transmission.

Nevertheless, we assume that a MCSM system lies within the coherence bandwidth B_{c} of a multi-path channel, which only leads to a distortion that can be described by a one-tap channel coefficient for all sub-carriers used. However, by the presence of a TO $\Delta\tau^{\mathsf{u}}$ per user u, the individual received signal (5.12) is additionally affected by a phase rotation by

$$\mathbf{y}^{\mathsf{u}} = \tilde{\mathbf{d}}^{\mathsf{u}} \otimes \left(\boldsymbol{\Sigma}^{\mathsf{u}}_{\mathrm{TO},\mathcal{S}_i}\mathbf{s}^{\mathsf{u}}\right) \quad , \tag{5.18}$$

where the main diagonal elements of the matrix $\boldsymbol{\Sigma}^{\mathsf{u}}_{\mathrm{TO},\mathcal{S}_i} = \mathrm{diag}\left\{\exp[\frac{jk_q\Delta\tau^{\mathsf{u}}}{N_{\mathrm{SC}}}]\right\}$ comes from the time-shift property of the Fourier transform with $k_q \in \mathcal{S}_i$ as sub-carriers indices used in the transmission. The multiplication leads to a chip-wise rotation of the spreading sequence $\mathbf{s}^{\mathsf{u}}$. Assuming that these offsets are not known to the receiver, the undistorted original spreading sequences are chosen as hypotheses.

The correlation between the hypotheses sequence $\mathbf{s}^{\mathsf{u}}$ as original sent and the rotated version $\tilde{\mathbf{s}}^{\mathsf{u}} = \mathbf{\Sigma}^{\mathsf{u}}_{\mathrm{TO},\mathcal{S}_i}\mathbf{s}^{\mathsf{u}}$ can be calculated like

$$\Psi_{\mathbf{ss}_{\mathrm{TO}}}\left(\iota, \Delta\tau^{\mathsf{u}}\right) = \langle \mathbf{s}^{\mathsf{u}}, \mathbf{\Sigma}^{\mathsf{u}}_{\mathrm{TO},\mathcal{S}_i}\mathbf{s}^{\mathsf{u}}\rangle = \sum_{q=0}^{N_{\mathrm{s}}-1} \mathbf{s}^{\mathsf{u}}_q \mathbf{s}^{\mathsf{u}*}_{q+\iota} e^{\frac{j2\pi k_q \Delta\tau^{\mathsf{u}}}{N_{\mathrm{SC}}}} \quad , \tag{5.19}$$

which can be interpreted as a discrete ambiguity function $A_{\mathbf{s},\mathbf{s}}\left(\iota, \Delta\tau^{\mathsf{u}}\right)$ [Fro16].

Carrier Frequency Offset In contrast to the TO, the presence of CFO $\Delta\nu^{\mathsf{u}}$ occurs, *e.g.*, due to a user-specific mismatch of the LO between a cheap sensor node and the BS, resulting in a user specific receive signal

$$\mathbf{y}^{\mathsf{u}} = \tilde{\mathbf{d}}^{\mathsf{u}} \otimes (\underbrace{\mathbf{I}_{\mathcal{S}_i}\mathbf{F}\mathbf{\Sigma}^{\mathsf{u}}_{\mathrm{CFO}}\mathbf{F}^{\mathsf{H}}\mathbf{I}^{\mathsf{T}}_{\mathcal{S}_i}}_{\mathbf{\Omega}_{\mathrm{CFO}}}\mathbf{s}^{\mathsf{u}}) \quad , \tag{5.20}$$

where $\mathbf{\Sigma}^{\mathsf{u}}_{\mathrm{CFO},\mathcal{S}_i} = \operatorname{diag}\left\{\exp[\frac{j2\pi k_q \Delta\nu^{\mathsf{u}}}{N_{\mathrm{SC}}}]\right\}$ comes from the frequency-shift property of the Fourier transform with $k_q \in \mathcal{S}_i$ as sub-carriers indices used in the transmission. The matrix $\mathbf{\Omega}_{\mathrm{CFO}}$ is not purely diagonal as in the TO case. It can be interpreted as a circular convolution matrix of sampled sinc function shifted by the CFO $\Delta\nu^{\mathsf{u}}$ due to the nature of the rectangular filter applied in CP-OFDM. This convolution results in a correlated sequences at the BS and the correlation of the affected sequence $\tilde{\mathbf{s}}^{\mathsf{u}} = \mathbf{\Omega}_{\mathrm{CFO}}\mathbf{s}^{\mathsf{u}}$ with the transmitted spreading sequence $\mathbf{s}^{\mathsf{u}}$ is given by

$$\Psi_{\mathbf{ss}_{\mathrm{CFO}}}\left(\iota, \Delta\nu^{\mathsf{u}}\right) = \langle \mathbf{s}^{\mathsf{u}}, \mathbf{\Omega}_{\mathrm{CFO}}\mathbf{s}^{\mathsf{u}}\rangle = \sum_{q=0}^{N_{\mathrm{s}}-1} \mathbf{s}^{\mathsf{u}}_q \mathbf{\Omega}_{\mathrm{CFO}} \mathbf{s}^{\mathsf{u}*}_{q+\iota} \quad . \tag{5.21}$$

The lack of knowledge of offsets, however, has a strong influence on the detection capability at the BS. The MIP (5.5), which is essentially based on the correlation of the columns of the spreading matrix $\mathbf{S}$ reflects no longer directly the recovery properties as this matrix not covers the influence by the introduced offsets. However, the correlation functions in (5.19) and (5.21) describe this mismatch.

In Fig. 5.15 we consider the auto- and cross correlation function (5.19) for PN, Gaussian, and RP sequences with $\iota = 0$ of spreading sequences affected by TO in the left columns. On the right side column the auto- and cross-correlation function $|\Psi_{\mathbf{s}^{\mathsf{u}}\mathbf{s}^{\mathsf{u}}}(0)|$ and $|\Psi_{\mathbf{s}^{q}\mathbf{s}^{\mathsf{u}}}(0)|\ \forall_{q\neq\mathsf{u}}$ (5.21) *w.r.t.* CFO are given. Here we use a spreading sequence length $N_{\mathrm{s}} = 20$. The TO is normalized by the symbol duration time T. The correlation of the PN, Gaussian and the RP sequences are given in the upper, middle and lower

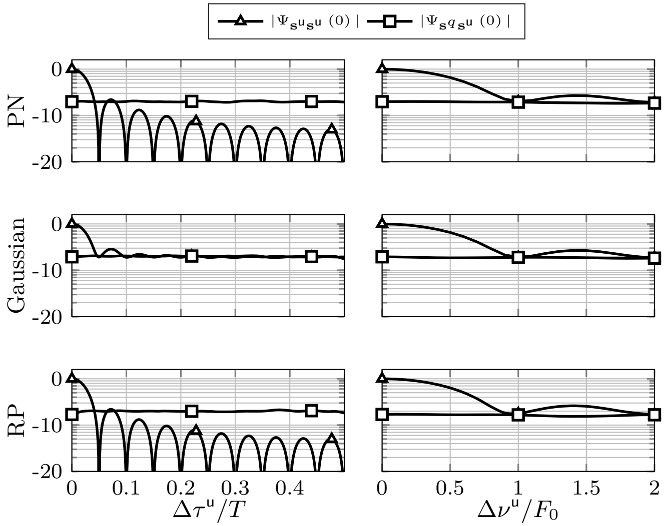

Figure 5.15: Correlation function with $\iota = 0$ for timing offsets and frequency offsets with different spreading sequences with unweighted spreading sequences.

sub-figures. As expected by (5.19), the sequences with constant amplitudes, namely the PN and the RP results in a correlation characteristic such as $|\Psi_{\mathbf{s}^{\mathsf{u}}\mathbf{s}^{\mathsf{u}}_{\mathrm{TO}}}(\iota = 0)| = |\operatorname{sinc}\left(\Delta\tau^{\mathsf{u}} N_{\mathrm{s}} \frac{1}{T}\right)|$. The result is reasonable, since the sequences with constant amplitudes can be interpreted as rectangular waveform of length $N_{\mathrm{s}}\frac{1}{T}$ by mapping in the frequency domain. The auto-correlation function of Gaussian sequence affected by a TO has roughly the same shape for low TO, but it has a “better” auto-correlation for higher TO, similar to the cross correlation performance. In the curves for the TO one can see that a 3dB drop of the correlation function is about $\Delta\tau^{\mathsf{u}}/T \approx 0.0296$ in all 3 cases. For the CFO the corresponding 3dB drop is at $\Delta\nu^{\mathsf{u}}/F_0 \approx 0.032$.

By the presence of CFO there is no visible difference between the different sequences. All cross correlation share roughly the same performance.

It is remarkable that the spreading sequence length N_{s} determines the correlation behavior under TO. Since the dimension of the measurement matrix determines the performance, the spreading sequence length N_{s} determines the sensitivity against TOs as it is a parameter of the sinc function.

Performance of Weighted Spreading Sequences To improve the auto-correlation under TO and to develop a more robust activity detection, we can use PN, Gaussian and RP sequences weighted with a general waveform as indicated in Fig. 5.12. This weighting is motivated by the correlation function (5.19) similar to a discrete ambiguity function. To this end, we generate new spreading sequences with

$$\hat{\mathbf{s}}^{\mathsf{u}} = \mathbf{G}\mathbf{s}^{\mathsf{u}} \tag{5.22}$$

with $\mathbf{G} = \operatorname{diag}\{\mathbf{g}\}$. The real-valued filter vector $\mathbf{g}$ contains filter coefficients of length N_{s}. The resulting auto- and cross-correlation are given by

$$\Psi_{\tilde{\mathbf{s}}\tilde{\mathbf{s}}_{\mathrm{TO}}}\left(\iota, \Delta\tau^{\mathsf{u}}\right) = \langle \mathbf{G}\mathbf{s}^{\mathsf{u}}, \boldsymbol{\Sigma}^{\mathsf{u}}_{\mathrm{TO},\mathcal{S}_i}\mathbf{G}\mathbf{s}^{\mathsf{u}}\rangle = \sum_{q=0}^{N_{\mathrm{s}}-1} \mathbf{G}\mathbf{s}^{\mathsf{u}}_q \mathbf{G}^* \mathbf{s}^{\mathsf{u}*}_{q+\iota} e^{\frac{j2\pi k_q \Delta\tau^{\mathsf{u}}}{N_{\mathrm{SC}}}} \quad , \tag{5.23}$$

$$\Psi_{\tilde{\mathbf{s}}\tilde{\mathbf{s}}_{\mathrm{CFO}}}\left(\iota, \Delta\nu^{\mathsf{u}}\right) = \langle \mathbf{G}\mathbf{s}^{\mathsf{u}}, \boldsymbol{\Omega}_{\mathrm{CFO}}\mathbf{G}\mathbf{s}^{\mathsf{u}}\rangle = \sum_{q=0}^{N_{\mathrm{s}}-1} \mathbf{G}\mathbf{s}^{\mathsf{u}}_q \boldsymbol{\Omega}_{\mathrm{CFO}} \mathbf{G}^* \mathbf{s}^{\mathsf{u}*}_{q+\iota} \quad . \tag{5.24}$$

The corresponding correlation functions by the application of a Gaussian waveform (3.18) (N_{s} samples in $t = \pm 1$ with $\rho = 1$) are shown in Fig. 5.16. It can be observed that the overall correlation function now has Gaussian-like characteristic and the auto-correlation function $|\Psi_{\mathbf{s}^{\mathsf{u}}\mathbf{s}^{\mathsf{u}}_{\mathrm{TO}}}\left(\iota = 0\right)|$ exhibits a broader shape than in the unweighted case shown in Fig. 5.15.

Here, the curves will have a 3dB drop of the correlation function at approx. $\Delta\tau^{\mathsf{u}}/T \approx 0.0704$ for the TO and $\Delta\nu^{\mathsf{u}}/F_0 \approx 0.032$ for the CFO. This leads to a gain of 3.76dB for the weighted spread sequence in the TOs case.

However, the cross correlation is higher than in the unweighted case due to the introduced filtering. This behavior now makes it possible to significantly improve the activity detection under unknown TOs by weighting the spreading sequences. But it is also clear that this only makes sense if one expects large offsets with constant spreading sequence lengths. The choice of take a shorter spreading sequence by the cost of efficiency, or to choose a weighting function to improve the performance is a compromise parameter for the system designer and depends on the system configuration.

System Model Suppose any arbitrary but fixed TO and CFO within a OFDM symbol per user, both effects can be summarized as

$$\mathbf{Y} \approx \widetilde{\mathbf{S}}\widetilde{\mathbf{D}} + \mathbf{N} \tag{5.25}$$

leading to a changed MMV-CS problem with an effective spreading matrix $\widetilde{\mathbf{S}} \in \mathbb{C}^{N_{\mathrm{s}} \times N_{\mathsf{u}}}$, where the columns are $\widetilde{\mathbf{S}}_{:,\mathsf{u}} = \boldsymbol{\Omega}^{\mathsf{u}}_{\mathrm{CFO}}\boldsymbol{\Sigma}^{\mathsf{u}}_{\mathrm{TO}}\mathbf{G}\mathbf{S}_{:,\mathsf{u}}$, with filter

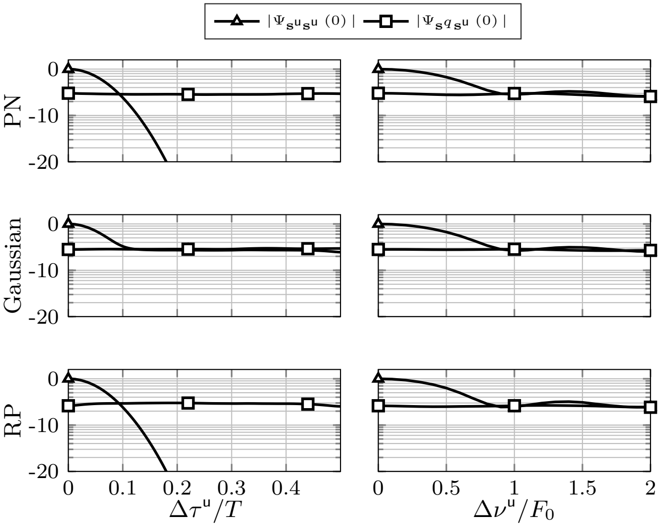

Figure 5.16: Correlation function with $\iota = 0$ for timing offsets and frequency offsets with weighted spreading sequences weighted by the Gaussian waveform.

matrix $\mathbf{G} \in \mathbb{C}^{N_{\mathrm{s}} \times N_{\mathrm{s}}}$, user specific CFO matrix $\mathbf{\Omega}^{\mathsf{u}}_{\mathrm{CFO}} \in \mathbb{C}^{N_{\mathrm{s}} \times N_{\mathrm{s}}}$, user specific TO matrix $\mathbf{\Sigma}^{\mathsf{u}}_{\mathrm{TO}} \in \mathbb{C}^{N_{\mathrm{s}} \times N_{\mathrm{s}}}$, one-tab channel affected symbol matrix $\widetilde{\mathbf{D}} \in \mathbb{C}^{N_{\mathsf{u}} \times N^{\mathrm{Frame}}_{\mathrm{Symbols}}}$, and observation matrix $\mathbf{Y} \in \mathbb{C}^{N_{\mathrm{s}} \times N^{\mathrm{Frame}}_{\mathrm{Symbols}}}$.

In general, the values of the offsets $\Delta\nu^{\mathsf{u}}$ and $\Delta\tau^{\mathsf{u}}$ are unknown for the BS. In this case, the GOMP algorithm can use the detection model in (5.16) instead of (5.25). However, both offsets affect the activity and data detection by changing the correlation properties.

5.4.3 Channel Estimation using Spread and Waveform Filtered Pilots

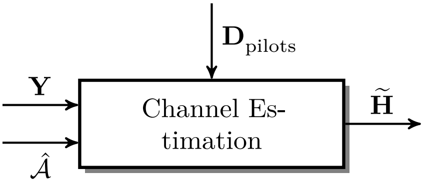

Figure 5.17: Block diagramm for channel estimation.

So far we have introduced the overall concept to create an MCSM transmission that is capable to serve a massive number of sensor nodes sporadically active and BS recovering the sensor data. Here we want to emphasize the influence of non-orthogonal channel estimation on the system. For this discussion we limit ourselves to the system model in (5.16) with pure sub-carrier mapping, the non-differential mapping in Section 5.4.1 and concentrate only on the MC symbols that carry the spread pilot sequences. The channel estimation (*cf.* Fig. 5.17) is based on the reduced activity aware system model (5.37). To estimate the channel, we use a least squares (LS) approach with

$$\widetilde{\mathbf{H}} = \mathbf{S}^{\dagger}_{:,\hat{\mathcal{A}}} \mathbf{Y}_{:,\mathcal{P}} \oslash \mathbf{D}_{\text{pilots}} \tag{5.26}$$

The pseudo inverse $\mathbf{S}^{\dagger}_{:,\hat{\mathcal{A}}} \in \mathbb{C}^{N_{\text{act}} \times N_{\text{s}}}$ covers only the N_{act} active estimated spreading sequences. The reduced observation matrix $\mathbf{Y}_{:,\mathcal{P}} \in \mathbb{C}^{N_{\text{s}} \times N_{\text{pilots}}}$ contains the observations at the pilot positions $\mathcal{P}$ and $\mathbf{D}_{\text{pilots}} \in \mathbb{C}^{N_{\text{act}} \times N_{\text{pilots}}}$ is the matrix with pilots used. Applying (5.26) results in an estimation matrix $\widetilde{\mathbf{H}} \in \mathbb{C}^{N_{\text{act}} \times N_{\text{pilots}}}$, which contains per row the estimated channel coefficients $\tilde{h}^{\mathsf{u}}$ per user for the pilots $\mathbf{D}_{\text{pilots}}$ used. The sign $\oslash$ determines the point-wise division.

We introduce the average MSE

$$\overline{\text{MSE}} = \frac{1}{N_{\text{aver}}} \sum_{q=0}^{N_{\text{aver}}-1} \left| \tilde{h}^{\mathsf{u}} - \frac{1}{N_{\text{s}}} \sum_{\iota=0}^{N_{\text{s}}-1} \mathbf{\Sigma}^{\mathsf{u}}_{\mathbf{H}\,\iota,\iota} \right|^2 \quad , \tag{5.27}$$

averaged over N_{aver} channel realizations, where the diagonal matrix $\mathbf{\Sigma}^{\mathsf{u}}_{\mathbf{H}}$ is the applied effective channel per user.

The result of this measurement is given in Fig. 5.18 for different parameter sets given in Table 5.1. We assume a sampling rate of $F_{\text{A}} = 26\text{MHz}$, Rayleigh fading channel coefficients with constant path loss for illustration and an inverse fast Fourier transform (IFFT) length $N_{\text{IFFT}} = 2048$. In this analysis, we use the unweighted RP spreading sequences in the left plots and on the right plots the RP spreading sequence is weighted by the same truncated Gaussian waveform as discussed in Fig. 5.16[3]. In the upper plots, we fix the spreading sequence length $N_{\text{s}} = 25$ and use a maximum delay spread of $\tau^{\max} = 0.05\mu\text{s}$. It can be observed in Fig. 5.18a) that, if only a single user is active the MSE between the estimated and the true average decreases linearly with higher SNR $1/\sigma_{\text{n}}^2$ in the unweighted case. In the unweighted case, the performance is mainly determined by the noise term,

---

[3] Related to (3.18) with $g_{\text{Rect}}\,(t/2) \cdot g^{(\rho=1)}_{\text{Gaussian}}\,(t)\Big|_{kT_{\text{A}}}$ and equidistant sampled resulting in N_{s} filter coefficients.

Table 5.1: Parameter Sets

Plots	fixed parameters	varying parameters
Fig. 5.18 a) & b)	$N_{\mathrm{s}} = 25$ $\tau^{\max} = 0.05\mu\mathrm{s}$	$N_{\mathrm{act}} = 3, 7, 10, 20, 30$ $1/\sigma_{\mathrm{n}}^2 = -5, \ldots, 30\mathrm{dB}$
Fig. 5.18 c) & d)	$N_{\mathrm{act}} = 7$ $1/\sigma_{\mathrm{n}}^2 = 15\mathrm{dB}$	$\tau^{\max} = 0.05, \ldots, 0.49\mu\mathrm{s}$ $N_{\mathrm{s}} = 10, \ldots, 30$
Fig. 5.18 e) & f)	$N_{\mathrm{s}} = 25$ $1/\sigma_{\mathrm{n}}^2 = 15\mathrm{dB}$	$N_{\mathrm{act}} = 3, 7, 10, 20, 30$ $\tau^{\max} = 0.05, \ldots, 0.49\mu\mathrm{s}$

as the underlying application of the pseudo inverse in (5.26) results in an identity matrix.

Contrary, the application of the pseudo inverse in (5.26) for the weighted case (5.22) results in a diagonal matrix unequal to the identity matrix due to weighting. In Fig. 5.18b, the average MSE results in an error floor due to the correlated sequence caused by weighting.

The channel estimation downgrades for a higher number of active users in both cases. Especially in the case, where the number of active users is larger than the spreading sequence length $N_{\mathrm{act}} \geq N_{\mathrm{s}}$, we see a huge gap, due to the under determined system used.

Fig. 5.18c and Fig. 5.18d show the MSE for a varying spreading sequence length N_{s} and for different maximum delay spread lengths $\tau^{\max}$. We consider a fixed number of active users exemplary $N_{\mathrm{act}} = 7$ and a SNR working point of $1/\sigma_{\mathrm{n}}^2 = 15\mathrm{dB}$. Similar to the correlation analysis in Fig. 5.15 and Fig. 5.16 for a low $\tau^{\max}$ the unweighted sequence has a lower MSE compared to the weighted version of roughly 1dB. Whereas, for higher maximum delay spread lengths, the weighted version achieves a significant lower average MSE up to $3 - 4\mathrm{dB}$.

The discussion for different maximum delay spread lengths $\tau^{\max}$ for a varying number of active nodes is illustrated in Fig. 5.18e and f. As expected, the MSE downgrades with higher $\tau^{\max}$. A huge gap is achieved with $N_{\mathrm{act}} \geq N_{\mathrm{s}}$, similar to the upper plots, due to amount of observations compared to number of estimations needed. Furthermore, the above indicated gain of roughly $3-4\mathrm{dB}$ for a medium number of active nodes $N_{\mathrm{act}} = 7, 10, 15$ can be observed.

Overall, we can observe that the non-orthogonal channel estimation needs a low user activity to achieve a low MSE, which fits well in the assumption of the setup we have in mind. Furthermore, the performance of the channel estimation is one of the critical points in the overall performance.

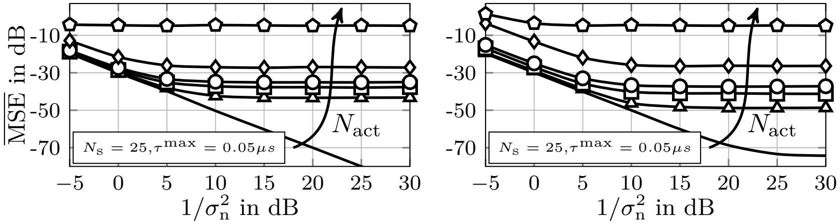

a) RP unweighted, MSE over SNR b) RP weighted, MSE over SNR

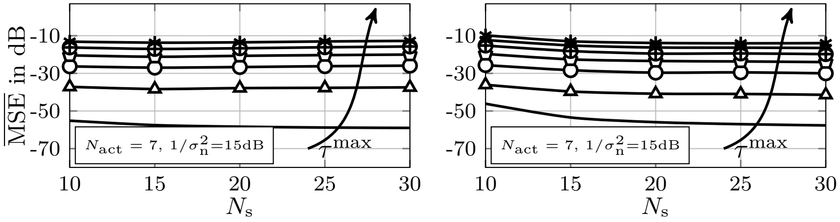

c) RP unweighted, MSE over N_s d) RP weighed, MSE over N_s

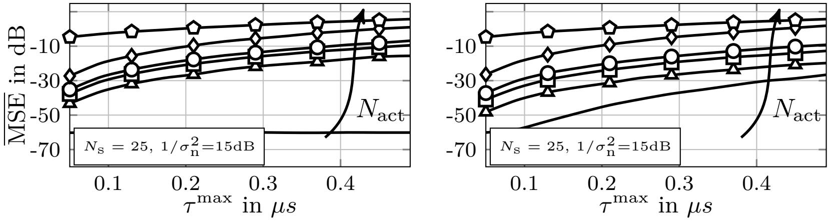

e) RP unweighed, MSE over τ^max f) RP weighed, MSE over τ^max

Figure 5.18: Average MSE of channel estimation with different configurations given by Table 5.1.

5.4.4 Resource Efficient Mapping

Beyond frequency hopping, MCSM implements a resource efficient TF mapping that is outlined in the following. So far we assumed a pure sub-carrier mapping, where we map the spread symbol matrix $\boldsymbol{\Theta}^\mathrm{u}$ column wise to a set $\mathcal{S}_i$ of N_SC sub-carrier resulting in $N_\mathrm{SC} = N_\mathrm{s}$ sub-carriers used and mathematically described in (5.14). It is assumed, that the MCSM lies within the coherence bandwidth of the wireless channel. Other mappings are possible and are preferable for different channel conditions. *E.g.* if the coherence bandwidth is too small to capture the whole spreading sequence, the spreading sequences could be aligned along the time axis as illustrated in

Fig. 5.19 as the right gray block. Mathematically, this can be described by

$$\mathbf{\Theta}^{\mathsf{u}} = \mathrm{vec}\{\mathbf{P}_{\mathrm{TS}}\,(\mathbf{s}^{\mathsf{u}} \otimes \mathbf{d}^{\mathsf{u}})\} \tag{5.28}$$

with the permutation matrix $\mathbf{P}_{\mathrm{TS}} = \mathbf{I}$ yielding for a pure time axis mapping as left gray block. The selection set $\mathcal{S}_i$ has to be reconfigured according to $|\mathcal{S}_i| = N_{\mathrm{Symbols}}^{\mathrm{Frame}}$ and the number of time symbols is changed to $N_{\mathrm{TS}} = N_{\mathrm{Symbols}}^{\mathrm{Frame}}$. Note that, by changing the direction of the spreading sequence to the time axis, will result in an interchanged behavior of TO and CFO impacts as well as the spreading sequences now should be allocated within the coherence time τ_{c} of the channel. The trade-off between the impacts of TO, CFO coherence bandwidth and coherence time can be achieved by a generalized mapping, where we use a permutation matrix $\mathbf{P}_{\mathrm{TS}}$ leading to arbitrary mapping as illustrated in Fig. 5.19. Also, the sub-carrier mapping can be generalized by

$$\mathbf{\Theta}^{\mathsf{u}} = \mathrm{vec}\{\mathbf{P}_{\mathrm{SC}}\,(\mathbf{d}^{\mathsf{u}} \otimes \mathbf{s}^{\mathsf{u}})\} \tag{5.29}$$

with $\mathbf{P}_{\mathrm{SC}} = \mathbf{I}$ for pure sub-carrier mapping and arbitrary permutation matrix $\mathbf{P}_{\mathrm{SC}}$ to achieve mappings like illustrated in Fig. 5.19 in the lower blocks. Moreover, both mappings can be mixed, yielding a joint TF mapping, which allows a flexible link adaptation. Note that the system model at the BS is changing according to the permutation and mapping used

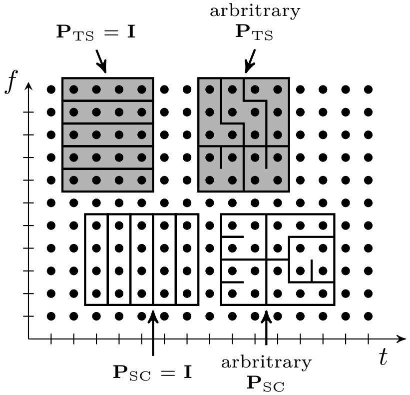

Figure 5.19: Illustration of one-to-one mapping of spread sequences over N_{SC} sub-carriers.

$$\begin{aligned} \text{SC: }\ \mathrm{vec}\{\mathbf{P}_{\mathrm{SC}}\mathbf{y}\} &\approx \mathbf{S}\widetilde{\mathbf{D}} + \mathrm{vec}\{\mathbf{P}_{\mathrm{SC}}\mathbf{n}\} && (5.30)\\ \text{TS: }\ \mathrm{vec}\{\mathbf{P}_{\mathrm{TS}}\mathbf{y}\}^{\mathsf{T}} &\approx \mathbf{S}\widetilde{\mathbf{D}} + \mathrm{vec}\{\mathbf{P}_{\mathrm{TS}}\mathbf{n}\}^{\mathsf{T}} && (5.31) \end{aligned}$$

And, in the special case of pure sub-carrier or time mapping this results in

$$\text{SC: } \mathbf{Y} \approx \mathbf{S}\widetilde{\mathbf{D}} + \mathbf{N} \tag{5.32}$$

$$\text{TS: } \mathbf{Y}^{\mathsf{T}} \approx \mathbf{S}\widetilde{\mathbf{D}} + \mathbf{N}^{\mathsf{T}} \tag{5.33}$$

5.4.5 General Multi-Carrier in MCSM

The use of a large number of devices within a given bandwidth is a major challenge. As we have stressed previously, the low data-rate within a industrial application could lead to a narrow-band transmission, which is also proposed in LTE for IoT [NO16]. The application within a given bandwidth by utilizing white spaces leads to a need of systems with a low OoBE, not interfering with other existing systems [KRS18]. So far, MCSM was analyzed with CP-OFDM as MC scheme, only. Within this subsection, we generalize MCSM to the application of general waveforms offering better spectral shape and, as we have seen in Chapter 4, an overall better performance for a wide range of offsets is achievable. Especially for an under determined system, where a synchronization is not precisely realizable we need a robust design.

First we will introduce the combination of MCSM with CP-FBMC, because this method introduces a symbol-wise CP just like CP-OFDM and thus represents the simple extension of this method. We will then give an outlook on the general GFDM procedure and show the extension of the system model.

Non-Orthogonal Design with Cyclic Prefix

Unlike synchronous CP-OFDM, CP-FBMC has an effective channel with a block-diagonal structure, as shown by (3.67) in Chapter 3. This property offers the application of the MMV-CS problem, if the channel can be approximated by a one tap coefficient as in the CP-OFDM case.

In this design criteria, the effective channel matrix is given by

$$\mathbf{H}^{\mathsf{u}}_{\mathcal{S}_i,i,i'} = \begin{cases} \mathbf{I}_{\mathcal{S}_i^+}\mathbf{F}\boldsymbol{\Sigma}^{\mathrm{Rx}}_{\mathbf{g}}\mathbf{F}^{\mathsf{H}}\boldsymbol{\Sigma}^{\mathsf{u}}_{h,i,i'}\mathbf{F}\boldsymbol{\Sigma}^{\mathrm{Tx}}_{\mathbf{g}}\mathbf{F}^{\mathsf{H}}\mathbf{I}^{\mathsf{T}}_{\mathcal{S}_i} & i = i' \\ \mathbf{0} & i \neq i' \end{cases} \tag{5.34}$$

related to (3.67) in Chapter 3 and, thus, in not of purely diagonal structure anymore.

The application of a general waveform with CP leads to the following new system model

$$\mathbf{Y} \approx \mathbf{S}_{\mathrm{w}}\widetilde{\mathbf{D}} + \mathbf{J} + \widetilde{\mathbf{N}} \tag{5.35}$$

derived in Appendix D.1. This system model is a generalized MCSM model, which also covers CP-OFDM with filter matrices $\mathbf{\Sigma}_{\mathbf{g}}^{\mathrm{Tx}} = \mathbf{\Sigma}_{\mathbf{g}}^{\mathrm{Rx}} = \mathbf{I}$. The noise matrix $\widetilde{\mathbf{N}} = \mathbf{F}\mathbf{\Sigma}_{\mathbf{g}}^{\mathrm{Rx}}\mathbf{N}$ is colored by the receive filter matrix $\mathbf{\Sigma}_{\mathbf{g}}^{\mathrm{Rx}}$ and the matrix $\mathbf{J}$ is an unknown interference term based on the waveform and the approximation of a one-tap channel.

The matrix $\mathbf{S}_{\mathrm{w}} = \mathbf{M}_{\mathrm{w}}\mathbf{S}$ captures the properties of the spreading sequences by $\mathbf{S}$ and of the given waveform by the waveform matrix $\mathbf{M}_{\mathrm{w}} \in \mathbb{C}^{|\mathcal{S}_i^+| \times |\mathcal{S}_i|}$ derived in (D.8), and it is fully known at the BS. The set $\mathcal{S}_i^+$ can be extended $|\mathcal{S}_i^+| = |\mathcal{S}_i| + 2N_{\mathrm{N}}^{\mathrm{SC}}$ by $N_{\mathrm{N}}^{\mathrm{SC}}$ neighbors collecting not only the assigned set $|\mathcal{S}_i| = N_{\mathrm{s}}$ of sub-carriers, but also the neighborhood of additional $N_{\mathrm{N}}^{\mathrm{SC}}$ sub-carriers on each side. As already discussed in the Section 4.5 of the TWRC chapter, the non-orthogonal waveform affect also neighboring sub-carriers. The $N_{\mathrm{N}}^{\mathrm{SC}}$ parameter stresses this impact. The CP-FBMC becomes interesting when the transmission is influenced by offsets and an orthogonal transmission with CP-OFDM can no longer be guaranteed.

The interference matrix $\mathbf{J}$, which will be also present for offset affected CP-OFDM also depends on the number of neighbors N_{N}. Especially for larger offsets, the unknown entries in the interference matrix $\mathbf{J}$ of CP-OFDM grow stronger than those of CP-OFDM, even if they are vanishing for CP-OFDM in the synchronized case, which has already been discussed in Chapter 3. The larger this number is chosen, the smaller is the effect of the disturbance. This argument follows similar principles as in Chapter 4, where only a few neighbors are collected within the equalizer. However, the neighboring sub-carriers can be allocated with other MCSM systems or completely different systems in such a way that the choice of N_{N} too large affects the total interference at the BS. Therefore, N_{N} is a compensation parameter to weight either the influence of useful signal power or interference.

Outlook to General Non-Orthogonal Waveform

So far, we have seen that by assuming an ISI-free MCSM transmission based on a GI vie CP, the resulting system model can be approximated by an MMV-CS problem with known measurement matrix and with symbols weighted with a one-tap channel. Contrarily to CP-OFDM, we introduced in CP-FBMC the extension of neighboring sub-carriers to capture the ICI introduced by the waveform, resulting still in a good approximation. To further increase the spectral shape and the spectral efficiency by avoiding the symbol-by-symbol guard interval time, we want to give a brief outlook to the extension of MCSM to QAM/FBMC or GFDM. Especially, the CP in GFDM allows still a robustness against TO, which is very important in a system with a massive number of nodes. These schemes are not directly applicable to the aforementioned MMV-CS problem since the system is not ISI-free. The approximation of a flat-fading channel is more stringent, due to higher influence of a symbol in the frequency and in the time domain, without the symbol-wise GI. However, if we can assume that a spread symbol vector is still affected roughly by just one channel tap and we consider $N_{\mathrm{N}}^{\mathrm{SC}}$ neighboring sub-carriers and $N_{\mathrm{N}}^{\mathrm{TS}}$ time symbols, the resulting system model yields

$$\underline{\mathbf{Y}} \approx \underline{\mathbf{S}}_{\mathrm{w}}\widetilde{\mathbf{D}} + \underline{\mathbf{J}} + \widetilde{\underline{\mathbf{N}}} \quad , \tag{5.36}$$

where $\underline{\mathbf{Y}}$ is a stacked matrix with $2N_{\mathrm{N}}^{\mathrm{TS}}+1$ sub-matrices capturing the $N_{\mathrm{N}}^{\mathrm{TS}}$ past symbols, the desired and $N_{\mathrm{N}}^{\mathrm{TS}}$ following symbols. Each sub-matrix is of size $\mathcal{S}_i^{+}$ to capture the neighboring sub-carriers similar to the CP-FBMC transmission. The waveform matrix $\underline{\mathbf{S}}_{\mathrm{w}} = \underline{\mathbf{M}}_{\mathrm{w}}\mathbf{S}$ is a stacked matrix of block diagonal structure considering the influence on the neighboring blocks with the waveform matrix

$$\underline{\mathbf{M}}_{\mathrm{w}} = \left(\mathbf{I}_{2N_{\mathrm{N}}^{\mathrm{TS}}+1} \otimes \mathbf{I}_{N_{\mathrm{s}}+2N_{\mathrm{N}}^{\mathrm{SC}}}\right) \left[\mathbf{M}_{\mathrm{w},i-N_{\mathrm{N}}^{\mathrm{TS}},i}, \dots, \mathbf{M}_{\mathrm{w},i,i}, \dots, \mathbf{M}_{\mathrm{w},i+N_{\mathrm{N}}^{\mathrm{TS}},i}\right]^{\mathsf{T}} .$$

The matrix $\mathbf{M}_{\mathrm{w},i',i}$ is the waveform matrix which connects the symbol i with i' and is fully known at the base-station. The generation of these matrices and the stacked interference and stacked noise matrices, *i.e.* $\underline{\mathbf{J}}$ and $\widetilde{\underline{\mathbf{N}}}$, follows the same ideas as derived in Appendix D.

For a proper chosen waveform under mild channel conditions, it is sufficient to chose $N_{\mathrm{N}}^{\mathrm{TS}} = 1, \dots, 2$ as shown in Chapter 4 resulting in an extended MMV-CS problem (5.36).

5.4.6 Overview of System models

The properties of the before mentioned system models are summarized in Table 5.2. All MCSM related systems can be represented by the MMV-CS problem. Thus, all schemes can be solved by the GOMP or any other MMV-CS related algorithm.

In contrast to the general system, MCSM can also be solved without channel knowledge. The original MCSM system in line two, which can be used well in synchronous scenarios, was first enhanced by other mapping procedures. To do this, the system enables mapping in time direction in line three. Depending on the coherence bandwidth or coherence time of the channel, the spreading sequences can be appropriately distributed on the time-frequency grid. The systems in lines four and five extend MCSM with non-orthogonal MC, which is more robust for offsets and offers a better spectral shape at the same time but introduces interference in synchronous

Table 5.2: Overview system models

Systems	System models	Comments
1. General system (5.2) & (5.9)	$\underline{\mathbf{y}} = \underline{\mathbf{M}}\underline{\mathbf{d}} + \underline{\mathbf{n}}$	SMV-CS, need full knowledge of $\mathbf{H}$, $\underline{\mathbf{M}}$ contains $\underline{\mathbf{H}}^{\mathsf{u}}$ (unknown at BS) and $\mathbf{S}$ (known at BS)
2. CP-OFDM, pure SC mapping (5.32)	$\mathbf{Y} \approx \mathbf{S}\widetilde{\mathbf{D}} + \mathbf{N}$	MMV-CS, $\mathbf{S} \in \mathbb{C}^{N_\mathrm{s} \times N_\mathsf{u}}$, with $N_\mathrm{s} = N_\mathrm{SC}$ is known
3. CP-OFDM, pure TS mapping (5.33)	$\mathbf{Y}^\mathsf{T} \approx \mathbf{S}\widetilde{\mathbf{D}} + \mathbf{N}^\mathsf{T}$	MMV-CS, $\mathbf{S} \in \mathbb{C}^{N_\mathrm{s} \times N_\mathsf{u}}$, with $N_\mathrm{s} = N_\mathrm{TS}$ is known
4. CP-FBMC, pure SC mapping (5.35)	$\mathbf{Y} \approx \mathbf{M}_\mathrm{w}\mathbf{S}\widetilde{\mathbf{D}} + \mathbf{J} + \widetilde{\mathbf{N}}$	MMV-CS, $\mathbf{S} \in \mathbb{C}^{N_\mathrm{s} \times N_\mathsf{u}}$, with $N_\mathrm{s} = N_\mathrm{SC}$ and $\mathbf{M}_\mathrm{w} \in \mathbb{C}^{N_\mathrm{s}+2N_\mathrm{N} \times N_\mathrm{s}}$ are known, $\mathbf{J}$ unknown
5. GFDM, pure SC mapping (5.36)	$\underline{\mathbf{Y}} \approx \underline{\mathbf{M}}_\mathrm{w}\mathbf{S}\widetilde{\mathbf{D}} + \underline{\mathbf{J}} + \underline{\widetilde{\mathbf{N}}}$	MMV-CS, $\mathbf{S} \in \mathbb{C}^{N_\mathrm{s} \times N_\mathsf{u}}$, with $N_\mathrm{s} = N_\mathrm{SC}$ and $\underline{\mathbf{M}}_\mathrm{w} \in \mathbb{C}^{\left(2N_\mathrm{N}^\mathrm{TS}+1\right)\left(N_\mathrm{s}+2N_\mathrm{N}^\mathrm{SC}\right) \times N_\mathrm{s}}$ are known, $\underline{\mathbf{J}}$ unknown

systems. Especially for the latter system, a very high interference level is expected, since the symbol-wise CP is dropped there.

5.5 New Concepts for Base-Station Processing

So far we have mainly looked at processing on a node. To recover the sent data we also want to have a short look at the processing at the base station.

In the original publication of MCSM [**MWBD15b**], a recovery algorithm based on least squares has always been used at the base station, namely the GOMP algorithm (Alg. 5.1) depicted in Fig. 5.20a, which directly uses LS as data estimation algorithm. In [MBD14, Mon17] the multiple measurement vector-successive interference cancellation (MMV-SIC) and in [Mon17] the Multiple Signal Classifier (MUSIC) algorithm are used for

a) Activity & data - detector

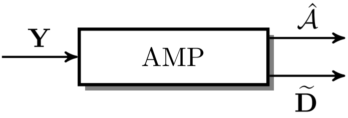

b) Full factor graph

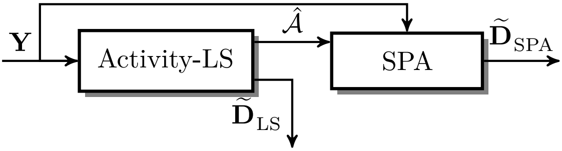

c) Two-step approach

Figure 5.20: Possible activity and data estimation schemes.

activity detection. As we have seen in Chapter 4, the waveform part can be efficiently exploited deriving a FG-based model. The main difference to Chapter 4 is the additional use of spreading sequences within the MC scheme, *i.e.* MC-CDMA. However, the full FG, which estimates the data symbols, the activity of a sensor node and the channel leads to a high computationally complexity to solve the estimation problem with the SPA. The approximate message passing (AMP) algorithm [Kab03] offers a more realizable implementation as it uses approximations *w.r.t.* the PDF of the symbols estimated as discussed in [Mon17] shown in Fig. 5.20b. Certainly, the complexity is still very high.

In this thesis, we restrict ourselves to the system shown in Fig. 5.20c, which is a two-step approach. In the first step an activity recovery algorithm is used to estimate the activity of the users before a FG-based data detection is performed in the second step. It should be noted that also other detection algorithms could be used like the soft interference cancellation algorithm in [WV99]. However, we limit ourselves to the use of the SPA.

We use the GOMP and the famous MUSIC algorithm as in [Sch86, Mon17] for the activity detection and afterwards, a symbol detection based on the

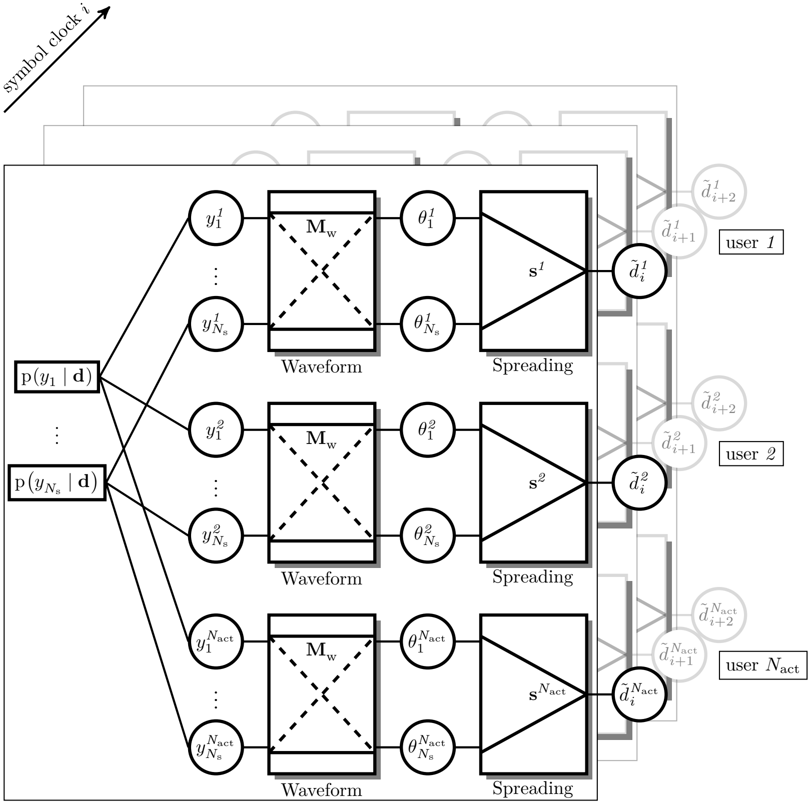

Figure 5.21: Factor graph of CP-FBMC in MCSM for reduced activity aware system model.

reduced activity aware system model is performed given by

$$\mathbf{Y} \approx \mathbf{S}_{\mathrm{w}}\widetilde{\mathbf{D}} + \widetilde{\mathbf{N}} \quad \xrightarrow{\hat{\mathcal{A}}} \quad \mathbf{Y} \approx \mathbf{S}_{\mathrm{w}:,\hat{\mathcal{A}}}\widetilde{\mathbf{D}}_{\hat{\mathcal{A}},:} + \widetilde{\mathbf{N}} \quad . \tag{5.37}$$

To convey the basic idea, the argumentation goes along the pure sub-carrier mapping related MCSM systems, both for CP-FBMC and for its special case CP-OFDM. The FG of the reduced activity aware system model in (5.37) is shown in Fig. 5.21. Each plane i describes the FG of a MC symbol. We ignore here the FG part of the underlying decoding scheme for simplicity's sake to illustrate the main parts of the MUD. However, the decoding part is connected across all i symbols for an active user and provides useful information in the detection process. As the system model

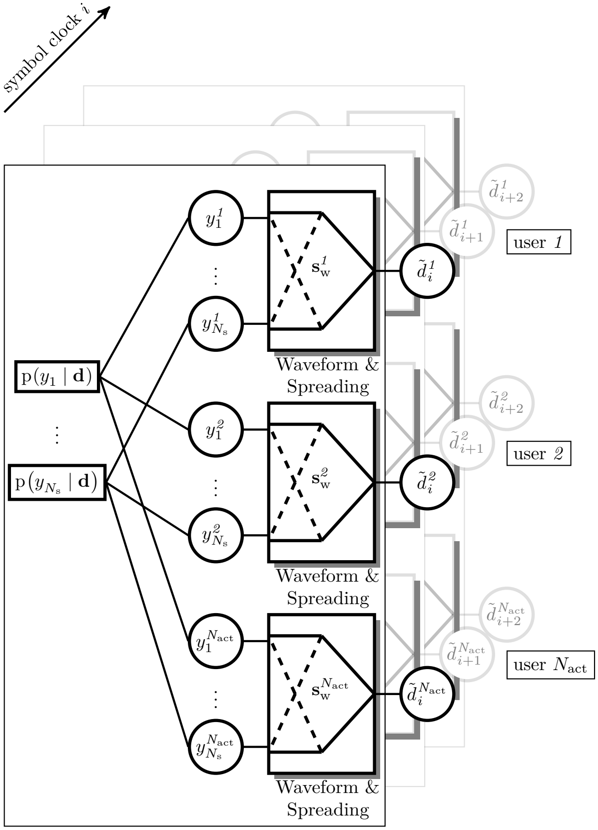

Figure 5.22: Factor graph of CP-FBMC in MCSM with closed function $\underline{\mathbf{S}}_\mathrm{w} = \underline{\mathbf{M}}_\mathrm{w}\mathbf{S}$.

can be decomposed into the two parts like

1. the MC part affected by the physical channel: $\mathbf{H}$ the dashed crossed lines denote the non-orthogonality of CP-FBMC, and
2. the spreading part: $\mathbf{S}$,

the corresponding FG also consists of two parts.

Some other important notes, the variable $\boldsymbol{\theta}$ depends on the chosen spreading order and the chosen symbol mapping. In section 5.3.6 we have discussed three different types of sequences, where the Gaussian and RP sequences are vectors, with elements either with continuous phase or elements in the entire complex plane. This has an effect on the calculation of the messages in the FG. Since the messages at an edge in a FG refer to the associated variable, the messages for the sequences are continuous function, *i.e.*, PDFs. In contrast, MLS-based spreading sequences result in discrete variables with a PMF of M values, here the calculation and storage are much easier than with the other sequences, since only M values have to be stored and processed per message.

By closing the function $\underline{\mathbf{S}}_{\mathrm{w}} = \underline{\mathbf{M}}_{\mathrm{w}}\mathbf{S}$ the FG in Fig. 5.22 is obtained. Closing functions and thus hide variables has the disadvantage that the full structure of the FG can no longer be exploited, but allows the simplification of calculations. For the application of CP-OFDM, the FG in Fig. 5.21 results in the same FG as in Fig. 5.22 as the waveform matrix $\mathbf{M}_{\mathrm{w}} = \mathbf{I}$. In this case the underlying structure is fully utilized. The FG of a GFDM implementation is not shown, however, a FG detector with GFDM would lead to cross connection between the planes due to the introduced ISI.

5.6 Monte Carlo Performance Evaluation

In this section we want to focus on the performance of some new concepts and compare them with the state of the art MCSM [**MWBD15b**], *i.e.*,

1) MC component: CP-OFDM
2) CS-MUD component: GOMP-LS and
3) Symbol Mapping component: differential.

In Table 5.3 we have first listed the system parameters that are to be used in the following analyses. Important here is the system load $\beta = 3$, where we have three times as many users in the system as the length of the spreading sequences.

Furthermore, we will look at the performance of the systems in asynchronous environments where the new general waveforms can play out their advantages. Especially the extension at the base station with the factor graph based detection will be able to show its advantages here.

5.6.1 Key Performance Indicators

As already introduced in Section 5.2.2, different error events exist within this system. We summarize all activity related errors, *i.e.* FA and MD, as average activity error rate (AER) at the BS. The FA can be considered as negligible as the implemented CRC will detect these errors. As already

Table 5.3: Parameter Sets for Monte Carlo Simulation

General Parameter	
Payload Size	$N_{\mathbf{b}} = 204\text{bit}$
Number of OFDM Symbols trans.	$N_{\text{TS}} = 228$ Symbols
Delay spread of channel	$\tau^{\max} = 2/3\mu\text{s} \Rightarrow 200\text{m}$
Length of sampled channel imp. resp.	$N_\gamma = 2$
Path-loss exponent	Path loss exponent = 2
Bandwidth of MCSM System	$B_{\text{MCSM}} = N_{\text{s}} F_0 = 120.8\text{kHz}$
Channel code	Half rate conv. $[31_8, 33_8]$ CRC
Symbol Mapping	D-M-PSK, M-PSK $M = 4$
Bandwidth efficiency	$\eta = 10\text{kbit/s}$
Frequency hopping	Every 12 MC symbol
Frequency hops per frame	17 hops
CS-MUD Specific Parameter	
Number of nodes	$N_{\mathsf{u}} = 36$
Spreading seq. length	$N_{\text{s}} = 12$
System load	$\beta = 3$ nodes per resource
Activity detection	GOMP w/ LS, MUSIC w/ LS
Data detection	Linear LS, SPA
Channel est. for D-M-PSK	No channel estimation
Channel est. for M-PSK	Aver. CSI ($\overline{\text{CSI}}$) by LS in (5.26)
Multi-carrier Specific Parameter	
Multi-carrier scheme	CP-OFDM, CP-FBMC,
Tx/Rx Filter	Rect., Gaussian w/ $\rho = 1$
Chip to sub-carrier multiplexing	Frequency oriented
Number of sub-carriers for MCSM	$\lvert \mathcal{S}_i \rvert = N_{\text{s}}$
Number of total sub-carriers used	$N_{\text{SC}} = 256$
Sub-carrier spacing	$F_0 = 10.671\text{kHz}$
MC symbol length	$T_0 = 99.3\mu\text{s}$
Cyclic-prefix length	$T_{\text{GI}} = \tau^{\max}$
Sampling time	$T_{\text{A}} = 388\text{ns}$

mentioned above, the system suffers an SNR loss by the occurrence of an FA,. Thus, the average AER is given by

$$\overline{\mathrm{AER}}_{\mathrm{BS}} = \frac{N_{\text{Activity-Frame-Errors}}}{N_{\text{Active-Frames}}} \quad , \tag{5.38}$$

where $N_{\text{Active-Frames}}$ are the number of active frames transmitted to the BS and $N_{\text{Activity-Frame-Errors}}$ are all active frames wrongly decided, *i.e.* FA and MD. And all data related errors are captured by the average FER at the BS $\overline{\mathrm{FER}}_{\mathrm{BS}}$, which is defined similar to (4.30) like

$$\overline{\mathrm{FER}}_{\mathrm{BS}} = \frac{N_{\text{Data-Frame-Errors}}}{N_{\text{Active-Frames}}} \quad , \tag{5.39}$$

where $N_{\text{Data-Frame-Errors}}$ is the number of erroneous frames received at the BS. The parameters used in the subsequent analysis are summarized in Table 5.3.

5.6.2 Synchronized Transmission

Before going into asynchronous transmission, let's look at the performance of the MCSM system with a fully synchronized setup.

Differential Symbol Mapping Thus, in Fig. 5.23 the average AER and average FER of a MCSM system with the parameters given in Tab. 5.3 without any additional TO or CFO are shown over $1/\sigma_{\mathrm{n}}^2$ in dB. As in the initial publication [**MWBD15b**], the symbol mapping of the MCSM system is D-M-PSK and modulation alphabet size $M = 4$. In this analysis, we focus on CP-OFDM and CP-FBMC as both systems are not affected by any ISI caused by channel delay spread. Besides the GOMP already introduced in Alg. 5.1, we use the famous MUSIC algorithm as activity detector. It can be observed in the left plot of Fig. 5.23 that the activity detection with GOMP algorithm with CP-OFDM get a lower $\overline{\mathrm{AER}}_{\mathrm{BS}}$ at roughly $1/\sigma_{\mathrm{n}}^2 = -5$dB and runs then into an error floor of $3 \cdot 10^{-3}$ for lower noise variances. This error floor comes from the inaccurate assumption of a flat channel as already discussed above. Contrarily, the MUSIC algorithm with CP-OFDM outperforms the GOMP as it has a significant lower error floor at around $1 \cdot 10^{-5}$.

By the application of the MC scheme CP-FBMC with a Gaussian waveform and filter parameter $\rho = 1$, the average AER significantly increases by the application of GOMP algorithm, whereas the average AER with the MUSIC algorithm only slightly increases. The intra-spread correlation of the spreading sequences by the application of CP-FBMC reduces activity

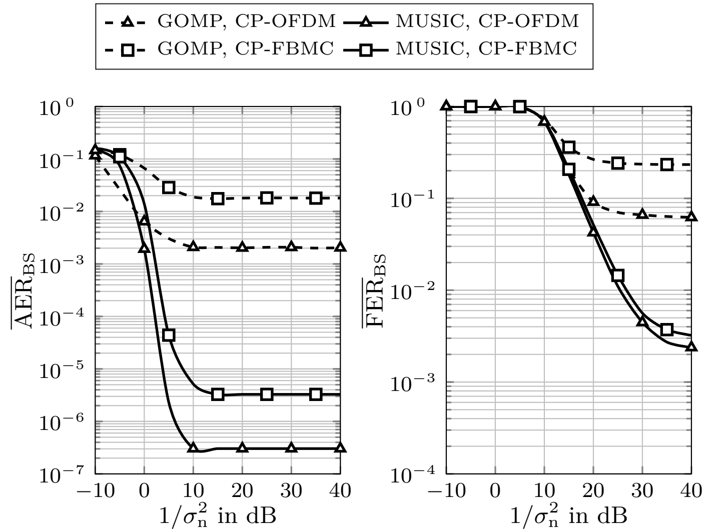

Figure 5.23: AER and FER of a synchronized CP-OFDM and CP-FBMC with LS data detection with differential-quaternary phase shift keying (D-QPSK).

detection capability of the GOMP by roughly one decade in the error floor performance. This behavior was already indicated by the measure MIP in (5.5) that a correlation of the sequences leads to a lower performance.

The average FER shown in the right plot of Fig. 5.23 of the MCSM system is mainly dominated by the AER and thus the average FER runs also in error floor. The performance of the data detection is far worse as the activity detection as for the activity detection more observations are available compared to one data symbol. It's no surprise that CP-OFDM outperforms CP-FBMC in the synchronous case. Especially in this case the non-orthogonal CP-FBMC cannot play out its advantages, because CP-OFDM is perfect orthogonal and therefore no interference is present. However, the MC schemes CP-OFDM and CP-FBMC have roughly the same FER performance with MUSIC algorithm in this synchronized system as the spreading gain dominates.

Non-Differential Symbol Mapping As mentioned above, we can use non-differential symbol mappings like M-PSK as well as differential symbol mappings. Here we use a the non-differential symbol mapping with $M = 4$, *i.e.* QPSK. By using this coherent symbol mapping, we need to estimate

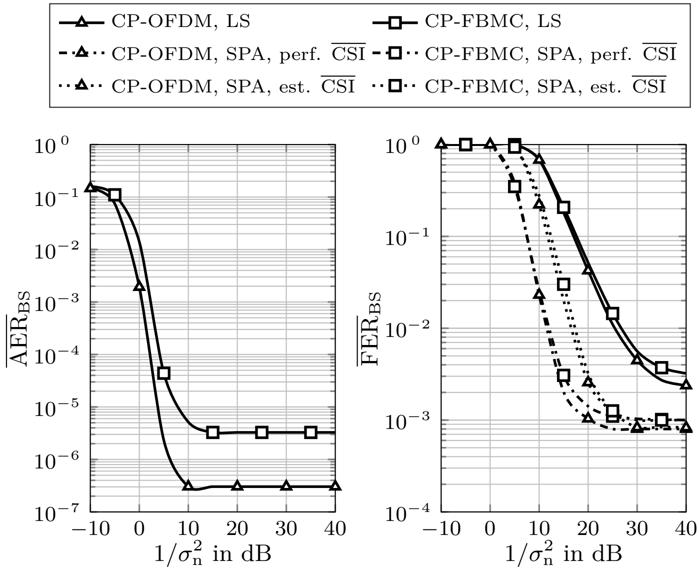

Figure 5.24: AER and FER of a synchronized CP-OFDM and CP-FBMC with SPA data detection perfect known and estimated mean channel state information.

the channel to further process the data as in Fig. 5.17. However, although only the average CSI is estimated as stated in 5.4.3, we can use the more sophisticated two-step approach based on the SPA shown in Fig. 5.22. The average AER and average FER performance of this two-step approach using MUSIC algorithms as activity detectors are shown in Fig. 5.24. The AER remains unchanged compared to Fig. 5.23 as nothing has been changed in the activity detection method. A huge improvement in the average FER is achieved by up to 10dB with perfect knowledge of the **mean** channel coefficient at the lower $1/\sigma_{\text{n}}^{2}$ region. For the higher regions up to 20dB are achievable. The performance by estimating the channel coefficient is shown Fig. 5.24 with dotted lines. As expected, the performance decreases compared to the perfect knowledge of the mean channel coefficient roughly 5dB, but still outperforms the data detection with simple LS detection by 5dB-25dB depending on the noise level. Since in contrast to the full channel knowledge with MCSM only the average channel coefficient is either perfectly known or estimated as shown in Fig. 5.18, the data error rate results in an error floor. The gains are mainly driven by the SPA-based data detection and in the synchronized case CP-OFDM always outperforms the non-orthogonal

CP-FBMC, but rather marginally.

5.6.3 Asynchronous Transmission

So far, we introduced a synchronized MCSM system without any offsets. Here, we now focus on asynchronous transmission. We introduced two different approaches to deal with an asynchronous reception. First, the weighted spreading sequences in Section 5.4.2 for TO and, second, the general waveform like CP-FBMC to deal in particular with CFO in MCSM.

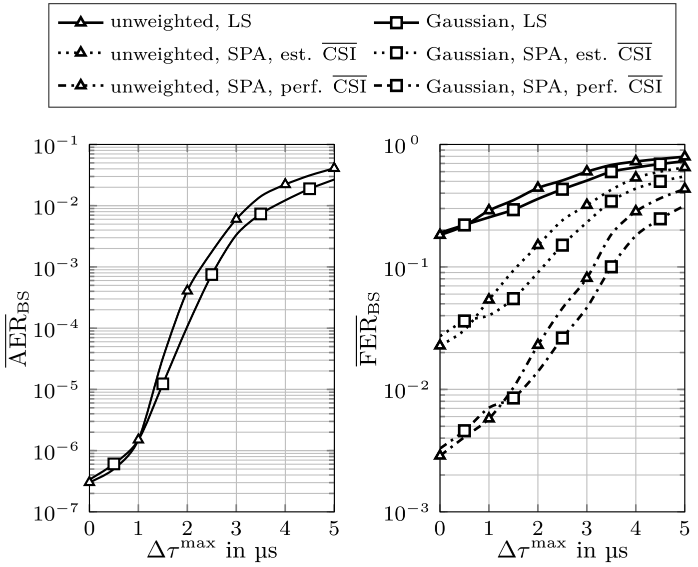

Figure 5.25: AER and FER of CP-OFDM with unweighted and Gaussian weighted spreading sequences affected by timing offset $\Delta\tau$.

The plots in Fig. 5.25 show the average AER and the average FER for CP-OFDM-based MCSM with unweighted and Gaussian weighted spreading sequences over TOs using MUSIC algorithm as activity detector. The TO of each user $\Delta\tau^{\text{u}}$ in this analysis comes from a random process with the uniform distribution within $\mathcal{U}(0, \Delta\tau^{\max})$. Both KPI performances, *i.e.* AER and FER, loose in performance with a higher maximum $\Delta\tau$. However, by the application of the weighted spreading sequences lower error rates are achieved among a wide range of offsets. These results coincide with the correlation analysis in Fig. 5.15, where also the Gaussian weighted spreading sequences achieve a higher correlation with higher TOs.

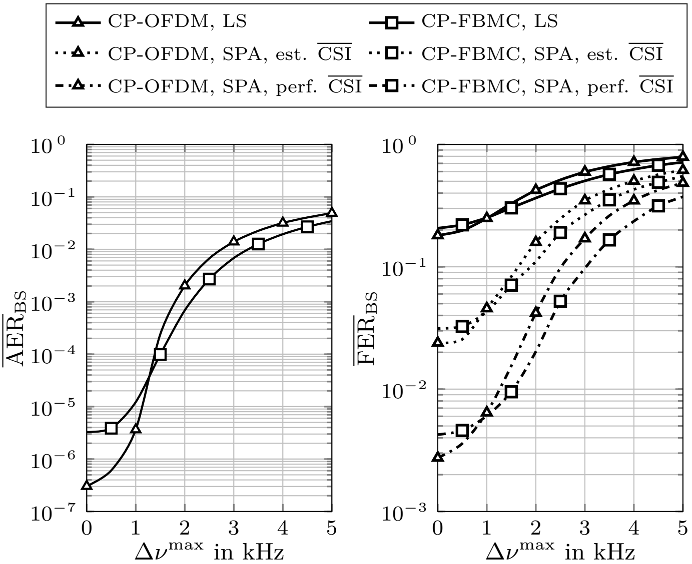

Figure 5.26: AER and FER CP-OFDM and CP-FBMC affected by a CFO $\Delta\nu$.

The plots in Fig. 5.26 show the AER and FER performance of CP-OFDM and CP-FBMC in MCSM over CFOs. Similar to the TO, the CFO of each user $\Delta\nu^{\mathrm{u}}$ is from random process with $\mathcal{U}\left(-\frac{\Delta\nu^{\max}}{2}, \frac{\Delta\nu^{\max}}{2}\right)$. Similar to the analysis in the TWRC in chapter 4, MCSM with a different waveform shows that the better localization property of the Gaussian waveform in CP-FBMC offers a more robust reception for higher CFO.

5.7 Chapter Summary

In this chapter, we examine a new system concept designed for sporadic mMTC. This new system concept called multi-carrier compressed sensing multi-user detection (MCSM), which was firstly published by the author in [**MWBD15b**] and further analyzed in [**MWBD15a, BMWD15, WMBD16**], and [Mon17] and filed in as patent in [**MWBD16a, MWBD15c, MWBD16b, MWDB18b, MWDB18a**] was further extended in this thesis. In contrast to the TWRC system, MCSM uses a spread sequences in MC-CDMA. The extension is a major contribution of this work and was developed to deal with MC schemes with general waveforms, weighted spread sequences and channel estimates at the base station. In addition to the original publication, where the use of differential symbol mapping avoids channel estimation for all users, we introduce non-differential symbol mapping into MCSM and spread pilot symbols. The spread pilots per user provide an average channel estimate among the resources used per user at the base-station. An analysis *w.r.t.* the quality of the channel estimation was performed and it was shown that, for sporadic access to the channel, an average channel estimation achieves a low MSE for low activity of the sensors. By the channel knowledge, the application of detection algorithms was enabled using soft information for the data estimation at the BS. Therefore, we introduced the use of a FG-based detection in MCSM, which resulted in gains of $5 - 30$dB compared to LS data detection used in the original publication, and closes the large difference between activity error rate and frame error rate of the data detection that has been achieved so far. Since CP-OFDM is strongly affected by asynchrony, the introduction of general waveforms and weighted spreading sequences provides robust reception for activity and data acquisition for a wide range of offsets.

Chapter 6

Summary

The extreme high demands for today communications systems increase steadily regarding very broad requirements like coverage, shorty latency, simple transmitter design. Especially, the latter point results in cheap and, thus, low-cost imprecise implementations, which results in a higher detection processing at a receiver. The goal of this thesis is to analyze such scenarios with the help of robust multi-carrier (MC) transmission schemes.

Numerous studies of the application of general MC in simple P2P scenarios were analyzed in the past. Therein, the advantages of the spectral shape as well as the robust behavior in the presence of offsets were frequently shown. Unfortunately, only some analysis were done with a high number of devices which transmit simultaneously to a receiver. Even today, where a huge growth in the number of devices is expected, a combination of MC with general waveforms and other multi-user techniques could be very promising.

In this thesis, two scenarios were selected representing the multiple user scenarios of the future systems. Firstly, two-way relaying channel (TWRC), which allows two users the exchange of data simultaneously over a helping relay on the same time and frequency resources. The challenging task is the detection of the joint message especially then when the transmission is affected with individual timing and frequency offsets. The other scenario was a setup, where it is assumed to have a massive number of users or sensor nodes which only want to transmit a small message to a joint base station. Also, here a perfect synchronous transmission cannot be guaranteed and is hardly realizable.

In **Chapter 2** the fundamentals for a general transmission were investigated. This includes a discussion of channel coding, symbol mapping, a very brief view on general MC transmission schemes. Further a rudimentary consideration of physical channels for single link communication between two users, two users communication via a relay node, and for a massive number of users communicating to a base-station. Because the subsequent discussed estimators be treated in a factor graph-based fashion, all mentioned blocks were depicted as factor graph and a detailed discussion on factor graphs was outsourced to **Appendix B**.

An integral part of this thesis was the consideration of general MC transmission schemes so that this topic even if it is well-known in literature was given an own chapter. In **Chapter 3** the basics of general MC procedures for single P2P communication were discussed in a significant deeper manner as the previous chapter. For that, first, the general MC system model with the different time-frequency grid spacings and the general waveforms has been introduced in terms of an effective channel matrix. Therein the main view has been focused on the ambiguity function, which is a representative of the waveforms used. Secondly, famous concrete MC transmission schemes like the CP-OFDM, OQAM/FBMC or QAM/FBMC were discussed in terms of orthogonality, time-frequency grid density and waveform localization. Especially, the effective channel matrix under offsets has been discussed. The orthogonal schemes share the nice property in synchronous transmission of having an effective channel matrix with only elements on the main diagonal. This leads to possible application of simple 1-tap frequency domain equalizers. However, under offsets the effective matrices will change significantly. Especially here, the non-orthogonal schemes with well-localized waveforms demonstrate their advantages. In a synchronous transmission the effective channel matrix of non-orthogonal MC schemes will have some off-diagonal elements, but the application of well-localized waveforms, like the Gaussian waveform, leads to roughly the same effective channel matrix even in highly asynchronous transmissions. Thus, they offer a higher robustness compared to the orthogonal counterparts even if the computational complexity for detection is higher in synchronous transmission.

At the beginning of **Chapter 4** the fundamental basics of TWRC in a single-carrier (SC) transmission with simple 1-tap channels have been discussed. First, the general scenario has been described before the two phase scenario was introduced, which compared to the other scenarios offers the advantage of a higher data rate. To keep this promise, the detector has to be able to detect the PLNC joint message at the relay. For this, three well-known algorithms, *i.e.* SCD, JCNC, and GJCNC, have been presented and were analyzed in synchronous flat-fading channels to first show the behavior of the algorithms. In particularly, all PLNC detection schemes are sensitive to phase differences and the error rates drop down significant for ambiguous symbol phase mappings. The joint message consists of the summation of both user signals affected by individual impacts like timing or frequency offset. The post-compensation of asynchronism of the two users at the relay is particularly difficult as the compensation can only by done on the joint message. To reduce these impacts a combination of TWRC and general MC transmission schemes with well localized waveform has been proposed. A famous example from literature is the OQAM-based MC transmission scheme, which applies a clever combination of well-localized filters and an arrangement of the symbols and interference on the time-frequency grid. This property results in an orthogonal or interference reduced transmission scheme ant leads to a higher robustness in P2P transmissions. However, in this work it was shown that the sensitivity of TWRC and the OQAM-based technique lead to a worse performance as the symbols are limited to purely real or purely imaginary domain. Contrarily to this, the QAM-based schemes, like the orthogonal CP-OFDM or the QAM/FBMC and its derivative GFDM have no phase sensitivity. Unfortunately, the famous MC scheme CP-OFDM is highly sensitive to frequency offsets. In the following analysis the PLNC detectors and general waveform has been presented as factor graphs based on the effective channel matrix. The QAM-based MC schemes with well-localized waveforms generate a very stable factor graph as the connections in the factor graph are directly related to the structure of effective channel matrix. This robustness comes by the choice of the waveform as the main energy is primary limited to the adjacent time-frequency grid points. This causes a significant improvement in error performance and the computational complexity stay within reasonable limits by considering only the adjacent time-frequency grid points in the factor graph. This is in contrast to the orthogonal transmission schemes based on the rectangular waveform, where a significant higher number of time-frequency grid points have to be considered to achieve a low error performance resulting in unreasonable high computational complexity. All these features make the combination a very promising technique to achieve high data rates with a good coverage in the TWRC scenario.

In **Chapter 5** a somehow similar overloaded scenario has been considered. This scenario was concerned with a massive number of MTC sensor nodes, where each node wants to transmit some short status information to a common base station (BS). In contrast to well-known schemes like WLAN, Bluetooth, and *etc.*, the activity and data of the sporadic active nodes should be detected in the PHY and data link layer, directly based on DRA medium access. To this end, a new PHY concept was presented, which is a skillful combination of narrow-band general MC transmission scheme, compressed sensing-multi-user detection (CS-MUD), and non-orthogonal pilots. CS-MUD is already known in the literature to estimate the activity and data of massive communication in such an industrial application. After a brief introduction of the underlying concept of CS-MUD, the combination of these three key components was introduced, and the system was called multi-carrier compressed sensing multi-user detection (MCSM). It was shown that with the assumption of transmitting within the coherence bandwidth of the channel, the MCSM system model results in a simple MMV-CS matrix model which can be solved by CS-MUD detection strategies. Especially the non-orthogonal pilots which can be implemented as differential symbol mapping or straight symbol mapping before spreading lead to reduction of signaling overhead before transmission. It was shown that these assumption works only in scenarios with sporadic transmission with low-activity and low data rate and will fail in full-blown high data rate systems. However, this was not intended be design. Similar to the TWRC scenario, the summation of all user signals including the impact of the individual offsets is the basis of the detection at the BS.

Using the new concepts introduced in this thesis, such as well-localized waveforms for the MC transmission schemes obtain a higher robustness for activity and data detection for a wide range of offsets even in this simple implementation of MCSM. Furthermore, by the application of factor graph (FG) data estimation a gain of roughly $5 - 30$dB compared to the simple LS can be achieved.

Overall, this work gave some deeper insight to MC applying well-localized waveforms and its applications. Especially, the use of well-localized waveforms and FG-based detection, utilizing the knowledge of the waveforms, a factor graph-based equalizer (FGE) has been developed which combine the advantages of both worlds. The results of these analyses yield the statement that MC concepts with well-localized waveform can improve the robustness in multiple access schemes.

Open Questions and Future Work

Even though this work aimed to demonstrate the robustness of general transmission schemes in high-end scenarios, it also raised some additional questions that could not be answered in the limited scope of this work. Below, some of these questions and related tasks for future work are briefly summarized:

- The combination of TWRC, general MC with well-localized waveforms and factor graph-based detection considered here is a promising approach. However, as we have seen here, the structure always has loops that lead to sub-optimal solutions, even if the performance is excellent. To improve the performance even further approaches could be used to close the cycles in the FG as in [LYWM05] by the application of an BCJR algorithm.

- Moreover, in addition to the above-mentioned point, especially for very different channels, adapted transmit waveforms can be used by each user to restrict the interference to a few neighbors in the time-frequency grid. This would still allow a very robust receiver design. Also, in addition, in such a case, a different adjusted time-frequency grid could be applied to control the interference similar to [SK15].
- The MCSM concept opens up a wide field of research activities. Especially in a variety of applications, the physical channels differ greatly and an analysis of different coherence bandwidths or coherence times in these scenarios would be useful to apply a suitable mapping to time-frequency grid and allows for better adaptation and greater performance.
- The data detection in the MCSM concept was implemented in this work with the help of a two-stage approach, which has minor disadvantages with very small frame sizes, since the activity detection is clearly more susceptible compared to the data detection here. The approach for small frames would then rather be the AMP used in [Mon17]. In addition, the information about successful data detection was not attributed to the activity estimator. Therefore, interference cancellation of already decided data would be a promising approach for extremely short frames.

Appendix A

Multi-Carrier Transmission Schemes

A.1 Effective Channel Coefficient

The main goal is the derivation of the effective channel coefficient $h_{r,s}$ used also in the matrix model (3.27). The derivation follows similar steps like in [DS07b, Du08, DS08].

After matched filtering the receive signal (2.7) in (3.9) with corresponding transmit signal $x(t)$ (*cf.* (3.5)) of one user (we skip the user index u in this discussion), the representation of the channel as delay-Doppler function $s(\tau,\nu)$ (*cf.* (2.9)) the receive signal at time-frequency (TF) grid point (k,ℓ) can be rewritten as

$$y_{k',\ell'} = \sum_{k}\sum_{\ell} d_{k,\ell} \underbrace{\iiint s(\tau,\nu)\, g^{\mathrm{Tx}}_{k,\ell}(t-\tau)\, g^{\mathrm{Rx}}_{k',\ell'}(t)\, e^{j2\pi\nu t} \mathrm{d}\tau \mathrm{d}\nu \mathrm{d}t}_{h\left(s(\tau,\nu), g^{\mathrm{Tx}}_{k,\ell}(t), g^{\mathrm{Rx}}_{k',\ell'}(t)\right)} + \tilde{n}_{k',\ell'}. \tag{A.1}$$

The term $h(s(\tau,\nu), g^{\mathrm{Tx}}_{k,\ell}(t), g^{\mathrm{Rx}}_{k',\ell'}(t))$ contains the impact of the channel $s(\tau,\nu)$ and the prototype Tx/Rx filters $g^{\mathrm{Tx}}_{k,\ell}(t)$ and $g^{\mathrm{Rx}}_{k',\ell'}(t)$. It will be termed *effective channel coefficient* throughout the work and it should be simplified herein by the use of the ambiguity function defined in (3.12).

The effective channel coefficient can be further simplified such that the waveform dependent part $\mathscr{W}$ is captured by only one integral like in

$$\begin{aligned}
&h\left(s\left(\tau,\nu\right),g_{k,\ell}^{\mathrm{Tx}}\left(t\right),g_{k',\ell'}^{\mathrm{Rx}}\left(t\right)\right)\\
&\quad=\iiint s\left(\tau,\nu\right)g_{k,\ell}^{\mathrm{Tx}}\left(t-\tau\right)g_{k',\ell'}^{\mathrm{Rx}}\left(-t\right)e^{j2\pi\nu t}\mathrm{d}\tau\mathrm{d}\nu\mathrm{d}t\\
&\quad=\iint s\left(\tau,\nu\right)\underbrace{\int g_{k,\ell}^{\mathrm{Tx}}\left(t-\tau\right)g_{k',\ell'}^{\mathrm{Rx}}\left(-t\right)e^{j2\pi\nu t}\mathrm{d}t}_{\text{Waveform dependent part }\mathscr{W}}\mathrm{d}\tau\mathrm{d}\nu
\end{aligned}$$

By inserting the definition of the transmit and receive filter like in (3.4) and (3.8), the waveform dependent parameter yields

$$\begin{aligned}
\mathscr{W}&=\int g_{k,\ell}^{\mathrm{Tx}}\left(t-\tau\right)g_{k',\ell'}^{\mathrm{Rx}}\left(-t\right)e^{j2\pi\nu t}\mathrm{d}t\\
&=\int g^{\mathrm{Tx}}\left(t-\ell T_0-\tau\right)e^{j2\pi kF_0(t-\tau)+j\phi_{k,\ell}}\\
&\qquad\times g^{\mathrm{Rx}}\left(-t-\ell' T_0\right)e^{j2\pi k'F_0(-t)+j\phi_{k',\ell'}}e^{j2\pi\nu t}\mathrm{d}t\\
&=\int g^{\mathrm{Tx}}\left(t-\ell T_0-\tau\right)g^{\mathrm{Rx}}\left(-t-\ell' T_0\right)\\
&\times e^{j2\pi\left(kF_0(t-\tau)-k'F_0t+\nu t\right)+j\left(\phi_{k',\ell'}+\phi_{k,\ell}\right)}\mathrm{d}t
\end{aligned}$$

Here, the matched filter condition $g^{\mathrm{Rx}}\left(t\right)=\left(g^{\mathrm{Tx}}\right)^{*}\left(-t\right)$ is used and the name Tx is skipped. Apply the substitution $t=t'+\frac{(\ell+\ell')T_0+\tau}{2}$, the parameter $\mathscr{W}$ will change to

$$\begin{aligned}
\mathscr{W}=&\int g\left(t'-\frac{\left(\ell-\ell'\right)T_0+\tau}{2}\right)g^{*}\left(t'+\frac{\left(\ell-\ell'\right)T_0+\tau}{2}\right)\\
&\times e^{j2\pi[\left(\left(k-k'\right)F_0+\nu\right)(t'+\frac{(\ell+\ell')T_0+\tau}{2})-kF_0\tau]+j\left(\phi_{k',\ell'}+\phi_{k,\ell}\right)}\mathrm{d}t'
\end{aligned}$$

By further substituting $t=t'$ and doing some rearrangement will result

$$\begin{aligned}
\mathscr{W}=&e^{j\pi\left[\left(\left(k-k'\right)F_0+\nu\right)\left(\left(\ell+\ell'\right)T_0+\tau\right)-2kF_0\tau\right]+j\left(\phi_{k',\ell'}+\phi_{k,\ell}\right)}\\
&\times\int g\left(t-\frac{\left(\ell-\ell'\right)T_0+\tau}{2}\right)g^{*}\left(t+\frac{\left(\ell-\ell'\right)T_0+\tau}{2}\right)e^{j2\pi\left(\left(k-k'\right)F_0+\nu\right)t}\mathrm{d}t
\end{aligned}$$

By using the abbreviation parameters for the Doppler spread $\overline{\nu}=\left(k-k'\right)F_0+\nu$, the delay spread $\overline{\tau}=\left(\ell-\ell'\right)T_0+\tau$ and the phase

$\overline{\phi} = -\pi \left(2kF_0\tau - \overline{\nu}\,\overline{\tau}\right)$, we achieve a compact form like

$$\mathscr{W} = e^{j\left(\phi_{k',\ell'}+\phi_{k,\ell}\right)} e^{j\overline{\phi}} \underbrace{\int g\left(t-\frac{\overline{\tau}}{2}\right) g^*\left(t+\frac{\overline{\tau}}{2}\right) e^{j2\pi\overline{\nu}t}\mathrm{d}t}_{A^*_{g,g}(\overline{\tau},\overline{\nu})}$$

We use the short-hand notation $h_{r,s} = h\left(s\left(\tau,\nu\right), g^{\mathrm{Tx}}_{k,\ell}\left(t\right), g^{\mathrm{Rx}}_{k',\ell'}\left(t\right)\right)$ with the transmit running index $s = f\left(k,\ell\right)$ and the receive running index $r = f\left(k',\ell'\right)$ for the prototype filters [1] and the effective channel coefficient yields

$$h_{r,s} = e^{j(\phi_r+\phi_s)} \int_{-\infty}^{\infty}\int_{-\infty}^{\infty} \underbrace{s\left(\tau,\nu\right)}_{\substack{\text{delay-}\\ \text{Doppler function}}} \quad e^{j\overline{\phi}} \underbrace{A^*_{g^{\mathrm{Tx}},g^{\mathrm{Rx}}}\left(\overline{\tau},\overline{\nu}\right)}_{\text{Tx/Rx Waveform}} \mathrm{d}\tau\mathrm{d}\nu \tag{A.2}$$

Inserting a general time-variant channel like in (2.13) represented by delta functions results finally in an effective channel coefficient:

$$h_{r,s} = e^{j(\phi_r+\phi_s)} \sum_{\gamma=0}^{N_{\mathrm{path}}-1} \varsigma_\gamma e^{j\overline{\phi}_\gamma} A^*_{g^{\mathrm{Tx}},g^{\mathrm{Rx}}}\left(\overline{\tau}_\gamma,\overline{\nu}_\gamma\right) \tag{A.3}$$

with the abbreviation parameters: $\overline{\nu}_\gamma = \left(k-k'\right)F_0+\nu_\gamma$, $\overline{\tau}_\gamma = \left(\ell-\ell'\right)T_0+\tau_\gamma$, $\overline{\phi}_\gamma = -\pi\left(2kF_0\tau_\gamma - \overline{\nu}_\gamma\overline{\tau}_\gamma\right)$.This effective channel coefficient is used throughout the thesis.

A.2 Orthogonality in Multi-Carrier Schemes

Herein, we check the orthogonality condition for QAM-based and OQAM-based transmission schemes. The derivation follows similar steps like in [DS07b, Du08, DS08].

Orthogonality with QAM Modulation In multi-carrier schemes with QAM modulation the complex inner product

$$\langle g^{\mathrm{Tx}}_{k,\ell}, g^{\mathrm{Rx}}_{k',\ell'}\rangle_{\mathbb{C}} = \int_{\mathbb{R}} g^{\mathrm{Tx}}_{k,\ell}\left(t\right) g^{*\mathrm{Rx}}_{k',\ell'}\left(t\right)\mathrm{d}t = \begin{cases} 1 & \text{if } \ell' = \ell \text{ and } k' = k \\ 0 & \text{otherwise} \end{cases} \tag{A.4}$$

is used. An orthogonal system design is achieved, if the inner product fulfills the condition:

$$\langle g^{\mathrm{Tx}}_{k,\ell}, g^{\mathrm{Rx}}_{k',\ell'}\rangle_{\mathbb{C}} = \begin{cases} 1 & \text{if } \ell' = \ell \text{ and } k' = k \\ 0 & \text{otherwise} \end{cases} . \tag{A.5}$$

---

[1] for a matrix notation later on, the running indices are below in (3.10).

By inserting the Tx/Rx waveforms (3.4) and (3.8), where the phases $\phi_{k,\ell} = \phi_{k',\ell'} = 0$ will result in

$$\langle g_{k,\ell}^{\mathrm{Tx}}, g_{k',\ell'}^{\mathrm{Rx}} \rangle_{\mathbb{C}} = \int_{\mathbb{R}} g\left(t - \ell T_0\right) e^{j2\pi k F_0 t} g^*\left(t - \ell' T_0\right) e^{-j2\pi k' F_0 t} \mathrm{d}t$$

using $t = t' + \frac{(\ell+\ell')T_0}{2}$ and perform some rearrangement yields

$$\begin{aligned}\langle g_{k,\ell}^{\mathrm{Tx}}, g_{k',\ell'}^{\mathrm{Rx}} \rangle_{\mathbb{C}} = &\int_{\mathbb{R}} e^{j2\pi\left(k-k'\right)F_0\left(t'+\frac{(\ell+\ell')T_0}{2}\right)} \\ &g\left(t' + \frac{\left(\ell+\ell'\right)T_0}{2} - \ell T_0\right) g^*\left(t' + \frac{\left(\ell+\ell'\right)T_0}{2} - \ell' T_0\right) \mathrm{d}t' \\ &= e^{j\pi\left(k-k'\right)\left(\ell-\ell'\right)F_0 T_0} \int_{\mathbb{R}} e^{j2\pi\left(k-k'\right)F_0 t'} \\ &g\left(t' + \frac{\left(\ell-\ell'\right)T_0}{2}\right) g^*\left(t' - \frac{\left(\ell-\ell'\right)T_0}{2}\right) \mathrm{d}t'\end{aligned}$$

Using the ambiguity function (3.12) the orthogonality condition yields

$$\langle g_{k,\ell}^{\mathrm{Tx}}, g_{k',\ell'}^{\mathrm{Rx}} \rangle_{\mathbb{C}} = e^{j\pi\left(k-k'\right)\left(\ell-\ell'\right)F_0 T_0} A\left(\underbrace{\left(\ell-\ell'\right)}_{\tilde{\ell}} T_0, \underbrace{\left(k-k'\right)}_{\tilde{k}} F_0\right). \quad \text{(A.6)}$$

To design an orthogonal transmission, the inner product has to fulfill (A.5). Thus, the ambiguity function should fulfill the condition

$$A\left(\tilde{\ell} T_0, \tilde{k} F_0\right) = \begin{cases} 1, & \tilde{\ell} = 0, \tilde{k} = 0 \\ 0, & \text{otherwise.} \end{cases}$$

Orthogonality with OQAM Modulation In FBMC with SMT (OQAM/FBMC) or CMT the real valued inner product is used like

$$\langle g_{k,\ell}^{\mathrm{Tx}}, g_{k',\ell'}^{\mathrm{Rx}} \rangle_{\mathbb{R}} = \Re\left\{\int_{\mathbb{R}} g_{k,\ell}^{\mathrm{Tx}}\left(t\right) g_{k',\ell'}^{*\mathrm{Rx}}\left(t\right) \mathrm{d}t\right\} = \begin{cases} 1 & \text{if } \ell' = \ell \text{ and } k' = k \\ 0 & \text{otherwise} \end{cases}. \quad \text{(A.7)}$$

The calculation are done for OQAM/FBMC, but can be easily exchanged to CMT.

$$\begin{aligned}
&\langle g^{\mathrm{Tx}}_{k,\ell}, g^{\mathrm{Rx}}_{k',\ell'}\rangle_{\mathbb{R}} \\
&= \Re\left\{\int_{\mathbb{R}} g\left(t-\ell T_0\right) e^{j2\pi k F_0 t} e^{j(\ell-k)\frac{\pi}{2}} g^*\left(t-\ell' T_0\right) e^{j2\pi k' F_0 t} e^{j\left(\ell'-k'\right)\frac{\pi}{2}} \,\mathrm{d}t\right\} \\
&= \Re\left\{\int_{\mathbb{R}} e^{j\frac{\pi}{2}\left[\left(k-k'\right)+\left(\ell-\ell'\right)\right]} e^{j\left(k-k'\right)2\pi F_0 t} g\left(t-\ell T_0\right) g^*\left(t-\ell' T_0\right) \mathrm{d}t\right\}
\end{aligned}$$

now by substituting $t = t' + \frac{\left(\ell+\ell'\right)T_0}{2}$

$$\begin{aligned}
&\langle g^{\mathrm{Tx}}_{k,\ell}, g^{\mathrm{Rx}}_{k',\ell'}\rangle_{\mathbb{R}} = \\
&\qquad \Re\left\{ e^{j\frac{\pi}{2}\left[\left(k-k'\right)+\left(\ell-\ell'\right)\right]} e^{j\left(k-k'\right)2\pi F_0 \frac{\left(\ell+\ell'\right)T_0}{2}} \int_{\mathbb{R}} e^{j\left(k-k'\right)2\pi F_0 t'} \right. \\
&\qquad \left. \times\, g\left(t' + \frac{\left(\ell+\ell'\right)T_0}{2} - \ell T_0\right) g^*\left(t' + \frac{\left(\ell+\ell'\right)T_0}{2} - \ell' T_0\right) \mathrm{d}t' \right\}
\end{aligned}$$

In OQAM/FBMC the following condition holds $\delta_{\mathrm{LD}}\left(\Lambda\right) = \frac{1}{F_0 T_0} = 2$ or in other words $F_0 T_0 = \frac{1}{2}$ leading to

$$\begin{aligned}
&\langle g^{\mathrm{Tx}}_{k,\ell}, g^{\mathrm{Rx}}_{k',\ell'}\rangle_{\mathbb{R}} = \\
&\Re\left\{ e^{j\frac{\pi}{2}\left[\left(k-k'\right)+\left(\ell-\ell'\right)+\left(k-k'\right)\left(\ell+\ell'\right)\right]} \right. \\
&\left. \times \int_{\mathbb{R}} e^{j\left(k-k'\right)2\pi F_0 t'} g\left(t' - \frac{\left(\ell+\ell'\right)T_0}{2}\right) g^*\left(t' + \frac{\left(\ell+\ell'\right)T_0}{2}\right) \mathrm{d}t' \right\}.
\end{aligned}$$

Finally, by using $e^{jn\frac{\pi}{2}} = j^n$, if $n \in \mathbb{Z}$, the real valued inner product results in

$$\langle g^{\mathrm{Tx}}_{k,\ell}, g^{\mathrm{Rx}}_{k',\ell'}\rangle_{\mathbb{R}} = \Re\left\{ \underbrace{j^{\left(\left(k-k'\right)+\left(\ell-\ell'\right)+\left(k-k'\right)\left(\ell+\ell'\right)\right)}}_{\textcircled{1}} \underbrace{A\left(\left(\ell-\ell'\right)T_0, \left(k-k'\right)F_0\right)}_{\textcircled{2}} \right\}.$$

In contrast to the transmission with QAM mapping, where the orthogonality can only designed by the ambiguity function (A.6), OQAM mapping offers an additional possibility ① to achieve an orthogonal transmission beside the ambiguity function ②. Having a deeper look at the indices's, it turns out that part ① is purely imaginary, if the condition

$$\left(\ell \mod 2, k \mod 2\right) = \left(\ell' \mod 2, k' \mod 2\right) \tag{A.8}$$

holds [Du08]. Hence, if the ambiguity function is purely real, which is achievable by using symmetric Tx/Rx filters, the condition on the ambiguity function to achieve an orthogonal transmission can be relaxed to

$$A\left(2\ell T_0, 2kF_0\right) = \begin{cases} 1, & \ell = 0, k = 0 \\ 0, & \text{otherwise.} \end{cases} \tag{A.9}$$

A.3 Mirabbasi and EGF Waveform

Here, the mathematical description of the two filter Mirabbasi and EGF waveforms mentioned in Section 3.2.2 on page 37 are given. It should be pointed out that the notation here is somehow related to the original paper and in some places contradicts the notation used in this work, due to a lack of Greek letters.

Mirabbasi Waveform According to [Mar98, MM02, Bel02, MM03, Bel10, SGA12] the Mirabbasi waveform used in the PHYDYAS project can be expressed by

$$g_{\text{Mirabbasi}}\left(t\right) = \begin{cases} 1 + 2\sum\limits_{q=1}^{Q-1} a_q \cos\left(2\pi \dfrac{qt}{QT_{\mathrm{S}}}\right) & \text{, for } -\frac{QT_{\mathrm{S}}}{2} \leq t \leq \frac{QT_{\mathrm{S}}}{2} \\ 0 & \text{, otherwise} \end{cases}, \tag{A.10}$$

in a non-causal representation, where the coefficients a_q are listed in Table A.1, with overlapping factor Q.

Table A.1: Coefficient a_q for Mirabbasi prototype filter

a_q	$Q = 3$	$Q = 4$	$Q = 5$	$Q = 6$	$Q = 7$	$Q = 8$
q_1	0.91143783	0.97195983	0.99184131	0.99818572	0.99938080	0.99932588
q_2	0.41143783	0.70710678	0.86541624	0.94838678	0.97838560	0.98203168
q_3	0	0.23514695	0.50105361	0.70710678	0.84390076	0.89425129
q_4	0	0	0.12747868	0.31711593	0.53649931	0.70710678
q_5	0	0	0	0.06021021	0.20678881	0.44756522
q_6	0	0	0	0	0.03518546	0.18871614
q_7	0	0	0	0	0	0.03671221

Extended Gaussian Function Waveform According to [SR00, Du08], the EGF waveform can be calculated by

$$g^{(\rho)}_{\mathrm{EGF},F_0,T_0}(t) = \frac{1}{2}\sum_{q=0}^{\infty} d_{q,\rho,F_0}\left[g^{(\rho)}_{\mathrm{Gaussian}}\left(t+\frac{q}{F_0}\right)+g^{(\rho)}_{\mathrm{Gaussian}}\left(t-\frac{q}{F_0}\right)\right] \cdot \sum_{\iota=0}^{\infty} d_{\iota,1/\rho,T_0}\cos\left(2\pi\iota\frac{t}{T_0}\right) \tag{A.11}$$

The EGF waveform is based on the sum of Gaussian waveforms (3.18) and thus depends on the filter parameter ρ and on the symbol spacing in time T_0 and frequency F_0. The approximated coefficients

$$d_{q,\rho,F_0} \approx \sum_{j=0}^{j_q} b_{q,j}\, e^{(-\pi\rho/2F_0^2)(2j+q)} \text{ with } 0 \le q \le Q \tag{A.12}$$

where j_q depends on q with $j_q = \lfloor (q-Q)/2 \rfloor$ and is a positive integer which insure an accuracy of $e^{-\frac{\pi\rho Q}{2F_0^2}}$ for the approximation due to truncation of the infinite summation of the original definition in [RS97]. with filter parameter in range $0.528F_0^2 < \rho < \frac{1}{0.528F_0^2}$. The coefficients $b_{q,j}$ are given in Table A.2.

A.4 Circulant Matrices

A matrix $\mathbf{H}$ with size $N \times N$ is circulant, if the following condition [Str16] holds

$$\mathbf{H} = \begin{bmatrix} h_0 & h_{N-1} & \cdots & h_2 & h_1 \\ h_1 & h_0 & h_{N-1} & & h_2 \\ \vdots & h_1 & h_0 & \ddots & \vdots \\ h_{N-2} & & \ddots & \ddots & h_{N-1} \\ h_{N-1} & h_{N-2} & \cdots & h_1 & h_0 \end{bmatrix} . \tag{A.13}$$

Any circulant matrix can be represented by the SVD [Str16] as

$$\mathbf{H} = \mathbf{F}_N^{\mathsf{H}} \mathbf{\Sigma} \mathbf{F}_N \quad , \tag{A.14}$$

where $\mathbf{F}_N$ and $\mathbf{F}_N^{\mathsf{H}}$ are the and Fourier and inverse Fourier matrix of length N, respectively, and $\mathbf{\Sigma}$ is a purely diagonal matrix with eigenvalues on the diagonal elements.

Table A.2: Coefficient $b_{q,j}$ for EGF prototype filter.

$b_{q,j}$	$j=0$	$j=1$	$j=2$	$j=3$	$j=4$	$j=5$	$j=6$	$j=7$
$q=0$	1	$\frac{3}{4}$	$\frac{105}{64}$	$\frac{675}{256}$	$\frac{76233}{16384}$	$\frac{457107}{65536}$	$\frac{12097169}{1048576}$	$\frac{13774755}{4194304}$
$q=1$	-1	$\frac{-15}{8}$	$\frac{-219}{64}$	$\frac{-6055}{1024}$	$\frac{-161925}{16384}$	$\frac{-2067909}{1311072}$	$\frac{-26060847}{1048576}$	0
$q=2$	$\frac{3}{4}$	$\frac{19}{16}$	$\frac{1545}{512}$	$\frac{9765}{2048}$	$\frac{596277}{65536}$	$\frac{3679941}{262144}$	$\frac{105421227}{16777216}$	0
$q=3$	$\frac{-5}{8}$	$\frac{-123}{128}$	$\frac{-2289}{1024}$	$\frac{-34871}{8192}$	$\frac{-969375}{131072}$	$\frac{-51182445}{4194304}$	0	0
$q=4$	$\frac{35}{64}$	$\frac{213}{256}$	$\frac{7797}{4096}$	$\frac{56163}{16384}$	$\frac{13861065}{2097152}$	$\frac{139896345}{8388608}$	0	0
$q=5$	$\frac{-63}{128}$	$\frac{-763}{1024}$	$\frac{-13875}{8192}$	$\frac{-790815}{262144}$	$\frac{-23600537}{4194304}$	0	0	0
$q=6$	$\frac{231}{512}$	$\frac{1395}{2048}$	$\frac{202281}{131072}$	$\frac{1434705}{524288}$	$\frac{142044345}{16777216}$	0	0	0
$q=7$	$\frac{-429}{1024}$	$\frac{-20691}{32768}$	$\frac{-374325}{262144}$	$\frac{-5297445}{2097152}$	0	0	0	0
$q=8$	$\frac{6435}{16384}$	$\frac{38753}{65536}$	$\frac{1400487}{1048576}$	$\frac{1458219}{4194304}$	0	0	0	0
$q=9$	$\frac{-12155}{32768}$	$\frac{-146289}{262144}$	$\frac{-2641197}{2097152}$	0	0	0	0	0
$q=10$	$\frac{46189}{131072}$	$\frac{277797}{524288}$	$\frac{20050485}{16777216}$	0	0	0	0	0
$q=11$	$\frac{-88179}{262144}$	$\frac{-2120495}{4194304}$	0	0	0	0	0	0
$q=12$	$\frac{676039}{2097152}$	$\frac{4063017}{8388608}$	0	0	0	0	0	0
$q=13$	$\frac{-1300075}{4194304}$	0	0	0	0	0	0	0
$q=14$	$\frac{5014575}{16777216}$	0	0	0	0	0	0	0

A.5 Windowed-OFDM

In this section, we derive the matrix description of the w-OFDM with and without CP. We start the considerations with the non-overlapping w-CP-OFDM, before we show the principle of the overlapping w-CP-OFDM.

A.5.1 Non-overlapping w-CP-OFDM

The sampling stays $F_\mathrm{A} = 1/T_\mathrm{A}$ and $t = qT_0/N_\mathrm{SC}$ and the filter length is $T_\mathrm{g} = N_\mathrm{g}T_0/N_\mathrm{SC}$, where *w.l.o.g.* N_g is an even number for a fixed number of time shifts ℓ shown in Fig. 3.14. Rewriting the transmit signal (3.5) with (3.44) and taking similar steps like in (3.28) and (3.29), the signal for each MC symbol

ℓ can be generated separately with $q = -(N_\mathrm{g}/2 + N_\mathrm{CP}), \ldots, N_\mathrm{SC} + N_\mathrm{g}/2 - 1$ as

$$x_\ell \left[q - \ell\left(N_\mathrm{SC} + N_\mathrm{CP} + N_\mathrm{g}\right)\right] = \sum_{k=0}^{N_\mathrm{SC}-1} d_{k,\ell} g^\mathrm{Tx} \left[q - \ell\left(N_\mathrm{SC} + N_\mathrm{CP} + N_\mathrm{g}\right)\right] e^{\frac{j2\pi kq}{N_\mathrm{SC}}}$$

assuming that the filter decay and ramp of two adjacent MC symbols have no intersection, like Fig. A.1a. Thus, the Tx signal can be separated into three (four) parts *w.r.t.* the Tx filter in Fig. A.1 (*cf.* Fig. 3.16):

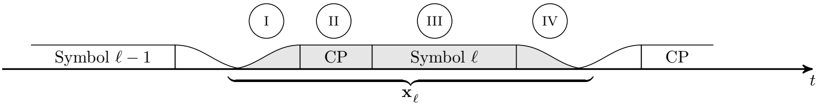

a) w-CP-OFDM without overlap

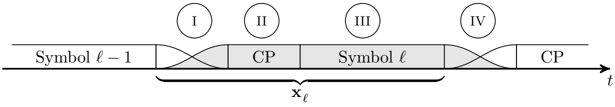

b) w-CP-OFDM with overlap

Figure A.1: Transmit signal generation by the separation into four parts for a) the non-overlapping and b) the overlapping w-CP-OFDM.

Part **I** rise time, Part **II** (optional) cyclic prefix, Part **III** core symbol, and Part **IV** decay time

Part I: During the rise time $q = -\frac{N_\mathrm{g}}{2} - N_\mathrm{CP}, \ldots, -N_\mathrm{CP} - 1$, where the filter is $g\left[q - \ell\left(N_\mathrm{SC} + N_\mathrm{g} + N_\mathrm{CP}\right)\right] = 0, ..., 1$ the transmit signal yields

$$\begin{aligned} x_\ell \left[q - \ell\left(N_\mathrm{SC} + N_\mathrm{g} + N_\mathrm{CP}\right)\right] =& g\left[q - \ell\left(N_\mathrm{SC} + N_\mathrm{g} + N_\mathrm{CP}\right)\right] \\ & \cdot \sum_{k=0}^{N_\mathrm{SC}-1} d_{k,\ell} e^{\frac{j2\pi kq}{N_\mathrm{SC}}} \quad . \end{aligned} \tag{A.15}$$

It should be noted that exponential function is integer periodic, thus, we use the substitution $q' = q + N_\mathrm{SC} = N_\mathrm{SC} - \frac{N_\mathrm{g}}{2} - N_\mathrm{CP}, \ldots, N_\mathrm{SC} - N_\mathrm{CP} - 1$. By this substitution, we can observe that this part I can now be calculated by the Fourier transform of the considered time symbols, weighted by the filter response.

- **Part II & III:** The flat middle part with $q = -N_{\mathrm{CP}}, \ldots, N_{\mathrm{SC}} - 1$, where the filter is constant $g\left[q - \ell\left(N_{\mathrm{SC}} + N_{\mathrm{g}} + N_{\mathrm{CP}}\right)\right] = 1$ yields

$$\begin{aligned} x_{\ell}\left[q - \ell\left(N_{\mathrm{SC}} + N_{\mathrm{g}} + N_{\mathrm{CP}}\right)\right] = &\sum_{k=0}^{N_{\mathrm{SC}}-1} d_{k,\ell} e^{\frac{j2\pi kq}{N_{\mathrm{SC}}}} \\ &\Rightarrow \mathbf{x}_{\ell} = \mathbf{T}_{\mathrm{I,CP}} \mathbf{F}^{\mathsf{H}} \mathbf{d}_{\ell} \end{aligned}$$

- **Part IV:** Finally, the ramp down part with discrete time index $q = N_{\mathrm{SC}}, \ldots, N_{\mathrm{SC}} + \frac{N_{\mathrm{g}}}{2} - 1$, where the filter decays $g\left[q - \ell\left(N_{\mathrm{SC}} + N_{\mathrm{g}} + N_{\mathrm{CP}}\right)\right] = 1, ..., 0$ yield

$$\begin{aligned} x_{\ell}\left[q - \ell\left(N_{\mathrm{SC}} + N_{\mathrm{g}}\right)\right] = &g\left[q - \ell\left(N_{\mathrm{SC}} + N_{\mathrm{g}} + N_{\mathrm{CP}}\right)\right] \\ &\cdot \sum_{k=0}^{N_{\mathrm{SC}}-1} d_{k,\ell} e^{\frac{j2\pi kq}{N_{\mathrm{SC}}}} \end{aligned} \tag{A.16}$$

  where we use again a substitution $q' = q - N_{\mathrm{SC}} = 0, \ldots, \frac{N_{\mathrm{g}}}{2} - 1$.

All in all, it can be observed that part **II&III** can be simply realized via the CP-OFDM signal in (3.39). Part **I** and **IV** can be realized by extending GI insertion matrix like

$$\mathbf{T}'_{\mathrm{I,NO}} = \begin{array}{c} \begin{bmatrix} \mathbf{0}_{N_{\mathrm{g}}/2 \times (N_{\mathrm{SC}} - N_{\mathrm{g}}/2 - N_{\mathrm{CP}})} \quad \boldsymbol{\Sigma}_{\mathbf{g}_1} \quad \mathbf{0}_{N_{\mathrm{g}}/2 \times N_{\mathrm{CP}}} \\ \mathbf{0}_{N_{\mathrm{GI}} \times N_{\mathrm{SC}} - N_{\mathrm{g}}/2 - N_{\mathrm{CP}}} \quad \mathbf{I}_{N_{\mathrm{GI}}} \\ \mathbf{I}_{N_{\mathrm{SC}}} \\ \boldsymbol{\Sigma}_{\mathbf{g}_2} \quad \mathbf{0}_{N_{\mathrm{g}}/2 \times (N_{\mathrm{SC}} - N_{\mathrm{g}}/2)} \end{bmatrix} \end{array} \begin{array}{c} \textcircled{\small I} \\ \textcircled{\small II} \\ \textcircled{\small III} \\ \textcircled{\small IV} \end{array} \tag{A.17}$$

This matrix captures the ramp up and down part $\textcircled{\small I}$&$\textcircled{\small IV}$, the CP part $\textcircled{\small II}$ and the core symbol part $\textcircled{\small III}$ within one matrix and the *non-overlapping* w-CP-OFDM yield

$$\mathbf{x}_{\ell} = \mathbf{T}'_{\mathrm{I,NO}} \mathbf{F}^{\mathsf{H}}_{N_{\mathrm{SC}}} \mathbf{d}_{\ell} \tag{A.18}$$

A.5.2 Overlapping w-CP-OFDM

As the ramp up and ramp down edges of the filter are deleted at the receiver they can be transmitted in an overlapping fashion as shown in Fig. A.1b. However, adjacent symbols now overlap. Thus, we get the matrix for the current symbol ℓ

$$\mathbf{T}'_{\mathrm{I,win}} = \left[\begin{array}{c} \mathbf{0}_{N_{\mathrm{g}}/2\times(N_{\mathrm{SC}}-N_{\mathrm{g}}/2-N_{\mathrm{CP}})} \quad \boldsymbol{\Sigma}_{\mathbf{g}_1} \quad \mathbf{0}_{N_{\mathrm{g}}/2\times N_{\mathrm{CP}}} \\ \mathbf{0}_{N_{\mathrm{GI}}\times N_{\mathrm{SC}}-N_{\mathrm{g}}/2-N_{\mathrm{CP}}} \quad \mathbf{I}_{N_{\mathrm{GI}}} \\ \mathbf{I}_{N_{\mathrm{SC}}} \end{array}\right] \begin{array}{c} \textcircled{I} \\ \textcircled{II} \\ \textcircled{III} \end{array} \tag{A.19}$$

and the previous symbol $\ell - 1$

$$\mathbf{T}''_{\mathrm{I,win}} = \left[\begin{array}{c} \boldsymbol{\Sigma}_{\mathbf{g}_2} \quad \mathbf{0}_{N_{\mathrm{g}}/2\times(N_{\mathrm{SC}}-N_{\mathrm{g}}/2)} \\ \mathbf{0}_{(N_{\mathrm{SC}}+N_{\mathrm{GI}}+N_{\mathrm{g}}/2)\times N_{\mathrm{SC}}} \end{array}\right] \begin{array}{c} \textcircled{IV} \\ \end{array} \tag{A.20}$$

The calculation in *overlapping* w-CP-OFDM is known as WOLA [Cro80, DM88, FB11, KK18] and works like

$$\mathbf{x}_\ell = \mathbf{T}'_{\mathrm{I,win}}\mathbf{F}^{\mathsf{H}}\mathbf{d}_\ell + \mathbf{T}''_{\mathrm{I,win}}\mathbf{F}^{\mathsf{H}}\mathbf{d}_{\ell-1} \quad . \tag{A.21}$$

Finally, by skipping part $\textcircled{II}$ in (A.20) or (A.17) corresponds to the respective version w-OFDM without CP.

A.6 Colored Noise

In this section, we are looking at the correlation property of colored noise *w.r.t.* a MC scheme with general waveforms.

General Noise Coloring of Multi-Carrier Schemes For that, we start at the receiver after matched filtering (3.9) and we focus on the additive noise part only. Thus, we have

$$\tilde{n}_r(t) = \int_{-\infty}^{\infty} g_r^{\mathrm{Rx}}(t')\, n(t-t')\, \mathrm{d}t' \tag{A.22}$$

The noise term (A.22) of a non-orthogonal MC transmission schemes is in general colored.

We are now looking at to different sampling points r_1 and r_2 and we want to calculate the correlation between these two sampling points like

$$\psi_{r_1 r_2}(\tau) = \psi_{\tilde{n}_{r_1}\tilde{n}_{r_2}}(\tau) = \lim_{T_0\to\infty} \int_{T_0}^{T_0} y_1(t)\, y_2(t-\tau)\, \mathrm{d}t \quad . \tag{A.23}$$

$$\begin{aligned}
\psi_{r_1 r_2}\left(\tau\right) &= \lim_{T_0 \to \infty} \int\limits_{T_0}^{T_0} \int\limits_{-\infty}^{\infty} g_1^{\mathrm{Rx}}\left(t'\right) n\left(t-t'\right) \mathrm{d}t' \int\limits_{-\infty}^{\infty} g_2^{\mathrm{Rx}}\left(\tau'\right) n\left(t-\tau-\tau'\right) \mathrm{d}\tau' \mathrm{d}t \\
&= \int\limits_{-\infty}^{\infty} g_1^{\mathrm{Rx}}\left(t'\right) \int\limits_{-\infty}^{\infty} g_2^{\mathrm{Rx}}\left(\tau'\right) \underbrace{\lim_{T_0 \to \infty} \int\limits_{T_0}^{T_0} n\left(t-t'\right) n\left(t-\tau-\tau'\right) \mathrm{d}t \, \mathrm{d}\tau' \mathrm{d}t'}_{\psi_{n\,n}\left(\tau'+\tau-t'\right)} \\
&= \int\limits_{-\infty}^{\infty} g_1^{\mathrm{Rx}}\left(t'\right) \left(g_2^{\mathrm{Rx}} * \psi_{n_1 n_2}\right)\left(t'-\tau\right) \mathrm{d}t' \\
&= \left(g_1^{\mathrm{Rx}} * g_2^{\mathrm{Rx}} * \psi_{nn}\right)\left(\tau\right) && \text{(A.24)} \\
&= \psi^{\mathrm{E}}_{g_1^{\mathrm{Rx}} g_2^{\mathrm{Rx}}}\left(\tau\right) * \psi_{nn}\left(\tau\right) \quad . && \text{(A.25)}
\end{aligned}$$

The energy cross correlation function defined in [KD18].

The question is how the cross correlation function looks like for a given receive filter? The receive filter for MC schemes are defined in (3.8) like

$$\begin{aligned}
g_1^{\mathrm{Rx}}\left(t\right) &= g^{\mathrm{Rx}}\left(t-\ell_1 T_0\right) e^{j2\pi k_1 F_0 t} e^{j\phi_{k_1,\ell_1}} \\
g_2^{\mathrm{Rx}}\left(t\right) &= g^{\mathrm{Rx}}\left(t-\ell_2 T_0\right) e^{j2\pi k_2 F_0 t} e^{j\phi_{k_2,\ell_2}}
\end{aligned}$$

Substituting the filters, the energy cross correlation yields

$$\begin{aligned}
\psi^{\mathrm{E}}_{g_1^{\mathrm{Rx}} g_2^{\mathrm{Rx}}}\left(\tau\right) &= \int\limits_{-\infty}^{\infty} g_1^{\mathrm{Rx}}\left(t\right) g_2^{\mathrm{Rx}}\left(t+\tau\right) \mathrm{d}t \\
&= e^{j2\pi k_2 F_0 \tau} e^{j\left(\phi_{k_1,\ell_1}+\phi_{k_2,\ell_2}\right)} \\
&\quad \cdot \int\limits_{-\infty}^{\infty} g_1^{\mathrm{Rx}}\left(t-\ell_1 T_0\right) g_2^{\mathrm{Rx}}\left(t+\tau-\ell_2 T_0\right) e^{j2\pi\left(k_2-k_1\right) F_0 t} \mathrm{d}t \quad .
\end{aligned} \tag{A.26}$$

Applying substitution $t = t' - \frac{\tau}{2} + \frac{\ell_1 T_0}{2} + \frac{\ell_2 T_0}{2}$ yields

$$\begin{aligned}\psi^{\mathrm{E}}_{g_1^{\mathrm{Rx}} g_2^{\mathrm{Rx}}}(\tau) = {} & \underbrace{e^{j2\pi k_2 F_0 \tau} e^{j2\pi (k_2-k_1) F_0 \left(-\frac{\tau}{2} + \frac{(k_1+k_2)F_0}{2}\right)} e^{j\left(\phi_{k_1,\ell_1} + \phi_{k_2,\ell_2}\right)}}_{e^{\overline{\phi}}} \\ & \cdot \underbrace{\int\limits_{-\infty}^{\infty} g_1^{\mathrm{Rx}}\Big(t - \frac{\tau + (\ell_1 - \ell_2)\, T_0}{2}\Big) g_2^{\mathrm{Rx}}\Big(t + \frac{\tau + (\ell_1 - \ell_2)\, T_0}{2}\Big) e^{-j2\pi (k_1-k_2) F_0 t} \mathrm{d}t}_{A((\ell_1-\ell_2)T_0+\tau, k_1-k_2F_0)}\end{aligned} \tag{A.27}$$

Finally, the resulting correlation between two signals are

$$\begin{aligned}\psi_{r_1 r_2}(\tau) &= \psi^{\mathrm{E}}_{g_1^{\mathrm{Rx}} g_2^{\mathrm{Rx}}}(\tau) * \psi_{nn}(\tau) \\ &= \left(e^{\overline{\phi}} A\left((\ell_1 - \ell_2)\, T_0 + \tau, (k_1 - k_2)\, F_0\right)\right) * \psi_{nn}(\tau) \quad .\end{aligned} \tag{A.28}$$

The correlation is dependent on the correlation of the noise and the cross energy correlation of the receive filter function describable by the ambiguity function. We assume a AWGN n such that $\psi_{nn}(\tau) = \sigma_{\mathrm{n}}^2 \delta(\tau)$. The resulting correlation depends on the ambiguity function of the receive filter used, only. Related to the matrix description the continuous correlation $\psi_{\tilde{n}_1 \tilde{n}_2}(\tau)$ and sampled at $\tau = 0$, a correlation matrix can be given like

$$\Psi_{\tilde{\mathbf{n}}\tilde{\mathbf{n}}} = \begin{bmatrix} \psi_{r_0 r_0} & \psi_{r_0 r_1} & \cdots \\ \psi_{r_1 r_0} & \psi_{r_1 r_1} & \cdots \\ \vdots & \vdots & \ddots \end{bmatrix} \tag{A.29}$$

Subsequently, we are looking for the correlation function for the different introduced MC schemes.

Noise Coloring of Multi-Carrier Schemes In this part, we want to investigate some features of the colored noise term $\tilde{\mathbf{n}}$ in the P2P system model (3.27). For that we consider the autocorrelation function $\Psi_{\tilde{\mathbf{n}}\tilde{\mathbf{n}}} = \mathrm{E}\{\tilde{\mathbf{n}}\tilde{\mathbf{n}}^{\mathsf{H}}\}$ derived in (A.28).

For the orthogonal schemes the characteristic of the noise are not influenced by the receiving filter:

1. OFDM: $\Psi_{\tilde{\mathbf{n}}\tilde{\mathbf{n}}} = \mathrm{E}\{\mathbf{F}\mathbf{n}\mathbf{n}^{\mathsf{H}}\mathbf{F}^{\mathsf{H}}\} = \sigma_{\mathrm{n}}^2 \mathbf{I}$
2. CP-OFDM: $\Psi_{\tilde{\mathbf{n}}\tilde{\mathbf{n}}} = \mathrm{E}\{\mathbf{T}_{\mathrm{R}}\mathbf{F}\mathbf{n}\mathbf{n}^{\mathsf{H}}\mathbf{F}^{\mathsf{H}}\mathbf{T}_{\mathrm{R}}^{\mathsf{H}}\} = \sigma_{\mathrm{n}}^2 \mathbf{I}$
3. ZP-OFDM: $\Psi_{\tilde{\mathbf{n}}\tilde{\mathbf{n}}} = \mathrm{E}\{\mathbf{F}_{1:2:2N_{\mathrm{SC}},:}\mathbf{n}\mathbf{n}^{\mathsf{H}}\mathbf{F}^{\mathsf{H}}_{1:2:2N_{\mathrm{SC}},:}\} = \sigma_{\mathrm{n}}^2 \mathbf{I}$

4. w-CP-OFDM: $\Psi_{\tilde{\mathbf{n}}\,\tilde{\mathbf{n}}} = \mathrm{E}\{\mathbf{T}'_{\mathrm{R}}\mathbf{F}\mathbf{n}\mathbf{n}^{\mathsf{H}}\mathbf{F}^{\mathsf{H}}\mathbf{T}'^{\mathsf{H}}_{\mathrm{R}}\} = \sigma_{\mathrm{n}}^2\mathbf{I}$

However, in case of a non-orthogonal MC scheme the noise gets colored, which will be important for the detection schemes later on.

1. CP-FBMC: $\Psi_{\tilde{\mathbf{n}}\,\tilde{\mathbf{n}}} = \mathrm{E}\{\mathbf{T}_{\mathrm{R}}\mathbf{F}\mathbf{\Sigma}_{\mathbf{g}}\mathbf{n}\mathbf{n}^{\mathsf{H}}\mathbf{\Sigma}_{\mathbf{g}}^{\mathsf{H}}\mathbf{F}^{\mathsf{H}}\mathbf{T}'^{\mathsf{H}}_{\mathrm{R}}\} = \sigma_{\mathrm{n}}^2\mathbf{F}\mathbf{\Sigma}_{\mathbf{g}}\mathbf{\Sigma}_{\mathbf{g}}^{\mathsf{H}}\mathbf{F}^{\mathsf{H}}$

2. GFDM: $\Psi_{\tilde{\mathbf{n}}\,\tilde{\mathbf{n}}} = \mathrm{E}\{\underline{\mathbf{T}}_{\mathrm{R}}\underline{\mathbf{G}}_{\mathrm{GFDM}}\mathbf{n}\mathbf{n}^{\mathsf{H}}\underline{\mathbf{G}}_{\mathrm{GFDM}}^{\mathsf{H}}\underline{\mathbf{T}}'^{\mathsf{H}}_{\mathrm{R}}\} = \sigma_{\mathrm{n}}^2\underline{\mathbf{G}}_{\mathrm{GFDM}}\underline{\mathbf{G}}_{\mathrm{GFDM}}^{\mathsf{H}}$

In Chapter 4 we will deal with APP-based detection schemes, expecting uncorrelated noise terms. One very popular receiver structure is known as Forney receiver [For72b], which applies a prewhitening filter to reduce the correlation of the noise term by a linear filter, like $\mathbf{P}$. Such that the system model changes to

$$\underline{\tilde{\mathbf{y}}} = \mathbf{P}\underline{\mathbf{y}} = \mathbf{P}\underline{\mathbf{H}}\underline{\mathbf{d}} + \mathbf{P}\underline{\mathbf{G}}_{\mathrm{GFDM}}\underline{\mathbf{n}} \tag{A.30}$$

The goal by the application of a prewhitening filter is to achieve an uncorrelated noise term. Having a deeper look to the autocorrelation function above yields $\Psi_{\tilde{\mathbf{n}}\,\tilde{\mathbf{n}}} = \sigma_{\mathrm{n}}^2\mathbf{P}\underline{\mathbf{G}}_{\mathrm{GFDM}}\underline{\mathbf{G}}_{\mathrm{GFDM}}^{\mathsf{H}}\mathbf{P}^{\mathsf{H}} = \mathbf{I}$.

In Appendix B the solution of the prewhitening are discussed related the receiver algorithm design.

A.7 Effective Channel Matrix

The amplitudes of the effective channel matrices with (3.33) for the orthogonal transmission schemes are illustrated with different channel conditions in Fig. A.2 for plain-OFDM, in Fig. A.3 for CP-OFDM, in Fig. A.4 for ZP-OFDM, in Fig. A.5 for w-CP-OFDM, respectively.

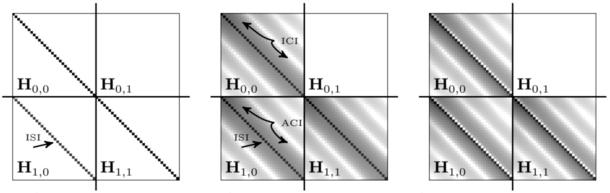

a) $\Delta\nu = 0, \Delta\tau = 0$ b) $\Delta\nu = 0, \Delta\tau = 0.1T_{\mathrm{S}}$ c) $\Delta\nu = 0.1F_0, \Delta\tau = 0.1T_{\mathrm{S}}$

Figure A.2: Illustration of the amplitudes of the effective channel matrix of for plain-OFDM.

The amplitudes, the real and imaginary part of the effective channel matrices for the OQAM-based schemes are illustrated in Fig. A.6 for plain-OQAM/OFDM, in Fig. A.7 for OQAM/FBMC with half-cosine filter, in Fig. A.8 for OQAM/FBMC with Gaussian waveform, respectively.

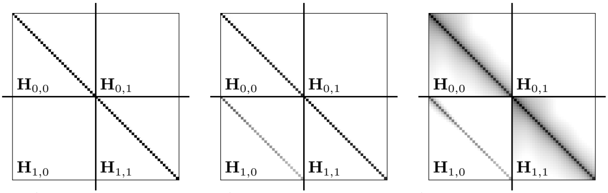

a) $\Delta\nu = 0, \Delta\tau = 0$ b) $\Delta\nu = 0, \Delta\tau = 0.1T_\mathrm{S}$ c) $\Delta\nu = 0.1F_0, \Delta\tau = 0.1T_\mathrm{S}$

Figure A.3: Illustration of the amplitudes of the effective channel matrix for CP-OFDM.

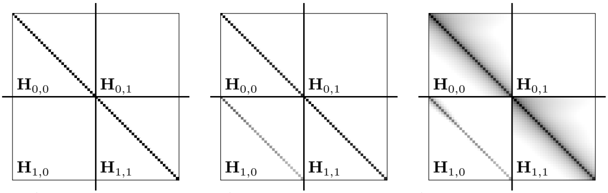

a) $\Delta\nu = 0, \Delta\tau = 0$ b) $\Delta\nu = 0, \Delta\tau = 0.1T_\mathrm{S}$ c) $\Delta\nu = 0.1F_0, \Delta\tau = 0.1T_\mathrm{S}$

Figure A.4: Illustration of the amplitudes of the effective channel matrix for ZP-OFDM.

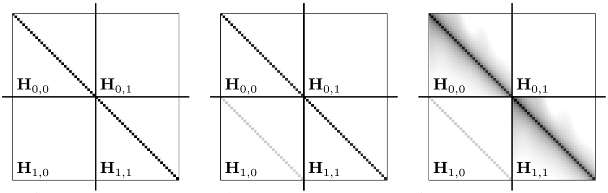

a) $\Delta\nu = 0, \Delta\tau = 0$ b) $\Delta\nu = 0, \Delta\tau = 0.1T_\mathrm{S}$ c) $\Delta\nu = 0.1F_0, \Delta\tau = 0.1T_\mathrm{S}$

Figure A.5: Illustration of the amplitudes of the effective channel matrix for w-CP-OFDM.

The amplitudes of the effective channel matrices for the non-orthogonal QAM-based schemes are illustrated in Fig. A.9 for QAM/FBMC with half-cosine filter, in Fig. A.10 for QAM/FBMC with Gaussian waveform, respectively.

The amplitudes of the effective channel matrices for the non-orthogonal GFDM related schemes are illustrated in Fig. A.11 for GFDM with Gaussian filter, in Fig. A.12 for CP-FBMC with Gaussian waveform, respectively.

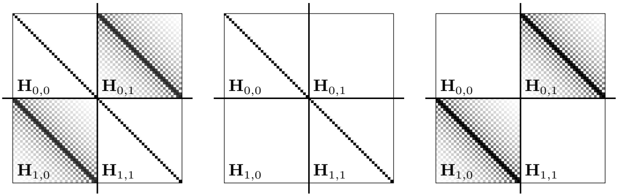

a) $|\mathbf{H}|$ b) $\Re\{\mathbf{H}\}$ c) $\Im\{\mathbf{H}\}$

Figure A.6: Illustration of the amplitudes of the effective channel matrix for OQAM/FBMC with rectangular filter.

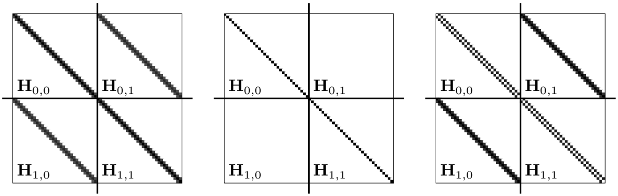

a) $|\mathbf{H}|$ b) $\Re\{\mathbf{H}\}$ c) $\Im\{\mathbf{H}\}$

Figure A.7: Illustration of the amplitudes of the effective channel matrix for OQAM/FBMC with half-cosine filter.

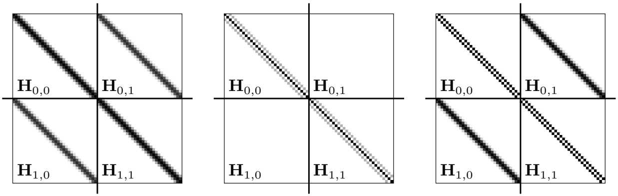

a) $|\mathbf{H}|$ b) $\Re\{\mathbf{H}\}$ c) $\Im\{\mathbf{H}\}$

Figure A.8: Illustration of the amplitudes of the effective channel matrix for OQAM/FBMC with Gaussian filter and localization parameter $\rho = 1$.

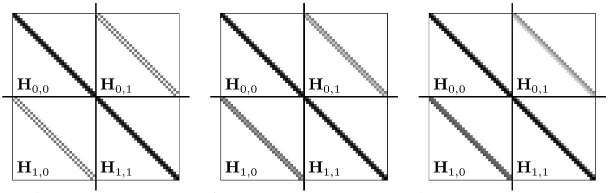

a) $\Delta\nu = 0, \Delta\tau = 0$ b) $\Delta\nu = 0.1F_0, \Delta\tau = 0.1T_\mathrm{S}$ c) $\Delta\nu = 0.2F_0, \Delta\tau = 0.2T_\mathrm{S}$

Figure A.9: Illustration of the amplitudes of the effective channel matrix for QAM/FBMC with half-cosine filter.

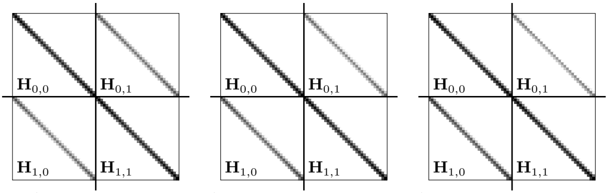

a) $\Delta\nu = 0, \Delta\tau = 0$ b) $\Delta\nu = 0.1F_0, \Delta\tau = 0.1T_\mathrm{S}$ c) $\Delta\nu = 0.2F_0, \Delta\tau = 0.2T_\mathrm{S}$

Figure A.10: Illustration of the amplitudes of the effective channel matrix for QAM/FBMC with Gaussian filter.

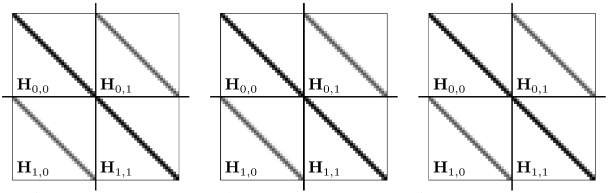

a) $\Delta\nu = 0, \Delta\tau = 0$ b) $\Delta\nu = 0, \Delta\tau = 0.1T_\mathrm{S}$ c) $\Delta\nu = 0.1F_0, \Delta\tau = 0.1T_\mathrm{S}$

Figure A.11: Illustration of the amplitudes of the effective channel matrix for GFDM with Gaussian filter and localization parameter $\rho = 1$.

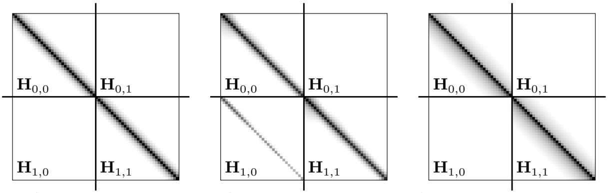

a) $\Delta\nu = 0, \Delta\tau = 0$ b) $\Delta\nu = 0, \Delta\tau = 0.1T_\mathrm{S}$ c) $\Delta\nu = 0.1F_0, \Delta\tau = 0.1T_\mathrm{S}$

Figure A.12: Illustration of the amplitudes of the effective channel matrix for CP-FBMC with Gaussian filter and localization parameter $\rho = 1$.

Appendix B

Estimators

B.1 Brief Recapitulation of General Estimators

The transmission via a channel distorts the transmission. The main purpose at the Rx is to recover the data of a sending user on the basis of the received signal with high accuracy. In this chapter we give a brief overview on Bayesian estimation theory on which the famous minimum mean square error (MMSE) and maximum a-posteriori (MAP) estimators are based and we further investigate graphical methods to represent the transmission over a disturbed channel into so-called factor graph (FG), which provides an intuitive representation of the underlying problem. Based on the graphical representation we solve the data estimation by the famous sum-product algorithm.

By means of abstraction, the problem definition can be refereed to the estimation problem depicted in Fig. B.1. where a vector of realizations $\mathbf{b}$ of a random process B with length $N_{\mathbf{b}}$ out of a set $\mathcal{B}^{N_{\mathbf{b}}}$ is transmitted over a channel with transition probability $\mathrm{p}_{B|Y}(\mathbf{b} \mid \mathbf{y})$ yielding an observation $\mathbf{y}$.

The vector of realizations $\mathbf{y}$ of the observation variable Y with length $N_{\mathbf{y}}$ is again a random variable with a set $\mathcal{Y}^{N_{\mathbf{y}}}$. The task is to build an estimator $\hat{\mathbf{b}} = \mathcal{E}\left(\mathbf{y}\right)$ giving an estimation $\hat{\mathbf{b}}$ based on the received signal $\mathbf{y}$ and the transition probability $\mathrm{p}_{B|Y}(B = \mathbf{b} \mid Y = \mathbf{y})$. Within this work we don't focus on the derivation of the basic ideas of the estimators and refer to [Wym07, KD18] for the interested reader. We further use the shorthand notation $\mathrm{p}(\mathbf{b} \mid \mathbf{y}) = \mathrm{p}_{B|Y}(B = \mathbf{b} \mid Y = \mathbf{y})$ to simplify the description of the PDF.

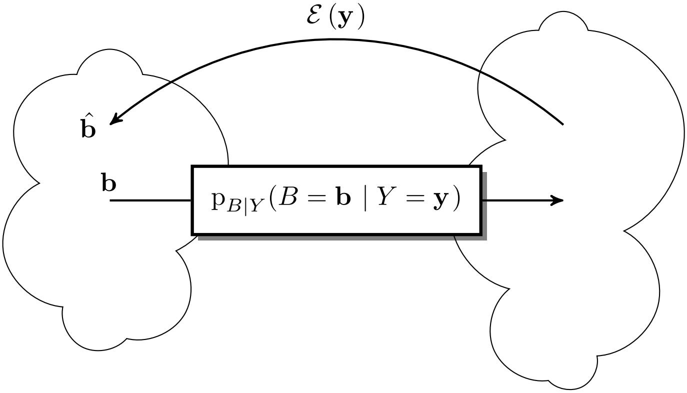

Figure B.1: General Estimation Problem.

B.1.1 Minimum Mean Square Error Estimation

A well-known estimator is based on minimizing the cost function $\|\mathbf{b}-\hat{\mathbf{b}}\|^2$, which is based on the euclidean distance between the true value $\mathbf{b}$ and the estimation $\hat{\mathbf{b}}=\mathcal{E}(\mathbf{y})$. This estimator results in

$$\mathcal{E}(\mathbf{y})=\int\limits_{\mathcal{B}^{N_\mathbf{b}}}\mathbf{b}\,\mathrm{p}(\mathbf{b}\mid\mathbf{y})\,\mathrm{d}\mathbf{b} \tag{B.1}$$

averaging over all transition probabilities, which can also be given by the expected value operator $\mathrm{E}\{\cdot\}$ in

$$\mathcal{E}(\mathbf{y})=\mathrm{E}\{\mathrm{p}(\mathbf{b}\mid\mathbf{y})\} \tag{B.2}$$

The estimate $\hat{\mathbf{b}}$ is called MMSE-based estimation. Simply spoken: the estimator based on the MMSE criterion is given by the mean of the a-posteriori probability (APP) distribution $\mathrm{p}(\mathbf{b}\mid\mathbf{y})$.

Linear MMSE When we consider a linear relationship between the transmit signal $\mathbf{b}$ and the received signal $\mathbf{y}$ like

$$\mathbf{y}=\mathbf{H}\mathbf{b}+\mathbf{n} \tag{B.3}$$

with a known matrix $\mathbf{H}$, an uncorrelated transmit signal $\mathbf{b}$ with zero mean and variance σ_b^2, and a noise vector $\mathbf{n}$ with $\mathcal{N}\left(0,\sigma_\mathrm{n}^2\right)$ uncorrelated to $\mathbf{b}$, the linear estimator $\hat{\mathbf{b}} = \mathcal{E}(\mathbf{y}) = \mathbf{G}_{\mathrm{LMMSE}}\mathbf{y}$ can be derived [Wym07, KD18] like

$$\mathbf{G}_{\mathrm{LMMSE}} = \mathbf{H}^{\mathsf{H}} \left(\mathbf{H}^{\mathsf{H}}\mathbf{H} + \frac{\sigma_{\mathrm{n}}^2}{\sigma_{\mathrm{b}}^2}\mathbf{I} \right)^{-1} \quad . \tag{B.4}$$

Maximum A-Posteriori Estimation Contrarily to the estimator using the mean, another famous sequence estimator takes that sequence $\hat{\mathbf{b}}$, which maximizes the APP distribution $\mathrm{p}(\mathbf{y} \mid \mathbf{b})$ like

$$\hat{\mathbf{b}} = \mathcal{E}(\mathbf{y}) = \underset{\mathbf{b} \in \mathcal{B}^{N_{\mathbf{b}}}}{\arg\max}\ \mathrm{p}(\mathbf{b} \mid \mathbf{y}) \equiv \underset{\mathbf{b} \in \mathcal{B}^{N_{\mathbf{b}}}}{\arg\max}\ \mathrm{p}(\mathbf{y} \mid \mathbf{b}) \Pr(\mathbf{b}) \tag{B.5}$$

Furthermore, a symbol-by-symbol MAP estimator can be defined like

$$\hat{b}_{\varpi} = \mathcal{E}(\mathbf{y}) = \underset{b_{\varpi} \in \mathcal{B}}{\arg\max}\ \mathrm{p}(b_{\varpi} \mid \mathbf{y}) \equiv \underset{b_{\varpi} \in \mathcal{B}}{\arg\max}\ \mathrm{p}(\mathbf{y} \mid b_{\varpi}) \Pr(b_{\varpi}) \tag{B.6}$$

which takes that symbol $\hat{b}_{\varpi}$, which maximizes the APP distribution.

Note, that Bayes theorem is applied to achieve the right-hand-side parts of (B.5), containing the *likelihood* $\mathrm{p}(\mathbf{y} \mid \mathbf{b})$ and the *a priori* $\Pr(\mathbf{b})$. A similar factorization can be done in (B.6).

B.2 Graph based Estimation in a Communication System

In digital communication systems, we are usually looking for binary sequences $\mathbf{b}$. Subsequently, we limit the considerations on binary sequences of length $N_{\mathbf{b}}$ like $\mathbf{b} \in \mathcal{B}^{N_{\mathbf{b}}}$. Based on the MAP sequence criterion in (B.5) we have seen that the task at the destination is to calculate the APP $\mathrm{p}(\mathbf{b} \mid \mathbf{y})$ for all combinations of the bit vector $\mathbf{b} \in \mathcal{B}^{N_{\mathbf{b}}}$.

This calculation requires a huge effort in terms of complexity and it is sometimes not feasible to solve this approach. The Viterbi algorithm introduced in [Vit67] by Andrew J. Viterbi in 1967 solves the MAP problem by interpreting the overall transmission as a trellis, which is a special kind of graphs. But, the algorithm scales exponentially with the number of memory elements of the system. Especially for the non-orthogonal MC schemes introduced in Chapter 3, where the crosstalk (which can be also interpreted as memory elements) occur in time and in frequency direction leading to a high number of memory elements as also discussed in [MKFK98, Mat98].

Another approach is to solve the approach in (B.6) with optimal bit-by-bit decisions by the BCJR algorithm firstly introduced by L. R. Bahl, J. Cocke, F. Jelinek, and J. Raviv in 1974 [BCJR74].

The BCJR algorithm is also based on a graphical memory model (also called state-space model [Wym07]), hence the complexity scales exponentially with the number of memory elements in the system.

The BCJR algorithm can be interpreted as FG augmented with variable describing the state of each node, leading to an acyclic FG. Within this work we focus on a FG, where these nodes are opened. On the one hand no additional variable determining the state is necessary reducing the complexity of the calculation, on the other hand the FG gets loopy and the calculation of the MAP solution gets non-optimal. However, as indicated in [OWM+12] and [LYWM05], the opened FG can approach the FER performance of the optimal BCJR.

In the sequel, the general FG is introduced briefly exemplify by the MAP problem. Furthermore, by factorization of the likelihood function the underlying structure get utilized. Finally, the calculation on the FG by the famous SPA is introduced [Gal62, Pea82] solving the MAP problem above.

However, these message passing algorithms are only exact on FG with a tree structure. We will see that in communication systems the underlying structure is not always a tree, but more often a structure with cycles. For that, an iterative SPA will be used One famous representation is the *conventional* FG representation [KFL01] another one is the *normal* FG by Forney in [For01]. We concentrate on the former one. In general a FG is a bipartite graph containing of factor nodes (function nodes), in our case $\mathrm{p}(\mathbf{y} \mid \mathbf{b})$ denoted by squares □ and variable nodes like $\mathbf{b}$ denoted by circles ○. Connections are allowed between variable and function nodes only and are called "edges". Fig. B.2 shows the FG of the right-hand-side of (B.5).

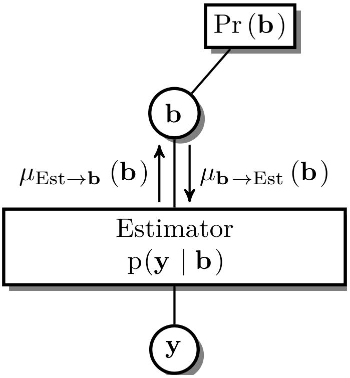

Figure B.2: FG given by equation (B.5).

The function node $\mathrm{p}(\mathbf{y} \mid \mathbf{b})$ is connected via an edge to the variable $\mathbf{b}$. We define two messages like

$$\hat{\mathbf{b}} = \mathcal{E}\left(\mathbf{y}\right) = \underset{\mathbf{b}\in\mathcal{B}^{N_\mathbf{b}}}{\arg\max}\ \underbrace{\mathrm{p}(\mathbf{y} \mid \mathbf{b})}_{\mu_{\mathrm{Est}\rightarrow\mathbf{b}}\left(\mathbf{b}\right)}\ \underbrace{\Pr\left(\mathbf{b}\right)}_{\mu_{\mathbf{b}\rightarrow\mathrm{Est}}\left(\mathbf{b}\right)}\ , \tag{B.7}$$

where the message $\mu_{\mathrm{Est}\rightarrow\mathbf{b}}\left(\mathbf{b}\right)$ is a message on an edge from the function "Estimator" to a variable node $\mathbf{b}$. The argument $\mathbf{b}$ is the concrete realization of the random variable $B = \mathbf{b}$ [1]. During this work we omit the function node of the a priori information $\Pr\left(\mathbf{b}\right)$ and the variable node of the observation variable $\mathbf{y}$ because it facilitates the representation of the FG. We can observe that the calculation in (B.7) can be done by the product of the incoming message to a variable $\mu_{\mathrm{Est}\rightarrow\mathbf{b}}\left(\mathbf{b}\right)$ with the outgoing message $\mu_{\mathbf{b}\rightarrow\mathrm{Est}}\left(\mathbf{b}\right)$. Thus, $\mu_{\mathbf{b}\rightarrow\mathrm{Est}}\left(\mathbf{b}\right)$ can be interpreted as the a priori message for the realization $\mathbf{b}$. Both messages are functions of the realization $\mathbf{b}$ and by solving the MAP sequence estimation all possible $|\mathcal{B}|^{N_\mathbf{b}} = 2^{N_\mathbf{b}}$ sequences have to be considered. This calculation is not feasible without utilizing the underlying structure, similar to the Viterbi or the BCJR algorithm. To simplify the calculation, the bit-by-bit estimator in (B.6) is used and similar to (B.7) the estimator is rewritten and can be interpreted by the multiplication of the

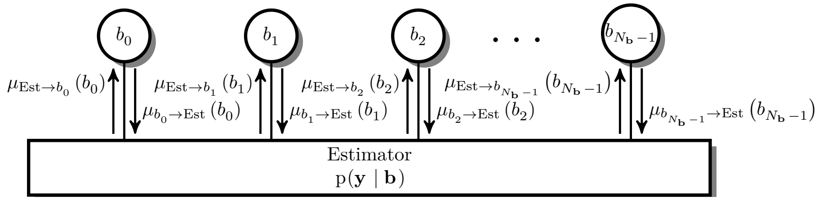

Figure B.3: FG given by equation (B.8).

---

[1] Instead of $\mu_{\mathrm{Est}\rightarrow B}\left(\mathbf{b}\right)$, we mostly use the term $\mu_{\mathrm{Est}\rightarrow\mathbf{b}}\left(\mathbf{b}\right)$ and do not differ between random variable and realization to keep the notation simple.

incoming message with the outgoing message like

$$\begin{aligned}
\hat{b}_{\varpi} = \mathcal{E}\left(\mathbf{y}\right) &= \operatorname*{arg\,max}_{b_{\varpi}\in\mathcal{B}} \mathrm{p}(b_{\varpi} \mid \mathbf{y}) && \text{(B.8a)}\\
&= \operatorname*{arg\,max}_{b_{\varpi}\in\mathcal{B}} \sum_{\sim\{b_{\varpi}\}} \mathrm{p}(\mathbf{b} \mid \mathbf{y}) && \text{(B.8b)}\\
&= \operatorname*{arg\,max}_{b_{\varpi}\in\mathcal{B}} \sum_{\sim\{b_{\varpi}\}} \mathrm{p}(\mathbf{y} \mid \mathbf{b}) \Pr\left(\mathbf{b}\right) && \text{(B.8c)}\\
&= \operatorname*{arg\,max}_{b_{\varpi}\in\mathcal{B}} \sum_{\sim\{b_{\varpi}\}} \mathrm{p}(\mathbf{y} \mid \mathbf{b}) \prod_{\iota} \Pr\left(b_{\iota}\right) && \text{(B.8d)}\\
&= \operatorname*{arg\,max}_{b_{\varpi}\in\mathcal{B}} \underbrace{\Pr\left(b_{\varpi}\right)}_{\mu_{b_{\varpi}\to\mathrm{Est}}(b_{\varpi})} \underbrace{\sum_{\sim\{b_{\varpi}\}} \mathrm{p}(\mathbf{y} \mid \mathbf{b}) \prod_{\iota\setminus\varpi} \underbrace{\Pr\left(b_{\iota}\right)}_{\mu_{b_{\iota}\to\mathrm{Est}}(b_{\iota})}}_{\mu_{\mathrm{Est}\to b_{\varpi}}(b_{\varpi})} && \text{(B.8e)}
\end{aligned}$$

The marginalization over all available bits in $\mathbf{b}$ without b_{ϖ} and by the application of Bayes' theorem[2] we get (B.8c)[3]. In (B.8d) we use the assumption of independent bits with known a priori probability $\Pr\left(\mathbf{b}\right) = \prod_{\varpi=0}^{N_{\mathbf{b}}-1} \Pr(b_{\varpi})$. This assumption can be interpreted as factorization of the variable nodes leading to the FG in Fig. B.3. We also define messages on this FG given by a rearrangement of the equation in (B.8e). In contrast to (B.7) the incoming message $\mu_{\mathrm{Est}\to b_{\varpi}}(b_{\varpi})$ and outgoing message $\mu_{b_{\varpi}\to\mathrm{Est}}(b_{\varpi})$ from a binary variable b_{ϖ} have a cardinality of just $|\mathcal{B}| = 2$, leading to a lower computational complexity of the calculation of the individual messages.

B.2.1 Factorization the Underlying Structure

To going deeper into the structure of a transmission from a source to a destination a general communication transmission scheme is considered and given by Fig. B.4. In particular, the overall transmission can be separated into encoding with encoder $\mathcal{C}$ with the probabilistic mapping $\mathrm{p}(\mathbf{c} \mid \mathbf{b})$, symbol mapping with modulator $\mathcal{M}$ and the probabilistic mapping $\mathrm{p}(\mathbf{d} \mid \mathbf{c})$ and transmission over a channel with transition mapping $\mathrm{p}(\mathbf{y} \mid \mathbf{d})$ [Wym07]. By extending the general estimator in (B.6) with the underlying structure, we can rewrite the estimation like

$$\mathcal{E}\left(\mathbf{y}\right) = \operatorname*{arg\,max}_{b_{\varpi}\in\mathcal{B}} \mathrm{p}(B = b_{\varpi} | Y = \mathbf{y}, D = \mathbf{y}, C = \mathbf{c}) \qquad \text{(B.9)}$$

---

[2] The Bayes' theorem states $\mathrm{p}(A \mid B) = \mathrm{p}(A)\,\mathrm{p}(B \mid A)\,/\,\mathrm{p}(B)$

[3] $\sum_{\sim\{b_{\varpi}\}}$ is a short hand notation for the sum over all realization in b_{ϖ}^{ι} with a fixed b_{ϖ}

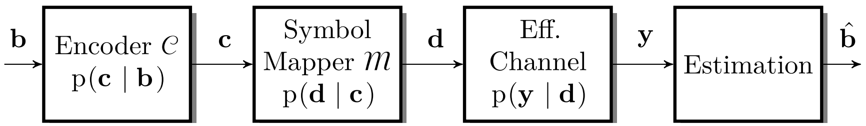

Figure B.4: Point-to-Point transmission applying encoding, symbol mapping and modulation by multi-carrier transmission over a physical channel.

where D is the random variable related to the modulated tranmsit symbols $\mathbf{d}$ and the random variable C corresponds to the code bits $\mathbf{c}$. Applying Bayes' rule several times on the first order Markov chain $Y \to D \to C \to B$ and omit the illustration of random variables yields

$$\hat{b}_\varpi = \mathcal{E}(\mathbf{y}) = \underset{b_\varpi \in \mathcal{B}}{\arg\max}\ \mathrm{p}(b_\varpi \mid \mathbf{y}, \mathbf{d}, \mathbf{c}) \tag{B.10a}$$

$$\equiv \underset{b_\varpi \in \mathcal{B}}{\arg\max} \sum_{\sim\{b_\varpi\}} \mathrm{p}(\mathbf{b} \mid \mathbf{y}, \mathbf{d}, \mathbf{c}) \tag{B.10b}$$

$$\equiv \underset{b_\varpi \in \mathcal{B}}{\arg\max} \sum_{\sim\{b_\varpi\}} \mathrm{p}(\mathbf{y}, \mathbf{d}, \mathbf{c} \mid \mathbf{b}) \Pr(\mathbf{b}) \tag{B.10c}$$

$$\equiv \underset{b_\varpi \in \mathcal{B}}{\arg\max} \sum_{\sim\{b_\varpi\}} \mathrm{p}(\mathbf{y} \mid \mathbf{d}, \mathbf{c}, \mathbf{b})\, \mathrm{p}(\mathbf{d}, \mathbf{c} \mid \mathbf{b}) \Pr(\mathbf{b}) \tag{B.10d}$$

$$\equiv \underset{b_\varpi \in \mathcal{B}}{\arg\max} \sum_{\sim\{b_\varpi\}} \mathrm{p}(\mathbf{y} \mid \mathbf{d})\, \mathrm{p}(\mathbf{d} \mid \mathbf{c}, \mathbf{b})\, \mathrm{p}(\mathbf{c} \mid \mathbf{b}) \Pr(\mathbf{b}) \tag{B.10e}$$

$$\equiv \underset{b_\varpi \in \mathcal{B}}{\arg\max} \sum_{\sim\{b_\varpi\}} \mathrm{p}(\mathbf{y} \mid \mathbf{d})\, \mathrm{p}(\mathbf{d} \mid \mathbf{c})\, \mathrm{p}(\mathbf{c} \mid \mathbf{b}) \prod_{\iota} \Pr(b^{\iota}_{\varpi}) \tag{B.10f}$$

$$\equiv \underset{b_\varpi \in \mathcal{B}}{\arg\max}\ \underbrace{\underbrace{\Pr(b_\varpi)}_{\text{a priori}}}_{\mu_{b_\varpi \to \text{Est.}}(b_\varpi)} \underbrace{\sum_{\sim\{b_\varpi\}} \underbrace{\mathrm{p}(\mathbf{y} \mid \mathbf{d})}_{\text{eff. Channel}} \underbrace{\mathrm{p}(\mathbf{d} \mid \mathbf{c})}_{\text{Mapping}} \underbrace{\mathrm{p}(\mathbf{c} \mid b_\varpi)}_{\text{Encoding}} \underbrace{\prod_{\iota \setminus \varpi} \Pr(b_\iota)}_{\mu_{b_\iota \to \text{Est.}}(b_\iota)}}_{\mu_{\text{Est} \to b_\varpi}(b_\varpi)} \tag{B.10g}$$

In (B.10b) the marginalization over all $\mathbf{b}$ is used. The Bayes rule is used to achieve (B.10c). Keeping in mind that this is a first order Markov chain yields $\mathrm{p}(\mathbf{y} \mid \mathbf{d}, \mathbf{c}, \mathbf{b}) = \mathrm{p}(\mathbf{y} \mid \mathbf{d})$ leading to (B.10d) and $\mathrm{p}(\mathbf{d} \mid \mathbf{c}, \mathbf{b}) = \mathrm{p}(\mathbf{d} \mid \mathbf{c})$ to (B.10e). In (B.10f) we use again (*cf.* (B.8d)) the assumption of independent bits with known a priori probability $\Pr(\mathbf{b}) = \prod_{\varpi=0}^{N_\mathbf{b}-1} \Pr(b_\varpi)$. Finally, by reordering the equation we yield the final description (B.10g). This factorization is illustrated in Fig. B.5, where each block on the right-hand side corresponds to one probabilistic mapping in (B.10g). Throughout this

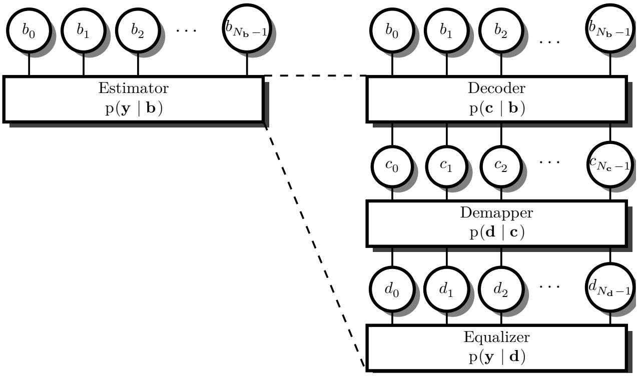

Figure B.5: FG given by equation (B.8) on the left and (B.10) on the right side.

work we focus on the transmission over under-determined systems like in Chapter 4 with a TWRC for a pair of users per resource leading to an overloaded system of $\beta = 2$ or in Chapter 5 with a load $\beta > 1$. The crucial part in both scenarios is the equalizer $\mathrm{p}(\mathbf{y} \mid \mathbf{d})$. Such we focus here in the appendix on the general concept of the equalizer with a single link ($\beta = 1$) and refer to the specific chapters for the FGE regarding higher loads.

The steps to generate a FG for the mapping and encoding part are not topic of this thesis, but the overall procedure is the same, we refer to [KFL01, Loe03, Wym07] for the interested reader.

Equalizer To further open the likelihood function $\mathrm{p}\left(\underline{\mathbf{y}} \mid \underline{\mathbf{d}}\right)$ we need this underlying structure of the transmission as also discussed in [LYWM05]. As we stressed in Chapter 3, this transmission can be described by a frame based receive signal (3.10) like $\underline{\mathbf{y}} = \underline{\mathbf{H}}\,\underline{\mathbf{d}} + \underline{\mathbf{n}}$ with channel matrix $\underline{\mathbf{H}} \in \mathbb{C}^{N'_{\mathrm{SC}} N'_{\mathrm{TS}} \times N_{\mathrm{SC}} N_{\mathrm{TS}}}$. We first assume that the transmission is affected by a noise vector $\underline{\mathbf{n}}$ with uncorrelated Gaussian characteristic to state the principle ideas, before we discuss colored noise terms later on in this chapter.

Additive White Gaussian Noise By assuming an AWGN vector $\underline{\mathbf{n}}$ with entries n_r coming from an iid random variable with Gaussian distribution $\mathcal{N}\left(0, \sigma_{\mathrm{n}}^2\right)$ determined by the PDF $\mathrm{p}_n(n)$ given by

$$\mathrm{p}_N(N = n_r) = \frac{1}{\sqrt{2\pi\sigma_{\mathrm{n}}^2}} e^{-\frac{n_r^2}{2\sigma_{\mathrm{n}}^2}} \tag{B.11}$$

the function node $\mathrm{p}\left(\underline{\mathbf{y}} \mid \underline{\mathbf{d}}\right)$ can be factorized by

$$\mathrm{p}\left(\underline{\mathbf{y}} \mid \underline{\mathbf{d}}\right) = \prod_{r=0}^{N'_{\mathrm{SC}}N'_{\mathrm{TS}}-1} \mathrm{p}(y_r \mid \underline{\mathbf{d}}) = \prod_{r=0}^{N'_{\mathrm{SC}}N'_{\mathrm{TS}}-1} \mathrm{p}_N\left(y_r - \underline{\mathbf{H}}_{r,:}\underline{\mathbf{d}}\right) \tag{B.12}$$

This factorization is shown in Fig. B.6. The connections of each function

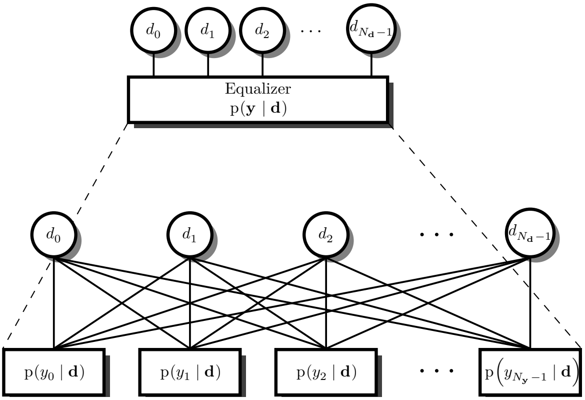

Figure B.6: General EQ Factorization with iid noise.

$\mathrm{p}_N\left(y_r - \underline{\mathbf{H}}_{r,:}\underline{\mathbf{d}}\right)$ are given by rows of the underlying channel matrix[4] $\mathbf{H}_{r,:}$. Hence, the entries in $\underline{\mathbf{H}}$ are responsible for the generation of the FG, *i.e.*, if an entry $h_{r,s}$ is unequal to zero, a connection between the corresponding observation y_r and the symbol d_s exist in the FG. For this let us introduce a helping *adjacency* matrix $\mathbf{A} \in \{0,1\}^{N'_{\mathrm{SC}}N'_{\mathrm{TS}} \times N_{\mathrm{SC}}N_{\mathrm{TS}}}$ of the same size as the effective channel matrix $\underline{\mathbf{H}}$. The entries in $\mathbf{A}$ are given by

$$a_{r,s} = \begin{cases} 1 & , \ h^{\mathsf{u}}_{r,s} \neq 0 \\ 0 & , \ \text{otherwise} \end{cases}, \tag{B.13}$$

and a row in $\mathbf{A}_{r,:}$ gives the connection between the r^{th} observation y_r and all connected symbols d_s and a column $\mathbf{A}_{:,s}$ determines all connections between the s^{th} symbol and all connected observations y_r. Furthermore, we can define the neighborhood of a factor and a variable node by the adjacency matrix, which gives the indices of all connected nodes. The neighborhood of a factor node $\mathrm{p}(y_r \mid \mathbf{d})$ is given by the set of variables connected like

$$\mathcal{N}_{y_r} = \{s \mid a_{r,s} = 1\} \tag{B.14}$$

---

[4] Here, we use a MATLAB like notation $\underline{\mathbf{H}}_{r,:} = \left[h_{r,0}, h_{r,1}, \ldots, h_{r,N_{\mathrm{SC}}N_{\mathrm{TS}}-1}\right]$

and the neighborhood of a variable d_s is given by the set of factor nodes connected

$$\mathcal{N}_{d_s} = \{r \mid a_{r,s} = 1\} \quad . \tag{B.15}$$

A simple example with three variables and four observations is drawn in Fig. B.7 with adjacency matrix

$$\mathbf{A} = \begin{bmatrix} 1\,1\,0 \\ 1\,1\,0 \\ 0\,1\,0 \\ 0\,1\,1 \end{bmatrix} . \tag{B.16}$$

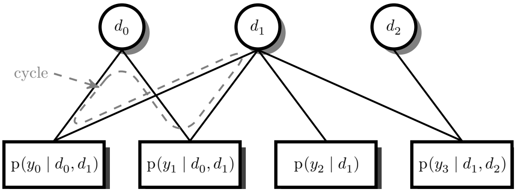

Figure B.7: Concrete equalizer factorization example with adjacency matrix **A**.

Here, the neighborhood sets are $\mathcal{N}_{y_0} = \{0, 1\}$, $\mathcal{N}_{y_1} = \{0, 1\}$, $\mathcal{N}_{y_2} = \{1\}$ and $\mathcal{N}_{y_3} = \{1, 2\}$ for the factor nodes and $\mathcal{N}_{d_0} = \{0, 1\}$, $\mathcal{N}_{d_1} = \{0, 1, 2, 3\}$ and $\mathcal{N}_{d_2} = \{3\}$ for the variable nodes.

It should be noted that this FG has a cycle illustrates by the dashed line in Fig. B.7, this has implications on the calculation of the SPA, discussed below.

Messages on the Factor Graph Within the FG we can differ mainly two types of messages [Loe03, KFL01, Wym07], 1) the message from a factor node to a variable node given by

$$\mu_{y_r \to d_s}(d_s) = \sum_{\sim\{d_s\}} \mathrm{p}\Big(y_r \mid d_s \in \mathcal{N}_{y_r^{\mathsf{R}}}\Big) \prod_{q \in \mathcal{N}_{y_r} \backslash s} \mu_{d_q \to y_r}(d_q) \quad , \tag{B.17}$$

and 2) the message from a variable node to a function node:

$$\mu_{d_s \to y_r}(d_s) = \mu_{\mathrm{Map.} \to d_s}(d_s) \prod_{q \in \mathcal{N}_{d_s} \backslash r} \mu_{y_q \to d_s}(d_s) \quad , \tag{B.18}$$

where $\mu_{\mathrm{Map.}\rightarrow d_s}(d_s)$ is the a priori message for variable d_s generated from the mapping function. The outgoing message to the mapping function is given by

$$\mu_{d_s \rightarrow \mathrm{Map.}}(d_s) = \prod_{q \in \mathcal{N}_{d_s}} \mu_{y_q \rightarrow d_s}(d_s) \quad . \tag{B.19}$$

Sum Product Algorithm The overall procedure calculating the messages from a variable to a function node is given in Alg. B.1. Since the FG most likely have cycles, the calculation of the SPA depends on the scheduling of the messages. This work does not focus on scheduling methods, so the messages are calculated in ascending order.

Algorithm B.1 Iterative SPA Equalizer

```
#Initialize FG #
Setup the edges based on the adjacency matrix like in (B.13)
#Initialize#
$\mu_{\mathrm{Demapper}\rightarrow d_s}(d_s) = 1/M$
#Start Calculation of SPA#
repeat
    #Calculate variable to factor message#
    for $s = 0, s \leq N_{\mathrm{SC}} N_{\mathrm{TS}} - 1, s = s + 1$ do
        calculate $\mu_{d_s \rightarrow y_r}(d_s)$ like in (B.18)
    end for
    #Calculate factor to variable message#
    for $r = 0, r \leq N'_{\mathrm{SC}} N'_{\mathrm{TS}} - 1, r = r + 1$ do
        calculate $\mu_{y_r \rightarrow d_s}(d_s)$ like in (B.17)
    end for
until Any stopping criterion is met
#calculate equalizer output message#
calculate $\mu_{d_s \rightarrow \mathrm{Map.}}(d_s)$ like in (B.19)
```

Complexity

The amount of messages exchanged within the FGE of the equalizer depends mainly on the number of iterations N_{It} and number of edges given by

$$N_{\mu,\mathrm{exchanged}} = N_{\mathrm{It}} \sum_{s=0}^{N_{\mathrm{SC}} N_{\mathrm{TS}} - 1} N_{\mathrm{edges}}^{d_s} = N_{\mathrm{It}} \sum_{r=0}^{N'_{\mathrm{SC}} N'_{\mathrm{TS}} - 1} N_{\mathrm{edges}}^{y_r} \tag{B.20}$$

where

$$N_{\text{edges}}^{d_s} = \sum_{j=0}^{N_{\text{SC}}N_{\text{TS}}-1} \mathbf{A}_{s,j} = \left|\mathcal{N}_{d_s}\right| \tag{B.21}$$

$$N_{\text{edges}}^{y_r} = \sum_{i=0}^{N'_{\text{SC}}N'_{\text{TS}}-1} \mathbf{A}_{i,r} = \left|\mathcal{N}_{y_r}\right| \quad . \tag{B.22}$$

are the number of edges of the connected symbols d_s and y_r, respectively. The number of messages exchanged $N_{\mu,\text{exchanged}}$ gives a first indication on the complexity of the calculation of the SPA. Furthermore, the complexity of the messages depends on their possible implementations, *e.g.*, probability domain, log domain or log likelihood ratio (LLR) domain and the system model. However, the calculation of the messages also scale with the number of edges per node and the modulation alphabet. By assuming the calculation in the probability domain and the same number of edges for simplicity like $N_{\text{edges}} = N_{\text{edges}}^{d_s} = N_{\text{edges}}^{y_r}$ omitting the indices's, the number of additions per message are given by

$$N_{\text{Additions,per Message}} = \frac{1}{2}\left(N_{\text{edges}}2^{N_{\text{edges}}}\right)\left(M\log_2\left(M\right)\right), \tag{B.23}$$

likewise, the number of multiplications per message is:

$$\begin{aligned} N_{\text{Multiplications,per Message}} = &\left(2N_{\text{edges}}2^{N_{\text{edges}}}\right)\left(M\log_2\left(M\right)\right) \\ &+ \left(N_{\text{edges}}-1\right)\log_2\left(M\right). \end{aligned} \tag{B.24}$$

The complexity grows linearly with the number of iterations N_{It} and the number of resources N_{SC} or N_{TS} within the multi-carrier scheme as shown in (B.20). However, the main impact is given by the modulation alphabet scaling with $M\log_2\left(M\right)$ and the number of edges scaling with $2N_{\text{edges}}2^{N_{\text{edges}}}$, which is mainly dominated by the channel and the waveform and controlled by the threshold ε in (B.13).

Symbol Mapper and Channel Coding Some symbol mapping and the channel encoding schemes are described in Chapter 2. The basic calculation procedure is the same as that of the equalizer, *i.e.*, we have two types of messages, one which are going to factor nodes and one going to variable nodes. For more information on symbol mapping and encoding, see [Loe03, KFL01, Wym07]. In addition, Chapter 4 and Chapter 5 includes the calculation of the symbol mapping and channel encoding schemes.

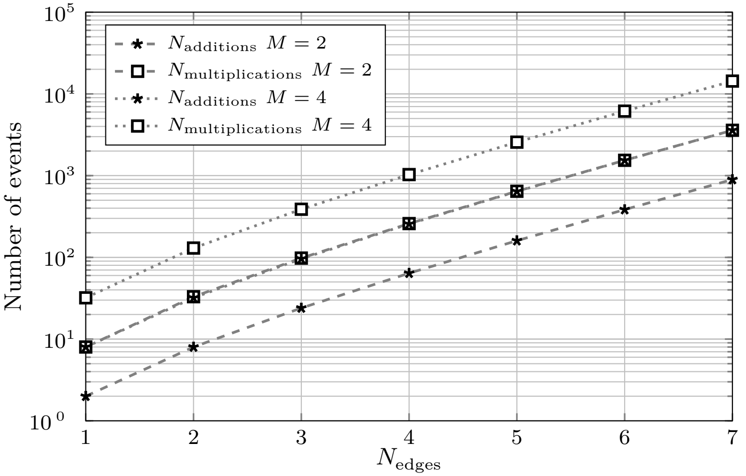

Figure B.8: Number of multiplications and additions for a given symbol mapping and different number of edges.

Correlated Noise Terms So far we addressed a system model considering white Gaussian noise, only. The system model considers a general not necessarily white noise process, which depends on the choice of the receive filter-bank. The corresponding autocorrelation function $\Psi_{\mathbf{n}\,\mathbf{n}}$ of the noise terms related to the considered waveform candidates are given in Chapter 3. In case of an orthogonal waveform,*e.g.* CP-OFDM, the correlation function $\Psi_{\mathbf{n}\,\mathbf{n}} = \sigma_{\mathrm{n}}^2\mathbf{I}$ yields an uncorrelated noise term, such that the Forney approach can be directly applied [For72b]. Contrarily, the application of a non-orthogonal waveform yields a correlation of the noise term as derived in A.6. The choice now is twofold, we can either use the Forney based receiver [For72b, For72a], where we need uncorrelated noise and thus the application of a prewithening filter is essential or we apply a FG approach based on Ungerboeck [Ung74], where we change the FG to deal with underlying correlation [OWM$^+$12]. In this work we focus on the former approach, hence a prewithening filter is needed. As the noise is modeled at the receiver, only, a prewithening filter based on the Rx analysis filter-bank has to be designed [Vog06]. We use a linear filter $\mathbf{P}$ such that the correlation yields

$$\Psi_{\tilde{\mathbf{n}}\,\tilde{\mathbf{n}}} = \mathrm{E}\{\mathbf{P}\mathbf{G}^{\mathrm{Rx}}\mathbf{n}\mathbf{n}^{\mathsf{H}}\mathbf{G}^{\mathrm{Rx}\mathsf{H}}\mathbf{P}^{\mathsf{H}}\} \overset{!}{=} \sigma_{\mathrm{n}}^2\mathbf{I} \tag{B.25}$$

$$\mathrm{E}\{\mathbf{P}\mathbf{G}^{\mathrm{Rx}}\mathbf{n}\mathbf{n}^{\mathsf{H}}\mathbf{G}^{\mathrm{Rx}\mathsf{H}}\mathbf{P}^{\mathsf{H}}\} = \underbrace{\mathbf{P}\mathbf{G}^{\mathrm{Rx}}\mathbf{G}^{\mathrm{Rx}\mathsf{H}}\mathbf{P}^{\mathsf{H}}}_{\overset{!}{=}\mathbf{I}}\sigma_{\mathrm{n}}^{2}\mathbf{I} \tag{B.26}$$

The condition $\mathbf{P}\mathbf{G}^{\mathrm{Rx}}\mathbf{G}^{\mathrm{Rx}\mathsf{H}}\mathbf{P}^{\mathsf{H}} \overset{!}{=} \mathbf{I}$ has to be fulfilled. This is the basis of the prewhitening filter design. In [Vog06], the solutions are given by $\mathbf{P} = \mathbf{G}^{-1}$ or $\mathbf{P} = \mathbf{F}\mathbf{G}^{-1}$. Another approach can be achieved by the application of the SVD like $\mathbf{G} = \mathbf{U}\Sigma\mathbf{V}^{\mathsf{H}}$ resulting in $\mathbf{P} = (\mathbf{U}\Sigma)^{-1}$. Especially, if the matrix $\mathbf{G}^{\mathrm{Rx}}$ has a circular structure, the eigenvalue decompensition results in $\mathbf{G} = \mathbf{F}\Sigma\mathbf{F}^{\mathsf{H}}$ and the prewhitening filter $\mathbf{P} = \left(\mathbf{F}\Sigma^{1/2}\mathbf{F}^{\mathsf{H}}\right)^{-1}$ can be used.

The application of all approaches result in uncorrelated noise terms, such that the Forney detection can be used. However, the application of the prewhitening filter $\mathbf{P}$ can result in a complete change of the structure of the effective channel matrix $\widetilde{\mathbf{H}} = \mathbf{P}\mathbf{H}$ and, hence, the complexity and performance of the SPA.

Consequently, it is dependent on the MC scheme used, which prewhitening should be used changing the structure of the effective channel only marginally.

Appendix C

Two-Way Relaying

C.1 TWRC Signals

In Table C.1 the possible combinations of code bits, symbols and noise/interference-free receive signal are given with QPSK and a mapping $d^{\mathsf{u}} = (-1)^{c^{\mathsf{u}}_{2c}} \cdot (j)^{\left(c^{\mathsf{u}}_{2c+1}\right)}$ and the set $\mathcal{D}^{\mathsf{u}}_{\mathrm{QPSK}} \in \{1, j, -1, -j\}$. The code word combination $c^{\mathsf{AB}} = c^{\mathsf{A}}_1 + c^{\mathsf{A}}_2 D + c^{\mathsf{B}}_1 D^2 + c^{\mathsf{B}}_2 D^3$ for QPSK is defined and given in the table with indeterminate D in a polynomial description as a short hand notation for the 16 different combinations living in the extension field $c^{\mathsf{AB}} \in \mathbb{F}_{2^{N_{\mathsf{u}} \log_2(M)}}$ [Wüb10, WL10, Wu17]. Furthermore, the mapping sets $\mathcal{D}^{D^{\mathsf{u}}=d^{\mathsf{u}}}_{\mathrm{SCD}}$ for SCD and $\mathcal{D}^{D^{\mathsf{A}\oplus\mathsf{B}}=d^{\mathsf{A}\oplus\mathsf{B}}}_{\mathrm{JCNC}}$ are given below.

Mapping Sets for SCD

- For user A: $\mathcal{D}^{D^{\mathsf{A}}=1}_{\mathrm{SCD}} = \{0, 4, 8, 12\}$, $\mathcal{D}^{D^{\mathsf{A}}=j}_{\mathrm{SCD}} = \{1, 5, 9, 13\}$, $\mathcal{D}^{D^{\mathsf{A}}=-1}_{\mathrm{SCD}} = \{2, 6, 10, 14\}$ and $\mathcal{D}^{D^{\mathsf{A}}=-j}_{\mathrm{SCD}} = \{3, 7, 11, 15\}$.
- For user B: $\mathcal{D}^{D^{\mathsf{B}}=1}_{\mathrm{SCD}} = \{0, 1, 2, 3\}$, $\mathcal{D}^{D^{\mathsf{B}}=j}_{\mathrm{SCD}} = \{4, 5, 6, 7\}$, $\mathcal{D}^{D^{\mathsf{B}}=-1}_{\mathrm{SCD}} = \{8, 9, 10, 11\}$ and $\mathcal{D}^{D^{\mathsf{B}}=-j}_{\mathrm{SCD}} = \{12, 13, 14, 15\}$.

Mapping Sets for JCNC

$\mathcal{D}^{D^{\mathsf{A}\oplus\mathsf{B}}=1}_{\mathrm{JCNC}} = \{0, 5, 10, 15\}$, $\mathcal{D}^{D^{\mathsf{A}\oplus\mathsf{B}}=j}_{\mathrm{JCNC}} = \{1, 4, 11, 14\}$, $\mathcal{D}^{D^{\mathsf{A}\oplus\mathsf{B}}=-1}_{\mathrm{JCNC}} = \{2, 7, 8, 13\}$ and $\mathcal{D}^{D^{\mathsf{A}\oplus\mathsf{B}}=-j}_{\mathrm{JCNC}} = \{3, 6, 9, 12\}$.

Mapping Sets for GJCNC

No explicit mapping is required for GJCNC, since the symbols have a direct assignment.

Table C.1: Possible combinations of code bits, symbols and noise & interference-free receive signals for QPSK.

i	c^{A}	c^{B}	$c^{\mathsf{A}\oplus\mathsf{B}}$	c^{AB}	d^{A}	d^{B}	$d^{\mathsf{A}\oplus\mathsf{B}}$	d^{AB}	noise/interference-free receive signal
0	0 0	0 0	0 0	0	1	1	1	$(1,1)$	$h^{\mathsf{A}} + h^{\mathsf{B}}$
1	0 1	0 0	0 1	1	j	1	j	$(j,1)$	$jh^{\mathsf{A}} + h^{\mathsf{B}}$
2	1 0	0 0	1 0	D	-1	1	-1	$(-1,1)$	$-h^{\mathsf{A}} + h^{\mathsf{B}}$
3	1 1	0 0	1 1	$D+1$	$-j$	1	$-j$	$(-j,1)$	$-jh^{\mathsf{A}} + h^{\mathsf{B}}$
4	0 0	0 1	0 1	D^2	1	j	j	$(1,j)$	$h^{\mathsf{A}} + jh^{\mathsf{B}}$
5	0 1	0 1	0 0	D^2+1	j	j	1	(j,j)	$jh^{\mathsf{A}} + jh^{\mathsf{B}}$
6	1 0	0 1	1 1	D^2+D	-1	j	$-j$	$(-1,j)$	$-h^{\mathsf{A}} + jh^{\mathsf{B}}$
7	1 1	0 1	1 0	D^2+D+1	$-j$	j	-1	$(-j,j)$	$-jh^{\mathsf{A}} + jh^{\mathsf{B}}$
8	0 0	1 0	1 0	D^3	1	-1	-1	$(1,-1)$	$h^{\mathsf{A}} - h^{\mathsf{B}}$
9	0 1	1 0	1 1	D^3+1	j	-1	$-j$	$(j,-1)$	$jh^{\mathsf{A}} - h^{\mathsf{B}}$
10	1 0	1 0	0 0	D^3+D	-1	-1	1	$(-1,-1)$	$-h^{\mathsf{A}} - h^{\mathsf{B}}$
11	1 1	1 0	0 1	D^3+D+1	$-j$	-1	j	$(-j,-1)$	$-jh^{\mathsf{A}} - h^{\mathsf{B}}$
12	0 0	1 1	1 1	D^3+D^2	1	$-j$	$-j$	$(1,-j)$	$h^{\mathsf{A}} - jh^{\mathsf{B}}$
13	0 1	1 1	1 0	D^3+D^2+1	j	$-j$	-1	$(j,-j)$	$jh^{\mathsf{A}} - jh^{\mathsf{B}}$
14	1 0	1 1	0 1	D^3+D^2+D	-1	$-j$	j	$(-1,-j)$	$-h^{\mathsf{A}} - jh^{\mathsf{B}}$
15	1 1	1 1	0 0	D^3+D^2+D+1	$-j$	$-j$	1	$(-j,-j)$	$-jh^{\mathsf{A}} - jh^{\mathsf{B}}$

Appendix D

Multi-Carrier Compressive Sensing Multi-User Detection

D.1 General Waveform in MCSM

D.1.1 Error Estimate of CP-FBMC

As we have seen in Chapter 3, the insertion of the frame-based waveform matrix (3.67) into equation (3.63) yields the effective channel matrix

$$\mathbf{H}^{\mathsf{u}}_{\mathcal{S}_i,i,i'} = \begin{cases} \mathbf{I}_{\mathcal{S}_i}\mathbf{F}\boldsymbol{\Sigma}^{\mathrm{Rx}}_{\mathbf{g}}\mathbf{F}^{\mathsf{H}}\boldsymbol{\Sigma}^{\mathsf{u}}_{h,i,i'}\mathbf{F}\boldsymbol{\Sigma}^{\mathrm{Tx}}_{\mathbf{g}}\mathbf{F}^{\mathsf{H}}\mathbf{I}^{\mathsf{T}}_{\mathcal{S}_i} & i'=i \\ \mathbf{0} & \text{otherwise} \end{cases} \quad . \tag{D.1}$$

which is a pure block-diagonal matrix, if the channel length not exceeds the CP. The question is: Do the assumption of transmitting within the coherence bandwidth still result in a one-tap channel coefficient per spreading sequence? To answer this question, we have a look on the user specific receive signal

$$\mathbf{y}^{\mathsf{u}}_{i} = \mathbf{H}^{\mathsf{u}}_{\mathcal{S}_i}\mathbf{s}^{\mathsf{u}}d^{\mathsf{u}}_{\mathsf{u}} \quad . \tag{D.2}$$

Due to the block diagonal structure and without loss of generality, we can rewrite the matrix multiplication in (D.1) as sum over $N_{\mathrm{Blocks}} = N_{\mathrm{IFFT}}/N_{\mathrm{s}}$ with $b = 1, \dots N_{\mathrm{Blocks}}$ corresponding to the set $\mathcal{S}_i = \mathcal{S}_i^{+}$ yielding the following equation

$$\mathbf{H}^{\mathsf{u}}_{\mathcal{S}_{\imath},\imath,\imath} = \sum_{\beta=1}^{N_{\text{Blocks}}} \left(\underbrace{\sum_{\kappa=1}^{N_{\text{Blocks}}} \mathbf{F}_{q,\kappa} \boldsymbol{\Sigma}_{\mathbf{g}}^{\text{Rx}\kappa,\kappa} \mathbf{F}^{\mathsf{H}}_{\beta,\kappa}}_{\mathbf{L}(q,\beta)} \boldsymbol{\Sigma}^{\mathsf{u}}_{h,\imath,\imath,\beta,\beta} \underbrace{\sum_{\kappa=1}^{N_{\text{Blocks}}} \mathbf{F}_{\beta,\kappa} \boldsymbol{\Sigma}_{\mathbf{g}}^{\text{Tx}\kappa,\kappa} \mathbf{F}^{\mathsf{H}}_{q,\kappa}}_{\mathbf{R}(\beta,q)} \right) . \tag{D.3}$$

With the left matrix $\mathbf{L}(q,\beta)$ and right matrix $\mathbf{R}(\beta,q)$ the user specific receive signal can be rewritten into

$$\mathbf{y}^{\mathsf{u}}_{\imath} = \left[\sum_{\beta=1}^{N_{\text{Blocks}}} \mathbf{L}(q,\beta) \boldsymbol{\Sigma}^{\mathsf{u}}_{h,\imath,\imath,\beta,\beta} \mathbf{R}(\beta,q) \right] \mathbf{s}^{\mathsf{u}} d^{\mathsf{u}}_{\imath} \tag{D.4}$$

Further, it is worth mentioning that $\mathbf{L}\,(q,\beta) = \mathbf{R}^{\mathsf{H}}\,(\beta,q)$.

By assuming now p is the block of sub-carriers related to the set $\mathcal{S}_{\imath}$, we can separate the sum into

$$\mathbf{y}^{\mathsf{u}}_{\imath} = \underbrace{\mathbf{L}(p,p) \boldsymbol{\Sigma}^{\mathsf{u}}_{\imath,\imath,p,p} \mathbf{R}(p,p) \mathbf{s}^{\mathsf{u}} d^{\mathsf{u}}_{\imath}}_{\text{desired part}} + \underbrace{\left[\sum_{\substack{\beta=1 \\ \beta\neq p}}^{N_{\text{Blocks}}} \mathbf{L}(p,\beta) \boldsymbol{\Sigma}^{\mathsf{u}}_{\imath,\imath,\beta,\beta} \mathbf{R}(\beta,p) \right] \mathbf{s}^{\mathsf{u}} d^{\mathsf{u}}_{\imath}}_{\text{Interference}} \tag{D.5}$$

Now we assume the transmission within the coherence bandwidth resulting in block-wise. Hence, each block can be represented by one channel coefficient $\boldsymbol{\Sigma}^{\mathsf{u}}_{\imath,\imath,\beta,\beta} = h^{\mathsf{u}}_{\beta}\mathbf{I}$. By this assumption, we can rewrite (D.5) to

$$\mathbf{y}^{\mathsf{u}}_{\imath} = \underbrace{h^{\mathsf{u}}_{p} \mathbf{L}(p,p) \mathbf{R}(p,p) \mathbf{s}^{\mathsf{u}} d^{\mathsf{u}}_{\imath}}_{\text{desired part}} + \underbrace{\left[\sum_{\substack{\beta=1 \\ \beta\neq p}}^{N_{\text{Blocks}}} h^{\mathsf{u}}_{\beta} \mathbf{L}(p,\beta) \mathbf{R}(\beta,p) \right] \mathbf{s}^{\mathsf{u}} d^{\mathsf{u}}_{\imath}}_{\text{Interference}} \tag{D.6}$$

And follow the same methodology using the vectorization operator like in CP-OFDM based MCSM in (5.15) and (5.16), the detection model for CP-FBMC based MCSM can be given as

$$\mathbf{Y} \approx \mathbf{S}_{\text{w}} \widetilde{\mathbf{D}} + \mathbf{J} + \widetilde{\mathbf{N}}, \tag{D.7}$$

where

$$\mathbf{S}_{\text{w}} = \underbrace{\mathbf{L}(p,p) \mathbf{R}(p,p)}_{\mathbf{M}_{\text{w}}} \mathbf{S} \tag{D.8}$$

and $\mathbf{J}$ covers the interference terms on the right-hand-side of (D.6) and $\widetilde{\mathbf{N}} = \mathbf{I}_{\mathcal{S}_i}\mathbf{F}\mathbf{\Sigma}_{\mathbf{g}}^{\mathrm{Rx}}\mathbf{F}^{\mathsf{H}}\mathbf{N}$.

CP-OFDM Applying CP-OFDM to (D.6) with the filter matrices $\mathbf{\Sigma}_{\mathbf{g}}^{\mathrm{Tx}} = \mathbf{\Sigma}_{\mathbf{g}}^{\mathrm{Rx}} = \mathbf{I}$, these left and right matrices yield:

$$\mathbf{L}(\mathscr{b}, q) = \mathbf{R}(q, \mathscr{b}) = \begin{cases} \mathbf{I} & , q = \mathscr{b} \\ \mathbf{0} & , q \neq \mathscr{b} \end{cases} . \tag{D.9}$$

Thus, the user specific receive signal results with $\mathbf{\Sigma}_{h,i,i,\mathscr{b},\mathscr{b}}^{\mathsf{u}} = \mathbf{I}_{\mathcal{S}_i}\mathbf{\Sigma}_{h,i,i}^{\mathsf{u}}\mathbf{I}_{\mathcal{S}_i}^{\mathsf{T}}$ in

$$\mathbf{y}_i^{\mathsf{u}} = \mathbf{I}_{\mathcal{S}_i}\mathbf{\Sigma}_{h,i,i}^{\mathsf{u}}\mathbf{I}_{\mathcal{S}_i}^{\mathsf{T}}\mathbf{s}^{\mathsf{u}}d_i^{\mathsf{u}} \tag{D.10}$$

as already given in Section 5.3.4 and further assuming within the coherence bandwidth results in the receive signal model for a frame in (5.16).

Acronyms

M-PSK	M-ary phase shift keying
M-QAM	M-ary quadrature amplitude modulation
3GPP	Third Generation Partnership Project
5G	5th Generation
5GNOW	5th Generation Non-Orthogonal Waveforms for Asynchronous Signalling
ACI	adjacent carrier interference
AER	activity error rate
AF	amplify and forward
ALOHA	ALOHA
AMP	approximate message passing
ANT	Arbeitsbereich Nachrichtentechnik
APP	a-posteriori probability
ARQ	automatic repeat request
AS-JCNC	arithmetic sum-joint channel decoding and physical-layer network coding
AWGN	additive white Gaussian noise
BC	broadcast
BCJR	Bahl-Cocke-Jelinek-Raviv
BER	bit error rate
BPSK	binary phase shift keying
BS	base station
CDMA	code division multiple access
CFO	carrier frequency offset

CMT cosine modulated multi-tone
COIN Communication in Interference Limited Networks
CP cyclic prefix
CP-FBMC cyclic prefix-based FBMC
CP-OFDM cyclic prefix-based orthogonal frequency division multiplexing
CRC cyclic redundancy check
CS compressed sensing
CS-MUD compressed sensing-multi-user detection
CSI channel state information

D-M-PSK differential-M ary-phase shift keying
D-QPSK differential-quaternary phase shift keying
DCT discrete cosine transform
DF decode and forward
DFG German Research Department
DFT discrete Fourier transform
DMT discrete multi tone
DRA direct random access
DSL digital subscriber line
DVB digital video broadcast
DVB-S2 digital video broadcast, satellite 2nd Generation
DVB-T digital video broadcast terrestrial
DVB-T2 digital video broadcast, terrestrial 2nd Generation

EDGE Enhanced Data Rates for GSM Evolution
EGF extended Gaussian function

FA false alarm
FB filter-bank
FBMC filter-bank multi-carrier
FBMC/FMT filter-bank multi-carrier/frequency multi-tone
FDMA frequency division multiple access
FEC forward error correction
FER frame error rate
FFT fast Fourier transform

FG factor graph
FGE factor graph-based equalizer
FMT frequency multi-tone

GFDM general frequency division multiplexing
GI guard interval
GJCNC generalized joint channel decoding and physical-layer network coding
GMIP group mutual incoherence property
GMSK Gaussian minimum shift keying
GOMP group orthogonal matching pursuit
GPRS General Packet Radio Service
GS guard symbol
GSM Global System for Mobile Communications

HSPA High Speed Packet Access

I4.0 Industry 4.0
IBI inter-block interference
ICI inter-carrier interference
IDFT inverse discrete Fourier transform
IDGT inverse discrete Gabor transform
IDMA interleaved division multiple access
IDSTFT inverse discrete short-time Fourier transform
IFFT inverse fast Fourier transform
IFI inter-frame interference
IGT inverse Gabor transform
iid independent and identically distributed
IoT Internet of Things
IOTA isotropic orthogonal transform algorithm
ISI inter-symbol interference
ISTFT inverse short-time Fourier transform

JCNC joint channel decoding and physical-layer network coding
JPEG Joint Photographic Experts Group

KPI key performance indicator

LDPC low density parity check
LE linear equalizer
LLR log likelihood ratio
LO local oscillator
LS least squares
LTE Long Term Evolution

M2M machine-to-machine
MA multiple access
MAC multiple access channel
MAP maximum a-posteriori
MC multi-carrier
MC-CDMA multi-carrier-code division multiple access
MCSM multi-carrier compressed sensing multi-user detection
MD missed detection
METIS Mobile and wireless communications Enablers for the Twenty-twenty Information Society
METIS-II Project: METIS-II
MF matched filter
MIMO multiple input multiple output
MIP mutual incoherence property
MLS maximum length sequence
MMSE minimum mean square error
mMTC *massive* machine type communication
MMV multiple measurement vector
MMV-CS multiple measurement vector-compressed sensing
MMV-SIC multiple measurement vector-successive interference cancellation
MSE mean square error
MTC machine type communication
MU multi-user
MUD multi-user detection
MUI multi-user interference
MUSIC Multiple Signal Classifier

NB-IoT narrow band Internet of Things

NC network coding
NGMN next generation mobile networks
NP non-deterministic polynomial-time

OFDM orthogonal frequency division multiplexing
OFDMA orthogonal frequency division multiple access
OMP orthogonal matching pursuit
OoBE out-of-band emissions
OQAM offset quadrature amplitude modulation
OQAM/FBMC offset quadrature amplitude modulation/filter-bank multi-carrier
OQAM/OFDM offset quadrature amplitude modulation/orthogonal frequency division multiplexing

P/S parallel to serial
P2P point-to-point
PAPR peak-to-average power ratio
PDF probability density function
PHY Physical
PHYDYAS Physical Layer For Dynamic Spectrum Access And Cognitive Radio
PLNC physical layer network coding
PMF probability mass function
PN pseudo noise
ppm parts per million
PPN polyphase network
PRACH physical random access channel
PSK phase shift keying

QAM quadrature amplitude modulation
QAM/FBMC quadrature amplitude modulation/filter-bank multi-carrier
QoS Quality of Service
QPSK quaternary phase shift keying
QR QR-factorization

RFID radio-frequency identification
RHS right-hand-side

RIP restricted isometric property
RP random phase
RRC root-raised-cosine
Rx receiver

S/P serial to parallel
SC single-carrier
SC-FDMA single-carrier-frequency division multiple access
SCD separate channel decoding
SF-SCD straightforward separate channel decoding
sIC soft interference cancellation
SISO single-input single-output
SMS short message service
SMT staggered multi-tone
SMV single measurement vector
SMV-CS single measurement vector-compressed sensing
SNR signal-to-noise ratio
SotA state of the art
SPA sum-product algorithm
STFT short-time Fourier transform
SVD singular value decompensation

TDD time division duplex
TF time-frequency
TFL time-frequency localization
TO timing offset
TWR two-way relaying
TWRC two-way relaying channel
Tx transmitter
Tx/Rx transmitter/receiver

UF-OFDM universal filtered - orthogonal frequency division multiplexing
UMTS Universal Mobile Telecommunication System

w-CP-OFDM windowed-cyclic prefix-orthogonal frequency division multiplexing
w-OFDM windowed-orthogonal frequency division multiplexing

WAP Wireless Application Protocol
WI-FI wireless-fidelity
WiMax Worldwide Interoperability for Microwave Access
WLAN Wireless Local Area Network
wLE windowed linear equalizer
WOLA weighted overlap-add

XO crystal oscillator
XOR eXclusive OR

ZP zero padded
ZP-OFDM zero padded-orthogonal frequency division multiplexing

List of Symbols

Functions and Operators

$\lvert\cdot\rvert$	Absolute value or Cardinality
$\lVert\cdot\rVert_0$	ℓ^0-pseudo norm of a vector
$\lVert\cdot\rVert_2$	ℓ^2-norm of a vector
$A_{g_1,g_2}(\tau,\nu)$	Ambiguity function of filter g_1 and g_2
$\arg\max$	Argument that maximizes expression
$\arg\min$	Argument that minimizes expression
$\Re(\cdot)$	Real part
$\Im(\cdot)$	Imaginary part
$\cos(\cdot)$	Cosinus function
$\det(\cdot)$	Determinant of a matrix
$\operatorname{diag}\{\cdot\}$	Diagonal of a matrix
$\mathcal{C}(\cdot)$	Encoding function
$\mathrm{E}_X\{\cdot\}$	Expectation *w.r.t.* X
$\exp(\cdot)$	Exponential function
$\mathbb{F}_q^N$	Galois field base q of dimension N
$\log_{10}(\cdot)$	logarithmus with base ten
$\log_2(\cdot)$	logarithmus with base two
$\mathcal{M}(\cdot)$	Symbol Mapping function
$\max$	Maximum
$\min$	Minimum
$\mathrm{p}_X(x)$	Probability density function for X with realization x
$\mathrm{p}_{X\mid Y}(x\mid y)$	Probability density funct. for X given Y w/ realizations x & y
$\mathrm{p}_{X,Y}(x,y)$	Probability density funct. for X & Y w/ realizations x & y
$\Pr(X=x)$	Probability of the random variable $X=x$

P	Power
$s\left(\tau, \nu\right)$	Doppler-variant impulse response
$s_{\mathrm{TF}}\left(f, \nu\right)$	Doppler-variant transfer function
$\sin\left(\cdot\right)$	Sinus function
$\mathrm{vec}\{\mathbf{A}\}$	Vectorization of a matrix $\mathbf{A}$
$\mathrm{vol}\left(\Lambda\right)$	Volume of a lattice Λ
$w\left(\tau, t\right)$	Time-variant impulse response
$W_{\mathrm{TF}}\left(f, t\right)$	Time-variant transfer function
$\underline{\mathbf{X}}$	Frame matrix
$\hat{\mathbf{x}}$	Hard estimated values of $\mathbf{x}$
$\mathbf{X}^{\mathsf{H}}$	Hermitian of matrix $\mathbf{X}$
$\mathbf{X}^{\dagger}$	Pseudo-inverse of matrix $\mathbf{X}$
$\tilde{\mathbf{x}}$	Soft estimated values of $\mathbf{x}$
$\mathbf{X}^{\mathsf{T}}$	Transpose of matrix $\mathbf{X}$
$\mathbf{x}_{q,\iota}$	qth column and ιth row element of matrix $\mathbf{X}$
$\underline{\mathbf{x}}$	Frame vector
$\mathbf{X}_{q,\iota}$	qth column and ιth row of sub-matrix
$\mathbf{x}_q$	qth column vector of matrix $\mathbf{X}$

General and Calligraphic Symbols

$\mathscr{b}$	Index for blocks
$\mathbb{C}^N$	Complex numbers of dimension N
$\mathcal{C}$	Complexity
$\mathbb{C}$	Complex numbers
c	Index for code bit
$\mathcal{C}$	Set of code bits c
$\mathscr{r}$	Discrete index for the delay
$\mathscr{C}$	Encoding function
$\mathcal{E}$	Estimator
$\mathcal{F}\left\{\cdot\right\}$	Fourier transform
$\mathcal{F}^{-1}\left(\cdot\right)$	Inverse Fourier transform
$\mathbb{Z}^N$	Natural numbers of dimension N
$\mathbb{Z}$	Natural numbers
$\mathcal{B}$	Set of information bits b

$\mathcal{M}$	Symbol mapping function
$\mathcal{N}\left(\overline{\mu}, \sigma^2\right)$	Complex normal distribution with mean $\overline{\mu}$ and variance σ^2
$\mathcal{O}$	Order
$\mathcal{P}$	Set of pilots
$\mathbb{R}^N$	Real numbers of dimension N
$\mathbb{R}$	Real numbers
$\mathcal{Y}$	Set of receive symbols
$\mathscr{s}$	Sparsity
$\hat{\mathcal{A}}$	Estimated set of active users
$\mathcal{A}$	Set of active users
$\mathcal{N}_{y_r^{\mathsf{R}}}$	Set of neighbors of y_r^{R}
$\mathcal{N}_d$	Set of neighbors of d
$\overline{\mathcal{N}}_{d_s^{\mathsf{AB}}}$	Set of neighbors not in $\mathcal{N}_{d_s^{\mathsf{AB}}}$
$\mathcal{N}_{d_s^{\mathsf{AB}}}$	Set of neighbors d_s^{AB}
$\mathcal{N}_{d_s}$	Set of neighbors of d_s
$\mathcal{S}_i^+$	Set of extended sub-carriers
$\mathcal{S}_i$	Set of sub-carriers
$\mathcal{D}$	Set of symbols d
$\mathcal{D}_{\text{JCNC}}$	Set of Symbols for JCNC
$\mathcal{D}_{\text{SCD}}$	Set of symbols for SCD
$\mathscr{S}(\cdot)$	Spreading function
$\mathcal{N}$	Set of neighbors
$\mathcal{X}$	Set of transmit symbols
$\mathcal{U}(a, b)$	uniform distribution within [a,b]
$\mathcal{W}$	Window operator
$\mathscr{w}$	Oversampling factor

Greek Symbols

α	Filter parameter for the RRC filter
β	Load of a system
γ	Normalized Power loss
γ	Path of a channel
$\delta(t)$	Dirac distribution

$\overline{\delta}_{\mathrm{LD}}(\Lambda)$	Average lattice density
$\delta_{\mathrm{LD}}(\Lambda)$	Lattice density
ζ	Index for iterations
η	Bandwidth efficiency
θ	Spread signal vector
Θ	Spread signal Matrix
ι	Context dependent index
κ	Direction parameter
Λ	Lattice
$\mu_{f\rightarrow B}(B=b)$	Factor graph from function to variable node
$\mu_{B\rightarrow f}(B=b)$	Factor graph from variable to function node
$\overline{\mu}$	Mean value
ν	Doppler shift
$\psi_{f_1 f_2}$	Continuous correlation function between f_1 and f_2
$\Psi_{\mathbf{xy}}$	Discrete correlation function between $\mathbf{x}$ and $\mathbf{y}$
ξ	Heisenberg-Gabor parameter
ϖ	Index for Information bits
Π	Interleaver function
π	pi
ρ	Filter parameter for the Gaussian filter
ϱ	Rate per complex symbol
ς	Index for channel tab
$\boldsymbol{\Sigma}$	Purely diagonal matrix
σ	Standard Deviation
σ^2	Variance
τ_{c}	Coherence time
$w(\tau,t)$	time impulse response of a channel
τ_{γ}	Delay spread
τ^{max}	Maximum delay spread
$\overline{\tau}$	Helping variable for delay
τ	Delay spread
$\Delta\tau$	Constant delay TO
ϕ	Phase value

Roman Symbols

$\overline{\mathrm{AER}}$	Average activity error rate
p_{a}	Activity probability
$\mathsf{A}, \mathsf{B}, \mathsf{R}, \mathsf{u}$	Different users
B_{c}	Coherence bandwidth
B	Bandwidth
b	Information bit
c	Code bit
$\mathring{d}$	Differential modulated transmit symbol
d	Transmit symbol
E_{b}/N_0	Bit over noise energy ratio
$\overline{\mathrm{FER}}$	Average frame error rate
F_0'	Symbol spacing in f for OQAM
F_0	Symbol spacing in f for QAM
f_0	Carrier frequency
ν_{D}	Doppler frequency
f	Frequency
T_{GI}	Guard Interval time
i	Content dependent index
j	Imaginary number, *i.e.* $j = \sqrt{-1}$
$\mathbf{L}$	Lattice generator matrix
m_{i}	Mutual interference property
M	Number of symbols in an alphabet
N_{act}	Number of active users
N_{aver}	Number of averaging
N_{Blocks}	Number of blocks
N_{CP}	Number of CP samples
$N_{\mathbf{c}}$	Number of code bits
N_{edges}	Number of edges in a factor graph
N_e	Number of errors
$N_{\mathrm{FFT}}, N_{\mathrm{IFFT}}$	FFT, IFFT size
N_{g}	Number of filter samples
N_{GS}	Number of guard symbols

N_{GI}	Number of GI samples
N_{hop}	Number of hops in MCSM
$N_{\mathbf{b}}$	Number of information bits
$N_{\mathrm{MacroPath}}$	Number of macro channel path
$N_{\mathrm{MicroPath}}$	Number of micro channel path
N_{N}	Number of neighbours
N_{path}	Number of channel paths
N_{pilots}	Number of pilots
$N_{\mathrm{Resources}}^{\mathrm{Frame}}$	Number of resources
$N_{\mathbf{y}}$	Number of observations
$N_{\mathrm{SC}}^{\mathscr{b}}$	Number of sub-carriers per block
N_{SC}'	Number of sub-carriers at the Rx
N_{SC}	Number of sub-carriers at the Tx
N_{s}	Spreading length
$N_{\mathrm{Symbols}}^{\mathrm{Frame}}$	Number of symbols per frame
$N_{\mathbf{d}}$	Number of symbols d
N_{TS}'	Number of MC symbols at Rx
N_{TS}	Number of MC symbols at Tx
N_{x}	Number of receive symbols y
N_{u}	Number of users
$N_{\mathcal{W}}$	Number of elements in a window $\mathcal{W}$
N_{ZP}	Number of zero added in ZP-OFDM
$N_{\mathrm{It}}^{\mathrm{FGE}}$	Number of iterations in a FGE
$N_{\mathrm{It}}^{\mathrm{outer}}$	Number of outer iterations
$N_{\mathrm{It}}^{\mathrm{sIC}}$	Number of iterations for sIC
N_{It}	Number of iterations
q	Content dependent index
R_{c}	Code rate
r	Receiving index
k'	Sub-carrier index at Rx
k	Sub-carrier index at Tx
T_{S}	Symbol interval time
T_0'	Symbol spacing in t for OQAM

T_0	Symbol spacing in t for QAM
ℓ'	Time symbol index at Rx
t	Time
ℓ	Time symbol index at Tx
$(k'F_0, \ell' T_0)$	TF grid point at Rx
$(kF_0, \ell T_0)$	TF grid point at Tx
$(0, 0)$	TF grid point at origin

Vectors and Matrices

$\mathbf{0}$	Zero matrix
$\mathbf{I}$	Identity matrix
$\mathbf{A}^{\mathsf{u},\mathrm{reduced}}$	reduced Adjacency matrix for user u
$\mathbf{A}$	Adjacency matrix
$\mathbf{D}_{\mathrm{pilots}}$	Pilot matrix
$\mathbf{e}$	Error vector
$\mathbf{F}$, $\mathbf{F}^{\mathsf{H}}$	Fourier and inverse Fourier matrix
$\mathbf{\Sigma}_{\mathbf{g}}$	Diagonal filter matrix
$\underline{\mathbf{G}}_{\mathrm{TWRC}}$	TWRC related filter matrix
$\mathbf{G}$	Filter matrix
$\underline{\mathbf{G}}_{\mathrm{GFDM}}$, $\underline{\mathbf{G}}^{\mathsf{H}}_{\mathrm{GFDM}}$	GFDM and inverse GFDM matrix
$\mathbf{G}$, $\mathbf{H}$	Generator and Parity check matrix in Chapter 2
$\mathbf{\Sigma}_{\mathbf{H},\ell',\ell}$	element ℓ, ℓ' of diagonal channel matrix
$\mathbf{\Sigma}_{\mathbf{H}}$	Diagonal channel matrix
$\overline{\mathbf{\Sigma}}_{\mathbf{H}}$	Off-diagonal channel matrix
$\mathbf{H}$	Channel matrix
$\mathbf{i}$	vector with one element equals one
$\mathbf{J}$	Interference matrix
$\mathbf{M}$	Multiple access matrix
$\mathbf{M}_{\mathrm{w}}$	Waveform matrix
$\mathbf{P}_{\mathrm{SC}}$	Permutation matrix for sub-carriers
$\mathbf{P}_{\mathrm{TS}}$	Permutation matrix for time symbols
$\mathbf{P}$	Prewithening matrix
$\mathbf{R}$	Residuum matrix
$\mathbf{S}_{\mathrm{w}}$	Waveform affected spreading matrix

$\mathbf{S}$	Spreading matrix
$\boldsymbol{\Theta}$	Spread signals
$\mathbf{T}''_{\mathrm{I,win}}$	Ramp down guard insertion matrix for w-OFDM
$\mathbf{T}'_{\mathrm{I,win}}$	Ramp up guard insertion matrix for w-OFDM
$\mathbf{T}_{\mathrm{I}}$	Guard insertion matrix
$\mathbf{T}_{\mathrm{R,win}}$	Guard removal matrix for w-OFDM
$\mathbf{T}_{\mathrm{R}}$	Guard removal matrix
$\boldsymbol{\Sigma}_{\mathrm{TO}}$	TO matrix
$\boldsymbol{\Phi}$	Sensing matrix
$\mathbf{W}_{\mathrm{conv}}$	Convolutional channel matrix
$\boldsymbol{\Omega}_{\mathrm{CFO}}$	CFO matrix

Own References

[BMWD15] C. Bockelmann, F. Monsees, M. Woltering, and A. Dekorsy, “Hardware-in-the-Loop Measurements of the Multi-Carrier Compressed Sensing Multi-User Detection (MCSM) System”, *Jahreskolloquium Kommunikation in der Automation (KommA)*, Magdeburg, November 2015.

[MWBD15a] F. Monsees, M. Woltering, C. Bockelmann, and A. Dekorsy, “A Potential Solution for MTC: Multi-Carrier Compressed Sensing Multi-User Detection”, *Conference Record - Asilomar Conference on Signals, Systems and Computers*, pp. 18–22, Pacific Grove, CA, USA, November 2015, ISBN 9781467385763.

[MWBD15b] F. Monsees, M. Woltering, C. Bockelmann, and A. Dekorsy, “Compressive Sensing Multi-User Detection for Multicarrier Systems in Sporadic Machine Type Communication”, *IEEE Vehicular Technology Conference*, Volume 2015, IEEE, Glasgow, Scotland, UK, May 2015, ISBN 9781479980888.

[MWBD15c] F. Monsees, M. Woltering, C. Bockelmann, and A. Dekorsy, “Patent: Mehrträger Compressed Sensing Multi-User System (LU92709A1)”, 2015.

[MWBD16a] F. Monsees, M. Woltering, C. Bockelmann, and A. Dekorsy, “Patent: Mehrträger Compressed Sensing Multi-User System (DE102015208344A1)”, 2016.

[MWBD16b] F. Monsees, M. Woltering, C. Bockelmann, and A. Dekorsy, “Patent: Mehrträger Compressed Sensing Multi-User System (EP3292649A1)”, 2016.

[MWBD16c] F. Monsees, M. Woltering, C. Bockelmann, and A. Dekorsy, “Patent: Multicarrier Multi-User MTC System Using Compressed Signal Sensing (WO2016177815)”, 2016.

[MWDB18a] F. Monsees, M. Woltering, A. Dekorsy, and C. Bockelmann, “Patent: Multi-Carrier Compressed Sensing Multi-User System (CN107690767A)”, 2018.

[MWDB18b] F. Monsees, M. Woltering, A. Dekorsy, and C. Bockelmann, “Patent: Multi-Carrier Compressed Sensing Multi-User System (US20180139019A1)”, 2018.

[SPS+15] M. Schellmann, P. Popovski, C. Stefanovic, H. Yomo, N. Pratas, F. Schaich, V. Braun, M. Bonomo, E. G. Gozalvez-Serrano David Ström, T. Svensson, S. Wanlu, M. Ivanov, M. Sternad, P. Weitkemper, A. Benjebbour, Y. Saito, Y. Kishiyama, M. El Hefnawy, N. He, J. Kronander, H. Lin, I. Siaud, P. Siohan, Z. Zhao, M. Schubert, E. Lähetkangas, J. Vihriälä, K. Pajukoski, G. Ascheid, S. Heinen, A. Ashok, A. Ishaque, A. Dekorsy, C. Bockelmann, M. Woltering, R. Sattiraju, L. Ji, N. Rajatheva, P. Pirinen, M. F. Bayramoglu, A. Baghdadi, F. Guilloud, and C. A. Nour, “METIS: Deliverable D2.4: Proposed Solutions for new Radio Access”, *Technical Report 1*, METIS, 2015.

[SWW+14] S. Schedler, M. Woltering, D. Wübben, V. Kühn, and A. Dekorsy, “Investigation on Gaussian Waveforms to Improve Robustness in Physical Layer Network Coding”, *18th International OFDM Workshop 2014 (InOWo’14)*, pp. 1–8, Essen, Germany, August 2014, ISBN 9783800735891.

[WLW+14] M. Wu, F. Ludwig, M. Woltering, D. Wübben, A. Dekorsy, and S. Paul, “Analysis and Implementation for Physical-Layer Network Coding with Carrier Frequency Offset”, *18th International ITG Workshop on Smart Antennas (WSA)*, pp. 1–8, Erlangen, Germany, March 2014, ISBN 9783800735846.

[WMBD16] M. Woltering, F. Monsees, C. Bockelmann, and A. Dekorsy, “Multi-Carrier Compressed Sensing Multi-User Detection System: A Practical Verification”, *19th International Conference on OFDM and Frequency Domain Techniques (ICOF 2016)*, Essen, Germany, August 2016.

[WSW+16] M. Woltering, S. Schedler, D. Wübben, A. Dekorsy, and V. Kühn, “Generalized Multi-Carrier Waveforms in Two-Way Relay Systems”, W. Utschick (Editor), *Communications in Interference-Limited Networks*, pp. 475–499, Springer International Publishing, Berlin, Germany, February 2016.

[WWD+13] M. Woltering, D. Wübben, A. Dekorsy, V. Braun, and U. Doetsch, “Performance of HARQ with Reduced Size Retransmissions using Network Coding Principles”, *IEEE Vehicular Technology Conference*, pp. 1–6, IEEE, Dresden, Germany, June 2013, ISBN 9781467363372.

[WWD+14] M. Woltering, D. Wübben, A. Dekorsy, V. Braun, and U. Doetsch, “Link Level Performance Assessment of Reliability-Based HARQ Schemes in LTE”, *2014 IEEE 79th Vehicular Technology Conference (VTC Spring)*, January, pp. 1–5, IEEE, Dresden, Germany, May 2014, ISBN 978-1-4799-4482-8.

[WWD15a] M. Woltering, D. Wübben, and A. Dekorsy, “Physical Layer Network Coding with Gaussian Waveforms using Soft Interference Cancellation”, *IEEE Vehicular Technology Conference*, Volume 2015, pp. 0–4, Glasgow, Scotland, UK, May 2015, ISBN 9781479980888.

[WWD$^+$15b] M. Woltering, D. Wübben, A. Dekorsy, S. Schedler, and V. Kühn, “Physical Layer Network Coding Using Gaussian Waveforms: A Link Level Performance Analysis”, *10th International ITG Conference on Systems, Communications and Coding (SCC 2015)*, pp. 1–6, Hamburg, Germany, February 2015, ISBN 9783800736591.

[WWD16] M. Woltering, D. Wübben, and A. Dekorsy, “Factor Graph based Equalizer for Two Way Relaying Channels with General Waveforms”, *20th International ITG Workshop on Smart Antennas*, Volume 2, pp. 429–436, Munich, Germany, March 2016, ISBN 9783800741779.

[WWD18] M. Woltering, D. Wübben, and A. Dekorsy, “Factor Graph-Based Equalization for Two-Way Relaying With General Multi-Carrier Transmissions”, *IEEE Transactions on Wireless Communications*, Volume 17, No. 2, pp. 1212–1225, February 2018.

[WZWD16] M. Woltering, M. Zhang, D. Wübben, and A. Dekorsy, “Comparison of General Multi-Carrier Schemes in Two Way Relaying Channels”, *20th International ITG Workshop on Smart Antennas*, 1, pp. 1–6, Munich, Germany, March 2016, ISBN 9783800741779.

Bibliography

[3GP11] 3GPP, “TS 136 101 - V8.2.0 - LTE; Evolved Universal Terrestrial Radio Access (E-UTRA); User Equipment (UE) radio transmission and reception (3GPP TS 36.101 version 8.2.0 Release 8)”, *Technical report*, 3GPP, June 2011.

[3GP13] 3GPP, “Study on Provision of low-cost MTC UEs based on LTE; Release 11”, *Technical Report Release 12*, 3GPP, November 2013.

[3GP17] 3GPP, “3GPP TR 21.900 V13.2.0 (2017-06): 3rd Generation Partnership Project; Technical Specification Group Services and System Aspects; Technical Specification Group working methods (Release 13) The”, *Technical Report Release 13*, 3GPP, June 2017.

[3GP18] 3GPP, “3GPP TR 21.915 V0.0.1 (2018-03): 3rd Generation Partnership Project; Technical Specification Group Services and System Aspects; Release 15 Description; Summary of Rel-15 Work Items (Release 15)”, *Technical Report Release 15*, 3GPP, March 2018.

[3GP19] 3GPP, “TR 21.915 V1.0.0 (2019-03): 3rd Generation Partnership Project; Technical Specification Group Services and System Aspects; Release 15 Description; Summary of Rel-15 Work Items (Release 15)”, *Technical Report Release 15*, 3GPP, March 2019.

[Abr70] N. Abramson, “The ALOHA System - Another alternative for computer communications”, *Proceedings of the November 17-19, 1970, fall joint computer conference on - AFIPS ’70 (Fall)*, Volume 37, p. 281, New York, NY, USA, November 1970.

[ACC$^+$07] A. Anastasopoulos, K. M. Chugg, G. Colavolpe, G. Ferrari, and R. Raheli, “Iterative Detection for Channels With Memory”, *Proceedings of the IEEE*, Volume 95, No. 6, pp. 1272–1294, June 2007.

[ACLY00] R. Ahlswede, N. Cai, S.-Y. R. Li, and R. W. Yeung, “Network Information Flow”, *IEEE Transactions on Information Theory*, Volume 46, No. 4, pp. 1204–1216, July 2000.

[AFRFB15] A. Aminjavaheri, A. Farhang, A. RezazadehReyhani, and B. Farhang-Boroujeny, “Impact of Timing and Frequency Offsets on Multicarrier

Waveform Candidates for 5G", *2015 IEEE Signal Processing and Signal Processing Education Workshop (SP/SPE)*, pp. 178–183, IEEE, Salt Lake City, UT, USA, August 2015, ISBN 978-1-4673-9169-6.

[BCJR74] L. R. Bahl, J. Cocke, F. Jelinek, and J. Raviv, "Optimal Decoding of Linear Codes for Minimizing Symbol Error Rate", *IEEE Transactions on Information Theory*, Volume 20, No. 2, pp. 284–287, March 1974.

[BD74] M. Bellanger and J. Daguet, "TDM-FDM Transmultiplexer: Digital Polyphase and FFT", *IEEE Transactions on Communications*, Volume 22, No. 9, pp. 1199–1205, September 1974.

[BD12] U. Bhat and T. M. Duman, "Decoding Strategies for Physical-Layer Network Coding over Frequency Selective Channels", *2012 IEEE Wireless Communications and Networking Conference (WCNC)*, pp. 12–17, IEEE, Paris, France, April 2012, ISBN 978-1-4673-0437-5.

[Bel02] M. Bellanger, "Specification and Design of a Prototype Filter for Filter Bank based Multicarrier Transmission", *2001 IEEE International Conference on Acoustics, Speech, and Signal Processing. Proceedings (Cat. No.01CH37221)*, pp. 2417–2420, IEEE, Salt Lake City, UT, USA, May 2002, ISBN 0-7803-7041-4.

[Bel10] M. Bellanger, "FBMC Physical Layer: A Primer", *Technical report*, PHYDYAS, 2010.

[Bel12] M. Bellanger, "FS-FBMC: An Alternative Scheme for Filter Bank Based Multicarrier Transmission", *5th International Symposium on Communications Control and Signal Processing, ISCCSP 2012*, pp. 1–4, IEEE, Rom, Italy, May 2012, ISBN 9781467302760.

[Ber74] E. R. Berlekamp, *Key Papers in the Developement of Coding Theory*, Taylor & Francis, 1974, ISBN 978-0879420314.

[BGT93] C. Berrou, A. Glavieux, and P. Thitimajshima, "Near Shannon Limit Error-Correcting Coding and Decoding: Turbo-Codes. 1", *ICC '93 - IEEE International Conference on Communications*, Volume 2, pp. 1064–1070, IEEE, Geneva, Switzerland, May 1993, ISBN 0-7803-0950-2.

[BKA04] S. ten Brink, G. Kramer, and A. Ashikhmin, "Design of Low-Density Parity-Check Codes for Modulation and Detection", *IEEE Transactions on Communications*, Volume 52, No. 4, pp. 670–678, April 2004.

[BMN11] L. G. Baltar, A. Mezghani, and J. A. Nossek, "A Method to Convert Near-Perfect into Perfect Reconstruction FIR Prototype Filters for Modulated Filter Banks", *Proceedings - IEEE International Symposium on Circuits and Systems*, pp. 1768–1771, Rio de Janeiro, Brazil, May 2011, ISBN 9781424494736.

[BN10] Q. Bai and J. A. Nossek, "On the Effects of Carrier Frequency Offset on Cyclic Prefix based OFDM and Filter Bank based Multicarrier

Systems", *IEEE Workshop on Signal Processing Advances in Wireless Communications, SPAWC*, Marrakech, Morocco, June 2010, ISBN 9781424469901.

[BN12] L. G. Baltar and J. A. Nossek, "Multicarrier Systems: A Comparison between Filter Bank based and Cyclic Prefix based OFDM", *OFDM 2012, 17th International OFDM Workshop 2012 (InOWo'12)*, pp. 1–5, Essen, Germany, August 2012.

[BPN$^+$16] C. Bockelmann, N. Pratas, H. Nikopour, K. Au, T. Svensson, C. Stefanovic, P. Popovski, and A. Dekorsy, "Massive Machine-type Communications in 5G: Physical and MAC layer Solutions", *IEEE Communications Magazine*, Volume 54, No. 9, pp. 1–13, September 2016.

[BPW$^+$18] C. Bockelmann, N. K. Pratas, G. Wunder, S. Saur, M. Navarro, D. Gregoratti, G. Vivier, E. de Carvalho, Y. Ji, C. Stefanovic, P. Popovski, Q. Wang, M. Schellmann, E. Kosmatos, P. Demestichas, M. Raceala-Motoc, P. Jung, S. Stanczak, and A. Dekorsy, "Towards Massive Connectivity Support for Scalable mMTC Communications in 5G networks", *IEEE Access*, Volume 6, pp. 1–20, April 2018.

[BSD13] C. Bockelmann, H. F. Schepker, and A. Dekorsy, "Compressive Sensing based Multi-User Detection for Machine-to-Machine Communication", *Transactions on Emerging Telecommunications Technologies*, Volume 24, No. 4, pp. 389–400, June 2013.

[CG05] G. Colavolpe and G. Germi, "On the Application of Factor Graphs and the Sum-Product Algorithm to ISI Channels", *IEEE Transactions on Communications*, Volume 53, No. 5, pp. 818–825, May 2005.

[Cha66] R. W. Chang, "Synthesis of Band-Limited Orthogonal Signals for Multichannel Data Transmission", *Bell System Technical Journal*, Volume 45, No. 10, pp. 1775–1796, December 1966.

[Cis19] Cisco, "Cisco Visual Networking Index (VNI) Global Mobile Data Traffic", *Technical report*, Cisco, 2019.

[Col06] G. Colavolpe, "On LDPC Codes over Channels with Memory", *IEEE Transactions on Wireless Communications*, Volume 5, No. 7, pp. 1757–1766, July 2006.

[CREKD05] S. F. Cotter, B. D. Rao, K. Engan, and K. Kreutz-Delgado, "Sparse Solutions to Linear Inverse Problems with Multiple Measurement Vectors", *IEEE Transactions on Signal Processing*, Volume 53, No. 7, pp. 2477–2488, July 2005.

[Cro80] R. Crochiere, "A Weighted Overlap-Add Method of Short-Time Fourier analysis/Synthesis", *IEEE Transactions on Acoustics, Speech, and Signal Processing*, Volume 28, No. 1, pp. 99–102, February 1980.

[CT05] E. Candes and T. Tao, "Decoding by Linear Programming", *IEEE Transactions on Information Theory*, Volume 51, No. 12, pp. 4203–4215, December 2005.

[CT06] E. J. Candes and T. Tao, “Near-Optimal Signal Recovery from Random Projections: Universal Encoding strategies?”, *IEEE Transactions on Information Theory*, Volume 52, No. 12, pp. 5406–5425, November 2006.

[CW10] Y. Chen and W. Wang, “Machine-to-Machine communication in LTE-A”, *2010 IEEE 72nd Vehicular Technology Conference - Fall (VTC2010)*, pp. 0–3, Ottawa, Canada, October 2010, ISBN 9781424435746.

[CY09] M. Chen and A. Yener, “Multiuser Two-Way Relaying: Detection and Interference Management Strategies”, *IEEE Transactions on Wireless Communications*, Volume 8, No. 8, pp. 4296–4305, August 2009.

[Dau90] I. Daubechies, “The Wavelet Transform, Time-Frequency Localization and Signal Analysis”, *IEEE Transactions on Information Theory*, Volume 36, No. 5, pp. 961–1005, September 1990.

[DBCK14] J.-B. Doré, V. Berg, N. Cassiau, and D. Kténas, “FBMC Receiver for Multi-User Asynchronous Transmission on Fragmented Spectrum”, *EURASIP Journal on Advances in Signal Processing*, Volume 2014, No. 1, p. 41, December 2014.

[Dek01] A. Dekorsy, *Kanakodierungskonzepte für Mehrträger-Codemultiplex in Mobilfunksystemen*, Ph.d. thesis, University of Bremen, January 2001.

[DFKH11] R. Datta, G. Fettweis, Z. Kollár, and P. Horváth, “FBMC and GFDM Interference Cancellation Schemes for Flexible Digital Radio PHY Design”, *2011 14th Euromicro Conference on Digital System Design*, pp. 335–339, IEEE, Oulu, Finland, August 2011, ISBN 978-1-4577-1048-3.

[DH01] D. L. Donoho and X. Huo, “Uncertainty Principle and Ideal Atomic Decompositions”, *IEEE Transactions on Information Theory*, Volume 47, No. 7, pp. 2845–2862, 2001.

[DM88] A. Dembo and D. Malah, “Signal Synthesis from Modified Discrete Short-Time Transform”, *IEEE Transactions on Acoustics, Speech, and Signal Processing*, Volume 36, No. 2, pp. 168–181, February 1988.

[DPS18] E. Dahlmann, S. Parkvall, and J. Skold, *5G NR: the Next Generation Wireless Access Technology*, Academic Press, August 2018, ISBN 978-0128143230.

[DS07a] R. J. Drost and A. C. Singer, “Factor-Graph Algorithms for Equalization”, *IEEE Transactions on Signal Processing*, Volume 55, No. 5, pp. 2052–2065, May 2007.

[DS07b] J. Du and S. Signell, “Comparison of CP-OFDM and OFDM/OQAM in Doubly Dispersive Channels.”, *Future Generation Communication* *and Networking (FGCN 2007)*, pp. 1–5, Jeju, South Korea, December 2007, ISBN 0-7695-3048-6.

[DS07c] J. Du and S. Signell, “Time Frequency Localization of Pulse Shaping Filters in OFDM / OQAM Systems”, *Time*, 2007.

[DS08] J. Du and S. Signell, “Pulse Shape Adaptivity in OFDM/OQAM Systems”, *Proceedings of the 2008 International Conference on Advanced Infocomm Technology - ICAIT ’08*, pp. 1–5, Shenzhen, China, July 2008, ISBN 9781605580883.

[Du08] J. Du, *Pulse Shape Adaptation and Channel Estimation in Generalised Frequency Division Multiplexing Systems*, Ph.D. Thesis, KTH, School of Information and Communication Technology, December 2008.

[EK12] Y. C. Eldar and G. Kutyniok (Editors), *Compressed Sensing: Theory and Applications*, Cambridge University Press, Cambridge, 2012, ISBN 9780511794308.

[ETS14] ETSI EN 302 307-1, “Digital Video Broadcasting (DVB); Second Generation Framing Structure, Channel Coding and Modulation Systems for Broadcasting, Interactive Services, News Gathering and Other Broadband Satellite Applications; Part 1: DVB-S2”, *Technical report*, ETSI, November 2014.

[ETS15] ETSI EN 302 755, “Digital Video Broadcasting (DVB); Frame structure Channel Coding and Modulalation for a Second Generation Digital Terrestrialial Television Broroadcasting System (DVB-T2)”, *Technical report*, ETSI, July 2015.

[FB11] B. Farhang-Boroujeny, “OFDM versus Filter Bank Multicarrier”, *IEEE Signal Processing Magazine*, Volume 28, No. 3, pp. 92–112, April 2011.

[FB14] B. Farhang-Boroujeny, “Filter Bank Multicarrier Modulation: A Waveform Candidate for 5G and Beyond”, *Advances in Electrical Engineering*, Volume 2014, pp. 1–25, December 2014.

[FBM15] B. Farhang-Boroujeny and H. Moradi, “Derivation of GFDM based on OFDM Principles”, *IEEE International Conference on Communications*, Volume 2015-Septe, pp. 2680–2685, London, UK, September 2015, ISBN 9781467364324.

[FBY10] B. Farhang-Boroujeny and C. H. Yuen, “Cosine Modulated and Offset QAM Filter Bank Multicarrier Techniques: A Continuous-Time Prospect”, *EURASIP Journal on Advances in Signal Processing*, Volume 2010, No. May 2011, pp. 1–17, May 2010.

[FFK+11] Z. M. Fadlullah, M. M. Fouda, N. Kato, A. Takeuchi, N. Iwasaki, and Y. Nozaki, “Toward Intelligent Machine-to-Machine Communications in Smart Grid”, *IEEE Communications Magazine*, Volume 49, No. 4, pp. 60–65, April 2011.

[FK00] K. Fazel and S. Kaiser, “Multi-Carrier Spread Spectrum”, *European Transactions on Telecommunications*, Volume 11, No. 6, pp. 523–526, November 2000.

[FK08] K. Fazel and S. Kaiser, *Multi-Carrier and Spread Spectrum Systems*, John Wiley & Sons, Ltd, Chichester, UK, October 2008, ISBN 9780470714249.

[FKB09] G. Fettweis, M. Krondorf, and S. Bittner, “GFDM - Generalized Frequency Division Multiplexing”, *Vehicular Technology Conference, 2009. VTC Spring 2009. IEEE 69th*, pp. 1–4, Barcelona, Spain, 2009, ISBN 9781424425174.

[Fli94] N. J. Fliege, *Multirate Digital Signal Processing: Multirate Systems, Filter Banks, Wavelets*, John Wiley & Sons, Inc., New York, NY, USA, 1994, ISBN 0471939765.

[For72a] G. Forney, “Lower Bounds on Error Probability in the Presence of Large Intersymbol Interference”, *IEEE Transactions on Communications*, Volume 20, No. February, pp. 76–77, February 1972.

[For72b] G. Forney, “Maximum-likelihood sequence estimation of digital sequences in the presence of intersymbol interference”, *IEEE Transactions on Information Theory*, Volume 18, No. 3, pp. 363–378, May 1972.

[For73] G. D. J. Forney, “The Viterbi Algorithm”, *Proceedings of the IEEE*, Volume 61, No. 3, pp. 268–278, March 1973.

[For01] G. D. J. Forney, “Codes on Graphs: Normal Realizations”, *IEEE Transactions on Information Theory*, Volume 47, No. 2, pp. 520–548, February 2001.

[FPT08] T. Fusco, A. Petrella, and M. Tanda, “Sensitivity of Multi-User Filter-Bank Multicarrier Systems to Synchronization Errors”, *2008 3rd International Symposium on Communications, Control and Signal Processing*, pp. 393–398, IEEE, March 2008, ISBN 978-1-4244-1687-5.

[FR13] S. Foucart and H. Rauhut, *A Mathematical Introduction to Compressive Sensing*, Applied and Numerical Harmonic Analysis, Springer New York, New York, NY, 2013, ISBN 978-0-8176-4947-0.

[Fri95] B. Friedrichs, *Kanalcodierung*, Springer Berlin Heidelberg, Berlin, Germany, 1995, ISBN 3540593535.

[Fro16] J.-P. Fromm, *Analyse von Multi-Carrier Compressive Sensing basierter Multi-User Detection mit Zeit-Offsets*, Bachelor thesis, University of Bremen, February 2016.

[FZCC16] C. Fangyu, M. Zhao, Y. Cai, and B. Champagne, “Low-complexity factor-graph-based MAP detector for filter bank multicarrier systems”, *Journal of Communications and Information Networks*, Volume 1, No. 3, pp. 10–22, October 2016.

[Gab46] D. Gabor, "Theory of Communication. Part 1: The Analysis of Information", *Analysis*, Volume 93, No. 26, pp. 429–441, November 1946.

[Gal62] R. G. Gallager, "Low-Density Parity-Check Codes", *IRE Transactions on Information Theory*, Volume 8, No. 1, pp. 21–28, January 1962.

[GMM+15] I. Gaspar, M. Matthe, N. Michailow, L. Leonel Mendes, D. Zhang, and G. Fettweis, "Frequency-Shift Offset-QAM for GFDM", *IEEE Communications Letters*, Volume 19, No. 8, pp. 1454–1457, August 2015.

[GMN+13] I. Gaspar, N. Michailow, A. Navarro, E. Ohlmer, S. Krone, and G. Fettweis, "Low Complexity GFDM Receiver Based on Sparse Frequency Domain Processing", *2013 IEEE 77th Vehicular Technology Conference (VTC Spring)*, pp. 1–6, IEEE, Dresden, Germany, June 2013, ISBN 978-1-4673-6337-2.

[GP08] Q. Guo and L. Ping, "LMMSE Turbo Equalization based on Factor Graphs", *IEEE Journal on Selected Areas in Communications*, Volume 26, No. 2, pp. 311–319, February 2008.

[Gro16] B. S. I. Group, "Bluetooth Core Specification v5.0", *Technical report*, Bluetooth Special Interest Group, December 2016.

[HB94] R. Haas and J.-C. Belfiore, "Multiple Carrier Transmission with Time-Frequency Well-Localized Impulses", *IEEE Second Symposium on Communications and Vehicular Technology in the Benelux*, 2, pp. 187–193, Univ. Catholique de Louvain, Louvain la Neuve, Belgium, 1994, ISBN VO -.

[HB97] R. Haas and J.-C. Belfiore, "A Time-Frequency Well-localized Pulse for Multiple Carrier Transmission", *Journal of Wireless Personal Communications*, Volume 5, No. 1, pp. 1–18, May 1997.

[HD08] J. Hu and T. M. Duman, "Graph-Based Detection Algorithms for Layered Space-Time Architectures", *IEEE Journal on Selected Areas in Communications*, Volume 26, No. 2, pp. 269–280, February 2008.

[HEA05] X.-Y. Hu, E. Eleftheriou, and D. Arnold, "Regular and Irregular Progressive Edge-Growth Tanner Graphs", *IEEE Transactions on Information Theory*, Volume 51, No. 1, pp. 386–398, January 2005.

[Hei27] W. Heisenberg, "Über den anschaulichen Inhalt der quantentheoretischen Kinematik und Mechanik", *Zeitschrift für Physik*, Volume 43, No. 3-4, pp. 172–198, March 1927.

[Hek13] M. Hekrdla, *Design of Modulations for Wireless (Physical-Layer) Network Coding*, Ph.D. Thesis, Czech Technical University in Prague, November 2013.

[HHS86] B. Hirosaki, S. Hasegawa, and A. Sabato, “Advanced Groupband Data Modem Using Orthogonally Multiplexed QAM Technique”, *IEEE Transactions on Communications*, Volume 34, No. 6, pp. 587–592, June 1986.

[Hir81] B. Hirosaki, “An Orthogonally Multiplexed QAM System Using the Discrete Fourier Transform”, *IEEE Transactions on Communications*, Volume 29, No. 7, pp. 982–989, July 1981.

[HLL14] I. W.-h. Ho, S.-C. Liew, and L. Lu, “Feasibility Study of Physical-Layer Network Coding in 802.11p VANETs”, *IEEE International Symposium on Information Theory (ISIT)*, Ici, pp. 646–650, Honolulu, HI, USA, 2014, ISBN 9781479951864.

[HS11] M. Hekrdla and J. Sykora, “Uniformly Most Powerful Alphabet for HDF Two-Way Relaying Designed by Non-Linear Optimization Tools”, *International Symposium on Wireless Communication Systems*, pp. 594–598, IEEE, Aachen, Germany, November 2011, ISBN 9781612844022.

[HSL17] S. Han, Y. Sung, and Y. H. Lee, “Filter Design for Generalized Frequency-Division Multiplexing”, *IEEE Transactions on Signal Processing*, Volume 65, No. 7, pp. 1644–1659, 2017.

[HT11] H. Holma and A. Toskala, *LTE for UMTS: Evolution to LTE-Advanced*, Wiley Publishing, 2nd Edition, 2011.

[HTH11] C.-W. Huang, P.-A. Ting, and C.-C. Huang, “A Novel Message Passing Based MIMO-OFDM Data Detector with a Progressive Parallel ICI Canceller”, *IEEE Transactions on Wireless Communications*, Volume 10, No. 4, pp. 1260–1268, April 2011.

[HV02] B. Hassibi and H. Vikalo, “On the Expected Complexity of Integer Least-Squares Problems”, *IEEE International Conference on Acoustics, Speech, and Signal Processing*, Volume 2, pp. II–1497–II–1500, Orlando, FL, USA, May 2002, ISBN 0-7803-7402-9.

[HWC$^+$17] X. He, F. Wang, X. Chen, D. Miao, and Z. Zhao, “Non-Orthogonal Waveforms for Machine Type Communication”, *2017 32nd General Assembly and Scientific Symposium of the International Union of Radio Science, URSI GASS 2017*, August, pp. 1–4, Montreal, QC, Canada, August 2017, ISBN 9789082598704.

[HZ11] J. Huang and S. Zhou, “Turbo Equalization for OFDM Modulated Physical Layer Network Coding”, *IEEE 12th International Workshop on Signal Processing Advances in Wireless Communications*, pp. 291–295, IEEE, San Francisco, CA, USA, June 2011, ISBN 978-1-4244-9333-3.

[IEE06] IEEE, “802.16e - IEEE Standard for Local and Metropolitan Area Networks Part 16: Amendment 2: Physical and Medium Access Control Layers for Combined Fixed and Mobile Operation in Licensed Bands”, *Technical Report February*, IEEE, February 2006.

[IEE09] IEEE, "802.11n - IEEE Standard for Local and Metropolitan Area Networks - Specific Requirements - Part 11: Wireless LAN Medium Access Control (MAC) and Physical Layer (PHY) Specifications - Amendment 5: Enhancements for Higher Throughput", *Technical report*, IEEE, October 2009.

[IEE12] IEEE, "IEEE Standard 802.11-2012 for Information technology–Telecommunications and Information Exchange Between Systems Local and Metropolitan Area Networks–Specific Requirements Part 11: Wireless LAN Medium Access Control (MAC) and Physical Layer (PHY) Specif", *Technical Report March*, IEEE, March 2012.

[IVS$^+$09] T. Ihalainen, A. Viholainen, T. H. Stitz, M. Renfors, and M. Bellanger, "Filter Bank Based Multi-Mode Multiple Access Scheme for Wireless Uplink", *European Signal Processing Conference*, Eusipco, pp. 1354–1358, Glasgow, Scotland, April 2009.

[JBD15] Y. Ji, C. Bockelmann, and A. Dekorsy, "Compressed Sensing Based Multi-User Detection with Modified Sphere Detection in Machine-to-Machine Communications", *SCC 2015; 10th International ITG Conference on Systems, Communications and Codingnce on Systems, Communications and Coding*, 1, pp. 1–6, Hamburg, Germany, March 2015, ISBN 9783800736591.

[JK16] W. Jiang and T. Kaiser, "From OFDM to FBMC: Principles and Comparisons", *Signal Processing for 5G: Algorithms and Implementations*, Chapter 3, pp. 47–66, John Wiley & Sons, Ltd, Chichester, UK, August 2016, ISBN 9781119116493.

[JKL$^+$16] H. Ji, Y. Kim, J. Lee, E. Onggosanusi, Y. Nam, J. Zhang, B. Lee, and B. Shim, "Overview of Full-Dimension MIMO in LTE-Advanced Pro", *IEEE Communications Magazine*, Volume 55, No. 2, pp. 176 – 184, October 2016.

[Kab03] Y. Kabashima, "A CDMA Multiuser Detection Algorithm on the Basis of Belief Propagation", *Journal of Physics A Mathematical and General*, Volume 36, No. 43, pp. 11111–11121, October 2003.

[Kai98] S. Kaiser, *Multi-carrier CDMA Mobile Radio Systems: Analysis and Optimization of Detection, Decoding, and Channel Estimation*, Ph.d. thesis, University of Kaiserslautern, January 1998.

[Kai02] S. Kaiser, "OFDM Code-Division Multiplexing in Fading Channels", *IEEE Transactions on Communications*, Volume 50, No. 8, pp. 1266–1273, August 2002.

[KD18] K.-D. Kammeyer and A. Dekorsy, *Nachrichtenübertragungstechnik*, Springer Vieweg, Wiesbaden, Germany, 6th Edition, December 2018, ISBN 978-3-658-17004-2.

[KDK05] M. Kaynak, T. Duman, and E. Kurtas, "Belief Propagation over MIMO Frequency Selective Fading Channels", *Joint International*

Conference on Autonomic and Autonomous Systems and International Conference on Networking and Services - (ICAS-ISNS'05), pp. 1367–1371, IEEE, Papeete, Tahiti, French Polynesia, October 2005.

[KDK07] M. Kaynak, T. Duman, and E. Kurtas, "Belief Propagation over SISO/MIMO Frequency Selective Fading Channels", *IEEE Transactions on Wireless Communications*, Volume 6, No. 6, pp. 2001–2005, June 2007.

[KFL01] F. R. Kschischang, B. J. Frey, and H.-A. Loeliger, "Factor Graphs and the Sum-Product Algorithm", *IEEE Transactions on Information Theory*, Volume 47, No. 2, pp. 498–519, February 2001.

[KK18] K.-D. Kammeyer and K. Kroschel, *Digitale Signalverarbeitung - Filterung und Spektralanalyse mit MATLAB-Übungen*, Springer Vieweg, Wiesbaden, Germany, 9th Edition, April 2018, ISBN 978-3-6582-0134-0.

[KM98] W. Kozek and A. Molisch, "Nonorthogonal Pulseshapes for Multicarrier Communications in Doubly Dispersive Channels", *IEEE Journal on Selected Areas in Communications*, Volume 16, No. 8, pp. 1579–1589, October 1998.

[KRS18] M. Krätzig, L. Rauchhaupt, and D. Schulze, "Validierung Kognitiver Mediumszugangsalgorithmen für Industrielle Funkanwendungen", *Kommunikation und Bildverarbeitung in der Automation*, pp. 85–96, Springer Berlin Heidelberg, Berlin, Heidelberg, 2018, ISBN 978-3-662-55232-2.

[LAB95] B. Le Floch, M. Alard, and C. Berrou, "Coded Orthogonal Frequency Division Multiplex", *Proceedings of the IEEE*, Volume 83, No. 6, pp. 982–996, June 1995.

[LCL11] S. Y. Lien, K. C. Chen, and Y. Lin, "Toward Ubiquitous Massive Accesses in 3GPP Machine-to-Machine Communications", *IEEE Communications Magazine*, Volume 49, No. 4, pp. 66–74, April 2011.

[Len16] F. Lenkeit, *IDMA-based Relaying for Future Mobile Communication Systems*, Ph.D. Thesis, University of Bremen, March 2016.

[LKK08] J. Luo, W. Keusgen, and A. Kortke, "Optimization of Time Domain Windowing and Guardband Size for Cellular OFDM Systems", *IEEE Vehicular Technology Conference*, pp. 1–5, Calgary, BC, Canada, October 2008, ISBN 9781424417223.

[LKK14] J. Luo, A. Kortke, and W. Keusgen, "Guardband Optimization for Cellular Systems Applying Raised Cosine Windowed OFDM", *Wireless Personal Communications*, Volume 78, No. 2, pp. 1375–1390, September 2014.

[LL12] L. Lu and S.-C. Liew, "Asynchronous Physical-Layer Network Coding", *IEEE Transactions on Wireless Communications*, Volume 11, No. 2, pp. 819–831, February 2012.

[LLZ15] S.-C. Liew, L. Lu, and S. Zhang, “A Primer on Physical-Layer Network Coding”, *Synthesis Lectures on Communication Networks*, Volume 8, No. 1, pp. 1–218, June 2015.

[Loe03] H.-A. Loeliger, “Some Remarks on Factor Graphs”, *Proc. 3rd International Symposium on Turbo Codes and Related Topics*, 3, pp. 111—-115, Brest, France, 2003.

[Loe04] H.-A. Loeliger, “An Introduction to Factor Graphs”, *IEEE Signal Processing Magazine*, Volume 21, No. 1, pp. 28–41, January 2004.

[LW10] Y. Lang and D. Wübben, “Generalized Joint Channel Coding and Physical Network Coding for Two-Way Relay Systems”, *Vehicular Technology Conference (VTC 2010-Spring), 2010 IEEE 71st*, pp. 1–5, IEEE, Taipei, Taiwan, May 2010, ISBN 978-1-4244-2518-1.

[LWK10] Y. Lang, D. Wubben, and K.-D. Kammeyer, “An Improved Physical Layer Network Coding Scheme for Two-Way Relay Systems”, *2010 International ITG Workshop on Smart Antennas (WSA)*, WSA, pp. 107–114, IEEE, Bremen, Germany, February 2010, ISBN 978-1-4244-6070-0.

[LWLZ13] L. Lu, T. Wang, S.-C. Liew, and S. Zhang, “Implementation of Physical-Layer Network Coding”, *Physical Communication*, Volume 6, pp. 74–87, March 2013.

[LYN03] S.-Y. Li, R. Yeung, and Ning Cai, “Linear Network Coding”, *IEEE Transactions on Information Theory*, Volume 49, No. 2, pp. 371–381, February 2003.

[LYWM05] B. Lu, G. Yue, X. Wang, and M. Madihian, “Factor-Graph-Based Soft Self-Iterative Equalizer for Multipath Channels”, *Eurasip Journal on Wireless Communications and Networking*, Volume 2005, No. 2, pp. 187–196, December 2005.

[LZ16] F.-L. Luo and C. J. Zhang (Editors), *Signal Processing for 5G: Algorithms and Implementations*, John Wiley & Sons, Ltd, Chichester, UK, October 2016, ISBN 9781119116493.

[LZL13] S.-C. Liew, S. Zhang, and L. Lu, “Physical-Layer Network Coding: Tutorial, Survey, and Beyond”, *Physical Communication*, Volume 6, pp. 4–42, March 2013.

[MA15] R. N. Mitra and D. P. Agrawal, “5G Mobile Technology: A Survey”, *ICT Express*, Volume 1, No. 3, pp. 132–137, 2015.

[Mar98] K. W. Martin, “Small Side-Lobe Filter Design for Multitone Data-Communication Applications”, *IEEE Transactions on Circuits and Systems II: Analog and Digital Signal Processing*, Volume 45, No. 8, pp. 1155–1161, August 1998.

[Mat98] K. Matheus, *Generalized Coherent Multicarrier Systems for Mobile Communications*, Ph.D. Thesis, University of Bremen, Germany, December 1998.

[MBD14] F. Monsees, C. Bockelmann, and A. Dekorsy, “Reliable Activity Detection for Massive Machine to Machine Communication via Multiple Measurement Vector Compressed Sensing”, *IEEE Globecom Workshops, GC Workshops*, pp. 1057–1062, Austin, TX, USA, December 2014, ISBN 9781479974702.

[MBD15] F. Monsees, C. Bockelmann, and A. Dekorsy, “Compressed Sensing Neyman-Pearson Based Activity Detection for Sparse Multiuser Communications”, *SCC 2015; 10th International ITG Conference on Systems, Communications and Coding*, pp. 1–6, Hamburg, Germany, February 2015, ISBN 9783800736591.

[MBH13] G. Matz, H. Bolcskei, and F. Hlawatsch, “Time-Frequency Foundations of Communications: Concepts and Tools”, *IEEE Signal Processing Magazine*, Volume 30, No. 6, pp. 87–96, November 2013.

[MBWD12] F. Monsees, C. Bockelmann, D. Wübben, and A. Dekorsy, “Sparsity Aware Multiuser Detection for Machine to Machine Communication”, *2012 IEEE Globecom Workshops*, pp. 1706–1711, Anaheim, CA, USA, March 2012, ISBN 9781467349413.

[MGK$^+$12] N. Michailow, I. Gaspar, S. Krone, M. Lentmaier, and G. Fettweis, “Generalized Frequency Division Multiplexing: Analysis of an Alternative Multi-Carrier Technique for Next Generation Cellular Systems”, *International Symposium on Wireless Communication Systems (ISWCS)*, pp. 171–175, IEEE, Paris, France, August 2012, ISBN 978-1-4673-0762-8.

[MH03] G. Matz and F. Hlawatsch, “Random Processes and Noise Analysis”, *Time Frequency Analysis*, Chapter 9, pp. 371–419, Elsevier Science, Oxford, 2003, ISBN 9780080443355.

[MH11] G. Matz and F. Hlawatsch, “Fundamentals of Time-Varying Communication Channels”, *Wireless Communications Over Rapidly Time-Varying Channels*, Chapter 1, pp. 1–63, Academic Press, Oxford, 2011, ISBN 9780123744838.

[MHMR18] A. Morgado, K. M. S. Huq, S. Mumtaz, and J. Rodriguez, “A Survey of 5G Technologies: Regulatory, Standardization and Industrial Perspectives”, *Digital Communications and Networks*, Volume 4, No. 2, pp. 87–97, 2018.

[Mic15] N. Michailow, *Generalized Frequency Division Multiplexing Transceiver Principles*, Ph.d. thesis, University of Dresden, October 2015.

[Min15] Z. Ming, *Comparison of Multi-Carrier Schemes with General Waveforms in Two-Way Relaying Channel*, Master thesis, University of Bremen, October 2015.

[MK97] K. Matheus and K.-D. Kammeyer, “Optimal Design of a Multicarrier Systems with Soft Impulse Shaping Including Equalization in Time or Frequency Direction", *GLOBECOM 97. IEEE Global Telecommunications Conference.*, pp. 310–314, Phoenix, AZ, USA, November 1997, ISBN 0780341988.

[MKFK98] K. Matheus, K. Knoche, M. Feuersanger, and K.-D. Kammeyer, "Two-Dimensional (Recursive) Channel Equalization for Multicarrier Systems with Soft Impulse Shaping (MCSIS)", *The Bridge to Global Integration. Global Telecommunications Conference (GLOBECOM 1998)*, Volume 2, pp. 956–961, IEEE, Sidney, Australia, November 1998, ISBN 0-7803-4984-9.

[MKT99] K. Matheus, K.-D. Kammeyer, and U. Tuisel, "Implementation of Polyphase Filterbanks for (Flexible) Multicarrier Systems", *2nd International Workshop on Multi-Carrier Spread-Spectrum (MC-SS 99) and Related Topics*, 49, Oberpfaffenhofen, Germany, September 1999.

[MM02] S. Mirabbasi and K. Martin, "Design of Prototype Filter for Near-Perfect-Reconstruction Overlapped Complex-Modulated Transmultiplexers", *2002 IEEE International Symposium on Circuits and Systems. Proceedings (Cat. No.02CH37353)*, Volume 1, pp. 821–824, Phoenix-Scottsdale, AZ, USA, May 2002, ISBN 0-7803-7448-7.

[MM03] S. Mirabbasi and K. Martin, "Overlapped Complex-Modulated Transmultiplexer Filters with Simplified Design and Superior Stopbands", *IEEE Transactions on Circuits and Systems II: Analog and Digital Signal Processing*, Volume 50, No. 8, pp. 456–469, August 2003.

[MMG$^+$14] N. Michailow, M. Matthe, I. S. Gaspar, A. N. Caldevilla, L. L. Mendes, A. Festag, and G. Fettweis, "Generalized Frequency Division Multiplexing for 5th Generation Cellular Networks", *IEEE Transactions on Communications*, Volume 62, No. 9, pp. 3045–3061, September 2014.

[MN97] D. MacKay and R. Neal, "Near Shannon Limit Performance of Low Density Parity Check Codes", *Electronics Letters*, Volume 33, No. 6, p. 457, March 1997.

[Mon17] F. Monsees, *Signal Processing for Compressed Sensing Multiuser Detection*, Ph.D. Thesis, University of Bremen, November 2017.

[MP13] L. Montreuil and R. Prodan, "OFDM TX Symbol Shaping 802.3bn", 2013.

[MSG$^+$07] G. Matz, D. Schafhuber, K. Gröchenig, M. Hartmann, and F. Hlawatsch, "Analysis, Optimization, and Implementation of Low-Interference Wireless Multicarrier Systems", *IEEE Transactions on Wireless Communications*, Volume 6, No. 5, pp. 1921–1930, May 2007.

[MZ93] S. G. Mallat and Z. Zhang, "Matching Pursuits With Time-Frequency Dictionaries", *IEEE Transactions on Signal Processing*, Volume 41, No. 12, pp. 3397–3415, December 1993.

[NO16] Nokia and O.V., “LTE Evolution for IoT Connectivity”, *Technical report*, Nokia, 2016.

[NSR17] R. Nissel, S. Schwarz, and M. Rupp, “Filter Bank Multicarrier Modulation Schemes for Future Mobile Communications”, *IEEE Journal on Selected Areas in Communications*, Volume 35, No. 8, pp. 1768–1782, August 2017.

[OMM16] A. Osseiran, J. F. Monserrat, and P. Marsch, *5G Mobile and Wireless Communications Technology*, June, Cambridge University Press, 2016, ISBN 9781107130098.

[OWM$^+$12] P. Ochandiano, H. Wymeersch, M. Mendicute, L. Martínez, and I. Sobrón, “Factor Graph based Detection Approach for High-Mobility OFDM Systems with Large FFT Modes”, *EURASIP Journal on Wireless Communications and Networking*, Volume 2012, No. 1, p. 331, December 2012.

[PB61] W. Peterson and D. Brown, “Cyclic Codes for Error Detection”, *Proceedings of the IRE*, Volume 49, No. 1, pp. 228–235, January 1961.

[Pea82] J. Pearl, “Reverend Bayes on Inference Engines: A Distributed Hierarchical Approach”, *Proceedings of the AAAI National Conference on AI*, pp. 133–136, August 1982.

[PKA09] P. Popovski and T. Koike-Akino, “Coded Bidirectional Relaying in Wireless Networks”, *New Directions in Wireless Communications Research*, pp. 291–316, August 2009.

[Pra04] R. Prasad, *OFDM for Wireless Communications Systems*, Artech House, 1st Edition, 2004, ISBN 1580537995.

[Pro07] J. G. Proakis, *Digital Communications*, Irwin Electronics & Computer Enginering, 5th Edition, 2007, ISBN 0072957166.

[PVM95] T. Pollet, M. Van Bladel, and M. Moeneclaey, “BER Sensitivity of OFDM Systems to Carrier Frequency Offset and Wiener Phase Noise”, *IEEE Transactions on Communications*, Volume 43, No. 2/3/4, pp. 191–193, February 1995.

[PY06a] P. Popovski and H. Yomo, “Bi-directional Amplification of Throughput in a Wireless Multi-Hop Network”, *2006 IEEE 63rd Vehicular Technology Conference*, Volume 2, pp. 588–593, IEEE, Melbourne, Vic., Australia, May 2006, ISBN 1-7803-9392-9.

[PY06b] P. Popovski and H. Yomo, “The Anti-Packets Can Increase the Achievable Throughput of a Wireless Multi-Hop Network”, *2006 IEEE International Conference on Communications*, pp. 3885–3890, IEEE, Istanbul, Turkey, June 2006, ISBN 1424403553.

[PY07] P. Popovski and H. Yomo, “Physical Network Coding in Two-Way Wireless Relay Channels”, *2007 IEEE International Conference on*

Communications, Volume 1, pp. 707–712, Ieee, Glasgow, UK, June 2007, ISBN 1-4244-0353-7.

[RMGV14] R. Ratasuk, N. Mangalvedhe, A. Ghosh, and B. Vejlgaard, “Narrowband LTE-M system for M2M communication”, *IEEE Vehicular Technology Conference*, Vancouver, BC, Canada, September 2014, ISBN 9781479944491.

[Roh16] Rohde & Schwarz, “5G Waveform Candidates”, 2016.

[RS97] C. Roche and P. Siohan, “A Family of Extended Gaussian Functions with a Nearly Optimal Localization Property”, *Multi-Carrier Spread-Spectrum*, pp. 179–186, Springer US, Boston, MA, 1997, ISBN 978-1-4615-6231-3.

[RU01] T. J. Richardson and R. L. Urbanke, “The Capacity of Low-Density Parity-Check Codes under Message-Passing Decoding”, *IEEE Transactions on Information Theory*, Volume 47, No. 2, pp. 599–618, February 2001.

[RV08] M. Rudelson and R. Vershynin, “On Sparse Reconstruction from Fourier and Gaussian Measurements”, *Communications on Pure and Applied Mathematics*, Volume 61, No. 8, pp. 1025–1045, August 2008.

[RW06] B. Rankov and A. Wittneben, “Achievable Rate Regions for the Two-way Relay Channel”, *2006 IEEE International Symposium on Information Theory*, 1, pp. 1668–1672, IEEE, Seattle, WA, USA, July 2006, ISBN 1-4244-0505-X.

[RW07] B. Rankov and A. Wittneben, “Spectral Efficient Protocols for Half-Duplex Fading Relay Channels”, *IEEE Journal on Selected Areas in Communications*, Volume 25, No. 2, pp. 379–389, February 2007.

[Sal67] B. Saltzberg, “Performance of an Efficient Parallel Data Transmission System”, *IEEE Transactions on Communication Technology*, Volume 15, No. 6, pp. 805–811, December 1967.

[SB03] T. Strohmer and S. Beaver, “Optimal OFDM Design for Time-Frequency Dispersive Channels”, *IEEE Transactions on Communications*, Volume 51, No. 7, pp. 1111–1122, July 2003.

[SBD13a] H. F. Schepker, C. Bockelmann, and A. Dekorsy, “Coping with CDMA Asynchronicity in Compressive Sensing Multi-User Detection”, *IEEE Vehicular Technology Conference*, Dresden, Germany, June 2013, ISBN 9781467363372.

[SBD13b] H. F. Schepker, C. Bockelmann, and A. Dekorsy, “Exploiting Sparsity in Channel and Data Estimation for Sporadic Multi-User Communication”, *Proceedings of the International Symposium on Wireless Communication Systems*, Volume 9, pp. 288–292, Ilmenau, Germany, Germany, August 2013, ISBN 9783800735297.

[Sch86] R. Schmidt, “Multiple Emitter Location and Signal Parameter Estimation”, *IEEE Transactions on Antennas and Propagation*, Volume 34, No. 3, pp. 276–280, March 1986.

[Sch01] H. Schmidt, *OFDM für die drahtlose Datenübertragung innerhalb von Gebäuden*, Ph.D. Thesis, University of Bremen, Germany, June 2001.

[Sch15] H. F. Schepker, *Compressive Sensing Multi-User Detection Approaches for Sporadic Communication*, Ph.D. Thesis, University of Bremen, 2015.

[Sch16] S. Schedler, *Generalized Frequency Division Multiplexing in the Two-Way-Relay Channel*, Ph.d. thesis, University of Rostock, 2016.

[SD11] H. F. Schepker and A. Dekorsy, “Sparse Multi-User Detection for CDMA Transmission using Greedy Algorithms”, *Proceedings of the International Symposium on Wireless Communication Systems*, pp. 291–295, Aachen, Germany, November 2011, ISBN 9781612844022.

[SFRU01] Sae-Young Chung, G. Forney, T. Richardson, and R. Urbanke, “On the Design of Low-Density Parity-Check Codes within 0.0045 dB of the Shannon Limit”, *IEEE Communications Letters*, Volume 5, No. 2, pp. 58–60, February 2001.

[SG12] A. Schmidt and W. Gerstacker, “Trellis-based Equalization Schemes for Physical Layer Network Coding”, *IEEE International Conference on Communications*, pp. 4746–4750, 2012.

[SGA12] A. Sahin, I. Güvenç, and H. Arslan, “A Survey on Prototype Filter Design for Filter Bank Based Multicarrier Communications”, *Online: http://arxiv. org/pdf/1212.3374. pdf*, December 2012.

[SGA13] A. Sahin, I. Güvenc, and H. Arslan, “A Survey on Multicarrier Communications: Prototype Filters, Lattice Structures, and Implementation Aspects”, *IEEE Communications Surveys & Tutorials*, Volume 16, No. 3, pp. 1312–1338, December 2013.

[She16] J. Shelnutt, “Service Provider Opportunities and Strategies in IoT”, 2016.

[SJ09] M. Schellmann and V. Jungnickel, “Multiple CFOs in OFDM-SDMA Uplink: Interference Analysis and Compensation”, *EURASIP Journal on Wireless Communications and Networking*, Volume 909075, No. 14, April 2009.

[SK15] S. Schedler and V. Kühn, “Influence of Lattice Spacing in Disturbed Generalized Frequency Division Multiplexing Systems”, *IEEE Vehicular Technology Conference*, Volume 2015, pp. 1–5, IEEE, Glasgow, UK, May 2015, ISBN 9781479980888.

[SK16] S. Schedler and V. Kühn, “Optimal Lattice Spacing for GFDM with Gaussian Waveform”, *IEEE Wireless Communications and*

Networking Conference, Volume 2016, Doha, Qatar, September 2016, ISBN 9781467398145.

[SKJ95] H. Sari, G. Karam, and I. Jeanclaude, "Transmission Techniques for Digital Terrestrial TV Broadcasting", *IEEE Communications Magazine*, Volume 33, No. 2, pp. 100–109, February 1995.

[SN96] G. Strang and T. Nguyen, *Wavelets and Filter Banks*, Wellesley-Cambridge Press, 1996.

[SR00] P. Siohan and C. Roche, "Cosine-Modulated Filterbanks based on Extended Gaussian Functions", *IEEE Transactions on Signal Processing*, Volume 48, No. 11, pp. 3052–3061, November 2000.

[SSG$^+$14] A. Sabharwal, P. Schniter, D. Guo, D. W. Bliss, S. Rangarajan, and R. Wichman, "In-Band Full-Duplex Wireless: Challenges and Opportunities", *IEEE Journal on Selected Areas in Communications*, Volume 32, No. 9, pp. 1637–1652, September 2014.

[SSL02] P. Siohan, C. Siclet, and N. Lacaille, "Analysis and Design of OFDM/OQAM Systems based on Filterbank Theory", *IEEE Transactions on Signal Processing*, Volume 50, No. 5, pp. 1170–1183, May 2002.

[STB11] S. Sesia, I. Toufik, and M. Baker, *LTE - The UMTS Long Term Evolution*, John Wiley & Sons, Ltd, Chichester, UK, July 2011, ISBN 9780470978504.

[Str98] T. Strohmer, "Numerical Algorithms for Discrete Gabor Expansions", *Gabor Analysis and Algorithms*, pp. 267–294, Birkhäuser Boston, Boston, MA, 1998.

[Str16] G. Strang, *Introduction to Linear Algebra, Fifth Edition*, Wellesley-Cambridge Press, 2016, ISBN 978-09802327-7-6.

[SW19] S. K. Sharma and X. Wang, "Towards Massive Machine Type Communications in Ultra-Dense Cellular IoT Networks: Current Issues and Machine Learning-Assisted Solutions", *IEEE Communications Surveys & Tutorials*, pp. 1–1, may 2019.

[SZL$^+$14] M. Schellmann, Z. Zhao, H. Lin, P. Siohan, N. Rajatheva, V. Luecken, and A. Ishaque, "FBMC-based Air Interface for 5G Mobile: Challenges and Proposed Solutions", *Proceedings of the 9th International Conference on Cognitive Radio Oriented Wireless Networks*, i, pp. 102 – 107, ICST, Oulu, Finland, July 2014, ISBN 978-1-63190-003-7.

[TJ18] M. Towliat and S. M. Javad Asgari Tabatabaee, "On the Time-Frequency Symbol Density of FBMC/QAM Systems", *International Journal of Communication Systems*, Volume 31, No. 6, p. e3516, April 2018.

[Tro04] J. A. Tropp, "Greed is good: Algorithmic results for sparse approximation", *IEEE Transactions on Information Theory*, Volume 50, No. 10, pp. 2231–2242, 2004.

[Ung74] G. Ungerboeck, "Adaptive Maximum-Likelihood Receiver for Carrier-Modulated Data-Transmission Systems", *IEEE Transactions on Communications*, Volume 22, No. 5, pp. 624–636, May 1974.

[Uts16] W. Utschick (Editor), *Communications in Interference Limited Networks*, Signals and Communication Technology, Springer International Publishing, Berlin, Germany, 2016, ISBN 978-3-319-22439-8.

[Vai93] P. P. Vaidyanathan, *Multirate Systems and Filter Banks*, Prentice-Hall, Inc., Upper Saddle River, NJ, USA, 1993, ISBN 0-13-605718-7.

[Ver98] S. Verdu, *Multiuser Detection*, Cambridge University Press, New York, NY, USA, 1st Edition, 1998, ISBN 9780521593731.

[Vit67] A. Viterbi, "Error Bounds for Convolutional Codes and an Asymptotically Optimum Decoding Algorithm", *IEEE Transactions on Information Theory*, Volume 13, No. 2, pp. 260–269, April 1967.

[Vog06] S. Vogeler, *Verfahren zur Kompensation von Doppler-Einflüssen in Mehrträger-Übertragungssystemen.*, Ph.D. Thesis, University of Bremen, Germany, Aachen, Germany, August 2006.

[VT16] R. Vannithamby and S. Talwar (Editors), *Towards 5G*, John Wiley & Sons, Ltd, Chichester, UK, December 2016, ISBN 9781118979846.

[VWS$^+$13] V. Vakilian, T. Wild, F. Schaich, S. Ten Brink, and J. F. Frigon, "Universal-filtered multi-carrier technique for wireless systems beyond LTE", *2013 IEEE Globecom Workshops, GC Wkshps 2013*, pp. 223–228, IEEE, Atlanta, GA, USA, December 2013, ISBN 9781479928514.

[Wan12] Q. Wang, *Performance Evaluation of Practical OFDM Systems with Imperfect Synchronization*, Ph.D. Thesis, Technische Universität Wien, 2012.

[WHZW13] Z. Wang, J. Huang, S. Zhou, and Z. Wang, "Iterative Receiver Processing for OFDM Modulated Physical-Layer Network Coding in Underwater Acoustic Channels", *IEEE Transactions on Communications*, Volume 61, No. 2, pp. 541–553, February 2013.

[Wil16] C. Willuweit, *Analyse und effziente Implementierung von MCSM als Zugriffsverfahren für die massive Kommunikation im Industrie 4.0 Umfeld*, diploma thesis, University of Bremen, October 2016.

[WJK$^+$14] G. Wunder, P. Jung, M. Kasparick, T. Wild, F. Schaich, Y. Chen, S. T. Brink, I. Gaspar, N. Michailow, A. Festag, L. Mendes, N. Cassiau, D. Kténas, M. Dryjański, S. Pietrzyk, B. Eged, P. Vago, and F. Wiedmann, "5GNOW: Non-Orthogonal, Asynchronous Waveforms for Future Mobile Applications", *IEEE Communications Magazine*, Volume 52, No. 2, pp. 97–105, February 2014.

[WL10] D. Wübben and Y. Lang, "Generalized Sum-Product Algorithm for Joint Channel Decoding and Physical-Layer Network Coding in Two-Way Relay Systems", *2010 IEEE Global Telecommunications*

Conference GLOBECOM 2010, pp. 1–5, IEEE, December 2010, ISBN 978-1-4244-5636-9.

[WLA$^+$17] Y.-P. P. E. Wang, X. Lin, A. Adhikary, A. Grövlen, Y. Sui, Y. Blankenship, J. Bergman, H. S. Razaghi, A. Grovlen, Y. Sui, Y. Blankenship, J. Bergman, and H. S. Razaghi, "A Primer on 3GPP Narrowband Internet of Things", *IEEE Communications Magazine*, Volume 55, No. 3, pp. 117–123, March 2017.

[WLW$^+$16a] M. Wu, F. Ludwig, D. Wübben, A. Dekorsy, K.-D. Kammeyer, and S. Paul, "Physical Layer Cooperation in One-Way Relaying Systems", W. Utschick (Editor), *Communications in Interference-Limited Networks*, pp. 431–450, Springer, 2016.

[WLW$^+$16b] M. Wu, F. Ludwig, D. Wübben, A. Dekorsy, and S. Paul, "Physical Layer Cooperation in Two-Way Relaying Systems", W. Utschick (Editor), *Communications in Interference-Limited Networks*, pp. 451–474, Springer, February 2016.

[Woo53] P. M. Woodward, *Probability and Information Theory, with Application to Radar*, Radar Library, Artech House, ˆ2 Edition, 1953, ISBN 9780890061039.

[WS01] A. Worthen and W. Stark, "Unified Design of Iterative Receivers using Factor Graphs", *IEEE Transactions on Information Theory*, Volume 47, No. 2, pp. 843–849, 2001.

[Wu17] M. Wu, *Physical-Layer Cooperation in Coded OFDM Relaying Systems*, Ph.D. Thesis, University of Bremen, December 2017.

[Wüb10] D. Wübben, "Joint Channel Decoding and Physical-Layer Network Coding in Two-Way QPSK Relay Systems by a Generalized Sum-Product Algorithm", *2010 7th International Symposium on Wireless Communication Systems*, September, pp. 576–580, IEEE, York, UK, September 2010, ISBN 978-1-4244-6315-2.

[Wun13] G. Wunder, "5GNOW: Deliverable D2.1: 5G Cellular Communications Scenarios and System Requirements", *Technical report*, 5GNOW, 2013.

[WV99] X. Wang and H. Vincent Poor, "Iterative (Turbo) Soft Interference Cancellation and Decoding for Coded CDMA", *IEEE Transactions on Communications*, Volume 47, No. 7, pp. 1046–1061, July 1999.

[WWD13a] M. Wu, D. Wübben, and A. Dekorsy, "Mutual Information Based Analysis for Physical-Layer Network Coding with Optimal Phase Control", *Proceedings of 2013 9th International ITG Conference on Systems, Communication and Coding (SCC)*, pp. 1–6, VDE, Munich, Germany, January 2013.

[WWD13b] M. Wu, D. Wübben, and A. Dekorsy, "Physical-Layer Network Coding in Coded OFDM Systems with Multiple-Antenna Relay", *2013 IEEE 77th Vehicular Technology Conference (VTC Spring)*, pp. 1–5, Ieee, Dresden, Germany, June 2013, ISBN 978-1-4673-6337-2.

[WWD14a] D. Wübben, M. Wu, and A. Dekorsy, "Adaptive Broadcast Transmission in Distributed Two-Way Relaying Networks", *European Signal Processing Conference*, 1, pp. 1143–1147, Lisbon, Portugal, September 2014, ISBN 9780992862619.

[WWD14b] D. Wübben, M. Wu, and A. Dekorsy, "Physical-Layer Network Coding with Multiple-Antenna Relays", M. M. da Silva and F. A. Monteiro (Editors), *MIMO Processing for 4G and Beyond*, pp. 491–513, CRC Press, 2014, ISBN 978-1-4665-9807-2.

[Wym07] H. Wymeersch, *Iterative Receiver Design*, Cambridge University Press, Cambridge, 2007, ISBN 9780511619199.

[XCT+11] R. Xu, M. Chen, C. Tian, X. Lu, and C. Diao, "Statistical Distributions of OFDM Signals on Multi-Path Fading Channel", *2011 International Conference on Wireless Communications and Signal Processing (WCSP)*, pp. 1–6, IEEE, Nanjing, China, November 2011, ISBN 978-1-4577-1010-0.

[XM10] X. Xu and R. Mathar, "Factor Graph based Detection and Channel Estimation for MIMO-OFDM Systems in Doubly Selective Channel", *Proceedings of the 2010 7th International Symposium on Wireless Communication Systems, ISWCS'10*, pp. 456–460, Ieee, York, UK, September 2010, ISBN 9781424463169.

[XXX12] X. Xia, K. Xu, and Y. Xu, "Asynchronous Physical-layer Network Coding Scheme for Two-way OFDM Relay", *arXiv preprint arXiv:1204.2692*, 2012.

[Yeu08] R. W. Yeung, *Information Theory and Network Coding*, Volume 55, Springer US, Boston, MA, 2008, ISBN 978-0-387-79233-0.

[ZBT+16] A. A. Zaidi, R. Baldemair, H. Tullberg, H. Bjorkegren, L. Sundstrom, J. Medbo, C. Kilinc, and I. Da Silva, "Waveform and Numerology to Support 5G Services and Requirements", *IEEE Communications Magazine*, Volume 54, No. 11, pp. 90–98, November 2016.

[ZCL+15] Z. Zhang, X. Chai, K. Long, A. V. Vasilakos, and L. Hanzo, "Full Duplex Techniques for 5G Networks: Self-Interference Cancellation, Protocol Design, and Relay Selection", *IEEE Communications Magazine*, Volume 53, No. 5, pp. 128–137, May 2015.

[ZG11] H. Zhu and G. B. Giannakis, "Exploiting Sparse User Activity in Multiuser Detection", *IEEE Transactions on Communications*, Volume 59, No. 2, pp. 454–465, 2011.

[ZL09] S. Zhang and S.-C. Liew, "Channel Coding and Decoding in a Relay System Operated with Physical-Layer Network Coding", *IEEE Journal on Selected Areas in Communications*, Volume 27, No. 5, pp. 788–796, June 2009.

[ZL10] S. Zhang and S.-C. Liew, “Applying Physical-Layer Network Coding in Wireless Networks”, *EURASIP Journal on Wireless Communications and Networking*, Volume 2010, pp. 1–12, January 2010.

[ZLL06a] S. Zhang, S.-C. Liew, and P. Lam, “On the Synchronization of Physical-Layer Network Coding”, *2006 IEEE Information Theory Workshop - ITW ’06 Chengdu*, pp. 404–408, IEEE, Punta del Este, Uruguay, October 2006, ISBN 1-4244-0035-X.

[ZLL06b] S. Zhang, S.-C. Liew, and P. P. Lam, “Hot Topic: Physical-Layer Network Coding”, *Proceedings of the 12th annual international conference on Mobile computing and networking - MobiCom ’06*, MobiCom ’06, p. 358, ACM Press, New York, New York, USA, 2006, ISBN 1595932860.

[ZLW13] S. Zhang, S.-C. Liew, and H. Wang, “Synchronization Analysis for Wireless TWRC Operated with Physical-layer Network Coding”, *Wireless Personal Communications*, Volume 68, No. 3, pp. 637–653, February 2013.

[ZSG$^+$16] Z. Zhao, M. Schellmann, X. Gong, Q. Wang, R. Böhnke, and Y. Guo, “Pulse Shaped OFDM for 5G Systems”, *arXiv preprint arXiv:1605.03731*, pp. 1–40, May 2016.

[ZY95] W. Zou and Yiyan Wu, “COFDM: An Overview”, *IEEE Transactions on Broadcasting*, Volume 41, No. 1, pp. 1–8, March 1995.

Index